



**Journal of
Mechanics of
Materials and Structures**

Volume 8, No. 2-4

April-June 2013



JOURNAL OF MECHANICS OF MATERIALS AND STRUCTURES

msp.org/jomms

Founded by Charles R. Steele and Marie-Louise Steele

EDITORIAL BOARD

ADAIR R. AGUIAR	University of São Paulo at São Carlos, Brazil
KATIA BERTOLDI	Harvard University, USA
DAVIDE BIGONI	University of Trento, Italy
IWONA JASIUK	University of Illinois at Urbana-Champaign, USA
THOMAS J. PENCE	Michigan State University, USA
YASUhide SHINDO	Tohoku University, Japan
DAVID STEIGMANN	University of California at Berkeley

ADVISORY BOARD

J. P. CARTER	University of Sydney, Australia
R. M. CHRISTENSEN	Stanford University, USA
G. M. L. GLADWELL	University of Waterloo, Canada
D. H. HODGES	Georgia Institute of Technology, USA
J. HUTCHINSON	Harvard University, USA
C. HWU	National Cheng Kung University, Taiwan
B. L. KARIHALOO	University of Wales, UK
Y. Y. KIM	Seoul National University, Republic of Korea
Z. MROZ	Academy of Science, Poland
D. PAMPLONA	Universidade Católica do Rio de Janeiro, Brazil
M. B. RUBIN	Technion, Haifa, Israel
A. N. SHUPIKOV	Ukrainian Academy of Sciences, Ukraine
T. TARNAI	University Budapest, Hungary
F. Y. M. WAN	University of California, Irvine, USA
P. WRIGGERS	Universität Hannover, Germany
W. YANG	Tsinghua University, China
F. ZIEGLER	Technische Universität Wien, Austria

PRODUCTION production@msp.org

SILVIO LEVY Scientific Editor

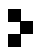
Cover photo: Mando Gomez, www.mandolux.com

See msp.org/jomms for submission guidelines.

JoMMS (ISSN 1559-3959) at Mathematical Sciences Publishers, 798 Evans Hall #6840, c/o University of California, Berkeley, CA 94720-3840, is published in 10 issues a year. The subscription price for 2013 is US\$555/year for the electronic version, and \$705/year (+\$60, if shipping outside the US) for print and electronic. Subscriptions, requests for back issues, and changes of address should be sent to MSP.

JoMMS peer-review and production is managed by EditFLOW® from Mathematical Sciences Publishers.

PUBLISHED BY

 **mathematical sciences publishers**
nonprofit scientific publishing

<http://msp.org/>

© 2013 Mathematical Sciences Publishers

A DIFFUSE COHESIVE ENERGY APPROACH TO FRACTURE AND PLASTICITY: THE ONE-DIMENSIONAL CASE

GIANPIETRO DEL PIERO, GIOVANNI LANCIONI AND RICCARDO MARCH

In the fracture model presented in this paper, the basic assumption is that the energy is the sum of two terms, one elastic and one cohesive, depending on the elastic and inelastic part of the deformation, respectively. Two variants are examined: a local model, and a nonlocal model obtained by adding a gradient term to the cohesive energy. While the local model only applies to materials which obey Drucker's postulate and only predicts catastrophic failure, the nonlocal model describes the softening regime and predicts two collapse mechanisms, one for brittle fracture and one for ductile fracture.

In its nonlocal version, the model has two main advantages over the models existing in the literature. The first is that the basic elements of the theory (the yield function, hardening rule, and evolution laws) are not assumed, but are determined as necessary conditions for the existence of solutions in incremental energy minimization. This reduces to a minimum the number of independent assumptions required to construct the model. The second advantage is that, with appropriate choices of the analytical shape of the cohesive energy, it becomes possible to reproduce, with surprising accuracy, a large variety of observed experimental responses. In all cases, the model provides a description of the entire evolution, from the initial elastic regime to final rupture.

1. Introduction

Since the pioneering paper [Francfort and Marigo 1998], the variational approach to fracture has been the object of intense research. A reason for this is the availability of numerical instruments supporting the theory, which are capable of solving practical problems in fracture mechanics. One such instrument is the regularization technique of Ambrosio and Tortorelli [1990], initially conceived for the image segmentation problem [Mumford and Shah 1989], and applied to fracture problems by Bourdin, Francfort and Marigo [2000]. The regularization consists in approximating the energy of a fractured body, which by its own nature is defined on discontinuous deformations with bounded variation, by a family of functionals defined in a Sobolev space. This makes it possible to solve fracture problems using standard finite element techniques.

The original paper [Francfort and Marigo 1998] and the subsequent developments were based on the brittle fracture model of Griffith [1920], in which the presence of singular discontinuity surfaces for the displacement is allowed at the interior of an elastic body. In fact, long before the appearance of [Francfort and Marigo 1998], more sophisticated models, based on Barenblatt's *cohesive fracture* hypothesis [Barenblatt 1962], were used in fracture mechanics. They were particularly efficient in situations in which fracture is preceded by a regime of large inelastic deformation, like in the rupture of concrete and other nonmetallic materials [Hillerborg 1991; Carpinteri and Massabò 1997]. In this respect, a fundamental

Keywords: nonlocal plasticity, strain localization, variational fracture, ductile fracture, incremental energy minimization.

role was played by the *cohesive crack model* of [Hillerborg et al. 1976]. The development of the theories of rupture for concrete over the following decades is documented in the review papers [Carpinteri 1982; Bažant and Chen 1997; Bažant and Jirásek 2002; Bažant and Le 2009].

With the cohesive energy model, two basic aspects of energy minimization became evident. The first is the relevance of local, versus global, minimization. This point has received significant attention in the recent literature [Dal Maso and Toader 2002; Marigo and Truskinovsky 2004], and is now generally accepted. The second aspect is the relevance of the role played by energy dissipation. Indeed, with a minimization constrained by a dissipation inequality it is possible to reproduce some sophisticated aspects of material response such as, for instance, elastic unloading in plasticity [Del Piero and Truskinovsky 2009].

The present paper originates from a reflection on similarities and differences between the cohesive energy scheme and the Ambrosio–Tortorelli approximation. For both, the energy functional depends on the elastic deformation plus a second variable which provides a regularized representation of fracture. But, while the cohesive energy is usually assumed to be a surface energy, the regularizing term in [Ambrosio and Tortorelli 1990] is a volume integral.

The question naturally arises, of whether or not it is convenient to assume a cohesive energy concentrated on singular surfaces. In ductile materials, before rupture, the appearance of a *process zone* is observed, in which the material becomes weaker and more deformable. This phenomenon can be described by damage [Babadjian 2011] or plasticity [Dal Maso and Toader 2010] theories. Cohesive energies diffused over the volume were recently considered in the modeling of brittle fracture [Volkh 2004] and damage [Benallal and Marigo 2007; Pham et al. 2011], and in the variational theory of fracture [Freddi and Royer-Carfagni 2010]. In particular, [Pham and Marigo 2010a] deals with a model of energy minimization, in which rupture is preceded by progressive damage. In it, the one-dimensional energy functional has the form

$$\int_0^l (w(u'(x), \gamma(x)) + \theta(\gamma(x))) dx, \quad (1-1)$$

where w is the bulk energy density, u' is the axial deformation, and γ is an internal variable representing the intensity of damage. In the present paper we consider the special case

$$\int_0^l (w(\epsilon(x)) + \theta(\gamma(x))) dx, \quad (1-2)$$

in which $\epsilon(x) = u'(x) - \gamma(x)$ is the elastic part of the deformation. Of the two energy densities w and θ , the first is assumed to be reversible and the second is assumed to be totally dissipated. By assuming w independent of γ , we purposely renounce any description of damage. Though our initial purpose was to construct something more general than a plasticity theory, to our surprise we realized that, as we shall see below, the energy (1-2) provides exactly the classical incremental theory of plasticity exposed, for example, in [Hill 1950].

A weak point of the model is that it fails to describe the *strain-softening response* which, as well-known from the literature, is associated with localization of the plastic deformation. These effects can be captured by adding a nonlocal term of the gradient type

$$\int_0^l (w(\epsilon(x)) + \theta(\gamma(x))) dx + \frac{1}{2}\alpha \int_0^l \gamma'^2(x) dx, \quad (1-3)$$

which successfully captures some specific effects of material response in a large variety of models, like the van der Waals model for capillarity [van der Waals 1893; Casal 1972], the Cahn–Hilliard model for phase transition [Cahn and Hilliard 1958], Mumford–Shah image segmentation theory [Mumford and Shah 1989], some theories of liquid crystals [Frank 1958; Ericksen 1990], and some numerical models for the rupture of concrete [Borst and Pamir 1996]. A nonlocal term was also used in [Truskinovsky 1996] to construct a cohesive zone model starting from the energy of interatomic attraction (Lennard-Jones potential).

The addition of a gradient term renders the expression (1-3) of the energy similar to the Ambrosio–Tortorelli functional

$$\int_0^l (s^2(x) + \kappa_\alpha) w(u'(x)) dx + \frac{1}{2} \alpha \int_0^l \left(s'^2(x) + \frac{c}{\alpha^2} (1 - s(x))^2 \right) dx. \quad (1-4)$$

Indeed, in both cases the total energy is the sum of a basic energy and a perturbing gradient term, and in both cases the deformation is accompanied by a second independent variable. The main difference is that in (1-3) the second variable is the inelastic part of the deformation, while in (1-4) the scalar field $s \in [0, 1]$ measures the *fracture intensity* in the regularized model. Also different is the nature of the smallness parameter α . In (1-4), α is the coefficient of a singular perturbation, and what is important is the asymptotic behavior of the solution when $\alpha \rightarrow 0$. In fracture theory, α is a fixed material constant, usually interpreted as an *internal length* determined by the microscopic structure of the material [Bažant and Pijaudier-Cabot 1989; Bažant and Jirásek 2002; Pham et al. 2011].

The value of α strongly influences the material’s response. Indeed, the ratio between internal length and the length l of the bar is an indicator of the brittleness of the fracture. A reduction of α has the same effect as an increase of l , that is, a transition from rupture preceded by a long regime of gradual weakening to sudden catastrophic failure. For fixed α and varying l , this is the well-known *size effect* of fracture mechanics.

The requirement of nonnegativeness of the first variation leads to Kuhn–Tucker conditions very similar, and sometimes identical, to the governing equations of the gradient theories of plasticity [Aifantis 1992; Fleck and Hutchinson 2001; Gurtin and Anand 2005] and damage [Benallal and Marigo 2007; Pham and Marigo 2010b; Pham et al. 2011], which, starting from the pioneering paper [Aifantis 1984], have been developed by several authors in the last two decades. In particular, the expression of the first variation of the energy given in Section 3.2 is the one-dimensional counterpart of the expression of the virtual power currently assumed in the theories of strain-gradient plasticity [Gurtin 2003; Gudmundson 2004; Gurtin and Anand 2005].

An accurate review, analysis, and comparison of such theories can be found in [Jirásek and Rolshoven 2009a; 2009b]. Most theories include a number of assumptions which fix the basic physical aspects of plastic response:

- the stress-strain elastic law,
- the hardening rule,
- the evolution laws,
- the loading-unloading conditions,
- the yield function.

The underlying continuum can be either a classical or a generalized continuum. In a classical continuum the plastic deformation is regarded as a state variable, the Cauchy stress is the unique stress measure, and supplementary generalized forces are defined as the conjugates of the gradients of the plastic deformation. In a generalized continuum, higher-order stresses appear as conjugates of the higher-order deformation gradients.

The two cases are analyzed in [Jirásek and Rolshoven 2009b] and [2009a], respectively. The number and variety of theories reported therein shows by itself that there is yet no agreement about the choice of a fully satisfactory model. The present paper has the ambition of presenting a mathematically sound model, based on very simple assumptions, and providing a very flexible description of the entire evolution from the initial elastic regime to final rupture.

The basic assumptions are the forms of the elastic energy and of the dissipative cohesive energy. Proceeding by incremental energy minimization, all classical hypotheses listed above are obtained as necessary conditions for a minimum. The analytical forms of the functions defined in the above hypotheses are already contained in the assumed form of the cohesive energy. In particular, the dissipative character assumed for the cohesive energy provides the basis for the description of elastic unloading, and the shape of the cohesive energy can be chosen to reproduce a large variety of responses, hardening or softening, and with the plastic strain diffusing over the body or localizing on small regions.

Surface cohesive energies have proved to be an efficient tool for formulating and solving fracture problems. Here we show that volume cohesive energies can be a very natural way for describing fracture as a terminal event in an evolution involving plasticity or damage. Of course, there is no claim of generality for the model presented here. It can be generalized in several directions. We just like to compare the simplicity of the starting assumptions and of the incremental minimizing procedure, with the richness of the responses that can be obtained by acting on the analytical shape of the cohesive energy.

Our analysis is restricted to the one-dimensional case. This allows us to get the basic results avoiding a number of technical complications, at the cost of neglecting some important aspects congenital to higher dimension. The paper is divided into four sections. After the present introduction, Sections 2 and 3 deal with the local and nonlocal models, respectively, and Section 4 reports some numerical simulations on the nonlocal model and compares them with experiments. The local model is introduced in Section 2.1, and in Section 2.2 the equilibrium configurations are identified with the stationary points of the energy (1-2). Due to the unilateral character of the dissipation constraint, the Euler equation is replaced by an inequality. This inequality provides an upper bound for the axial force, depending on the current value of the plastic deformation. In this way, the *yield condition* is obtained.

The minimum properties of the stationary points are investigated in Section 2.3. The following subsections deal with the quasistatic evolution of the inelastic deformation under varying load, along a path made of energy minimizers. For simplicity, we only consider a bar under a hard device, for which the load consists of displacements applied at the endpoints. Section 2.4 is devoted to incremental energy minimization. In a first-order approximation, the minimization consists in determining the direction of steepest descent under the given load increment. The result is that along that direction the inelastic deformation does not change in the elastic regime, that is, when the yield condition is satisfied as a strict inequality. On the contrary, in the inelastic regime the inelastic strain rate remains unspecified.

For its determination, a second-order minimization is required. In it, some basic properties of classical plasticity, such as the *hardening rule*, the *consistency condition* for the inelastic deformation at loading,

and the property of *elastic unloading* are obtained as necessary conditions for a minimum. The minimization leads to a first-order differential problem, involving the current values of the inelastic deformation and of the inelastic strain rate. This problem is studied in Section 2.5. In the inelastic regime, at each time t the response is determined by the sign of the second derivative of θ at the current deformation γ_t : the response is work-hardening for $\theta''(\gamma_t) > 0$ and perfectly plastic for $\theta''(\gamma_t) = 0$. For $\theta''(\gamma_t)$ negative, the deformation concentrates at a single point, determining catastrophic rupture.

The local model provides a classical incremental plasticity theory [Hill 1950], obeying Drucker's *material stability postulate* [Drucker 1952]:

$$\dot{\sigma}_t \dot{\gamma}_t \geq 0, \quad (1-5)$$

which does not allow for a strain-softening response. Within this restricted context, the model correctly describes a plastic response followed by brittle fracture in the sense of Griffith's theory.

The nonlocal model based on the energy (1-3) is discussed in Section 3. Due to the presence of a gradient term, more regularity and supplementary boundary conditions are required. The additional regularity assumptions are made in Section 3.1, and two different options for the supplementary boundary conditions are considered in Section 3.2. The choice of the supplementary boundary conditions is a delicate problem; see, for example, the discussion in [Jirásek and Rolshoven 2009b, §3.4]. Our choice of imposing a null inelastic deformation γ at the boundary is motivated by a closer adherence to the constraint devices used in laboratory tests.

The minimum properties of the equilibrium configurations, still identified with the stationary points of the energy, are investigated in Section 3.3. Due to the stabilizing effect of the nonlocal term, the necessary conditions for a minimum are weaker than in the local model. In particular, moderate negative values of $\theta''(\gamma(x))$ become acceptable, and this renders admissible a strain-softening response. In the language of [Jirásek and Rolshoven 2009a; 2009b], the nonlocal term acts as a *localization limiter*, since it opposes the localization of the inelastic deformation.

The quasistatic evolution under a given load process is studied in Section 3.4. A first-order minimization still provides the direction of steepest descent for the energy functional. Along this direction, the inelastic strain rate $\dot{\gamma}_t(x)$ is zero in the *elastic zone*, that is, at points x at which the yield condition is satisfied as a strict inequality. Surprisingly enough, this conclusion is partially contradicted in the second-order minimization, in which nonnull inelastic strain rates are allowed inside the elastic zone, at points sufficiently close to the interface with the inelastic zone.

The second-order minimization provides a set of Kuhn–Tucker conditions, which governs the quasistatic evolution of the inelastic deformation. Due to the presence of the nonlocal terms, closed-form solutions can be found only in some special cases. One of them is the onset of the inelastic regime, studied in detail in Section 3.5. In the determination of the incremental response at the onset, a fundamental role is played by the nondimensional ratio l/l_i , where

$$l_i \doteq 2\pi \sqrt{\frac{\alpha}{-\theta''(0)}} \quad (1-6)$$

is the *internal length of the material at the onset*. Indeed, the response is work-hardening if $l < l_i/2$ and strain-softening if $l > l_i/2$. Moreover, for $l < l_i$ the response is *full-size*, that is, the inelastic strain rate is diffused over the whole bar, while for $l > l_i$ the inelastic strain rate localizes on a region of length l_i .

It is possible that catastrophic failure occurs just at the onset of the inelastic regime. This circumstance, which we call *totally brittle fracture*, depends on a second nondimensional ratio l/l_c , where

$$l_c \doteq 2\pi \sqrt{\frac{\alpha}{w''(\beta_c)}} \quad (1-7)$$

is the *characteristic length* at the onset and β_c is the value of the load β at the onset. In fact, totally brittle fracture occurs when l/l_c is less than a given function of l/l_i .

A qualitative analysis of the response in the inelastic regime is made in Section 3.6. In it, internal length and characteristic length are considered as functions of the current inelastic and elastic deformation

$$l_{it} = 2\pi \sqrt{\frac{\alpha}{-\theta_t''}}, \quad l_{ct} = 2\pi \sqrt{\frac{\alpha}{w''(\epsilon_t)}}, \quad (1-8)$$

respectively, where θ_t'' is an average of $\theta''(\gamma_t(x))$ over the bar in the current inelastic deformation γ_t . In this way, by extrapolation of the exact results obtained at the onset, it is possible to obtain an approximate picture of the bar's evolution up to final rupture.

In particular, from this qualitative analysis two fundamental types of evolution emerge. They depend on the convexity-concavity properties of the derivative θ' of the cohesive energy, and determine two very different collapse mechanisms. If θ' is concave, an increasing load produces a progressive localization of the inelastic deformation, and a progressive increase of the negative slope of the force-elongation response curve. In the limit, an extreme localization and an infinite slope of the response curve produce catastrophic failure. On the contrary, if θ' is convex, under increasing load the inelastic deformation diffuses over larger and larger zones, and the negative slope of the curve decreases. In the limit the slope tends to zero, and the bar elongates indefinitely at constant force.

The two collapse mechanisms are typical of materials with crystalline structure and with random structure, respectively. In Section 4 both are investigated by means of numerical simulations, with the purpose of reproducing the response curves of two real materials, concrete and steel. The correspondence of the simulations with the experimental curves is obtained by fitting a very small number of parameters, that is, the material constants necessary to represent the cohesive energy θ as a piecewise polynomial function. The result is impressive. It shows that an appropriate choice of the expression of the cohesive energy can indeed capture not only the overall behavior, but also many detailed features of the response curve, in the whole evolution from the initial natural state up to rupture.

Roughly, the main results of the present study can be summarized as follows.

- In its nonlocal version, the diffuse cohesive energy model captures both brittle and ductile fracture modes. In brittle fracture the inelastic deformation tends to localize on singular surfaces, and in ductile fracture it tends to spread over the whole bar. Brittle fracture may also take place without any preliminary regime of inelastic deformation.
- A convex cohesive energy produces a full-size work-hardening response. A concave energy may produce a full-size or localized, work-hardening or strain-softening response, depending on the ratio between the current internal length and the length of the bar.
- For θ concave, a convex θ' produces brittle fracture, and a concave θ' produces ductile fracture.

- Brittle fracture occurs when the current internal length reaches a critical value depending on the current characteristic length.

Some of these results, reflecting an earlier stage of the present research, were announced in [Del Piero et al. 2012]. But even the present results are not complete, since many problems are left open. Specifically, it seems very difficult to reach the same level of detail in a two or three-dimensional context. Also, a big challenge is how to find general, physically motivated correlations between the convexity-concavity properties of θ and θ' and the microstructural properties of real materials. This would require a truly interdisciplinary effort, far beyond the domain of classical continuum mechanics.

2. The local model

2.1. Basic assumptions. Consider a straight bar of length l , homogeneous, with a constant cross-section, subject to prescribed axial displacements at the endpoints

$$u(0) = 0, \quad u(l) = \beta l, \tag{2-1}$$

and free of applied loads. In what follows, the term *load* will be used to denote the relative elongation β . A deformed configuration is described by the axial displacements $u(x)$ of the points x of the bar's axis, and the derivative $u'(x)$ is a measure of the axial deformation at x .

We make four basic assumptions. The first is that at every x the deformation can be split into the sum of an elastic part $\epsilon(x)$ and an inelastic part $\gamma(x)$:

$$u'(x) = \epsilon(x) + \gamma(x), \quad x \in (0, l). \tag{2-2}$$

A pair (ϵ, γ) of functions continuous in $[0, l]$ is a *configuration* of the bar. By integration, from the boundary conditions (2-1) it follows that

$$\beta = \bar{\epsilon} + \bar{\gamma}, \tag{2-3}$$

with

$$\bar{\epsilon} = \frac{1}{l} \int_0^l \epsilon(x) dx, \quad \bar{\gamma} = \frac{1}{l} \int_0^l \gamma(x) dx. \tag{2-4}$$

Our second assumption is that the strain energy of the bar has the form

$$E(\epsilon, \gamma) = \int_0^l (w(\epsilon(x)) + \theta(\gamma(x))) dx, \tag{2-5}$$

where w and θ are the volume densities of the *elastic strain energy* and of the *cohesive energy*, respectively. We assume that w is C^2 and strictly convex, and that

$$w(0) = w'(0) = 0. \tag{2-6}$$

Then w' is strictly increasing, and

$$w(\epsilon) > 0, \quad \forall \epsilon \neq 0, \quad w'(\epsilon) \begin{cases} > 0, & \forall \epsilon > 0, \\ < 0, & \forall \epsilon < 0, \end{cases} \quad w''(\epsilon) > 0, \quad \forall \epsilon \in \mathbb{R}.$$

We also assume that θ is C^2 and monotonic increasing, and that

$$\theta(0) = 0, \quad \theta'(0) > 0, \quad \lim_{\gamma \rightarrow +\infty} \theta(\gamma) < +\infty. \quad (2-7)$$

The third assumption is that the elastic part of the deformation is related to the axial force σ by the constitutive equation

$$\sigma = w'(\epsilon), \quad (2-8)$$

and the fourth assumption is that w can be stored, while θ is totally dissipated. That is, in every *deformation process* $t \mapsto (\epsilon_t, \gamma_t)$, at every x the *cohesive power* is nonnegative:

$$\theta'(\gamma_t(x)) \dot{\gamma}_t(x) \geq 0. \quad (2-9)$$

Here and in the following, a superimposed dot denotes the *right derivative* with respect to the parameter t . Due to the rate-independent character of the model, t may be any monotonic nondecreasing function of the physical time. In what follows we consider the case of θ strictly monotonic, for which the *dissipation inequality*

$$\dot{\gamma}_t(x) \geq 0 \quad (2-10)$$

holds at all x and for all t .

2.2. Equilibrium. For a given configuration (ϵ, γ) , a *perturbation* is a pair $(\delta\epsilon, \delta\gamma)$ such that

$$\delta\epsilon(x) = \dot{\epsilon}_t(x), \quad \delta\gamma(x) = \dot{\gamma}_t(x),$$

in some deformation process with $(\epsilon_t, \gamma_t) = (\epsilon, \gamma)$. While $\delta\epsilon$ is unrestricted, $\delta\gamma$ is subject to the condition

$$\delta\gamma(x) \geq 0, \quad \forall x \in (0, l), \quad (2-11)$$

due to the dissipation inequality (2-10). We say that (ϵ, γ) is an *equilibrium configuration* if the first variation of the energy

$$\begin{aligned} \delta E(\epsilon, \gamma, \delta\epsilon, \delta\gamma) &= \lim_{\lambda \rightarrow 0^+} \frac{1}{\lambda} (E(\epsilon + \lambda \delta\epsilon, \gamma + \lambda \delta\gamma) - E(\epsilon, \gamma)) \\ &= \int_0^l (w'(\epsilon(x)) \delta\epsilon(x) + \theta'(\gamma(x)) \delta\gamma(x)) dx \end{aligned} \quad (2-12)$$

is nonnegative for all perturbations which preserve the length of the bar

$$\delta\bar{\epsilon} + \delta\bar{\gamma} = 0, \quad \delta\bar{\epsilon} = \frac{1}{l} \int_0^l \delta\epsilon(x) dx, \quad \delta\bar{\gamma} = \frac{1}{l} \int_0^l \delta\gamma(x) dx. \quad (2-13)$$

In particular, for perturbations with $\delta\gamma = 0$ the first variation is

$$\delta E(\epsilon, \gamma, \delta\epsilon, 0) = \int_0^l w'(\epsilon(x)) \delta\epsilon(x) dx.$$

By (2-13), $\delta\bar{\epsilon} = 0$ for such perturbations. Then, a standard argument of the calculus of variations leads to the conclusion that the first variation is nonnegative if and only if $w'(\epsilon(x))$ is a constant.

By the constitutive equation (2-8), this implies that the axial force σ is constant. Moreover, by the strict convexity of w , the derivative w' is strictly increasing and, therefore, invertible. Then, ϵ is constant as well:

$$\epsilon = (w')^{-1}(\sigma). \quad (2-14)$$

By (2-13), for constant ϵ the first variation reduces to

$$\delta E(\epsilon, \gamma, \delta\epsilon, \delta\gamma) = \int_0^l (\theta'(\gamma(x)) - w'(\epsilon)) \delta\gamma(x) dx,$$

and because $\delta\gamma(x)$ is arbitrary nonnegative, the condition

$$w'(\epsilon) \leq \theta'(\gamma(x)), \quad \forall x \in (0, l), \quad (2-15)$$

follows. Conversely, for every configuration (ϵ, γ) obeying this condition the first variation is nonnegative. Therefore, *an equilibrium configuration is a configuration (ϵ, γ) , with constant ϵ , which satisfies condition (2-15) for all x .*

An equilibrium configuration is equilibrated with the load β given by (2-3). Then inequality (2-15), rewritten in the form

$$w'(\beta - \bar{\gamma}) \leq \theta'(\gamma(x)), \quad \forall x \in (0, l), \quad (2-16)$$

shows that an equilibrium configuration can be defined alternatively as a pair (β, γ) which satisfies (2-11) and (2-16). There are many γ for which (β, γ) is an equilibrium configuration. Indeed, by the assumptions made on w and θ , all configurations (β, γ) with $\bar{\gamma} > \beta$ satisfy inequality (2-16), because the right side of the inequality is nonnegative, while for $\beta < \bar{\gamma}$ the left side is negative.

With every equilibrium configuration (β, γ) are associated the axial force

$$\sigma = w'(\beta - \bar{\gamma}) \quad (2-17)$$

and the energy

$$E^{\text{eq}}(\beta, \gamma) \doteq lw(\beta - \bar{\gamma}) + \int_0^l \theta(\gamma(x)) dx. \quad (2-18)$$

The set of all x at which inequality (2-16) is strict is the elastic zone

$$\mathcal{E}(\beta, \gamma) \doteq \{x \in (0, l) \mid w'(\beta - \bar{\gamma}) < \theta'(\gamma(x))\}, \quad (2-19)$$

and the complementary set

$$\mathcal{F}(\beta, \gamma) \doteq (0, l) \setminus \mathcal{E}(\beta, \gamma)$$

at which (2-16) is verified as an equality is the *inelastic zone*. We say that the bar is in the *elastic regime* if $\mathcal{E}(\beta, \gamma) = (0, l)$, and that it is in the *inelastic regime* otherwise.

The equilibrium condition (2-16), rewritten in the form

$$\sigma \leq \theta'(\gamma(x)), \quad \forall x \in (0, l), \quad (2-20)$$

shows that there is an upper limit for σ . In the language of plasticity, this inequality is a *yield condition*, which imposes that the current stress σ not be greater than the *yield limit* θ' . The difference $\theta' - \sigma$ is the *yield function*.

2.3. Energy minimizers. Among all inelastic deformations γ equilibrated with a given β , of interest are those which minimize the energy $E^{\text{eq}}(\beta, \cdot)$. A necessary condition for a minimum at γ is that, in the expansion

$$E^{\text{eq}}(\beta, \gamma + \lambda \delta\gamma) - E^{\text{eq}}(\beta, \gamma) = \lambda \int_0^l (\theta'(\gamma(x)) - w'(\beta - \bar{\gamma})) \delta\gamma(x) dx \\ + \frac{1}{2} \lambda^2 \int_0^l (\theta''(\gamma(x)) \delta\gamma^2 + w''(\beta - \bar{\gamma}) \delta\bar{\gamma}^2) dx + o(\lambda^2),$$

the first variation be nonnegative for all perturbations $\delta\gamma$ and for all positive values of the smallness parameter λ . By (2-11) and (2-16), this is true if and only if (β, γ) is an equilibrium configuration. Therefore, all minimizers for $E^{\text{eq}}(\beta, \cdot)$ are equilibrium configurations.

A second necessary condition is that the second variation be nonnegative for all $\delta\gamma$ for which the first variation is zero. In particular, it must be nonnegative for all $\delta\gamma$ with support in the inelastic zone $\mathcal{F}(\beta, \gamma)$. For this, it is necessary that

$$\theta''(\gamma(x)) \geq 0, \quad \text{a.e. } x \in \mathcal{F}(\beta, \gamma). \quad (2-21)$$

Indeed, if $\theta''(\gamma(x))$ is negative on a subset of $\mathcal{F}(\beta, \gamma)$ with nonnull measure, a negative second variation is obtained by concentrating $\delta\gamma$ on that set. The existence of perturbed configurations $(\beta, \gamma + \delta\gamma)$ with arbitrarily large negative energy characterizes a fractured configuration. Then, (2-21) is *in fact a safety condition against fracture*.

The nonnegativeness of the first variation joined with the stronger condition

$$\theta''(\gamma(x)) > 0, \quad \forall x \in (0, l), \quad (2-22)$$

is sufficient for a local minimum at γ with respect to the L^∞ norm:

$$\|\delta\gamma\| = \sup_{x \in (0, l)} |\delta\gamma(x)|. \quad (2-23)$$

Indeed, since θ is C^2 and γ is continuous in the closed set $[0, l]$, the map $\theta''(\gamma(\cdot))$ is uniformly continuous. Then for all $\varepsilon > 0$ there is a $\delta > 0$ such that

$$|a| < \delta \implies |\theta''(\gamma(x) + a) - \theta''(\gamma(x))| < \varepsilon, \quad \forall x \in (0, l).$$

Consider the finite expansion of $E^{\text{eq}}(\beta, \cdot)$ with Lagrange remainder

$$E^{\text{eq}}(\beta, \gamma + \delta\gamma) \\ = E^{\text{eq}}(\beta, \gamma) + \delta E^{\text{eq}}(\beta, \gamma, \delta\gamma) + \frac{1}{2} \int_0^l (\theta''(\gamma(x) + \xi(x) \delta\gamma(x)) \delta\gamma^2(x) + w''(\beta - \bar{\gamma} - \bar{\xi} \delta\bar{\gamma}) \delta\bar{\gamma}^2) dx,$$

with $\bar{\xi}$ and all $\xi(x)$ in $(0, 1)$. For every perturbation $\delta\gamma$ with $\|\delta\gamma\| < \delta$, from the nonnegativeness of the first variation and the positiveness of w'' we have

$$E^{\text{eq}}(\beta, \gamma + \delta\gamma) - E^{\text{eq}}(\beta, \gamma) \geq \frac{1}{2} \int_0^l (\theta''(\gamma(x)) - \varepsilon) \delta\gamma^2(x) dx.$$

If (2-22) holds, the map $\theta''(\gamma(\cdot))$ is positive and continuous, and therefore it has a positive minimum c in $[0, l]$. It is then sufficient to take $\varepsilon < c$ to have a nonnegative right-hand side. Because this holds for all $\delta\gamma$ with $\|\delta\gamma\| < \delta$, γ is a local minimizer with respect to the norm (2-23).

2.4. Quasistatic evolutions. A load process is a continuous function $t \mapsto \beta_t$. A quasistatic evolution from γ_0 associated with $t \mapsto \beta_t$ is a family $t \mapsto \gamma_t$ of inelastic deformations such that

- (i) $\gamma_t = \gamma_0$ at the initial time $t = t_0$,
- (ii) for all t the function $x \mapsto \gamma_t(x)$ is continuous, for all x the function $t \mapsto \gamma_t$ is nondecreasing, and the family $t \mapsto \gamma_t$ is continuous in $L^\infty(0, l)$, and
- (iii) for all $t \geq t_0$, γ_t is a local minimizer for $E^{\text{eq}}(\beta_t, \cdot)$.

In (ii), the requirement of γ_t nondecreasing is imposed by the dissipation inequality (2-10), and continuity in $L^\infty(0, l)$ means that for every $t \geq t_0$ and for every $\delta > 0$ there is a $\tau_o > 0$ such that

$$\|\gamma_{t+\tau} - \gamma_t\| < \delta, \quad \forall \tau \in (0, \tau_o),$$

where $\|\cdot\|$ is the L^∞ norm (2-23). By consequence, in the time interval $(0, \tau_o)$ the evolution $\tau \mapsto \gamma_{t+\tau}$ takes place inside the ball $\mathcal{B}(\gamma_t, \delta)$ of $L^\infty(0, l)$ of radius δ centered at γ_t .

Assume that $\gamma_t(\cdot)$ is a deformation with constant value $\bar{\gamma}_t$, and that $\theta''(\bar{\gamma}_t)$ is positive. Then it is possible to choose δ such that $\theta''(\gamma(x)) > 0$ for all γ in $\mathcal{B}(\bar{\gamma}_t, \delta)$, so that the restriction of the energy to $\mathcal{B}(\bar{\gamma}_t, \delta)$ is strictly convex for all $\tau < \tau_o$. Therefore, by Jensen's inequality,

$$E^{\text{eq}}(\beta_{t+\tau}, \gamma_{t+\tau}) \geq E^{\text{eq}}(\beta_{t+\tau}, \bar{\gamma}_{t+\tau}), \quad \forall \tau \in (0, \tau_o),$$

where $\bar{\gamma}_{t+\tau}$ is the homogeneous deformation defined as in (2-4), and equality holds only if $\gamma_{t+\tau} = \bar{\gamma}_{t+\tau}$. That is, the unique minimizer of the energy at time $t + \tau$ is a homogeneous deformation. Consequently, for every quasistatic evolution from a homogeneous deformation $\bar{\gamma}_t$ with $\theta''(\bar{\gamma}_t) > 0$ there is a time interval $(0, \tau_o)$ in which $\gamma_{t+\tau}$ is a homogeneous deformation.

From here onwards we consider homogeneous deformation processes $t \mapsto \gamma_t$, and we identify the functions $\gamma_t(\cdot)$ and $\dot{\gamma}_t(\cdot)$ with their constant values, which we denote by γ_t and $\dot{\gamma}_t$. For $\theta''(\gamma_t) > 0$ and for δ and τ_o as above, the determination of a quasistatic evolution from (β_t, γ_t) reduces to the following incremental minimization problem: for a given $\tau \leq \tau_o$, find the homogeneous deformation $\gamma_{t+\tau}$ which minimizes the energy $E^{\text{eq}}(\beta_{t+\tau}, \cdot)$ in $\mathcal{B}(\gamma_t, \delta)$.

An approximate solution is obtained by replacing $\beta_{t+\tau}$ and $\gamma_{t+\tau}$ by the piecewise linear approximations

$$\beta_{t+\tau} \approx \beta_t + \tau \dot{\beta}_t, \quad \gamma_{t+\tau} \approx \gamma_t + \tau \dot{\gamma}_t, \quad (2-24)$$

and then determining $\dot{\gamma}_t$ as the minimizer for the first-order approximation

$$E_{t+\tau}(\dot{\gamma}) \approx E_t + \tau \dot{E}_t(\dot{\gamma}) \quad (2-25)$$

of the energy $E^{\text{eq}}(\beta_{t+\tau}, \gamma_{t+\tau})$, where

$$E_t = E^{\text{eq}}(\beta_t, \gamma_t) = l(w(\epsilon_t) + \theta(\gamma_t)), \quad \dot{E}_t(\dot{\gamma}) = l(\sigma_t(\dot{\beta}_t - \dot{\gamma}) + \theta'(\gamma_t)\dot{\gamma}), \quad (2-26)$$

with $\sigma_t = w'(\epsilon_t)$ and $\epsilon_t = \beta_t - \gamma_t$. This minimization determines the direction of *steepest descent* for the energy. Because E_t and $\dot{\beta}_t$ are known, the problem reduces to the minimization of the linear function

$$I(\dot{\gamma}) = (\theta'(\gamma_t) - \sigma_t)\dot{\gamma}, \quad (2-27)$$

under the condition $\dot{\gamma} \geq 0$. In the elastic regime, in which $(\theta'(\gamma_t) - \sigma_t)$ is positive, the minimum is zero and is attained at $\dot{\gamma} = 0$. In the inelastic regime, $I(\dot{\gamma})$ is identically zero because $(\theta'(\gamma_t) - \sigma_t)$ is zero. That is, the direction of steepest descent is undetermined.

The determination of a quasistatic evolution in the inelastic regime then requires a second-order approximation of the energy

$$E_{t+\tau}(\dot{\gamma}) \approx E_t + \tau \dot{E}_t(\dot{\gamma}) + \frac{1}{2} \tau^2 \ddot{E}_t(\dot{\gamma}), \quad (2-28)$$

where

$$\ddot{E}_t(\dot{\gamma}) = I(w''(\epsilon_t)(\dot{\beta}_t - \dot{\gamma})^2 + \theta''(\gamma_t)\dot{\gamma}^2). \quad (2-29)$$

After elimination of the terms independent of $\dot{\gamma}$, the problem reduces to the minimization of the quadratic function

$$J(\dot{\gamma}) = (\theta'(\gamma_t) - \sigma_t - \tau w''(\epsilon_t)\dot{\beta}_t)\dot{\gamma} + \frac{1}{2} \tau (\theta''(\gamma_t) + w''(\epsilon_t))\dot{\gamma}^2, \quad (2-30)$$

under the condition $\dot{\gamma} \geq 0$. The sum $(\theta''(\gamma_t) + w''(\epsilon_t))$ is positive by the strict convexity of w and the necessary condition (2-21) on $\theta''(\gamma)$. Then, J is strictly convex. If the bar is in the elastic regime, $\theta'(\gamma_t) - \sigma_t > 0$, the coefficient of $\dot{\gamma}$ is positive for sufficiently small τ . Then the global minimum is zero, and is achieved at $\dot{\gamma} = 0$. In this case, the elastic incremental response

$$\dot{\sigma}_t = w''(\epsilon_t)\dot{\beta}_t \quad (2-31)$$

follows from the incremental force-elongation relation

$$\dot{\sigma}_t = w''(\epsilon_t)(\dot{\beta}_t - \dot{\gamma}_t), \quad (2-32)$$

obtained by time differentiation of (2-17). This confirms the result of the first-order minimization, that *there is no increase of inelastic deformation in the elastic regime*.

In the inelastic regime, $\theta'(\gamma_t) = \sigma_t$, the minimum is still achieved at $\dot{\gamma} = 0$ at unloading, $\dot{\beta}_t \leq 0$. Then, *there is no increase of inelastic deformation at unloading*. At loading, $\dot{\beta}_t > 0$, the minimum of J is achieved at

$$\dot{\gamma}_t = \frac{w''(\epsilon_t)}{\theta''(\gamma_t) + w''(\epsilon_t)} \dot{\beta}_t, \quad (2-33)$$

and, by (2-32), the inelastic response is

$$\dot{\sigma}_t = \frac{\theta''(\gamma_t)w''(\epsilon_t)}{\theta''(\gamma_t) + w''(\epsilon_t)} \dot{\beta}_t. \quad (2-34)$$

The different response at loading and unloading in the inelastic regime is a peculiar property of plastic behavior. At loading, from (2-33) and (2-34) it follows that

$$\dot{\sigma}_t = \theta''(\gamma_t)\dot{\gamma}_t, \quad (2-35)$$

whence

$$\sigma_{t+\tau} \approx \sigma_t + \tau \dot{\sigma}_t = \theta'(\gamma_t) + \tau \theta''(\gamma_t) \dot{\gamma}_t \approx \theta'(\gamma_{t+\tau}). \quad (2-36)$$

Equation (2-35) is the hardening rule, which in classical plasticity specifies $\dot{\sigma}$ as a function of the current value of γ . Equation (2-36) states that, within the approximation (2-24), at time $t + \tau$ the yield condition holds as an equality. That is, the inelastic regime is preserved. This is the consistency condition of classical plasticity. At unloading, the response (2-31) expresses the property of elastic unloading. Classically, the hardening rule, consistency, and elastic unloading are assumptions originating from experimental observation. Here, they come as necessary conditions for a minimum in the second-order energy minimization.

Equation (2-34) provides the slope $d\sigma_t/d\beta_t = \dot{\sigma}_t/\dot{\beta}_t$ of the force-elongation response curve at loading. For $\theta''(\gamma_t) > 0$ this slope is positive but smaller than the slope $w''(\epsilon_t)$ at unloading. A positive slope at loading characterizes a *work-hardening response*.

For $\theta''(\gamma_t) = 0$, the restriction to homogeneous deformations is no longer possible. In the inelastic regime, $\sigma_t = \theta'(\gamma_t)$, the function $J(\dot{\gamma})$ reduces to

$$J(\dot{\gamma}) = -\tau w''(\epsilon_t) \dot{\beta}_t \bar{\dot{\gamma}} + \frac{1}{2} \tau w''(\epsilon_t) \bar{\dot{\gamma}}^2.$$

The minimum is achieved at $\bar{\dot{\gamma}}_t = \dot{\beta}_t$, which corresponds to $\dot{\sigma}_t = 0$, that is, to *perfectly plastic response*. In this case, the incremental minimization specifies the average $\bar{\dot{\gamma}}_t$, but the punctual values $\dot{\gamma}_t(x)$ are not determined. Thus, in this case the evolution from a homogeneous configuration need not be homogeneous.

The case of $\theta''(\gamma_t)$ negative, corresponding to a negative slope, that is, to a strain-softening response, is excluded by condition (2-21). Multiplication of (2-35) by $\dot{\gamma}_t$ shows that Drucker's postulate (1-5) is obeyed only if $\theta''(\gamma_t)$ is nonnegative. This shows that the local model provides a valid response only for materials which obey Drucker's postulate.

The indeterminacy of the minimizers in a perfectly plastic response and the impossibility of reproducing the softening response are two major drawbacks of the local model.

2.5. Evolution from the natural configuration. Let us determine the quasistatic evolution for a load process $t \mapsto \beta_t$, with $\dot{\beta}_t > 0$ for all t , from the natural configuration $(\beta_0, \gamma_0) = (0, 0)$. At $t = 0$ we have

$$\sigma_0 = 0, \quad \theta'(\gamma_0) = \theta'(0) > 0,$$

so that inequality (2-20) is strict and $\dot{\gamma}_0$ is zero. By continuity, inequality (2-20) remains strict, and therefore $\dot{\gamma}_t$ remains equal to zero, over a time interval $(0, t_c)$. Because $\gamma_0 = 0$, γ_t is zero in this interval. Then an elastic regime takes place, with

$$\epsilon_t = \beta_t, \quad \sigma_t = w'(\beta_t).$$

This regime ends when, at some $t_c > 0$, β_t reaches the value

$$\beta_c = (w')^{-1}(\theta'(0)), \quad (2-37)$$

at which, since $\sigma_{t_c} = w'(\beta_c) = \theta'(0)$, inequality (2-20) becomes an equality. At $t = t_c$, all points of the bar switch from the elastic to the inelastic zone.

The response at $t = t_c$ is work-hardening if $\theta''(0) > 0$ and perfectly plastic if $\theta''(0) = 0$. In the work-hardening regime, by (2-33), the evolution $t \mapsto \gamma_t$ is determined by the solution of the differential equation

$$\dot{\gamma}_t = \frac{w''(\beta_t - \gamma_t)}{\theta''(\gamma_t) + w''(\beta_t - \gamma_t)} \dot{\beta}_t, \quad t \geq t_c, \quad (2-38)$$

under the initial condition $\gamma_{t_c} = 0$. A work-hardening regime persists as long as $\dot{\beta}_t$ and $\theta''(\gamma_t)$ remain positive. For $\dot{\beta}_t \leq 0$ elastic unloading takes place, and for $\theta''(\gamma_t) = 0$ the response becomes perfectly plastic. Fracture occurs as soon as γ_t becomes larger than

$$\gamma_r \doteq \inf\{\gamma \geq 0 \mid \theta''(\gamma) < 0\}. \quad (2-39)$$

Indeed, for $\gamma > \gamma_r$ there are perturbed configurations with arbitrarily large negative energy. Because the energy suddenly drops from a finite value to $-\infty$, the fracture has a catastrophic character. This fracture mode is called *brittle fracture*. If $\theta''(0) < 0$, fracture occurs without any intermediate inelastic regime. This is the case of totally brittle fracture.

In conclusion, in the inelastic regime at loading the response at (β_t, γ_t) is work-hardening if $\theta''(\gamma_t)$ is positive, and perfectly plastic if $\theta''(\gamma_t) = 0$. For $\theta''(\gamma_t) > 0$, a quasistatic evolution from a homogeneous deformation is made of homogeneous deformations. The fracture is always catastrophic, and occurs as soon as γ_t becomes larger than γ_r .

3. The nonlocal model

3.1. Basic assumptions. The local model provides only a rough description of the bar's behavior. In particular, it does not describe ductile fracture and strain-softening response. These phenomena are captured by adding to the energy (2-5) a nonlocal term proportional to the square of the derivative of γ :

$$E(\epsilon, \gamma) = \int_0^l (w(\epsilon(x)) + \theta(\gamma(x)) + \frac{1}{2}\alpha\gamma'(x)^2) dx,$$

with α a positive constant. The new term requires a stronger regularity of γ . We assume that γ is C^1 on $[0, l]$ and piecewise C^2 , that is, that γ'' is continuous except at a finite number of jump points x_i , at which the left limit $\gamma''(x_i-)$ and the right limit $\gamma''(x_i+)$ exist. The difference

$$[[\gamma'']](x_i) \doteq \gamma''(x_i+) - \gamma''(x_i-) \quad (3-1)$$

is the *jump* of γ'' at x .

Like in the local model, the part of the energy depending on the inelastic deformation is supposed to be dissipative. That is, the cohesive power

$$\theta'(\gamma_t(x))\dot{\gamma}_t(x) + \alpha\gamma_t'(x)\dot{\gamma}_t'(x) \quad (3-2)$$

is assumed to be nonnegative in every deformation process $t \mapsto \gamma_t$. For this, it is necessary that the product $\theta'(\gamma_t(x))\dot{\gamma}_t(x)$ be nonnegative at all x . Indeed, if it is negative at some x_o , since $\dot{\gamma}_t'(x_o)$ may have opposite signs in different deformation processes from $\gamma_t(x_o)$, for at least one choice the power (3-2) is negative.

By the assumed strict monotonicity of θ' , the dissipation inequality $\dot{\gamma}_t(x) \geq 0$ is necessary for dissipativity. In the following subsection we show that, if the yield limit is nonnegative, this condition is sufficient to guarantee the global dissipativity, that is, the nonnegativeness of the integral of (3-2) over $(0, l)$, in every equilibrium process.

3.2. Equilibrium. In the nonlocal model, an equilibrium configuration is a configuration (ϵ, γ) at which the first variation

$$\delta E(\epsilon, \gamma, \delta\epsilon, \delta\gamma) = \int_0^l (w'(\epsilon(x)) \delta\epsilon(x) + \theta'(\gamma(x)) \delta\gamma(x) + \alpha\gamma'(x) \delta\gamma'(x)) dx$$

is nonnegative for all $C^1([0, l])$ and piecewise C^2 perturbations $(\delta\epsilon, \delta\gamma)$, which satisfy the dissipation inequality (2-11) and the boundary condition (2-13). Proceeding as in Section 2.2, using perturbations with $\delta\gamma = 0$ we find that σ and ϵ must be constant over the bar. Then setting $w'(\epsilon) = \sigma$ and $\delta\epsilon = -\delta\bar{\gamma}$ and integrating by parts, we get

$$\delta E(\epsilon, \gamma, -\delta\bar{\gamma}, \delta\gamma) = \int_0^l (\theta'(\gamma(x)) - \sigma - \alpha\gamma''(x)) \delta\gamma(x) dx + \alpha[\gamma'(x) \delta\gamma(x)]_0^l.$$

The nonnegativeness of the first variation for all nonnegative $\delta\gamma$ requires

$$\sigma \leq \theta'(\gamma(x)) - \alpha\gamma''(x), \quad (3-3)$$

in $(0, l)$, and

$$\gamma'(l) \delta\gamma(l) \geq 0, \quad \gamma'(0) \delta\gamma(0) \leq 0, \quad (3-4)$$

at the boundary. Inequality (3-3) is the nonlocal version of the yield condition (2-20). The difference with the local model is that, while the yield limit $\theta'(\gamma(x))$ of the local model depends only on the value of γ at x , the additional term $\alpha\gamma''(x)$ introduces a dependence on the values taken by γ at the neighboring points.

There are two ways of satisfying the boundary conditions (3-4). If $\delta\gamma$ is allowed to take arbitrary positive values at the boundary, these conditions reduce to $\gamma'(l) \geq 0$ and $\gamma'(0) \leq 0$, respectively. The alternative is to require that

$$\gamma(l) = \gamma(0) = 0, \quad (3-5)$$

and, therefore, to take perturbations $\delta\gamma$ such that

$$\delta\gamma(l) = \delta\gamma(0) = 0. \quad (3-6)$$

We choose this second possibility, which better describes the standard experimental conditions. Indeed, while this choice keeps the inelastic deformations away from the boundary, the other choice favors the concentration of the inelastic deformation at the boundary. For a similar effect in different models, see [Yalcinkaya et al. 2011, Figures 9 and 10], [Benallal and Marigo 2007, Figure 3a], and the discussion in [Jirásek and Rolshoven 2009b]. In laboratory tests this effect is carefully avoided, either by reinforcing the specimen's end sections, or by weakening the central part of the bar, for example, with the creation of a notch.

Thus, our choice allows for a comparison, at least qualitative, with the standard experimental curves. The alternative possibility of imposing a null derivative γ' was chosen in [Benallal and Marigo 2007;

Pham and Marigo 2010b; Pham et al. 2011]. This choice has the advantage of allowing for homogeneous inelastic equilibrium configurations, and this greatly facilitates the study of the inelastic regime. Unfortunately, due to the devices used to fix the bar's ends in real experiments, this circumstance is hardly reproducible in practice.

In conclusion, for the nonlocal model an equilibrium configuration is a pair (ϵ, γ) , with ϵ a constant and γ a $C^1([0, l])$ and piecewise C^2 function, which satisfies inequality (3-3) at the interior points and conditions (3-5) at the boundary.

Assume that the dissipation inequality (2-10) holds, and that the yield limit $\theta'(\gamma) - \alpha\gamma''$ is nonnegative. After integrating over $(0, l)$, an integration by parts yields

$$0 \leq \int_0^l (\theta'(\gamma(x)) - \alpha\gamma''(x))\dot{\gamma}(x) dx = \int_0^l (\theta'(\gamma(x))\dot{\gamma}(x) + \alpha\gamma'(x)\dot{\gamma}'(x)) dx - \alpha[\gamma'(x)\dot{\gamma}(x)]_0^l.$$

On the right side the integral is the total cohesive power. Moreover, by (3-4), the remaining term is nonpositive in any equilibrium process. This proves that, if the yield limit is nonnegative, the dissipation inequality (2-10) guarantees the global dissipativity in every equilibrium process.

An equilibrium configuration (ϵ, γ) is equilibrated with the load β given by (2-3). Alternatively, an equilibrium configuration can be defined as a pair (β, γ) , and the energy can be redefined by

$$E^{\text{eq}}(\beta, \gamma) = lw(\beta - \bar{\gamma}) + \int_0^l \theta(\gamma(x)) dx + \frac{1}{2}\alpha \int_0^l \gamma'^2(x) dx. \quad (3-7)$$

For an equilibrium configuration (β, γ) defined in this way, the elastic and inelastic zones are

$$\mathcal{E}(\beta, \gamma) = \{x \in (0, l) \mid w'(\beta - \bar{\gamma}) < \theta'(\gamma(x)) - \alpha\gamma''(x)\}, \quad \mathcal{I}(\beta, \gamma) = (0, l) \setminus \mathcal{E}(\beta, \gamma), \quad (3-8)$$

respectively. As in the local model, we say that the bar is in the elastic regime if $\mathcal{E}(\beta, \gamma) = (0, l)$, and that it is in the inelastic regime otherwise.

3.3. Energy minimizers. To determine the inelastic deformations γ which minimize the energy $E^{\text{eq}}(\beta, \cdot)$, consider the expansion

$$\begin{aligned} E^{\text{eq}}(\beta, \gamma + \delta\gamma) - E^{\text{eq}}(\beta, \gamma) &= \int_0^l (\theta'(\gamma(x)) \delta\gamma(x) - w'(\epsilon) \delta\bar{\gamma} + \alpha\gamma'(x) \delta\gamma'(x)) dx \\ &\quad + \frac{1}{2} \int_0^l (\theta''(\gamma(x)) \delta\gamma^2(x) + w''(\epsilon) \delta\bar{\gamma}^2 + \alpha \delta\gamma'^2(x)) dx + o(\|\delta\gamma\|^2), \end{aligned}$$

with $\epsilon = \beta - \bar{\gamma}$, and with perturbations $\delta\gamma$ nonnegative and satisfying the boundary conditions (3-6). A necessary condition for a minimum is the nonnegativeness of the first variation. Because this requirement characterizes an equilibrium configuration, all minimizers are equilibrium configurations.

Another necessary condition is that the second variation be nonnegative for all $\delta\gamma$ for which the first variation is zero, and in particular, for all $\delta\gamma$ with support in the inelastic zone $\mathcal{I}(\beta, \gamma)$. If $(a, a + l_j)$ is an interval in the inelastic zone, the second variation is nonnegative only if the smallest eigenvalue of the eigenvalue problem

$$\int_a^{a+l_j} (\theta''(\gamma(x)) \delta\gamma^2(x) + \frac{l}{l_j} w''(\epsilon) \delta\bar{\gamma}^2 + \alpha \delta\gamma'^2(x)) dx = \alpha\rho \int_a^{a+l_j} \delta\gamma^2(x) dx, \quad (3-9)$$

is nonnegative for all perturbations $\delta\gamma$ with support in this interval. This problem can be identified with problem (A.15), with H as in (A.9) due to the presence of the constraint $\delta\gamma(x) \geq 0$, and with

$$a = 0, \quad l_j = L, \quad \theta''(\gamma(x)) = \alpha h(x), \quad \delta\gamma(x) = y(x), \quad \delta\bar{\gamma} = \frac{l_j}{l} \bar{y}.$$

The last equality follows from the definitions

$$\bar{y} = \frac{1}{l_j} \int_a^{a+l_j} y(x) dx, \quad \delta\bar{\gamma} = \frac{1}{l} \int_0^l \delta\gamma(x) dx = \frac{1}{l} \int_0^{l_j} \delta\gamma(x) dx,$$

which hold for $\delta\gamma(x) = y(x)$ with support in $(0, l_j)$. Then, from the identification

$$\frac{l}{l_j} w''(\epsilon) \delta\bar{\gamma}^2 = \alpha \omega \bar{y}^2,$$

comes the relation

$$\omega = \frac{l_j}{l} \frac{w''(\epsilon)}{\alpha}.$$

The smallest eigenvalue $\alpha\rho_o$ has the upper bound (A.17). It provides the necessary condition for nonnegativeness:

$$\alpha\lambda_{o_j}^2 + \theta''_{o_j} \geq 0, \quad (3-10)$$

where λ_{o_j} is a solution of (A.14), now rewritten in the form

$$\lambda_{o_j}^2 = \frac{l_j}{l} \frac{w''(\epsilon)}{\alpha} \psi_o(\lambda_{o_j} l_j), \quad (3-11)$$

with ψ_o as in (A.13). Moreover, θ''_{o_j} is defined as in (A.16),

$$\theta''_{o_j} = \frac{\int_a^{a+l_j} \theta''(\gamma(x)) y_{o_j}^2(x) dx}{\int_a^{a+l_j} y_{o_j}^2(x) dx}, \quad (3-12)$$

with y_{o_j} given by (A.8) if $\omega L^2 = l_j^3 w''(\epsilon)/\alpha l \leq 4\pi^2$, and given by (A.12) if $l_j^3 w''(\epsilon)/\alpha l > 4\pi^2$. Because λ_{o_j} is a decreasing function of l_j , inequality (3-10) must be satisfied for the largest interval contained in the inelastic zone.

To find a sufficient condition for a local minimum of $E^{\text{eq}}(\beta, \gamma)$, write the finite expansion with a Lagrange remainder:

$$\begin{aligned} E^{\text{eq}}(\beta, \gamma + \delta\gamma) &= E^{\text{eq}}(\beta, \gamma) + \int_0^l (\theta'(\gamma(x)) \delta\gamma(x) - w'(\epsilon) \delta\bar{\gamma} + \alpha \gamma'(x) \delta\gamma'(x)) dx \\ &\quad + \frac{1}{2} \int_0^l (\theta''(\gamma(x) + \xi(x) \delta\gamma(x)) \delta\gamma^2(x) + w''(\epsilon - \bar{\xi} \delta\bar{\gamma}) \delta\bar{\gamma}^2 + \alpha \delta\gamma'^2(x)) dx, \end{aligned}$$

with $0 \leq \xi(x) \leq 1$ for all x and $0 \leq \bar{\xi} \leq 1$. The first integral, which is the first variation, is nonnegative. We wish to find conditions for which the second integral is nonnegative as well.

By the continuity of θ'' and w'' , for every $\varepsilon > 0$ there is a positive δ such that

$$\sup_{x \in (0, l)} |\theta''(\gamma(x) + \xi(x) \delta\gamma(x)) - \theta''(\gamma(x))| < \varepsilon, \quad |w''(\epsilon - \bar{\xi} \delta\bar{\gamma}) - w''(\epsilon)| < \varepsilon,$$

for all $\delta\gamma$ with $\|\delta\gamma\| < \delta$. For all such $\delta\gamma$, the second integral is greater than or equal to

$$\int_0^l (\theta''(\gamma(x)) \delta\gamma^2(x) + w''(\epsilon) \delta\bar{\gamma}^2 + \alpha \delta\gamma'^2(x)) dx - \varepsilon \int_0^l (\delta\gamma^2(x) + \delta\bar{\gamma}^2) dx.$$

The first integral is the same as in (A.15), with

$$l = L, \quad \delta\gamma = y, \quad w''(\epsilon) = \alpha\omega, \quad \theta''(\gamma(x)) = \alpha h(x).$$

Therefore,

$$E^{\text{eq}}(\beta, \gamma + \delta\gamma) \geq E^{\text{eq}}(\beta, \gamma) + (\alpha\rho_o - 2\varepsilon) \int_0^l \delta\gamma^2(x) dx.$$

By the arbitrariness of ε , γ is a minimizer if the smallest eigenvalue ρ_o is strictly positive. By (A.19), a sufficient condition for a minimum is

$$\alpha\lambda_o^2 + \theta''_{\min} > 0, \tag{3-13}$$

with λ_o the solution of (A.14) for the given ω , and with θ''_{\min} the smallest value of $\theta''(\gamma(x))$ in $(0, l)$.

Conditions (3-10) and (3-13) improve the corresponding conditions (2-21) and (2-22) of the local model. In particular, they show that moderate negative values of $\theta''(\gamma(x))$ are allowed in an energy minimizer. As remarked in the Appendix, the two conditions can be far away from each other. In the special case of $l_j = l$ and constant $\theta''(\gamma(x))$ they coincide, save for the fact that the second inequality is strict.

3.4. Quasistatic evolutions. For a given load process $t \mapsto \beta_t$, a quasistatic evolution from a given deformation γ_0 at $t = t_0$ is a family $t \mapsto \gamma_t$ of inelastic deformations such that

- (i) γ_{t_0} is equal to γ_0 ,
- (ii) for all $t \geq t_0$, the function $\gamma_t(\cdot)$ is C^1 and piecewise C^2 in $[0, l]$,
- (iii) for all $t \geq t_0$, γ_t is a local minimizer for $E^{\text{eq}}(\beta_t, \cdot)$.

The regularity of the time derivative $\dot{\gamma}_t$ is determined by Hadamard's kinematic compatibility condition:

$$\llbracket \dot{\gamma}_t \rrbracket(x) = -\llbracket \gamma_t'' \rrbracket(x) \frac{dx}{dt},$$

where dx/dt is the velocity of a moving jump of γ_t' . This condition tells us that for a moving jump of γ_t'' there is a corresponding moving jump of $\dot{\gamma}_t'$. Therefore, if γ_t is C^1 and piecewise C^2 , $\dot{\gamma}_t$ is only continuous, piecewise C^1 , and piecewise C^2 .

Like in the local model, item (iii) implies that all configurations (β_t, γ_t) are equilibrium configurations. Note that, because of the boundary conditions (3-5), γ_t is homogeneous only if $\gamma_t = 0$. Therefore, while in the local model it is sometimes possible to restrict the analysis to quasistatic evolutions made of homogeneous deformations, here there are no homogeneous deformations besides $\gamma_t = 0$.

Repeating the procedure followed for the local model, fix a time step τ and consider the piecewise linear approximations (2-24) of $t \mapsto \beta_t$ and $t \mapsto \gamma_t$. For them, we first determine the direction $\dot{\gamma}_t$ of steepest descent, by minimizing the first-order approximation (2-25) of the energy. The problem reduces to the minimization of the linear functional

$$I(\dot{\gamma}) = \int_0^l (\theta'(\gamma_t(x))\dot{\gamma}(x) - \sigma_t \bar{\gamma} + \alpha \gamma_t'(x)\dot{\gamma}'(x)) dx = \int_0^l f_t(x)\dot{\gamma}(x) dx,$$

where $\sigma_t = w'(\beta_t - \bar{\gamma}_t)$, and

$$f_t(x) \doteq \theta'(\gamma_t(x)) - \sigma_t - \alpha \gamma_t''(x) \quad (3-14)$$

is the yield function. The domain of I is the set of all $\dot{\gamma}$ which satisfy the dissipation inequality (2-10) and the boundary conditions

$$\dot{\gamma}(0) = \dot{\gamma}(l) = 0, \quad (3-15)$$

which follow from (3-6). In the first variation

$$\delta I(\dot{\gamma}_t, \delta \dot{\gamma}) = \int_0^l f_t(x) \delta \dot{\gamma}(x) dx,$$

the perturbations $\delta \dot{\gamma}$ satisfy the boundary conditions

$$\delta \dot{\gamma}(0) = \delta \dot{\gamma}(l) = 0, \quad (3-16)$$

and the inequality

$$\dot{\gamma}_t(x) + \delta \dot{\gamma}(x) \geq 0, \quad \forall x \in (0, l). \quad (3-17)$$

This is because, in a quasistatic evolution, $(\dot{\gamma}_t + \delta \dot{\gamma})$ is the derivative of γ_t in some deformation process starting from (β_t, γ_t) , and therefore it obeys the boundary conditions (3-15) and the dissipation inequality (2-10). The nonnegativeness of the first variation requires that

$$f_t(x) \delta \dot{\gamma}(x) \geq 0, \quad \text{a.e. } x \in (0, l).$$

By (3-17), at points at which $\dot{\gamma}_t(x) = 0$ the perturbation $\delta \dot{\gamma}(x)$ is arbitrary nonnegative, and therefore $f_t(x)$ must be nonnegative. At points at which $\dot{\gamma}_t(x) > 0$ the perturbation may have any sign, and therefore $f_t(x)$ must be zero. Together with the dissipation inequality (2-10) and the yield condition (3-3), this leads to the Kuhn–Tucker conditions

$$\dot{\gamma}_t(x) \geq 0, \quad f_t(x) \geq 0, \quad f_t(x)\dot{\gamma}_t(x) = 0, \quad \text{a.e. } x \in (0, l), \quad (3-18)$$

as necessary conditions for a minimum of I at $\dot{\gamma}_t$. The last equality, called the *complementarity condition*, requires that $\dot{\gamma}_t(x) = 0$ if $f_t(x) > 0$, that is, at all points in the elastic zone $\mathcal{E}(\beta_t, \gamma_t)$.

For all $\dot{\gamma}_t$ which satisfy conditions (3-18), $I(\dot{\gamma}_t)$ is zero and $\dot{E}_t(\dot{\gamma}_t)$ is equal to $l\sigma_t\dot{\beta}_t$. Thus, like in the local model, the direction $\dot{\gamma}_t$ of steepest descent is not determined in the inelastic zone. For this, it is necessary to minimize the second-order approximation (2-28) of the energy. This reduces to the minimization of the functional

$$J(\dot{\gamma}) = \int_0^l f_t(x)\dot{\gamma}(x) dx + \frac{1}{2}\tau \left(\int_0^l (\theta''(\gamma_t(x))\dot{\gamma}^2(x) + w''(\epsilon_t)\bar{\gamma}^2 + \alpha \dot{\gamma}'^2(x)) dx - 2lw''(\epsilon_t)\dot{\beta}_t\bar{\gamma} \right), \quad (3-19)$$

with respect to all perturbations $\delta\dot{\gamma}$ which satisfy conditions (3-16) and (3-17). For the minimizers of J we keep the same symbol $\dot{\gamma}_t$ used for the minimizers of I . While a minimizer for I is a direction of steepest descent, a minimizer for J will be called a *continuation* of the quasistatic evolution at t . The first variation of J is

$$\begin{aligned} \delta J(\dot{\gamma}_t, \delta\dot{\gamma}) &= \int_0^l f_t(x) \delta\dot{\gamma}(x) dx + \tau \int_0^l (\theta''(\gamma_t(x))\dot{\gamma}_t(x) \delta\dot{\gamma}(x) - \dot{\sigma}_t \delta\dot{\gamma}(x) + \alpha\dot{\gamma}'_t(x) \delta\dot{\gamma}'(x)) dx \\ &= \int_0^l f_t(x) \delta\dot{\gamma}(x) dx + \tau \left(\int_0^l (\theta''(\gamma_t(x))\dot{\gamma}_t(x) - \dot{\sigma}_t - \alpha\dot{\gamma}''_t(x)) \delta\dot{\gamma}(x) dx - \alpha \sum_i \llbracket \dot{\gamma}'_t \rrbracket(x_i) \delta\dot{\gamma}(x_i) \right) \\ &= \int_0^l (f_t(x) + \tau \dot{f}_t(x)) \delta\dot{\gamma}(x) dx - \tau \alpha \sum_i \llbracket \dot{\gamma}'_t \rrbracket(x_i) \delta\dot{\gamma}(x_i). \end{aligned}$$

The derivative $\dot{\gamma}''_t(x)$ which appears in $\dot{f}_t(x)$ is the *regular part* of the distributional derivative of $\dot{\gamma}'_t$, while the singular part is given by the jumps $\llbracket \dot{\gamma}'_t \rrbracket(x_i)$ at the jump points x_i . The necessary conditions for a minimum at $\dot{\gamma} = \dot{\gamma}_t$ are

$$\begin{aligned} (f_t(x) + \tau \dot{f}_t(x)) \delta\dot{\gamma}(x) &\geq 0, & \text{a.e. } x \in (0, l), \\ \llbracket \dot{\gamma}'_t \rrbracket(x) \delta\dot{\gamma}(x) &\leq 0, & \forall x \in (0, l). \end{aligned} \quad (3-20)$$

The jump condition has been imposed at all x and not only at the jump points, since $\llbracket \dot{\gamma}'_t \rrbracket(x)$ is zero at all x which are not jump points.

By (3-17), at points at which $\dot{\gamma}_t(x) = 0$ a perturbation $\delta\dot{\gamma}(x)$ is arbitrary positive, and therefore $(f_t(x) + \tau \dot{f}_t(x))$ must be nonnegative and $\llbracket \dot{\gamma}'_t \rrbracket(x)$ must be nonpositive. At points at which $\dot{\gamma}_t(x) > 0$ a perturbation may have any sign, and therefore the same terms must be zero. Then, the sets of Kuhn–Tucker conditions for f_t

$$\dot{\gamma}_t(x) \geq 0, \quad f_t(x) + \tau \dot{f}_t(x) \geq 0, \quad (f_t(x) + \tau \dot{f}_t(x))\dot{\gamma}_t(x) = 0, \quad \text{a.e. } x \in (0, l), \quad (3-21)$$

and for the jumps of $\dot{\gamma}'_t$,

$$\dot{\gamma}_t(x) \geq 0, \quad \llbracket \dot{\gamma}'_t \rrbracket(x) \leq 0, \quad \llbracket \dot{\gamma}'_t \rrbracket(x)\dot{\gamma}_t(x) = 0, \quad \forall x \in (0, l), \quad (3-22)$$

follow. At every jump point x_o for $\dot{\gamma}'_t$,

$$\llbracket \dot{\gamma}'_t \rrbracket(x_o) = \dot{\gamma}'_t(x_o+) - \dot{\gamma}'_t(x_o-) = \lim_{\varepsilon \rightarrow 0^+} \frac{\dot{\gamma}_t(x_o + \varepsilon) - \dot{\gamma}_t(x_o)}{\varepsilon} - \lim_{\varepsilon \rightarrow 0^-} \frac{\dot{\gamma}_t(x_o + \varepsilon) - \dot{\gamma}_t(x_o)}{\varepsilon}.$$

For $\dot{\gamma}_t(x_o) = 0$ the right-hand side is nonnegative, and therefore $\llbracket \dot{\gamma}'_t \rrbracket(x_o)$ is nonnegative. But it is also nonpositive by (3-22)₂. Hence, a point at which $\dot{\gamma}_t(x_o) = 0$ cannot be a jump point for $\dot{\gamma}'_t$. On the other hand, when $\dot{\gamma}_t(x_o)$ is positive, $\llbracket \dot{\gamma}'_t \rrbracket(x_o)$ is zero by the complementarity condition (3-22)₃. Then $\llbracket \dot{\gamma}'_t \rrbracket(x_o)$ is zero in all cases, that is, *there is no creation of new jump points for $\dot{\gamma}'_t$* in the second-order minimization. In particular, if $\dot{\gamma}'_t$ is continuous at initial time t_0 , it remains continuous at all subsequent t . In what follows, we only consider processes in which $\dot{\gamma}'_t$ is continuous instead of piecewise continuous.

The assumed continuity of $\dot{\gamma}'_t$ requires a couple of comments. The first is that it does not imply the continuity of γ''_t . Indeed, by Hadamard's condition, this is true only if $dx/dt \neq 0$. That is, a discontinuity of γ''_t is possible, provided that it does not change its position with t . The second comment is that the

continuity of γ_t'' has been deduced only for the discretized problem. It need not be preserved in the limit when the time step τ tends to zero. In fact, in the numerical simulations in Section 4 we will find a situation in which the continuity is not preserved in the limit.

The solutions of (3-21) and (3-22) depend on the time step τ , and *do not imply* the conditions obtained from the first-order minimization. Specifically, the complementarity condition (3-18)₃ *does not hold* in the second-order minimization. Therefore, the solutions for $\tau > 0$ are not, in general, directions of steepest descent.

Another necessary condition for a minimum of J at $\dot{\gamma}_t$ is that the second variation

$$\delta^2 J(\delta\dot{\gamma}) = \int_0^l (\theta''(\gamma_t(x)) \delta\dot{\gamma}^2(x) + w''(\epsilon_t) \delta\bar{\gamma}^2 + \alpha \delta\dot{\gamma}'^2(x)) dx \quad (3-23)$$

be nonnegative for all $\delta\dot{\gamma}$ for which the first variation

$$\delta J(\dot{\gamma}_t, \delta\dot{\gamma}) = \int_0^l (f_t(x) + \tau \dot{f}_t(x)) \delta\dot{\gamma}(x) dx$$

is zero. For x in the elastic zone, $f_t(x)$ is positive, and $(f_t(x) + \tau \dot{f}_t(x))$ is positive for sufficiently small τ . Then, by (3-20)₁, for sufficiently small τ the first variation is zero only for perturbations with $\delta\dot{\gamma}(x) = 0$ almost everywhere in the elastic zone.

In the inelastic zone, where $f_t(x) = 0$ by definition, conditions (3-21) reduce to

$$\dot{\gamma}_t(x) \geq 0, \quad \dot{f}_t(x) \geq 0, \quad \dot{f}_t(x) \dot{\gamma}_t(x) = 0, \quad \text{a.e. } x \in \mathcal{F}(\beta_t, \gamma_t), \quad (3-24)$$

and, by (3-20)₁, the first variation is zero only if

$$\dot{f}_t(x) \delta\dot{\gamma}(x) = 0 \quad (3-25)$$

almost everywhere in the inelastic zone. In any interval at which $\dot{\gamma}_t(x) = 0$, we have

$$\dot{f}_t(x) = \theta''(\gamma_t(x)) \dot{\gamma}_t(x) - \dot{\sigma}_t - \alpha \dot{\gamma}_t''(x) = -\dot{\sigma}_t.$$

Because $\dot{f}_t(x) \geq 0$ by (3-24)₂, such intervals do not exist in a hardening response, $\dot{\sigma}_t > 0$, and may exist only with $\dot{f}_t(x) = 0$ in a perfect plastic response or only with $\dot{f}_t(x) > 0$ in a softening response. Then in a softening response condition (3-25) requires $\delta\dot{\gamma}(x) = 0$. Leaving aside the exceptional case of a perfectly plastic response, we conclude that the first variation is zero only if $\delta\dot{\gamma}(x)$ is zero in the elastic zone and at almost all points of the inelastic zone at which $\dot{\gamma}_t(x) = 0$.

Therefore, it is sufficient to consider perturbations $\delta\dot{\gamma}$ with support in the part of the inelastic zone at which $\dot{\gamma}_t > 0$. Let $(a, a + l_j)$ be an interval in this region. A necessary condition for a minimum is that the integral

$$\int_a^{a+l_j} \left(\theta''(\gamma_t(x)) \delta\dot{\gamma}^2(x) + \frac{l_j}{l_j} w''(\epsilon_t) \delta\bar{\gamma}^2 + \alpha \delta\dot{\gamma}'^2(x) \right) dx \quad (3-26)$$

be nonnegative for all perturbations $\delta\dot{\gamma}$ with $\delta\dot{\gamma}(a) = \delta\dot{\gamma}(a + l_j) = 0$. This corresponds to the nonnegativeness of the smallest eigenvalue ρ_1 of problem (A.15), with H as in (A.5), and with

$$a = 0, \quad l_j = L, \quad \theta''(\gamma_t(x)) = \alpha h(x), \quad \frac{l_j}{l_j} w''(\epsilon_t) = \alpha \omega, \quad \delta\dot{\gamma}(x) = y(x), \quad \delta\bar{\gamma} = \frac{l_j}{l} \bar{y}.$$

The last equality follows from the definitions

$$\bar{y} = \frac{1}{l_J} \int_0^{l_J} y(x) dx, \quad \delta \bar{\gamma} = \frac{1}{l} \int_0^l \delta \dot{\gamma}(x) dx = \frac{1}{l} \int_0^{l_J} \delta \dot{\gamma}(x) dx,$$

which hold for $\delta \dot{\gamma}(x) = y(x)$ with support in $(0, l_J)$. Then the relation between $w''(\epsilon_t)$ and ω comes from the identification

$$\frac{l}{l_J} w''(\epsilon_t) \delta \bar{\gamma}^2 = \alpha \omega \bar{y}^2.$$

The upper bound (A.17) for ρ_1 provides the necessary condition

$$\alpha \lambda_{o_J}^2 + \theta''_{o_J} \geq 0, \quad (3-27)$$

where λ_{o_J} is the smallest eigenvalue of problem (A.1). It is the solution of (A.7), now rewritten in the form

$$\frac{l_J}{l} \frac{w''(\epsilon_t)}{\alpha} l_J^2 = \frac{\lambda_{o_J}^3 l_J^3}{\lambda_{o_J} l_J - 2 \tan \lambda_{o_J} l_J / 2},$$

and θ''_{o_J} is as in (3-12), with y_{o_J} given by (A.8).

Because the first variation $\delta J(\dot{\gamma}_t, y_{o_J})$ is zero and J is quadratic, one has

$$J(\dot{\gamma}_t + c y_{o_J}) = J(\dot{\gamma}_t) + \frac{1}{2} \tau c^2 \delta^2 J(\dot{\gamma}_t, y_{o_J}) = J(\dot{\gamma}_t) + \frac{1}{2} \tau c^2 \rho_1 \int_0^l y_{o_J}^2(x) dx,$$

for every positive constant c . Therefore, $\rho_1 \geq 0$ is a necessary condition for a minimum of J . Moreover, for any other perturbation with support in $(0, l_J)$, since the first variation is nonnegative and ρ_1 is the smallest eigenvalue,

$$J(\dot{\gamma}_t + \delta \dot{\gamma}) \geq J(\dot{\gamma}_t) + \frac{1}{2} \tau \delta^2 J(\dot{\gamma}_t, \delta \dot{\gamma}) \geq J(\dot{\gamma}_t) + \frac{1}{2} \tau \rho_1 \int_0^l \delta \dot{\gamma}^2(x) dx.$$

Therefore, $\rho_1 \geq 0$ is also a sufficient condition for a minimum. The lower bound (A.19) for ρ_1 provides the explicit sufficient condition

$$\alpha \lambda_{o_J}^2 + \theta''_{\min} \geq 0, \quad (3-28)$$

with

$$\theta''_{\min} = \inf_{x \in (0, l_J)} \theta''(\gamma_t(x)).$$

For ρ_1 negative, $J(\dot{\gamma}_t + c y_{o_J})$ can take unlimited negative values. Like in the local model, this event corresponds to brittle fracture. Therefore, $\rho_1 \geq 0$ is a necessary and sufficient condition for a minimum of J , and a negative ρ_1 corresponds to brittle fracture.

It is of interest to see in which cases the continuations are elastic, $\dot{\gamma}_t = 0$. From (3-19),

$$\begin{aligned} J(\dot{\gamma}) &= \int_0^l (f_t(x) - \tau w''(\epsilon_t) \dot{\beta}_t) \dot{\gamma}(x) dx + \frac{1}{2} \tau \int_0^l (\theta''(\gamma_t(x)) \dot{\gamma}^2(x) + w''(\epsilon_t) \bar{\gamma}^2 + \alpha \dot{\gamma}'^2(x)) dx \\ &\geq \int_0^l (f_t(x) - \tau w''(\epsilon_t) \dot{\beta}_t) \dot{\gamma}(x) dx + \frac{1}{2} \tau \alpha \rho_1 \int_0^l \dot{\gamma}^2(x) dx \geq \int_0^l \left(c \dot{\gamma}(x) + \frac{1}{2} \tau \alpha \rho_1 \dot{\gamma}^2(x) \right) dx, \end{aligned}$$

where

$$c \doteq f_{\min} - \tau w''(\epsilon_t) \dot{\beta}_t, \quad f_{\min} \doteq \inf_{x \in (0, l)} f_t(x).$$

Because $J(0) = 0$, $\dot{\gamma} = 0$ is a minimizer if the right-hand side of the inequality is nonnegative. In particular, $\dot{\gamma} = 0$ is a minimizer if both ρ_1 and c are nonnegative.

There are two remarkable cases in which c is positive. The first is the case of $\dot{\beta}_t < 0$. That $\dot{\gamma}_t = 0$ for $\dot{\beta}_t < 0$ is the nonlocal version of the property (2-31) of elastic unloading for the local model. The second is the case of a *strictly elastic regime*, that is, of configurations (β_t, γ_t) for which $f_{\min} > 0$. Indeed, in this case c is positive for sufficiently small τ . This is a relaxed version of the condition found in the local model, that there is no increase of inelastic deformation in the elastic regime. Here, the same is true only in a strictly elastic regime.

The foregoing discussion can be summarized as follows:

$$\begin{aligned} \rho_1 \geq 0 & \iff \text{there are minimizers,} \\ \rho_1 < 0 & \iff \text{brittle fracture.} \\ \rho_1 \geq 0 \text{ and } \dot{\beta}_t < 0 & \implies \dot{\gamma}_t = 0 \text{ is a minimizer,} \\ \rho_1 \geq 0 \text{ and } f_{\min} > 0 & \implies \dot{\gamma}_t = 0 \text{ is a minimizer.} \end{aligned} \tag{3-29}$$

The last two implications tell us that, in a quasistatic evolution, fracture may occur only at loading, $\dot{\beta}_t \geq 0$, and in a regime which is not strictly elastic.

To determine the explicit form of a continuation $\dot{\gamma}_t$ when $c < 0$ is not as easy as it was in the local model. Indeed, in the region at which $\dot{\gamma}_t(x) = 0$, the introduction of the nonlocal term transforms the incremental equilibrium equation $\dot{\sigma}_t = \theta''(\gamma_t(x))\dot{\gamma}_t(x)$ into the differential equation

$$\dot{\sigma}_t = \theta''(\gamma_t(x))\dot{\gamma}_t(x) - \alpha \dot{\gamma}_t''(x).$$

This region is not known a priori, since its determination is a part of the solution of the problem. Moreover, only in some special cases is a closed-form solution available. One of them is the onset of the inelastic regime, studied in the next subsection.

3.5. The onset of the inelastic regime. Consider a load process $t \mapsto \beta_t$ from the natural configuration $(\beta_{t_0}, \gamma_{t_0}) = (0, 0)$, with $\dot{\beta}_t > 0$ for all t . At $t = t_0$ we have

$$f_{t_0}(x) = \theta'(\gamma_{t_0}(x)) - \sigma_{t_0} - \alpha \gamma_{t_0}''(x) = \theta'(0) > 0,$$

so that the whole bar is in a strictly elastic regime. By continuity, this regime persists over a finite time interval (t_0, t_c) . In this interval $\dot{\gamma}_t = 0$ by (3-29)₄, and $\gamma_t = 0$ because of the initial condition $\gamma_{t_0} = 0$. The deformation of the bar is homogeneous, with

$$u'(x, t) = \epsilon_t = \beta_t, \quad \sigma_t = w'(\beta_t), \quad f_t = \theta'(0) - w'(\beta_t). \tag{3-30}$$

The elastic regime ends at the time t_c at which β reaches the critical value β_c given by (2-37). At this time f_t becomes zero, and all points of the bar switch from the elastic to the inelastic zone. This is the onset of the inelastic regime.

To determine the continuation $\dot{\gamma}_t$ at $t = t_c$, we start from the complementarity condition (3-24)₃:

$$0 = \dot{f}(x)\dot{\gamma}(x) = \theta''(0)\dot{\gamma}^2(x) - \dot{\sigma}\dot{\gamma}(x) - \alpha\dot{\gamma}''(x)\dot{\gamma}(x). \quad (3-31)$$

Here and in the following, for simplicity, we omit all subscripts t_c . Integrating over $(0, l)$ and recalling that $\dot{\gamma}'$ has no jumps if $\dot{\gamma}$ is a minimizer for J , we get

$$\dot{\sigma} \int_0^l \dot{\gamma}(x) dx = \int_0^l (\theta''(0)\dot{\gamma}^2(x) + \alpha\dot{\gamma}'^2(x)) dx.$$

If $\theta''(0) \geq 0$, the right-hand side is positive and therefore $\dot{\sigma}$ is positive. Moreover, $\dot{\gamma}(x)$ is strictly positive almost everywhere in $(0, l)$. Indeed, if $\dot{\gamma}(x) = 0$ in some interval (a, b) , from inequality (3-24)₂ on that interval we have

$$0 \leq \dot{f}(x) = -\dot{\sigma},$$

in contradiction with the positiveness of $\dot{\sigma}$. Therefore, $\dot{\gamma}$ is a solution of the differential problem

$$\theta''(0)\dot{\gamma}(x) - \dot{\sigma} - \alpha\dot{\gamma}''(x) = 0, \quad \forall x \in (0, l), \quad \dot{\gamma}(0) = \dot{\gamma}(l) = 0, \quad (3-32)$$

subject to the dissipation condition $\dot{\gamma}(x) \geq 0$. For $\theta''(0) > 0$ the solution is

$$\dot{\gamma}(x) = \frac{\dot{\sigma}}{\theta''(0)} \left(1 - \frac{\cosh \kappa(l/2 - x)}{\cosh \kappa l/2} \right), \quad (3-33)$$

with $\kappa = (\theta''(0)/\alpha)^{1/2}$. By integration over $(0, l)$,

$$\bar{\dot{\gamma}} = \frac{\dot{\sigma}}{\theta''(0)} \varphi(\kappa l), \quad \varphi(\kappa l) \doteq 1 - \frac{\tanh \kappa l/2}{\kappa l/2},$$

and, because $\dot{\sigma} = w''(\beta_c)(\dot{\beta} - \bar{\dot{\gamma}})$,

$$\dot{\sigma} = \frac{\theta''(0)w''(\beta_c)}{\theta''(0) + \varphi(\kappa l)w''(\beta_c)} \dot{\beta}. \quad (3-34)$$

Comparing with the solution (2-34) of the local model, we see that the nonlocal effect is concentrated in the factor $\varphi(\kappa l)$. Because this factor is positive and less than one, the slope $\dot{\sigma}/\dot{\beta}$ of the response curve (σ, β) is positive and greater than the slope predicted by the local model, but smaller than the slope $w''(\beta_c)$ at unloading.

For $\theta''(0) = 0$, the solution is

$$\dot{\gamma}(x) = \frac{\dot{\sigma}}{2\alpha} x(l - x). \quad (3-35)$$

By integration over $(0, l)$,

$$\bar{\dot{\gamma}} = \frac{\dot{\sigma} l^2}{12\alpha}, \quad (3-36)$$

and from $\dot{\sigma} = w''(\beta_c)(\dot{\beta} - \bar{\dot{\gamma}})$,

$$\dot{\sigma} = \frac{12\alpha w''(\beta_c)}{12\alpha + l^2 w''(\beta_c)} \dot{\beta}. \quad (3-37)$$

Thus, for $\theta''(0) = 0$ the perfectly plastic response $\dot{\sigma} = 0$ of the local model is replaced by a work-hardening response.

For $\theta''(0) < 0$, the solution is

$$\dot{\gamma}(x) = \frac{w''(\beta_c)(\dot{\beta} - \bar{\gamma})}{\theta''(0)} \left(1 - \frac{\cos k(l/2 - x)}{\cos kl/2} \right), \quad (3-38)$$

with $k = (-\theta''(0)/\alpha)^{1/2}$. Integrating over $(0, l)$ we find

$$\bar{\gamma} = \frac{w''(\beta_c)(\dot{\beta} - \bar{\gamma})}{\theta''(0)} \psi(kl), \quad \psi(kl) = 1 - \frac{\tan kl/2}{kl/2}, \quad (3-39)$$

and, therefore,

$$\bar{\gamma} = \frac{\psi(kl)w''(\beta_c)}{\theta''(0) + \psi(kl)w''(\beta_c)} \dot{\beta}. \quad (3-40)$$

Again, the difference with (2-33) is due to a single factor, which now is $\psi(kl)$. This factor is negative for $kl < \pi$ and positive for $\pi < kl < 2.861\pi$, with a jump from $-\infty$ to $+\infty$ at $kl = \pi$.

The solution (3-38) satisfies the dissipation inequality (2-10) for all x only if $kl \leq 2\pi$. Indeed, for $kl > 2\pi$, $\dot{\gamma}(x)$ takes negative values near the boundary. For such kl , let us consider the possibility of *localized solutions*, that is, of solutions of (3-31) which satisfy the differential equation (3-32) in a subinterval $(a, a + l_i)$ of $(0, l)$ and are zero outside. Without loss of generality, we take the interval $(0, l_i)$, with $l_i < l$. The boundary conditions are

$$\dot{\gamma}(0) = \dot{\gamma}(l_i) = 0, \quad \dot{\gamma}'(l_i) = 0, \quad (3-41)$$

where $\dot{\gamma}(0) = 0$ is condition (3-15)₁, and the two remaining conditions are due to the continuity of $\dot{\gamma}$ and $\dot{\gamma}'$, which are zero on (l_i, l) . The first two conditions determine a solution of the form (3-38) with l replaced by l_i , and the third determines the length

$$l_i = 2\pi/k. \quad (3-42)$$

Therefore, the solution is

$$\dot{\gamma}(x) = \frac{w''(\beta_c)(\dot{\beta} - \bar{\gamma})}{\theta''(0)} (1 - \cos kx), \quad x \in (0, l_i). \quad (3-43)$$

It holds for $l_i < l$, that is, for $kl > 2\pi$. For $kl = 2\pi$, it coincides with (3-38). By integration over $(0, l_i)$ it follows that

$$l\bar{\gamma} = l_i \frac{w''(\beta_c)(\dot{\beta} - \bar{\gamma})}{\theta''(0)},$$

and, therefore,

$$\bar{\gamma} = \frac{w''(\beta_c)}{w''(\beta_c) + \theta''(0)l/l_i} \dot{\beta}. \quad (3-44)$$

It is convenient to introduce the positive constant

$$\psi_f \doteq -\frac{\theta''(0)}{w''(\beta_c)}. \quad (3-45)$$

With this constant, and with ψ_o as in (A.13), (3-40) and (3-44) take the common form

$$\bar{\gamma} = \frac{\psi_o(kl)}{\psi_o(kl) - \psi_f} \dot{\beta}. \quad (3-46)$$

For $kl < \pi$, $\psi_o(kl)$ is negative. Therefore, the condition $\bar{\gamma} \geq 0$ is satisfied. For $kl > \pi$ the numerator becomes positive, and $\bar{\gamma}$ is positive only if

$$\psi_o(kl) > \psi_f. \quad (3-47)$$

From (3-46), using (2-32), we get the incremental response law

$$\dot{\sigma} = \frac{\theta''(0)}{\psi_o(kl) - \psi_f} \dot{\beta}. \quad (3-48)$$

The slope $\dot{\sigma} / \dot{\beta}$ of the response curve is positive if $kl < \pi$, and negative if $kl > \pi$ and condition (3-47) holds. Therefore, at the onset of the inelastic regime, for $\theta''(0)$ negative the continuation is

$$\begin{aligned} &\text{work-hardening} && \text{if } kl < \pi, \\ &\text{strain-softening} && \text{if } kl > \pi \text{ and } \psi_o(kl) > \psi_f. \end{aligned}$$

In the separating case $kl = \pi$ the continuation is perfectly plastic. For $kl > \pi$ and $\psi_o(kl) \leq \psi_f$, by (3-47), there is no continuation obeying the dissipation inequality (2-10).

We already know that in the solution (3-40) $\dot{\gamma}(x)$ is zero only at the boundary, while in the solution (3-43) $\dot{\gamma}(x)$ is zero on a portion of $(0, l)$ of positive length $(l - l_i)$. We say that the first is a *full-size solution*, and that the second is a *localized solution*. Therefore, for $\theta''(0)$ negative, at the onset of the inelastic regime the continuations are

$$\begin{aligned} &\text{full-size} && \text{if } kl \leq 2\pi, \\ &\text{localized} && \text{if } kl > 2\pi. \end{aligned}$$

From (3-34) and (3-37) it is clear that for $\theta''(0) \geq 0$ all continuations are work-hardening and full-size.

The continuations (3-38) and (3-43) have been determined using the Kuhn–Tucker conditions (3-21) and (3-22), which are necessary for a minimum for the functional J defined in (3-19). It remains to check whether or not these continuations are indeed minimizers. At the onset, f_t is zero. Then, neglecting the factor $\tau/2$, J has the form

$$J(\dot{\gamma}) = \int_0^l (\theta''(0) \dot{\gamma}^2(x) + w''(\beta_c) \bar{\gamma}^2 + \alpha \dot{\gamma}'^2(x) - 2w''(\beta_c) \dot{\beta}_t \dot{\gamma}(x)) dx,$$

and direct computation yields

$$J(\dot{\gamma} + \delta\dot{\gamma}) = J(\dot{\gamma}) + 2 \int_0^l f_t(x) \delta\dot{\gamma}(x) dx + \int_0^l (\theta''(0) \delta\dot{\gamma}^2(x) + w''(\beta_c) \delta\bar{\gamma}^2 + \alpha \delta\dot{\gamma}'^2(x)) dx.$$

On the right side, the first integral is nonnegative by (3-20)₁, and the second integral has the form (3-26). Then we can use the results of Section 3.4. In the present case, both constants θ''_{oJ} and θ''_{\min} which appear in the bounds (3-27) and (3-28) are equal to $\theta''(0)$, and the two bounds coincide. They provide the necessary and sufficient condition $\alpha\lambda_o^2 \geq -\theta''(0)$, that is,

$$\lambda_o^2 \geq k^2, \quad (3-49)$$

where λ_o^2 is the smallest eigenvalue of problem (A.1), with H as in (A.5).

Consider first the case $\pi < kl \leq 2\pi$, for which the continuation (3-38) is positive over $(0, l)$. In this case, λ_o is the solution of (A.7) with

$$L = l, \quad \omega = w''(\beta_c)/\alpha, \quad y(x) = \delta\dot{\gamma}(x),$$

that is,

$$\frac{w''(\beta_c)}{\alpha} l^2 = \frac{\lambda_o^2 l^2}{\psi(\lambda_o l)}. \quad (3-50)$$

Recalling the definition (3-45) of ψ_f , we have

$$\frac{w''(\beta_c)}{\alpha} = \frac{-\theta''(0)}{\alpha\psi_f} = \frac{k^2}{\psi_f}, \quad (3-51)$$

and, therefore,

$$\psi_f = \frac{k^2}{\lambda_o^2} \psi(\lambda_o l).$$

If $k \leq \lambda_o$, then

$$\psi(\lambda_o l) \leq \psi(kl) = \psi_o(kl),$$

because ψ is a decreasing function and, by (A.13), coincides with ψ_o for $\pi < kl \leq 2\pi$. Then, $k \leq \lambda_o$ implies inequality (3-47). Conversely, if $k > \lambda_o$ the above inequality is reversed. That is, for $\pi < kl \leq 2\pi$ the condition (3-49) for a minimum coincides with the condition (3-47) for a nonnegative $\bar{\gamma}$.

Now consider the case $kl > 2\pi$, for which the continuation (3-43) is positive only on $(0, l_i)$, with $l_i = 2\pi/k < l$. In this case, λ_o is the solution of (A.7) with

$$L = l_i, \quad \omega = \frac{l_i}{l} \frac{w''(\beta_c)}{\alpha}, \quad y(x) = \delta\dot{\gamma}(x), \quad \bar{y} = \frac{l}{l_i} \delta\bar{\gamma},$$

as shown in Section 3.4. Using (3-51), (A.7) takes the form

$$\frac{l_i}{l} \frac{k^2}{\psi_f} l_i^2 = \frac{\lambda_o^2 l_i^2}{\psi(\lambda_o l_i)}.$$

Recalling that for $kl > 2\pi$, by (A.13),

$$\psi_o(kl) = \frac{2\pi}{kl} = \frac{l_i}{l},$$

we finally get

$$\psi_f = \frac{k^2}{\lambda_o^2} \psi_o(kl) \psi(\lambda_o l_i).$$

If $k \leq \lambda_o$, then $\lambda_o l_i \geq kl_i = 2\pi$. Therefore,

$$\psi(\lambda_o l_i) \leq \psi(2\pi) = 1,$$

and inequality (3-47) follows. If $k > \lambda_o$, then $2\pi > \lambda_o l_i$, and the reversed inequality holds. Thus, the coincidence of (3-47) with (3-49) is proved for all $kl > \pi$.

The incremental response law (3-48) shows that, when these inequalities are satisfied as equalities, the slope $\dot{\sigma}/\dot{\beta}$ of the response curve becomes infinite. This is the totally brittle fracture, that is, the

catastrophic fracture at the onset of the inelastic deformation already described by the local model. The difference is that, while in the local model brittle fracture occurs as soon as θ'' ceases to be positive, here it occurs at negative values of θ'' . Therefore, the sharp inequality (3-47) is a safety condition against totally brittle fracture.

It is commonly asserted that the nonlocal energy term introduces an internal length of the material. Here, this length can be identified with the length l_i defined by (3-42), which is the length of the localization zone in a localized continuation. As seen before, the ratio $l/l_i = kl/2\pi$ determines the quality of the response, hardening or softening, full-size or localized.

The present analysis suggests the definition of a second *characteristic length*

$$l_c = 2\pi \sqrt{\frac{\alpha}{w''(\beta_c)}}, \quad (3-52)$$

with which the no-fracture condition (3-47) takes the form $\psi_o(2\pi l/l_i) > l_c^2/l_i^2$, that is,

$$l/l_c > \frac{l/l_i}{\sqrt{\psi_o(2\pi l/l_i)}} \doteq \Psi(l/l_i). \quad (3-53)$$

The parameters which determine the response at the onset are the bar length l and the material constants $w''(\beta_c)$, $\theta''(0)$, and α . With the above definitions, they reduce to the ratios l/l_c and l/l_i . A complete representation of the response is given in Figure 1. In it, each point of the plane represents a bar. The points located below the curve $l/l_c = \Psi(l/l_i)$ correspond to bars which undergo totally brittle fracture at the onset of the inelastic deformation. The region above the curve is divided into three subregions,

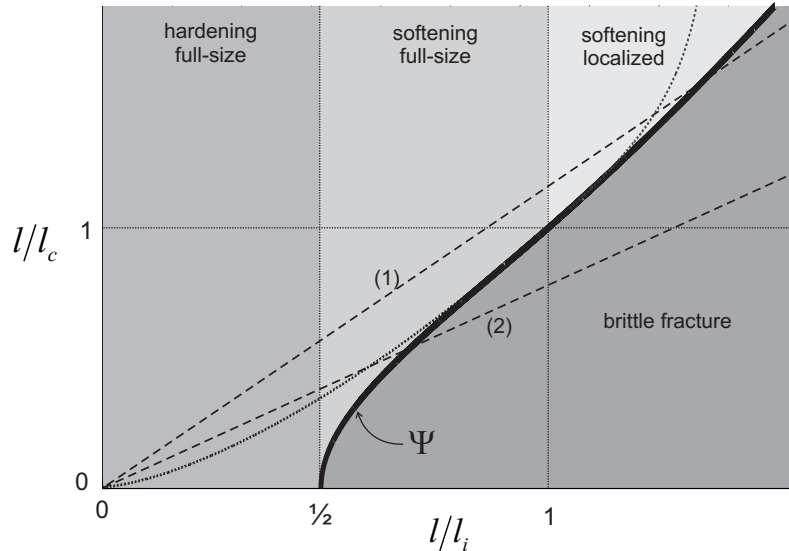


Figure 1. The response at the onset of the inelastic deformation. The three regions above the curve correspond to hardening full-size, softening full-size, and softening localized responses. The region below the curve corresponds to totally brittle fracture. Lines (1) and (2) represent families of bars made of the same material and with varying length.

corresponding to full-size and hardening ($l/l_i < 1/2$), full-size and softening ($1/2 < l/l_i < 1$), and localized and softening ($l/l_i > 1$) continuations, respectively.

The straight lines from the origin represent families of bars made of the same material and with l growing with the distance from the origin. All families have full-size hardening continuations for small l , softening continuations for intermediate l , and catastrophic failure for large l . Moreover, for families with slope $l_i/l_c > 1$ the softening continuations may be both full-size and localized, while for those with $l_i/l_c < 1$, corresponding to straight lines which do not cross the third region above the curve, the softening continuations can only be full-size.

3.6. Collapse mechanisms. In the nonlocal model there are two possible collapse mechanisms, *brittle fracture* and *ductile fracture*. Both are characterized by the slope $\dot{\sigma}/\dot{\beta}$ of the response curve, which is $-\infty$ for brittle fracture and zero for ductile fracture. Brittle fracture coincides with the unique collapse mode provided by the local model. As shown in the next section, the two collapse modes are observed in steel and in concrete, respectively.

In a quasistatic evolution $t \mapsto (\beta_t, \gamma_t)$, assume that $\theta''(\gamma_t(x))$ is negative at all x , and that it can be approximated by a negative constant θ_t'' . Define the current values of k and ψ_f :

$$k_t \doteq \sqrt{\frac{-\theta_t''}{\alpha}}, \quad \psi_{ft} \doteq \frac{-\theta_t''}{w''(\epsilon_t)}. \quad (3-54)$$

With them, the relations (3-46) and (3-48), obtained for the onset of the inelastic regime, can be extrapolated to the subsequent evolution

$$\bar{\gamma}_t = \frac{\psi_o(k_t l)}{\psi_o(k_t l) - \psi_{ft}} \dot{\beta}_t, \quad \dot{\sigma}_t = \frac{\theta_t''}{\psi_o(k_t l) - \psi_{ft}} \dot{\beta}_t, \quad (3-55)$$

and condition (3-47) against brittle fracture can be replaced by

$$\psi_o(k_t l) > \psi_{ft}. \quad (3-56)$$

This extrapolation helps us to understand some general features of the bar's response in the softening regime. Of course, the conclusions are purely qualitative, since the exact values of θ_t'' and k_t are not known. More precise results can only be obtained from numerical simulation.

Assume that $-\theta''$ is monotonic increasing. For all x , the function $t \mapsto -\theta''(\gamma_t(x))$ is increasing as well, because $t \mapsto \gamma_t(x)$ is increasing by the dissipation inequality (2-10). Then the average $-\theta_t''$ is increasing, k_t is increasing, and $\psi_o(k_t l)$ is decreasing. Supposing $w''(\epsilon_t)$ substantially independent of t , ψ_{ft} is increasing. Therefore, the positive denominator in (3-55) decreases with t . When it becomes zero, the negative slope of the response curve becomes infinite, and catastrophic failure takes place.

On the contrary, for $-\theta''$ monotonic decreasing, $-\theta_t''$ decreases with t , and the slope $|\dot{\sigma}_t/\dot{\beta}_t|$ in (3-55) decreases as well. If $-\theta_t''$ tends to zero, the slope tends to zero, and this corresponds to ductile fracture. Thus, brittle fracture takes place for $-\theta''$ increasing, that is, for θ' concave, and ductile fracture takes place for θ' convex. In spite of some early statements and more recent observations, see [Hillerborg 1991] and [Jirásek and Rolshoven 2009b, Figure 16], respectively, this correlation between fracture modes and the concavity-convexity properties of θ' has not received adequate attention in the literature.

This correlation is illustrated by Figure 1. If θ_t'' increases with t , the internal length $l_{it} = 2\pi/k_t$ decreases and the ratio l/l_{it} increases, while l/l_c stays approximately constant. The point representing

the current status of the bar moves horizontally to the right, tending to brittle fracture which, at the onset, occurs at the curve Ψ . On the contrary, if θ_t'' decreases with t the point moves to the left, tending to the perfectly plastic response which, at the onset, takes place at the line $l/l_i = 1/2$.

The function θ' cannot be concave for all $\gamma > 0$. Indeed, concavity implies

$$\theta'(\gamma) \leq \theta'(0) + \gamma\theta''(0),$$

and for $\theta''(0) < 0$ the assumption $\theta'(\gamma) > 0$ is violated for sufficiently large γ . On the other hand, the assumption (2-7)₃ that θ has a finite limit at $+\infty$ requires that

$$\lim_{\gamma \rightarrow +\infty} \theta''(\gamma) = 0.$$

Then $-\theta''$ has a maximum at a finite γ . Brittle fracture occurs only if this maximum produces a k_t sufficiently large to violate inequality (3-56).

4. Numerical simulations

For the nonlocal model, quasistatic evolution in the inelastic regime has been investigated by performing a number of numerical simulations. An iterative procedure was used: after fixing a time step τ , for each $t = n\tau$ the continuation $\dot{\gamma}_t$ at (β_t, γ_t) was determined approximately by solving a sequence of discretized minimum problems, with the data taken from the solution at $t = (n-1)\tau$.

In the case of loading, $\dot{\beta} > 0$, the parameter t is identified with the load β , so that $\dot{\beta} = 1$, and the time step τ is in fact a load step. The discretized problem consists in minimizing a quadratic approximation of the energy $E^{\text{eq}}(\beta_t + \tau\dot{\beta}, \gamma_t + \tau\dot{\gamma})$. For convenience, we refer to the more general functional

$$\begin{aligned} F(\beta, \gamma, \tau, \delta\gamma) = & \int_0^l \left(\theta(\gamma(x)) + w(\beta - \bar{\gamma}) + \frac{1}{2}\alpha\gamma'^2(x) \right) dx \\ & + \tau \int_0^l \left(\theta'(\gamma_t(x)) \delta\gamma(x) + w'(\beta - \bar{\gamma})(1 - \delta\gamma(x)) + \alpha\gamma'(x) \delta\gamma'(x) \right) dx \\ & + \frac{1}{2}\tau^2 \left(\int_0^l \left(\theta''(\gamma(x)) \delta\gamma^2(x) + \alpha \delta\gamma'^2(x) \right) dx + lw''(\beta - \bar{\gamma})(1 - \delta\bar{\gamma})^2 \right), \end{aligned} \quad (4-1)$$

such that $F(\beta_t, \gamma_t, 0, 0)$ coincides with $E^{\text{eq}}(\beta_t, \gamma_t)$, and $F(\beta_t, \gamma_t, \tau, \dot{\gamma})$ coincides with the second-order approximation (2-28) of $E^{\text{eq}}(\beta_t + \tau\dot{\beta}, \gamma_t + \tau\dot{\gamma})$ for the given τ .

4.1. The algorithm. In the solution procedure an iterative algorithm, implemented in an ad hoc finite element code, was used. At each iteration step, for a given initial configuration (β_0, γ_0) , with γ_0 a local minimizer for $F(\beta_0, \cdot, 0, 0)$, the configuration $(\beta_0 + \tau, \gamma_0 + \tau\dot{\gamma}_0)$ is determined by minimizing the function $F(\beta_0, \gamma_0, \tau, \cdot)$, constrained by the dissipation inequality (2-10) and by the boundary conditions (3-6). At each load step, the solution accuracy is refined through an iterative procedure acting on the quadratic approximation

$$F_2(\beta_0, \gamma, \delta\gamma) \doteq F(\beta_0, \gamma, 0, 0) + \frac{\partial}{\partial(\delta\gamma)} F(\beta_0, \gamma, 0, 0) \delta\gamma + \frac{1}{2} \frac{\partial^2}{\partial(\delta\gamma)^2} F(\beta_0, \gamma, 0, 0) \delta\gamma^2$$

of $F(\beta_0, \gamma, 0, \delta\gamma)$. The algorithm runs as follows.

1. *Incremental step.*

(i) Compute

$$\dot{\gamma}_0 = \operatorname{argmin}\{F(\beta_0, \gamma_0, \tau, \cdot) \mid \delta\gamma(x) \geq 0, \delta\gamma(0) = \delta\gamma(l) = 0\}.$$

(ii) Set $\beta_1 = \beta_0 + \tau$, $\gamma_1^0 = \gamma_0 + \tau\dot{\gamma}_0$.2. *Iterative refinement.*

(i) Compute

$$\delta\gamma^1 = \operatorname{argmin}\{F_2(\beta_1, \gamma_1^0, \cdot) \mid \delta\gamma(x) \geq \gamma_0(x) - \gamma_1^0(x), \delta\gamma(0) = \delta\gamma(l) = 0\},$$

and set $\gamma_1^1 = \gamma_1^0 + \delta\gamma^1$.

(ii) Compute

$$\delta\gamma^i = \operatorname{argmin}\{F_2(\beta_1, \gamma_1^{i-1}, \cdot) \mid \delta\gamma(x) \geq \gamma_0(x) - \gamma_1^{i-1}(x), \delta\gamma(0) = \delta\gamma(l) = 0\},$$

and set $\gamma_1^i = \gamma_1^{i-1} + \delta\gamma^i$.(iii) Stop when the L^2 norm of $(\gamma_1^i - \gamma_1^{i-1})$ is less than a given tolerance $\hat{\gamma}$.3. *End.*(i) Take as γ_1 the last γ_1^i in the preceding iteration.(ii) If the L^2 norm of $(\gamma_1 - \gamma_0)$ is less than a given tolerance $\tilde{\gamma}$, perform a new incremental step from (β_1, γ_1) . Otherwise, repeat the computation with τ replaced by $\tau/2$.

The last control avoids the overcoming of energy barriers due to exceedingly large incremental steps. In the numerical code, the spatial variable x is discretized using linear finite elements. The quadratic programming problems involving the minimization of F_2 are solved using the projection method [Polak 1971; Gill et al. 1981] implemented in the `quadprog.m` function of MATLAB. The code generates a mesh refinement when the number of elements in the inelastic zone is smaller than a certain number (100 in the simulations presented below). In this case, each element is split into two subelements.

4.2. Choice of energy densities. For the elastic strain energy density we take the quadratic expression

$$w(\epsilon) = \frac{1}{2} EA\epsilon^2, \quad (4-2)$$

where the axial stiffness EA is the product of the Young modulus E of the material and the area A of the cross-section. For the cohesive energy density we take the piecewise cubic function

$$\theta(\gamma) = A_i + B_i\gamma + \frac{1}{2}C_i\gamma^2 + \frac{1}{6}D_i\gamma^3, \quad \gamma \in [\gamma_{i-1}, \gamma_i], \quad (4-3)$$

where

$$\{[\gamma_{i-1}, \gamma_i], i = 1, \dots, n, \}$$

is a subdivision of the interval $[\gamma_0, \gamma_n]$ into n adjacent subintervals, with $\gamma_0 = 0$ and $\gamma_n \leq +\infty$. The coefficients A_i , B_i , C_i and D_i satisfy the $3(n-1)$ conditions

$$\begin{aligned} B_{i+1} &= B_i - 3(A_{i+1} - A_i)\gamma_i^{-1}, \\ C_{i+1} &= C_i + 6(A_{i+1} - A_i)\gamma_i^{-2}, \quad i = 1, \dots, (n-1), \\ D_{i+1} &= D_i - 6(A_{i+1} - A_i)\gamma_i^{-3}, \end{aligned}$$

which guarantee the continuity of θ , θ' , and θ'' at γ_i . We fix $A_1 = \theta(0) = 0$, while $B_1 = \theta'(0)$, the value of the axial force at the onset of the inelastic regime, is identified on the experimental curve. The remaining constants are determined by fixing $n+1$ coefficients, for example, C_1 , D_1 , and A_j for $j = 2, \dots, n$. In the following simulations these constants are selected with the purpose of reproducing the response curves of two specific experimental tests, one on a steel bar and one on a concrete specimen.

4.3. Simulation 1: The tensile response of a steel bar. For the first simulation, the data were obtained from a test on a steel bar, stretched to rupture under controlled end displacements. The test was made in Ancona, at the Laboratorio Prove Materiali e Strutture of the Università Politecnica delle Marche. The specimen was a ribbed bar, made of B450C (FeB44k) steel, with diameter $\phi = 16$ mm and length $l = 200$ mm. The axial stiffness

$$EA = 42 \times 10^3 \text{ kN}$$

is the product of the Young modulus of steel, $E = 210 \text{ kN/mm}^2$, and the cross-sectional area $A = \pi\phi^2/4$. The axial force at the onset of the inelastic deformation, measured on the response diagram, is

$$B_1 = 109.5 \text{ kN}.$$

With the purpose of investigating the size effect, simulations with three different lengths,

$$l = 100, 200, 300 \text{ mm},$$

were made. The nonlocality parameter α was taken equal to

$$\alpha = 10 \text{ kN mm}^2.$$

This is a tentative value. The criteria for choosing the value of α are still under investigation.

For the time step τ , mesh size h , and tolerances $\hat{\gamma}$ and $\tilde{\gamma}$ introduced in Section 4.1, the values

$$\tau = 10^{-4}, \quad h = 0.5 \text{ mm}, \quad \hat{\gamma} = 10^{-6}, \quad \tilde{\gamma} = 10^{-3},$$

were chosen. These values provide good accuracy and, at the same time, keep a moderate size for the discretized problem. For the cohesive energy density a function θ_1 of the form (4-3) was taken, with

$$\begin{aligned} n &= 4, \quad \gamma_i = (0.10, 1.62, 2.01, 10), \quad C_1 = 380 \text{ kN}, \\ D_1 &= -3800 \text{ kN}, \quad A_i = (0, -0.61, 499.69, 223.74) \text{ kN}. \end{aligned}$$

This energy, plotted at the top in Figure 2, is convex for $\gamma < 0.1$ and concave for $\gamma > 0.1$.

In Figure 3, the experimental response curve (the dotted line) is compared with the response curves of simulations with lengths $l = 100, 200, 300$ mm. In the experimental curve, the initial hardening regime is followed by a softening regime, in which the negative slope of the curve increases with β , and becomes

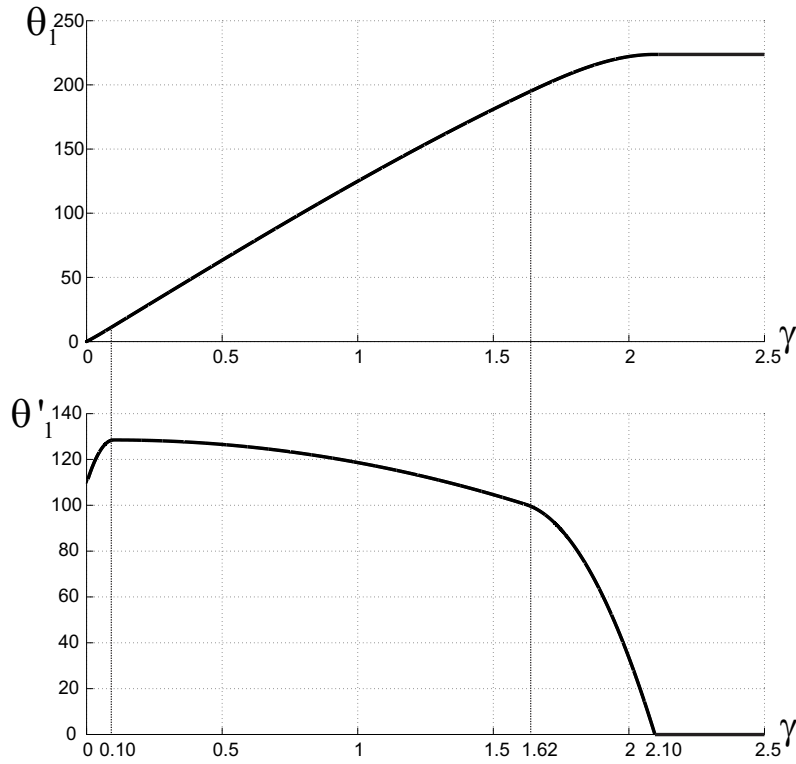


Figure 2. Simulation 1: the cohesive energy θ_1 (top) and its derivative θ'_1 (bottom).

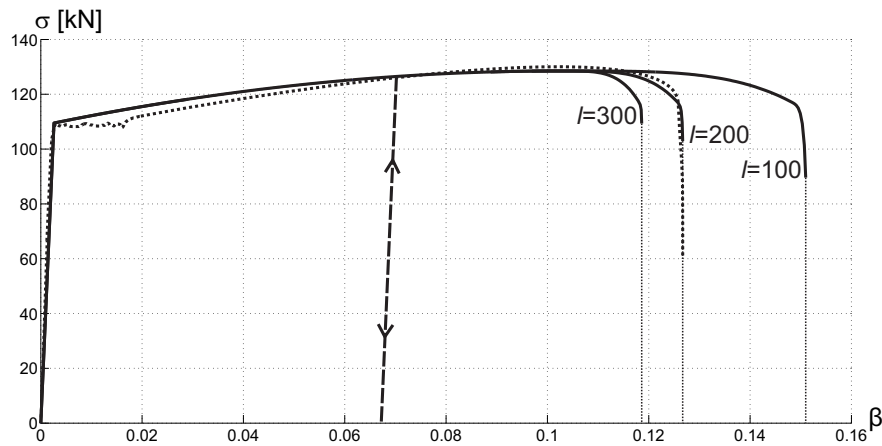


Figure 3. Simulation 1: the experimental response curve (dotted line), and the response curves of simulations with different values of l . The dashed line shows the model's response to unloading and reloading.

infinite at rupture. In the model, this behavior is reproduced by taking θ_1 initially convex, and then concave with growing concavity.

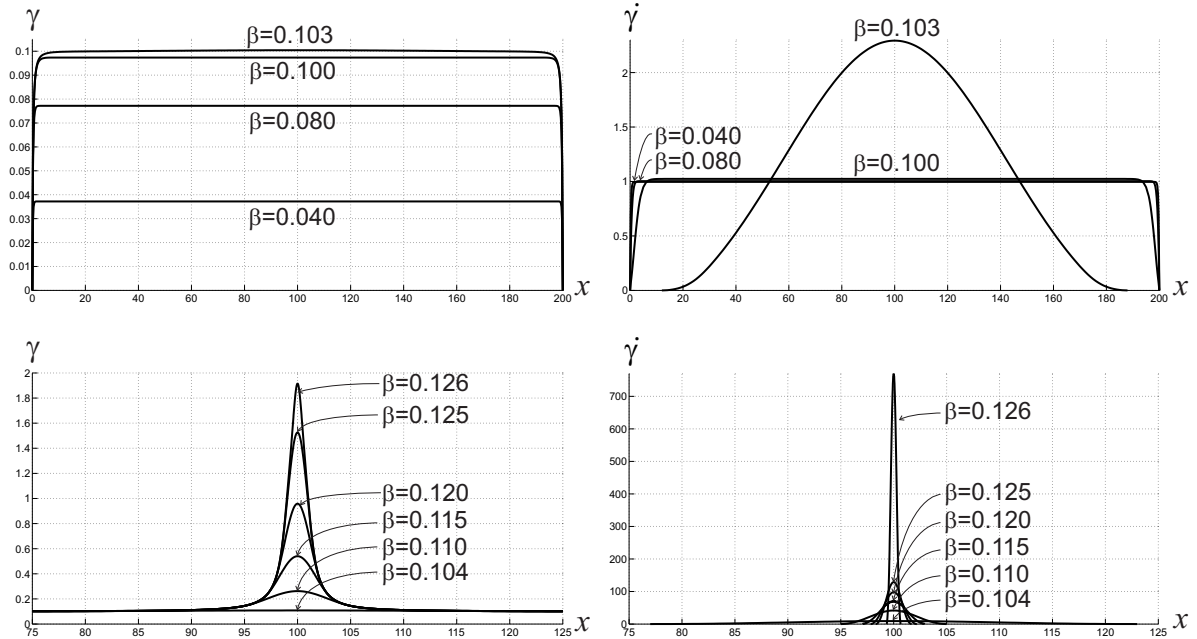


Figure 4. Simulation 1 with $l = 200$ mm. Evolution of γ (left column) and $\dot{\gamma}$ (right column) for increasing β .

The response curve of the simulation with $l = 200$ mm, which is the specimen's length, is very close to the experimental curve. Of course, this is due to an appropriate choice of the material constants. Anyway, it is remarkable that a small number of constants is sufficient to reproduce the evolution of the bar's deformation from the natural configuration to final rupture. Also remarkable is the perfect reproduction of the elastic unloading, shown by the dashed line in the figure, and obtained by reversing the sign of β up to complete unloading, $\sigma = 0$, and then reloading. As shown in the figure, the reloading curve traces back the unloading line and then continues along the loading curve of monotonic loading.

In the three simulations shown in Figure 3, the hardening parts of the response curves are identical. The hardening regime ends at $\beta \approx 0.102$, where the force σ reaches its maximum and a softening regime starts. Shortly after, strain localization begins, and the three curves separate. The figure shows that for longer bars the softening regime produces larger negative slopes, and rupture occurs at smaller β . This size effect agrees with the theoretical preview (3-55)₂.

The evolution of γ and $\dot{\gamma}$ in the simulation with $l = 200$ mm is shown in Figure 4. In the initial hardening regime, represented in the upper part of the figure, both γ and $\dot{\gamma}$ are constant, except near the boundary, where $\gamma(x) = \dot{\gamma}(x) = 0$ as required by the boundary conditions.

The regime of full-size softening response is very short. Indeed, it starts at $\beta \approx 0.102$ and ends at $\beta \approx 0.103$ when, as shown in the two right panels in the figure, localization takes place. For larger β , the deformation concentrates at shorter and shorter central zones of the bar. The left half of Figure 5 reproduces the curves of Figure 4, bottom left; note the close similarity of these diagrams with the results of experiments made long ago by Miklowitz [1950], shown on the right in Figure 5. Also, the evolution curves for γ are qualitatively the same as the curves in [Jirásek and Rolshoven 2009b, Figure 17.1].

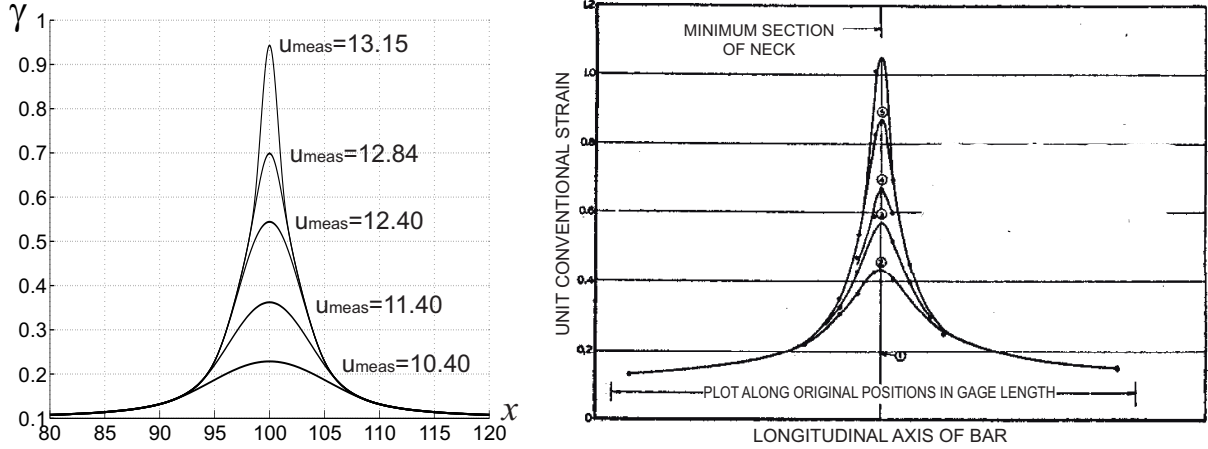


Figure 5. Left: detail of Figure 4, bottom left. Right: experiments on a cylindrical bar of medium-carbon steel, taken from [Miklowitz 1950].

4.4. Simulation 2: The tensile response of a concrete specimen. The aim of our second simulation was to reproduce the experimental force-elongation curve of a prismatic specimen made of lightweight concrete, taken from [Hordijk 1992, Figure 38]. The specimen is prismatic, with dimensions of $50 \times 50 \times 150$ mm, Young's modulus $E = 18 \text{ kN/mm}^2$, and maximum aggregate size of 8 mm. In the simulation we take

$$EA = 45 \times 10^3 \text{ kN}, \quad B_1 = 6.3 \text{ kN},$$

with B_1 the axial force at the onset of the inelastic regime, read on the experimental curve. We consider the three lengths

$$l = 100, 150, 200 \text{ mm}.$$

For the nonlocality parameter α we take

$$\alpha = 3497 \text{ kN mm}^2.$$

This value corresponds to an internal length $l_i = 2\pi/k = 8$ mm, equal to the maximum aggregate size. For the time step τ , mesh size h , and tolerances $\hat{\gamma}$ and $\tilde{\gamma}$ we choose

$$\tau = 10^{-7}, \quad h = 0.25 \text{ mm}, \quad \hat{\gamma} = 10^{-6}, \quad \tilde{\gamma} = 10^{-3}.$$

For the cohesive energy we take the function θ_2 represented in Figure 6. This is an energy of the form (4-3), with

$$n = 4, \quad \gamma_i = (0.7, 1.2, 65.0, 100.0) \times 10^{-4},$$

and with

$$C_1 = 18 \times 10^3 \text{ kN}, \quad D_1 = -25.7143 \times 10^7 \text{ kN}, \quad A_i = (0, -0.12, -0.25, 154.27) \times 10^{-4} \text{ kN}.$$

This energy is convex for $\gamma < 0.7 \times 10^{-4}$ and concave for $\gamma > 0.7 \times 10^{-4}$.

The force-elongation response curves for the three considered values of l are shown in Figure 7. The correspondence with the experimental curve is good, but not as good as in the preceding simulation.

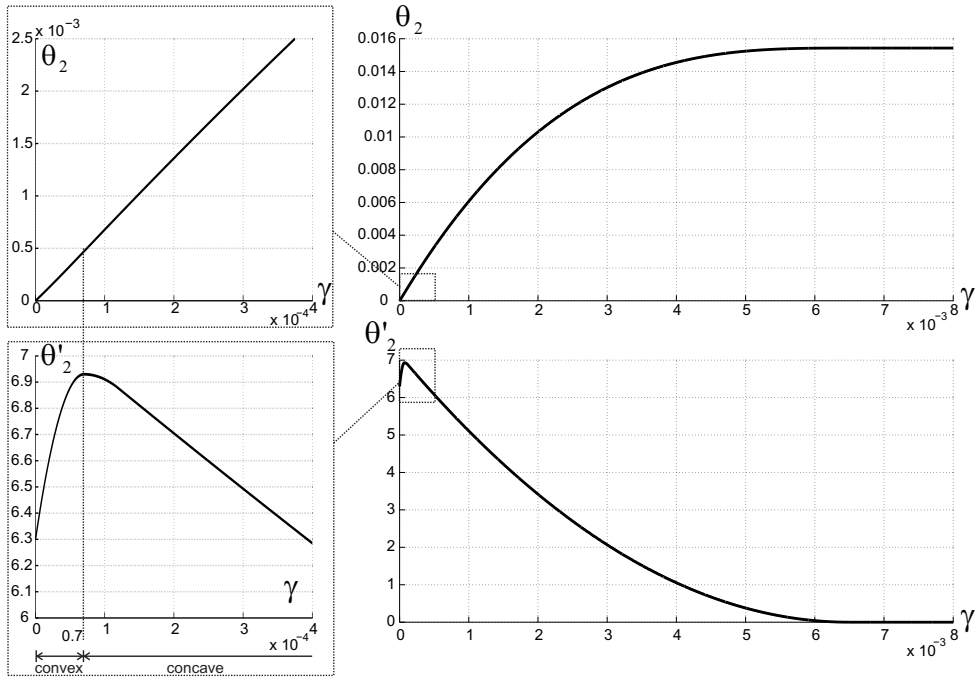


Figure 6. Simulation 2: the cohesive energy θ_2 (top) and its derivative θ'_2 (bottom).

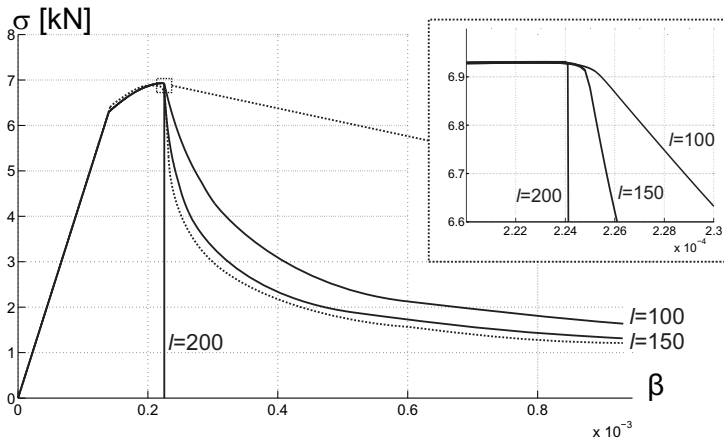


Figure 7. Simulation 2: the experimental (dotted line) and the numerical response curves (solid line).

This may be due to the fact that in the experimental curve in [Hordijk 1992] the elongation $\beta_m l_m$ was measured on a central zone of the bar, of length $l_m = 35$ mm, while here the total elongation was evaluated with the approximate formula

$$\beta l \approx \beta_m l_m + (l - l_m)(\beta - \bar{\gamma}),$$

obtained by neglecting the inelastic deformation outside the central zone.

Another cause of discrepancy is that in the experiment the specimen had a central notch, which was not considered in the simulation. Generally, the data fitting was more difficult than in Simulation 1, where all data came from our own experiment and not from one taken from the literature.

As in the preceding simulation, the three numerical curves coincide in the elastic regime and in the subsequent hardening and full-size softening regimes. They start to differ at the onset of localization, at $\beta \approx 2.23 \times 10^{-4}$. In the localized softening regime, in accordance with the size effect, the negative slope of the response curve is larger for longer bars. The curve for $l = 200$ mm exhibits brittle fracture at the onset of localization. This agrees with the safety condition (3-56) against brittle fracture, which now takes the form

$$\frac{2\pi}{k_t l} > \frac{\alpha k_t^2}{EA}$$

Indeed, in a localized solution $\psi_o(k_t l)$ is equal to $2\pi/k_t l$ by (A.13), and ψ_{ft} is equal to $\alpha k_t^2/EA$ by (3-54) and (4-2). Setting $k_t = 2\pi/l_t$, with $l_t = 8$ mm equal to the maximum aggregate size, condition (3-56) becomes

$$l < \frac{2\pi EA}{k_t^3 \alpha} = \frac{EA l_t^3}{4\pi^2 \alpha} \approx 167 \text{ mm.}$$

For the bars with $l = 100$ mm and 150 mm, the convex shape of θ'_2 determines a ductile fracture mechanism. For $l = 150$ mm, as shown in Figure 8, at $\beta \approx 2.22 \times 10^{-4}$ the inelastic strain rate $\dot{\gamma}$ begins to localize and the force starts to decrease. The length of the localized zone attains a minimum of about 8 mm at $\beta \approx 2.25 \times 10^{-4}$, and then steadily increases. Numerical investigations not reported here

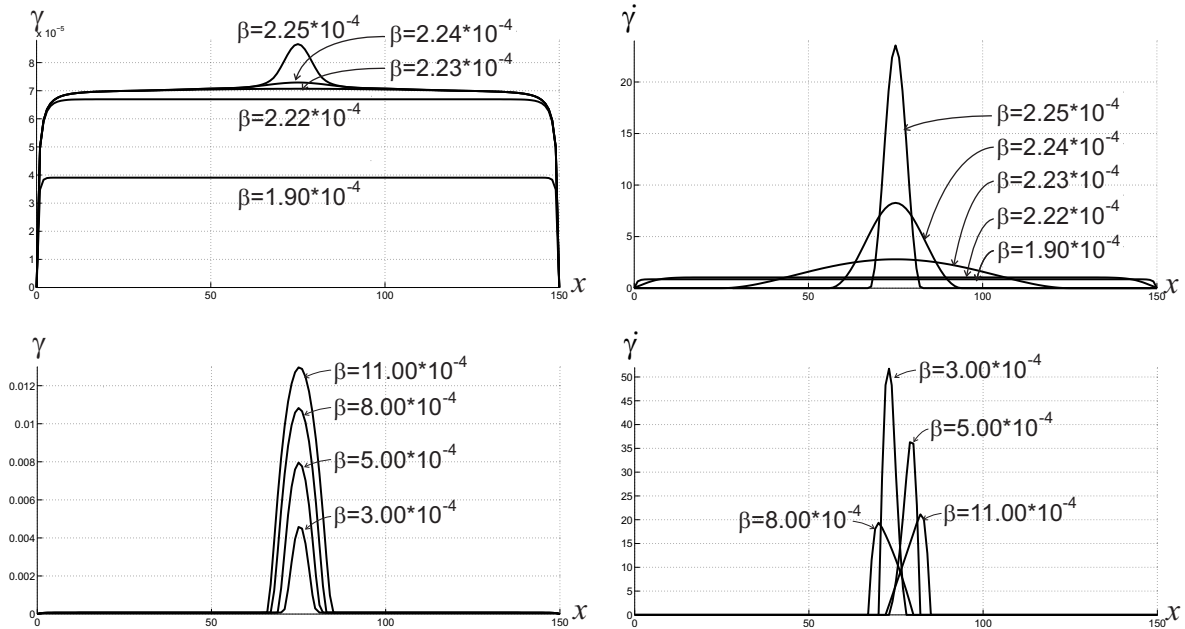


Figure 8. Simulation 2: evolution of the inelastic deformation for $l = 150$ mm.

show that the localization zone eventually diffuses over the whole bar. For the bar with $l = 200$ mm, catastrophic failure occurs at $\beta \approx 2.24 \times 10^{-4}$.

The evolution of γ and $\dot{\gamma}$ is shown in Figure 8. The asymmetries of the diagrams of $\dot{\gamma}$ in the bottom right panel of Figure 8 are purely numerical, and random in nature. This is confirmed by the symmetry of their time integral γ in the bottom left panel. For $\beta \approx 10^{-3}$ the inelastic deformation γ is concentrated on a portion of the bar of length of about 20 mm. This agrees with an estimate given in [Bažant and Pijaudier-Cabot 1989], according to which the characteristic length of concrete is about 2.7 times the maximum aggregate size.

By effect of the expansion of the inelastic zone the force decreases, and tends to a horizontal asymptote. In [Jirásek 1998; Jirásek and Rolshoven 2009a], the expansion of the inelastic zone is considered as unphysical, and the *stress locking*, that is, the convergence of the force to a positive limit, is considered as a proof of this.

While the horizontal asymptotes of the response curve shown in [Jirásek 1998, Figure 3], are about 80% of the maximum σ , a numerical investigation, not reported here, shows that in the present simulation the horizontal asymptote is only about 2% of the maximum σ . This modest residual force cannot be eliminated. Indeed, looking at the diagrams of γ in the bottom left panel of Figure 8 we see that, for $\beta > 4.5 \times 10^{-4}$, the largest value $\gamma(l/2)$ of γ is greater than 6×10^{-3} . Therefore, as shown by the constitutive curve of Figure 6, bottom, the corresponding value of θ' is zero. Because the point $x = l/2$ is in the inelastic zone, from the yield condition (3-2) with $\theta' = 0$ it follows that

$$\sigma = -\alpha\gamma''(l/2),$$

with $\gamma''(l/2)$ strictly negative because γ has a maximum at $x = l/2$.

Appendix: Solution of some eigenvalue problems

Consider the eigenvalue problem

$$\int_0^L (y'^2(x) + \omega\bar{y}^2) dx = \lambda^2 \int_0^L y^2(x) dx, \quad y \in H, \quad (\text{A.1})$$

with ω a given positive constant, and

$$\bar{y} = \frac{1}{L} \int_0^L y(x) dx. \quad (\text{A.2})$$

The eigenfunctions are the solutions of the Euler equation

$$y''(x) - \omega\bar{y} + \lambda^2 y(x) = 0, \quad (\text{A.3})$$

and have the form

$$y(x) = A \sin \lambda x + B \cos \lambda x + \omega\lambda^{-2}\bar{y}. \quad (\text{A.4})$$

We wish to determine the smallest eigenvalue λ_0^2 and the corresponding eigenfunctions y_0 , for two different choices of the domain H .

(i) Let H be the set

$$H = \{y \in H^1(0, L) \mid y(0) = y(L) = 0\}. \quad (\text{A.5})$$

In this case, the constants A and B are

$$A = -\omega\lambda^{-2}\bar{y} \tan \lambda L/2, \quad B = -\omega\lambda^{-2}\bar{y}. \quad (\text{A.6})$$

Moreover, integrating (A.4) over $(0, L)$ we get

$$L\bar{y} = \omega\lambda^{-3}\bar{y}((\cos \lambda L - 1) \tan \lambda L/2 - \sin \lambda L + \lambda L) = \omega\lambda^{-3}\bar{y}(\lambda L - 2 \tan \lambda L/2),$$

that is,

$$\omega L^2 = \frac{\lambda^3 L^3}{\lambda L - 2 \tan \lambda L/2} = \frac{\lambda^2 L^2}{\psi(\lambda L)}, \quad (\text{A.7})$$

with ψ as in (3-39)₂. The right-hand side is an increasing function of λL , and is equal to zero at $\lambda L = \pi$ and to $+\infty$ at $\lambda L \approx 2.861\pi$. Therefore, for every $\omega L^2 > 0$ there exists a unique λL in $(\pi, 2.861\pi)$ which satisfies (A.7). It determines the smallest eigenvalue λ_o^2 for given ω and L . The corresponding eigenfunctions are the scalar multiples of

$$y_o(x) = \cos \lambda_o(L/2 - x) - \cos \lambda_o L/2. \quad (\text{A.8})$$

The problem has been formulated in $H^1(0, L)$, which is the largest space in which the integrals which appear in (A.1) exist. However, the eigenfunction y_o belongs to $C^\infty[0, L]$. So the solution does not change if H is taken to be any space included between $C^\infty[0, L]$ and $H^1(0, L)$.

(ii) Now let H be the set

$$H = \{y \in H^2(0, L) \mid y(0) = y(L) = 0, y(x) \geq 0, \forall x \in (0, L)\}. \quad (\text{A.9})$$

In (A.8), y_o satisfies condition $y(x) \geq 0$ only for $\lambda_o L \leq 2\pi$. By (A.7), this corresponds to $\omega L^2 \leq 4\pi^2$. For larger values of ωL^2 , $y_o(x)$ becomes negative near the boundary.

For $\omega L^2 > 4\pi^2$ we look for solutions y which are of the form (A.4) in a subinterval $(0, L_y)$ of $(0, L)$ and zero outside. To belong to $H^2(0, L)$, they must satisfy the conditions

$$y(0) = y(L_y) = 0, \quad y'(L_y) = 0.$$

By (A.4), the first two conditions are satisfied by

$$A = -\omega\lambda^{-2}\bar{y} \tan \lambda L_y/2, \quad B = -\omega\lambda^{-2}\bar{y},$$

and the third condition is satisfied if $A = 0$. This implies $\tan \lambda L_y/2 = 0$, that is,

$$\lambda L_y = 2\pi. \quad (\text{A.10})$$

Because L_y is smaller than L , this solution is possible only for $\lambda L > 2\pi$, that is, for $\omega L^2 > 4\pi^2$. But this is exactly the range not covered by the solution (A.7) and (A.8). For $A = 0$ and $B = -\omega\lambda^{-2}\bar{y}$, the integration of (A.4) yields

$$\omega L^2 = \frac{\lambda^2 L^3}{L_y} = \frac{\lambda^3 L^3}{2\pi}. \quad (\text{A.11})$$

Therefore, for all $\omega L^2 > 4\pi^2$ the smallest eigenvalue is the solution λ_o^2 of this equation. The corresponding eigenfunction

$$y_o(x) = \begin{cases} 1 - \cos \lambda_o x, & \text{if } x \leq 2\pi/\lambda_o, \\ 0, & \text{if } x > 2\pi/\lambda_o, \end{cases} \quad (\text{A.12})$$

satisfies the condition $y_o(x) \geq 0$ for all x . Therefore, λ_o^2 is the smallest eigenvalue, and y_o is a corresponding eigenfunction.

In conclusion, the smallest eigenvalue of problem (A.1) with H as in (A.9) is the solution of (A.7) if $\omega L^2 \leq 4\pi^2$, and of (A.11) if $\omega L^2 > 4\pi^2$. By defining

$$\psi_o(\lambda L) \doteq \begin{cases} \psi(\lambda L), & \text{if } 0 \leq \lambda L \leq 2\pi, \\ \frac{2\pi}{\lambda L}, & \text{if } 2\pi < \lambda L, \end{cases} \quad (\text{A.13})$$

both (A.7) and (A.11) take the form

$$\lambda^2 = \omega \psi_o(\lambda L), \quad (\text{A.14})$$

and the smallest eigenvalue λ_o^2 is the unique solution of this equation. The function ψ_o is C^∞ in $(\pi, +\infty)$, except at the point $\lambda L = 2\pi$, where it is continuous and has a continuous derivative.

Now consider the eigenvalue problem

$$\int_0^L (y'^2(x) + \omega \bar{y}^2 + h(x)y^2(x)) dx = \rho \int_0^L y^2(x) dx, \quad y \in H, \quad (\text{A.15})$$

with ω a given positive constant and h an integrable function. We wish to determine upper and lower bounds for the smallest eigenvalue ρ_o , both for H as in (A.5) and as in (A.9).

For H as in (A.5), let λ_o^2 be the smallest eigenvalue of problem (A.1) and let y_o be a corresponding eigenfunction. Define

$$h_o \doteq \frac{\int_0^L h(x)y_o^2(x) dx}{\int_0^L y_o^2(x) dx}. \quad (\text{A.16})$$

Then, by (A.1),

$$\int_0^L (y_o'^2(x) + \omega \bar{y}_o^2 + h_o y_o^2(x)) dx = (\lambda_o^2 + h_o) \int_0^L y_o^2(x) dx.$$

That is, $(\lambda_o^2 + h_o)$ is an eigenvalue of (A.15) and y_o is a corresponding eigenfunction. Therefore, an upper bound for ρ_o is

$$\lambda_o^2 + h_o \geq \rho_o. \quad (\text{A.17})$$

To get a lower bound, set

$$h_{\min} = \inf_{x \in (0, L)} h(x). \quad (\text{A.18})$$

Then the left-hand side of (A.15) is greater than or equal to

$$\int_0^L (y'^2(x) + \omega \bar{y}^2 + h_{\min} y^2(x)) dx \geq (\lambda_o^2 + h_{\min}) \int_0^L y^2(x) dx, \quad \forall y \in H,$$

and the lower bound

$$\rho_o \geq \lambda_o^2 + h_{\min} \tag{A.19}$$

follows. Depending on the given function h , the two bounds can be far away from each other. On the other hand, they coincide if h is a constant, $h(x) = \bar{h}$. Indeed, in this case $h_o = h_{\min} = \bar{h}$ and, therefore,

$$\rho_o = \lambda_o^2 + \bar{h}. \tag{A.20}$$

For H as in (A.9) the same bounds hold, with λ_o^2 and y_o replaced by the smallest eigenvalue of problem (A.1) and by a corresponding eigenfunction, respectively.

References

- [Aifantis 1984] E. C. Aifantis, “On the microstructural origin of certain inelastic models”, *J. of Engng. Materials and Technology, ASME* **106** (1984), 326–330.
- [Aifantis 1992] E. C. Aifantis, “On the role of gradients in the localization of deformation and fracture”, *Int. J. Engng. Sci.* **30** (1992), 1279–1299.
- [Ambrosio and Tortorelli 1990] L. Ambrosio and V. M. Tortorelli, “Approximation of functionals depending on jumps by elliptic functionals via Γ -convergence”, *Comm. Pure Appl. Math.* **43**:8 (1990), 999–1036.
- [Babadjian 2011] J.-F. Babadjian, “A quasistatic evolution model for the interaction between fracture and damage”, *Arch. Ration. Mech. Anal.* **200**:3 (2011), 945–1002.
- [Barenblatt 1962] G. I. Barenblatt, “The mathematical theory of equilibrium cracks in brittle fracture”, pp. 55–129 in *Advances in applied mechanics*, vol. 7, Academic Press, New York, 1962.
- [Bažant and Chen 1997] Z. P. Bažant and E. P. Chen, “Scaling of structural failure”, *Appl. Mech. Rev.* **50** (1997), 593–627.
- [Bažant and Jirásek 2002] Z. P. Bažant and M. Jirásek, “Nonlocal integral formulations of plasticity and damage: survey of progress”, *ASCE J. of Engng. Mechanics* **128** (2002), 1119–1149.
- [Bažant and Le 2009] Z. P. Bažant and J. L. Le, “Size effect on strength and lifetime distributions of quasibrittle structures”, *Proc. ASME Int. Mech. Engng. Congress IMECE* (2009), 1–9.
- [Bažant and Pijaudier-Cabot 1989] Z. P. Bažant and G. Pijaudier-Cabot, “Measurement of characteristic length of nonlocal continuum”, *ASCE J. of Engng. Mechanics* **115** (1989), 755–767.
- [Benallal and Marigo 2007] A. Benallal and J.-J. Marigo, “Bifurcation and stability issues in gradient theories with softening”, *Modelling and Simulation in Materials Science and Engineering* **15** (2007), S283–S295.
- [Borst and Pamin 1996] R. D. Borst and J. Pamin, “Gradient plasticity in numerical simulation of concrete cracking”, *Eur. J. Mech.* **A/15** (1996), 295–320.
- [Bourdin et al. 2000] B. Bourdin, G. A. Francfort, and J.-J. Marigo, “Numerical experiments in revisited brittle fracture”, *J. Mech. Phys. Solids* **48**:4 (2000), 797–826.
- [Cahn and Hilliard 1958] J. W. Cahn and J. E. Hilliard, “Free energy of a nonuniform system, I: Interfacial free energy”, *J. Chem. Physics* **28** (1958), 258–267.
- [Carpinteri 1982] A. Carpinteri, “Application of fracture mechanics to concrete structures”, *ASCE J. Struct. Division* **108** (1982), 833–848.
- [Carpinteri and Massabò 1997] A. Carpinteri and R. Massabò, “Continuous vs discontinuous bridged-crack model for fiber-reinforced materials in flexure”, *Int. J. Solids Structures* **34** (1997), 2321–2338.
- [Casal 1972] P. Casal, “La théorie du second gradient et la capillarité”, *C. R. Acad. Sc. Paris* **274** (1972), A1571–1574.

- [Dal Maso and Toader 2002] G. Dal Maso and R. Toader, “A model for the quasi-static growth of brittle fractures: existence and approximation results”, *Arch. Ration. Mech. Anal.* **162**:2 (2002), 101–135.
- [Dal Maso and Toader 2010] G. Dal Maso and R. Toader, “Quasistatic crack growth in elasto-plastic materials: the two-dimensional case”, *Arch. Ration. Mech. Anal.* **196**:3 (2010), 867–906.
- [Del Piero and Truskinovsky 2009] G. Del Piero and L. Truskinovsky, “Elastic bars with cohesive energy”, *Contin. Mech. Thermodyn.* **21**:2 (2009), 141–171.
- [Del Piero et al. 2012] G. Del Piero, G. Lancioni, and R. March, “Diffuse cohesive energy in plasticity and fracture”, *Technische Mechanik* **32** (2012), 174–188.
- [Drucker 1952] D. C. Drucker, “A more fundamental approach to plastic stress-strain relations”, pp. 487–491 in *Proceedings of the First U. S. National Congress of Applied Mechanics* (Chicago, 1951), The American Society of Mechanical Engineers, New York, 1952.
- [Ericksen 1990] J. L. Ericksen, “Liquid crystals with variable degree of orientation”, *Arch. Rational Mech. Anal.* **113**:2 (1990), 97–120.
- [Fleck and Hutchinson 2001] N. A. Fleck and J. W. Hutchinson, “A reformulation of strain gradient plasticity”, *J. Mech. Phys. Solids* **49** (2001), 2245–2271.
- [Francfort and Marigo 1998] G. A. Francfort and J.-J. Marigo, “Revisiting brittle fracture as an energy minimization problem”, *J. Mech. Phys. Solids* **46**:8 (1998), 1319–1342.
- [Frank 1958] F. C. Frank, “On the theory of liquid crystals”, *Discuss. Faraday Soc.* **25** (1958), 19–28.
- [Freddi and Royer-Carfagni 2010] F. Freddi and G. Royer-Carfagni, “Regularized variational theories of fracture: a unified approach”, *J. Mech. Phys. Solids* **58**:8 (2010), 1154–1174.
- [Gill et al. 1981] P. E. Gill, W. Murray, and M. H. Wright, *Practical optimization*, Academic Press [Harcourt Brace Jovanovich Publishers], London, 1981.
- [Griffith 1920] A. A. Griffith, “The phenomena of rupture and flow in solids”, *Phil. Trans. Roy. Soc.* **A221** (1920), 163–198.
- [Gudmundson 2004] P. Gudmundson, “A unified treatment of strain gradient plasticity”, *J. Mech. Phys. Solids* **52**:6 (2004), 1379–1406.
- [Gurtin 2003] M. E. Gurtin, “On a framework for small-deformation viscoplasticity: free energy, microforces, strain gradients”, *Int. J. of Plasticity* **19** (2003), 47–90.
- [Gurtin and Anand 2005] M. E. Gurtin and L. Anand, “A theory of strain-gradient plasticity for isotropic, plastically irrotational materials, I: Small deformations”, *J. Mech. Phys. Solids* **53**:7 (2005), 1624–1649.
- [Hill 1950] R. Hill, *The Mathematical Theory of Plasticity*, Oxford, at the Clarendon Press, 1950.
- [Hillerborg 1991] A. Hillerborg, “Application of the fictitious crack model to different types of materials”, *Int. J. of Fracture* **51** (1991), 95–102.
- [Hillerborg et al. 1976] A. Hillerborg, M. Mod er, and P. Peterson, “Analysis of crack formation and crack growth in concrete by means of fracture mechanics and finite elements”, *Cement and Concrete Research* **6** (1976), 773–782.
- [Hordijk 1992] D. A. Hordijk, “Tensile and tensile fatigue behaviour of concrete: experiments, modelling and analyses”, *Heron* **37** (1992), 1–79.
- [Jir sek 1998] M. Jir sek, “Nonlocal models for damage and fracture: comparison of approaches”, *Int. J. Solids Structures* **35**:31-32 (1998), 4133–4145.
- [Jir sek and Rolshoven 2009a] M. Jir sek and S. Rolshoven, “Localization properties of strain-softening gradient plasticity models, I: Strain-gradient theories”, *Int. J. Solids Structures* **46** (2009), 2225–2238.
- [Jir sek and Rolshoven 2009b] M. Jir sek and S. Rolshoven, “Localization properties of strain-softening gradient plasticity models, II: Theories with gradients of internal variables”, *Int. J. Solids Structures* **46** (2009), 2239–2254.
- [Marigo and Truskinovsky 2004] J.-J. Marigo and L. Truskinovsky, “Initiation and propagation of fracture in the models of Griffith and Barenblatt”, *Contin. Mech. Thermodyn.* **16**:4 (2004), 391–409.
- [Miklowitz 1950] J. Miklowitz, “The influence of the dimensional factors on the mode of yielding and fracture in medium-carbon steel. II. The size of the round tensile bar”, *J. Appl. Mech* **17** (1950), 159–168.

- [Mumford and Shah 1989] D. Mumford and J. Shah, “Optimal approximations by piecewise smooth functions and associated variational problems”, *Comm. Pure Appl. Math.* **42:5** (1989), 577–685.
- [Pham and Marigo 2010a] K. Pham and J.-J. Marigo, “Approche variationnelle de l’endommagement, I: Les concepts fondamentaux”, *C. R. Mécanique* **338** (2010), 191–198.
- [Pham and Marigo 2010b] K. Pham and J.-J. Marigo, “Approche variationnelle de l’endommagement, II: Les modèles à gradient”, *C. R. Mécanique* **338** (2010), 199–206.
- [Pham et al. 2011] K. Pham, H. Amor, J.-J. Marigo, and C. Maurini, “Gradient damage models and their use to approximate brittle fracture”, *Int. J. Damage Mechanics* **20** (2011), 618–652.
- [Polak 1971] E. Polak, *Computational methods in optimization: A unified approach*, Mathematics in Science and Engineering **77**, Academic Press, New York, 1971.
- [Truskinovsky 1996] L. Truskinovsky, “Fracture as a phase transition”, in *Contemporary Research in the Mechanics and Mathematics of Materials*, edited by R. C. Batra and M. F. Beatty, Barcelona, 1996.
- [Volokh 2004] K. Y. Volokh, “Nonlinear elasticity for modeling fracture of isotropic brittle solids”, *J. Appl. Mech.* **71** (2004), 141–143.
- [van der Waals 1893] J. D. van der Waals, “Thermodynamische theorie der capillariteit in de onderstelling van continue dichtheidsverandering”, *Verh. Kon. Akad. Wet.* (1) **33:8** (1893), 1–56. Translated in *J. Stat. Phys.* **20** (1979), 197–244, DOI 10.1007/BF01011514.
- [Yalcinkaya et al. 2011] T. Yalcinkaya, W. A. M. Brekelmans, and M. G. D. Geers, “Deformation patterning driven by rate dependent non-convex strain gradient plasticity”, *J. Mech. Phys. Solids* **59:1** (2011), 1–17.

Received 6 Jul 2012. Revised 28 Mar 2013. Accepted 10 Apr 2013.

GIANPIETRO DEL PIERO: dlpgpt@unife.it

Dipartimento di Ingegneria, Università di Ferrara, Via Saragat 1, 44100 Ferrara, Italy

GIOVANNI LANCIONI: g.lancioni@univpm.it

Dipartimento di Ingegneria Civile, Edile e Architettura, Università Politecnica delle Marche, Via Brecce Bianche 12, 60131 Ancona, Italy

RICCARDO MARCH: r.march@iac.cnr.it

Istituto per le Applicazioni del Calcolo “Mauro Picone”, Consiglio Nazionale delle Ricerche, Via dei Taurini 19, 00185 Roma, Italy

CONTINUUM DEPLOYABLE SHELLS MADE OF THIN PLATES

VLADIMIR A. GRACHEV AND YURIY S. NEUSTADT

This paper investigates deployable systems assembled from trapezoidal plates. When the plate package is unwrapped, a net shell with six loop cells is formed. Additional degrees of freedom appear when correlations are present between the sizes of the six loop faces. When thin plates are used, the continuum approximation of the deployed net can be interpreted as a shell with a wide variety of local curvatures. The kinematics of the continuum model are analyzed using the Cartan moving hedron method. Several practical applications of the continuum nets are demonstrated.

1. Introduction

A great deal of interest has been directed to the subject of deployable (transformed) mechanical systems over the past several decades. Deployable mechanisms can be easily “packed into a small box” and can create a surface with a large area after deployment [Gantes 2001; Jensen and Pellegrino 2002; Gan and Pellegrino 2006; Leung and Guest 2007; Chen and You 2008a; 2008b]. With a variety of designs, these systems have numerous potential engineering applications.

Transformed systems have one specific feature: all known stable deployable systems are standard machines; that is, they are a set of absolute solids connected with cylindrical and spherical hinges. The hinges are “internal degrees of freedom” that make controlled transformation of the mechanism possible. Thus, the design of the links does not matter for deployment (kinematics) of the relevant mechanism. The elements of the system could be given any rigidity, and the required internal degrees of freedom could be achieved using a sufficient number of hinges. Until recently, new forms of deployable systems have been limited to mechanisms with rigid parts and few degrees of freedom [Vepa 2010; Sclater and Chironis 2011].

Basically, standard machines are prestressed systems [Otto and Rasch 1995; Luchsinger et al. 2004] because the latter can be interpreted as continuum sets consisting of infinitely small rigid members (frameworks or shells) connected with spherical hinges. Such systems have numerous degrees of freedom and can sustainably move (or balance) at prestressed and special loads. This is why it would be an interesting challenge to make machines with additional degrees of freedom by replacing absolutely rigid parts with flexible ones. At the same time the number of degrees of freedom should not be large, in order to ensure sustainable control over the structure. State-of-the-art technologies allow the making of such machines.

When elastic and flexible thin plates were used as loops that could twist, the system had additional degrees of freedom that enabled a nonstandard mechanism to be deployed. In this case, a minimum amount of energy was required for a system with a high bearing capacity. The current paper describes a

Keywords: continuum deployable shells, manifold, Cartan moving hedron, homogenization, Gauss–Codazzi equations, practical application.

similar type of mechanism, and the systems presented in this paper consist of 3D six-link loops that are not simply mechanisms arbitrarily correlated between their sizes. For this reason, the six-link loops with internal degrees of freedom are extracted first. Next, a continuum model (subsequently referred to as the continuum net or continuum shell) that approximates the finite-dimensional net of the six-link loops is constructed. The mechanical behavior of the continuum nets is studied, assuming that the cylindrical hinges between the plates are ideal and have no friction.

The paper contains an illustration of possible applications of continuum nets in engineering.

2. Kinematics of deployable shells assembled from trapezoidal plates

If a net constructed by sticking several paper six-link loops together consists of equal rectangular plates (shown in Figure 1, Sketch 2), unwrapping the package would cause the middle lines of the plates to form a plane. The same result would be observed if rectilinear strips of hinged rectangles were used instead of six-link loops (Figure 1, Sketch 1).

The net represents a mechanism with sides of arbitrary sizes, regardless of the number of plates it includes. The hinged hexagon has six degrees of freedom on the plane, while each glued face removes three degrees of freedom.

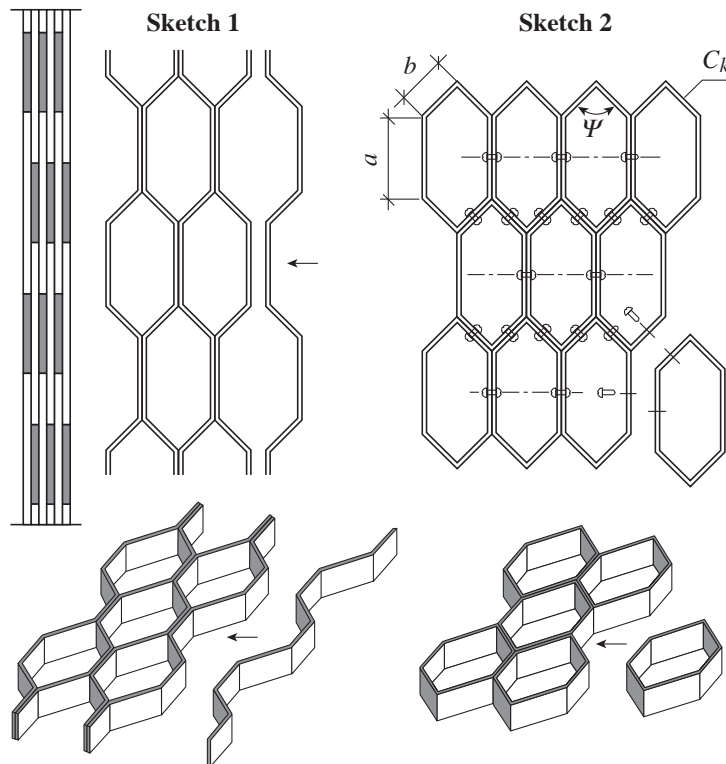


Figure 1. Net of rectangles connected with cylindrical hinges.

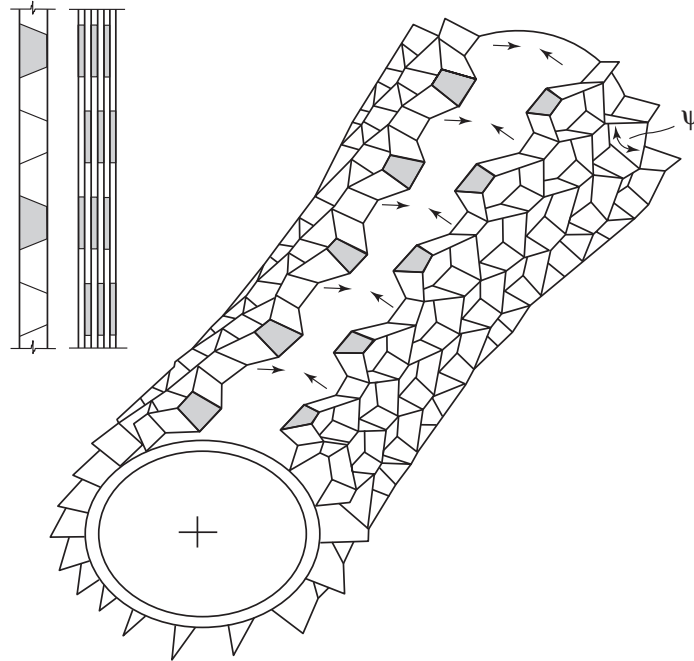


Figure 2. Net of strips assembled from trapezoids.

If undistorted rectangles in the cell were replaced with trapezoids using cylindrical hinges as a connection, the assembled net would not deploy because a six-link loop of absolute solids is usually a rigid body, while a net of N six-link loops (as shown in Figure 1, Sketch 2) has $12N$ redundant constraints.

Assuming that the cell is symmetrical (the cell consists of two part types) and the plates are thin (their rigidity for twist and bending is small), the package can be deployed into a shell (Figure 2).

The present structure was invented by Swank [1991] (in the USA) and Grachev and Neustadt [1999a] (in Russia). The research of the latter [Grachev and Neustadt 1995; 1996] covers the mechanical fundamentals of deployable systems assembled from identical trapezoidal plates. The concepts of the above-mentioned articles and [Grachev and Neustadt 1999a; 1999b] are represented in a general geometrical context that enables larger classes of transformed shells to be reviewed from a common standpoint.

Making a net of trapezoidal plates according to Figure 1, Sketch 1, is more technically feasible; however, it is more convenient to construct theoretical designs according to Figure 1, Sketch 2. Therefore, the second option is used in the subsequent presentation.

Let us consider the mirror-symmetrical six-link loop that is symmetrical against two planes and is assembled from two types of trapezoids (light and dark) connected with cylindrical hinges (Figure 3). The black points are located on the middle lines of the trapezoids. Point O is the center of gravity of trapezoids 2 and 5. Vector $\vec{\beta}_1$ is tangential to the circumference passing through the intersection of the middle lines of trapezoids 2 and 5, and vector $\vec{\beta}_2$ is tangential to the arc of the circle passing through points 4, O , and 1.

First, it must be confirmed that the mirror-symmetrical six-link loop is a mechanism with one degree of freedom, and the surface built on the middle lines of the trapezoids serves as an approximation of

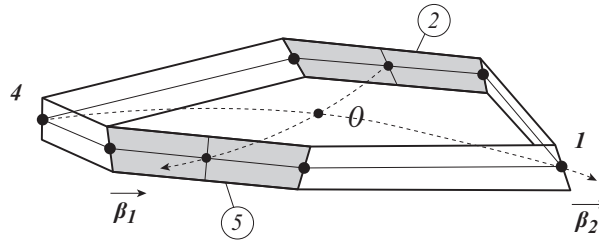


Figure 3. Six-link loop cell.

the smooth shell. For this reason, the cell shown with relevant projections in Figure 4 is considered. The values in the circles refer to the numbers of the trapezoids that comprise the hinged six-link loop. Intersections of the trapezoid centerlines are denoted with Arabic numerals.

The same values describe a linear hinge between the faces. The radius vectors of the middle lines are designated by $\vec{r}_i, i = 1, \dots, 6$, while vector \vec{r}_0 connects the center of gravity of the cell with point 1 (Figure 5).

The angular velocity vector of the side number i relative to the side $(i + 1)$ is designated with $\vec{\omega}_i$, while the vectors of dihedral angles between the neighboring plates are designated by $\vec{\Psi}_i, i = 1, 2, \dots, 6$. The length of the middle line of sides 1, 3, 4, and 6 is equal to a , while the length of sides 2 and 5 is equal to b . The thickness of all plates is considered to be the same and equal to t . Cartesian X and Y axes are located along the plane of the vectors \vec{r}_2 , whereas \vec{r}_0 and the Z axis are perpendicular to the X and Y axes, respectively.

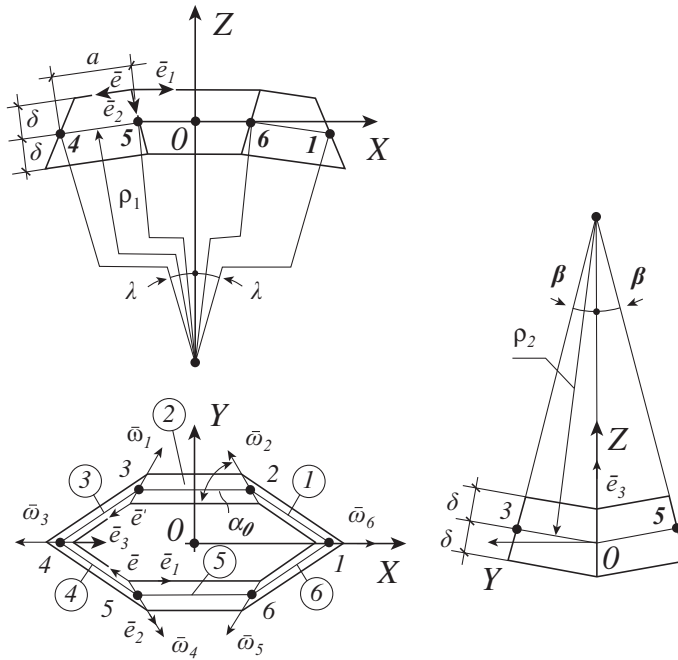


Figure 4. Sizes of the six-link loop cell.

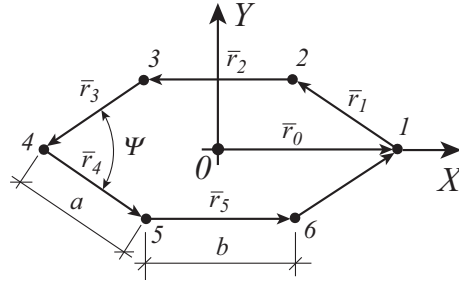


Figure 5. Middle lines of the trapezoid within the cell.

It should be noted that if the sides of the six-link loop are absolutely rigid plates connected with linear cylindrical hinges, the structure is not actually a mechanism. In fact, the number of degrees of freedom in the six-link loop is equal to

$$F = 6 \times 6 - 6 \times 5 = 6$$

because each rigid plate has six degrees of freedom, and the linear hinge subtracts five degrees of freedom. Thus, the arbitrarily scaled six-link loop can move through space only as an absolute solid. For additional degrees of freedom to appear, the mechanism should be specially designed. The symmetrical six-link loop needs at least one degree of freedom, which could be angle Ψ (Figure 4).

Limitations are set on the six angular velocities $\vec{\omega}_i$ [Lurye 1961] in this study. The closure of the polyhedron and the theorem of composition of angular velocities give

$$\sum_{i=1}^{i=6} \vec{\omega}_i = 0. \quad (1)$$

The three equations (1) are supplemented with another triple representing the fact that the velocity of the point located at the intersection of the sides is identical regardless of the side upon which it is calculated:

$$\begin{aligned} \vec{\omega}_1 \times \vec{r}_1 + (\vec{\omega}_1 + \vec{\omega}_2) \times \vec{r}_2 + (\vec{\omega}_1 + \vec{\omega}_2 + \vec{\omega}_3) \times \vec{r}_3 + (\vec{\omega}_1 + \vec{\omega}_2 + \vec{\omega}_3 + \vec{\omega}_4) \times \vec{r}_4 \\ + (\vec{\omega}_1 + \vec{\omega}_2 + \vec{\omega}_3 + \vec{\omega}_4 + \vec{\omega}_5) \times \vec{r}_5 + (\vec{\omega}_1 + \vec{\omega}_2 + \vec{\omega}_3 + \vec{\omega}_4 + \vec{\omega}_5 + \vec{\omega}_6) \times \vec{r}_6 = 0. \end{aligned}$$

The last equality with

$$\sum_{i=1}^{i=6} \vec{r}_i = 0, \quad (2)$$

implies that the sum of $\vec{\omega}_i$ vector moments with respect to point O is equal to zero. When \vec{r}_i is constant, (1) and (2) prove that there is always a trivial solution

$$\vec{\omega}_i = 0$$

when the six-link loop remains geometrically unchanged. However, nontrivial solutions exist with additional limitations. It will be demonstrated that (1) and (2) allow for a nontrivial solution for a cell that is symmetrical with respect to the X axis.

Assuming $\vec{\omega}_1, \vec{\omega}_2, \vec{\omega}_3,$ and $\vec{\omega}_6$ are unknown, the Y -axis projection equation and two moment equations with respect to the X and Y axes can be identically satisfied by symmetry of vectors. Thus, only three independent equations exist for four unknown vectors. Therefore, a symmetrical cell is a mechanism with one degree of freedom, due to

$$\frac{d\vec{\Psi}_i}{dt} = \vec{\omega}_i \quad (3)$$

and the symmetrical configuration at the initial instant.

This conclusion can be reached if a three-link loop consisting of plates 1, 2, and 3 is considered (the plates generally have arbitrary sizes), and the initial position on the XOZ axis (Figure 4) is located on the fixed axis 1. The position of axis 4 is a function of the three dihedral angles $\vec{\Psi}_1/2, \vec{\Psi}_2,$ and $\vec{\Psi}_3$.

If the angle $\vec{\Psi}_1$ is determined arbitrarily, the other two can be determined such that axis 4 is on the XOZ plane. Flipping the three-link loop against this plane proves that the six-link loop is a system with one degree of freedom.

The same result can be obtained if a cell has two axes of symmetry. In this case, $|\vec{\omega}_3| = |\vec{\omega}_6|,$ and $|\vec{\omega}_1| = |\vec{\omega}_2|.$ Only one equation (the equation for the angular velocity of the Z -axis projection) out of six for two unknown vectors is not identically satisfied. The angle Ψ is chosen as the only generalized coordinate of the cell's symmetrical deformation (Figure 4). With this angle, all angles of the cell can be calculated. The calculated cells will be designated by $\Psi_i, i = 1, 2, \dots, 6,$ for $\Psi_4 = \Psi.$ The dihedral angle between plates 3 and 4 $|\vec{\Psi}_1| = \Psi$ (Figure 4) is considered the only generalized coordinate of the cell with symmetrical distortion. Knowing this angle, all of the other dihedral angles of the cell can be calculated.

The set of cells can be connected according to Figure 1, Sketch 2, by gluing trapezoids of the same size. This operation is feasible when $\Psi = 0.$ If the plates are thin, and the sizes of the six-link loops are small compared to the shell dimensions (the net contains a large number of mirror-symmetrical cells), then the strip package can be unwrapped into a two-dimensional surface almost without applying any external forces.

Because the plates comprising the net are thin (the t/δ ratio is small), only a small amount of force is required to twist and bend them. Thus, the twist angles of the plates to a first approximation can be considered to be additional degrees of freedom of the lattice system.

The size of the honeycombs is assumed to be small. This assumption is equivalent to the distances between close points regarded as differentials of the relevant functions. Therefore, it is possible to parameterize and homogenize a system that contains a large number of honeycombs.

Let us connect $2n$ strips from the trapezoids (the strips are numbered with Arabic numerals) at the initial instant shown in Figure 1, Sketch 1 (gluing even and odd strips), and unwrap the package (refer to Figure 6).

Broken lines connecting the middle lines of the odd strips (shown with a dotted line) are termed coordinate lines $\alpha_1.$ Similarly, the lines α_2 are drawn through the centers of the glued trapezoids. The Lagrangian coordinate lines α_1 are considered equal to the actual length along the middle lines of the trapezoids measured from the fixed point $B.$ When moving to the neighboring cell, the change in the coordinate α_2 is equal to $2b.$ The discrete coordinate net formed in this manner is supplemented with continuous points of two-dimensional manifolds.

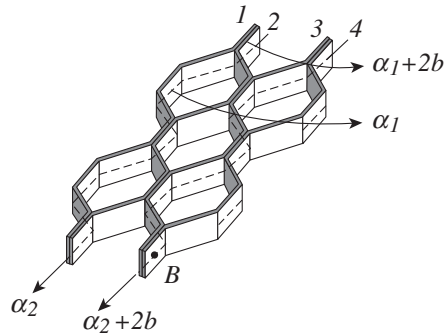


Figure 6. Lagrangian coordinates of the shell.

If the coordinate lines are closely spaced, it is possible to linearly approximate the joint coordinates of the net that are located on the middle lines of the trapezoids across the entire two-dimensional manifold; the first and second quadratic forms of the built continuum surface can also be calculated. The approximation results in a surface, a small section of which is shown in Figure 7. The lines of the main curvature are designated by β_1 and β_2 . The tangent plane passing through the center of gravity of the middle cell O is designated Π .

The map consisting of projections of the middle lines of the five cells on plane Π (Figure 7) has $3 \times (8 - 6) = 6$ degrees of freedom in space (assuming that it is possible to rotate the osculating trapezoids against the middle lines). Because all cells are mirror-symmetrical, the map (Figure 7) can be supplemented with two more cells (marked as 6 and 7 in circles in Figure 8) such that the seven cell units have six degrees of freedom in space.

The middle line between points 2 and 3 of cell 6 coincides with the relevant line of the middle cell and ensures two degrees of freedom in the entire system. This number is sufficient to combine the line between points 3 and 4 of cell 6 with the system assembled earlier in Figure 7 without applying extra forces. The other lines are matched automatically, due to the symmetry of the map along the X and Y

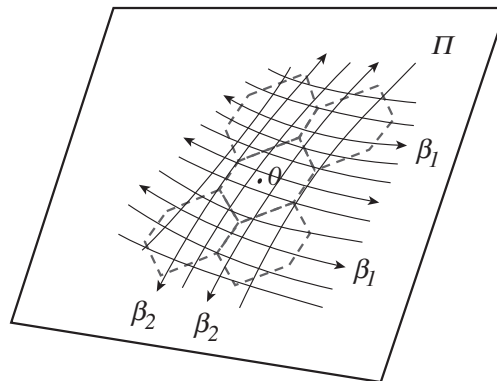


Figure 7. Section of the continuum shell.

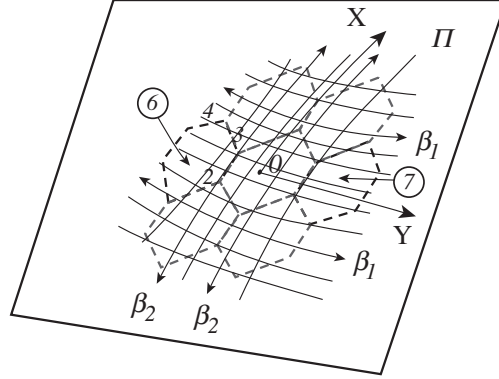


Figure 8. Local map of the shell.

axes. In other words, the distance between points A and B (with coordinates $(\alpha_{1A}, \alpha_{2A})$ and $(\alpha_{1B}, \alpha_{2B})$, respectively) within the small map Π (Figure 8) is defined by the opening of only one angle Ψ .

Homogenization of the discrete system is performed in two steps. First, the free deformation of one cell and the small map Π (that is, the deformation that does not have any external limitations) are considered. Second, the cells are joined into the continuum net using a specific rule.

For the first step, we consider that the sharp angle α_0 is close to a straight angle. The assumption is that angle $\alpha_0 \neq \pi/2$, and the square of the cosine of this angle, $\alpha = \cos \alpha_0$, can be neglected in the calculations below.

Let us identify the projections of the unit length vectors:

$$\begin{aligned} \vec{e}_4 = \{0, 0, 1\}, \quad \vec{e}_1 = \{1, 0, 0\}, \quad \vec{e}_2 = \{-a_1\alpha, a_2\alpha, a_3\}, \quad \vec{e} = \{-\psi_1, \psi_2, -\alpha\psi_3\}, \\ \vec{e}' = \{-\psi_1, -\psi_2, -\alpha\psi_3\}, \quad \text{and} \quad \vec{e}_3 = \{-\alpha a'_1, 0, a'_3\}. \end{aligned}$$

Considering the relations

$$\vec{e}_2 \cdot \vec{e} = -\alpha, \quad \vec{e}_1 \cdot \vec{e}_2 = -\alpha, \quad \vec{e}_3 \cdot \vec{e} = \alpha, \quad \vec{e}_1^2 = \vec{e}^2 = \vec{e}_2^2 = \vec{e}_3^2 = 1,$$

and the fact that vectors \vec{e} , \vec{e}_2 , and \vec{e}_3 are located on the same plane, or

$$(\vec{e}_2 \times \vec{e}) \cdot \vec{e}_3 = 0,$$

we have

$$\begin{aligned} a_1 = 1, \quad -a_1\psi_1 + a_2\psi_2 - a_3\psi_3 = 1, \quad \psi_1 a'_1 - \psi_3 a'_3 = 1, \\ \underline{\alpha^2 \psi_3^2} + \psi_1^2 + \psi_2^2 = 1, \quad \underline{a_1^2 \alpha^2} + \underline{a_2^2 \alpha^2} + a_3^2 = 1, \quad \underline{\alpha^2 a_1'^2} + a_3'^2 = 1, \quad (4) \\ \underline{a_2 \psi_3 \alpha^2} + a_3 a'_1 \psi_2 + a'_3 a_1 \psi_2 + a'_3 a_2 \psi_1 = 0. \end{aligned}$$

There are eight unknowns in the seven equations. If all the unknowns are expressed through one parameter ψ_1 , and α is a small number that allows the underlined elements in (4) to be omitted, the

result is

$$a_1 = 1, \quad a_3^2 = a_3'^2 = 1, \quad \psi_1^2 + \psi_2^2 = 1,$$

$$\psi_3 = -\psi_1^3 + \psi_1^2 - \psi_2^2\psi_1 + \psi_2^2, \quad a_1' = \frac{1 - \psi_3}{\psi_1}, \quad a_2 = \frac{1 - \psi_3 - \psi_1}{\psi_2}.$$

The angle between the Z axis and vector $(\vec{e} + \vec{e}')$ is designated by λ , while the angle between surfaces 2 and 5 is expressed as 2β (Figure 4). According to the designations introduced earlier, we obtain

$$\lambda = \alpha\psi_3 \quad \text{and} \quad \beta = \alpha a_2.$$

The length of the line between the centers of sides 2 and 5 equals $2b\psi_2$, while the length between points 1 and 4 (measured along the middle line of the trapezoid) equals $b(1 + 2\psi_1)$. Therefore, the principal curvature radii can be grouped with the symmetrical free cell (and with the small map Π) by

$$\rho_1 = \frac{b(1 + 2\psi_1)}{2\alpha\psi_3} \quad \text{and} \quad \rho_2 = \frac{b\psi_2}{\alpha a_2}. \quad (5)$$

When $\psi_1 \rightarrow 1$, the values of a_2 and ψ_3 approach zero; furthermore, the curvature radii at the location where the “folded” shape of the cell meets are equal to infinity.

When the coordinate α_1 is changed by b within the small map Π (Figure 8) without connecting the incorporated cells, the distance along the line β_1 on the tangent plane Π is equal to $b(1 + \psi_1)/2$; when the coordinate α_2 is changed by b , the segment is equal to $b\psi_2$.

Therefore, when the cells are only in contact along the middles lines of the osculating trapezoids close to point O (including the small number of free cells that are inside map Π), the first and the second quadratic forms of the surface can be calculated using

$$ds^2 = A_1^2 d\alpha_1^2 + A_2^2 d\alpha_2^2, \quad (6)$$

$$A_1 = (1 + \psi_1)/2, \quad A_2 = \psi_2, \quad (7)$$

$$B(d\alpha_1, d\alpha_2) = \frac{A_1^2 d\alpha_1^2}{\rho_1} + \frac{A_2^2 d\alpha_2^2}{\rho_2}. \quad (8)$$

The written correlations define the connectivity described with the quadratic forms ω^i and ω_i^j [Cartan 1945] that are linear against the differentials $d\vec{\beta}_1$ and $d\vec{\beta}_2$. In addition,

$$d\vec{r} = \omega^i \vec{\beta}_i \quad \text{and} \quad d\vec{\beta}_i = \omega_i^j \vec{\beta}_j. \quad (9)$$

Equation (9) and the subsequent formulas use a tensor notation and contracted repetitive indices, where $d\vec{r}$ means a vector of destination between the points on surface Π that differ by the Lagrangian coordinates of $(d\alpha_1, d\alpha_2)$.

In the second step of homogenization, the basic assumption describing the global transformation of the net containing mirror-symmetrical six-link loops is made. The cells connected according to the sketch in Figure 2 deploy into a shell in such a way that the connectivity (expressed by (9)) is locally converted, with both surfaces Π and Π_1 being smooth manifolds. This is performed by rigidly displacing the small free segment of the tangent plane from initial position Π (the fragment of which is shown in Figure 9) to position Π_1 , which is shown on the left side of the same picture. This requirement ensures

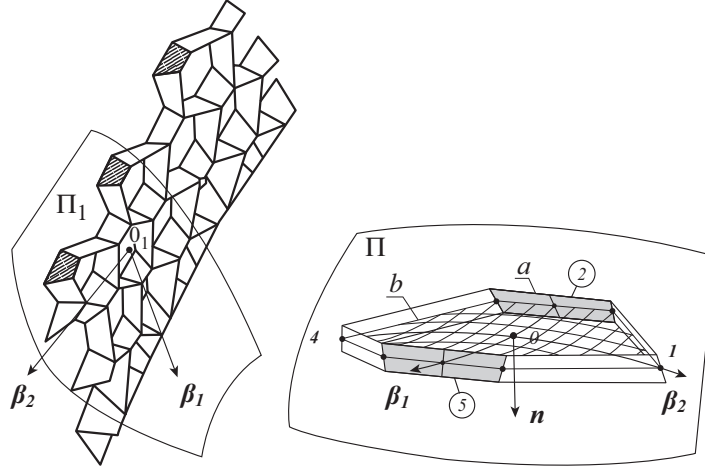


Figure 9. Movement of the local map in space.

the deformation of the shell without stretching the middle surface. Only those plates that connect the strips can be twisted.

Because the thickness of any plate is insignificant compared to its length and width, the potential energy of the elastic deformation of the shell is minimal; the deployment method described above would therefore require less extra energy than any other deployment technique.

To specify the forms of ω^i and ω_i^j relative to surface Π_1 , it is sufficient to convert vectors $d\vec{\alpha}_i$, $\vec{\alpha}_i$, and $d\vec{r}$ by making them consistent with the Euler angles that appear after aligning points O and O_1 . The converted forms of ω^i and ω_i^j should satisfy the three Gauss–Codazzi relations, which are equations ensuring the system integrability condition (9) [Novozhilov 1962].

Due to the linearity of the forms (9) against $d\vec{\beta}_1$, $d\vec{\beta}_2$, $\vec{\beta}_1$, and $\vec{\beta}_2$ and the basic assumption on deformation of the net described above, the Euler angles would not be a part of the Gauss–Codazzi equations. Therefore, the resolved system of three equations would only have one variable function Ψ and would become overdetermined. To ensure the integrability of the Gauss–Codazzi equations without changing the symmetry of the cells and the metrics of the shell, plate-twisting should be considered.

Equations (5) and (8) can be expressed in terms of plate-twisting as

$$b_{11} = \frac{A_1^2(2a\psi_3 - \phi_{11})}{b(1 + 2\psi_1)}, \quad b_{12} = 0, \quad \text{and} \quad b_{22} = \frac{A_2^2(\alpha a_2 - \phi_{22})}{b\psi_2}, \quad (10)$$

where b_{11} , b_{12} , and b_{22} are coefficients of the second quadratic form of surface $B(d\alpha_1, d\alpha_2) = b_{ij} d\alpha_i d\alpha_j$ (indices i and j are 1 and 2, respectively); the functions ϕ_{11} and ϕ_{22} will be defined. The coefficient b_{12} is considered equal to zero because the curvature lines in symmetrical cells are always orthogonal.

The coefficients of the first and second quadratic forms from (6) and (10) depend on three functions (ϕ_{11} , ϕ_{22} , and Ψ), and they need to meet the criteria of the three Gauss–Codazzi compatibility equations

$$\frac{\partial}{\partial \alpha_2} \left(\frac{\partial A_1}{A_2 \partial \alpha_2} \right) + \frac{\partial}{\partial \alpha_1} \left(\frac{\partial A_2}{A_1 \partial \alpha_1} \right) = -\frac{A_1 A_2}{\rho_1 \rho_2}, \quad \frac{\partial}{\partial \alpha_2} \left(\frac{\partial A_1}{\rho_1} \right) = \frac{\partial A_1}{\rho_2 \partial \alpha_2}, \quad \frac{\partial}{\partial \alpha_1} \left(\frac{A_2}{\rho_2} \right) = \frac{\partial A_2}{\rho_1 \partial \alpha_1}. \quad (11)$$

Therefore, (5)–(8), (10), and (11) enable the shape of the surface to be uniquely defined (continuously approximating the location of the trapezoid middle line in space) when the coordinates of the shell reference contour are known. Basically, three differential equations (11) for the three functions ψ_1 , ϕ_{11} , and ϕ_{22} define the field (smooth manifold) in the coordinates α_1 and α_2 , spread in three-dimensional space. The solution to (11) makes it possible to study the kinematics of the lattice shells without prior stress analysis of small plates.

3. Application to specific problems

Let us apply general correlations to the rotational shells. Equation (11) is simplified, and the derivatives with respect to argument α_2 disappear; nevertheless, $\phi_{11} = 0$. Therefore, two equations remain, and ρ_2 can be determined from the first equation:

$$\frac{1}{\rho_2} = -\frac{\rho_1}{A_1 A_2} \frac{\partial}{\partial \alpha_1} \left(\frac{\partial A_2}{A_1 \partial \alpha_1} \right). \quad (12)$$

If this expression is substituted into the second equation in (11), we have an ordinary differential equation of the second order for the function $\psi_0 = \partial \psi_2 / \partial \alpha_1$:

$$\frac{\partial}{\partial \alpha_1} \left(\frac{\rho_1 \partial}{A_1 \partial \alpha_1} \left(\frac{\psi_0}{A_1} \right) \right) = -\frac{\psi_0}{\rho_1}. \quad (13)$$

Once ψ_2 is determined from this equation (up to two constants), the twisting parameter for the plate ϕ_{22} can be calculated only based on (11) and (12).

Knowing the function $\psi_2(\alpha_1)$, we can find the coordinates of the shell surface. In this equation, the closed shell is a finite-dimensional mechanism with the geometry dependent on the opening of only two cells located on the curvatures of D_1 and D_2 (Figure 10). It is also important to address the structure (13), which is close to the differential equation of second order with a large coefficient on the top derivative, and a rotational curvature that is close to the chain line approximating a straight line when the α angle is small.

The maximum opening of the cell is limited, and the closed rotational shell has the following interesting feature (Figure 10). If the shell is turned over with its cells open to the limit on the bottom, and the “bases” D_1 and D_2 are switched, the shell has to take the original shape because of its gravity and the lack of friction on base D_2 .

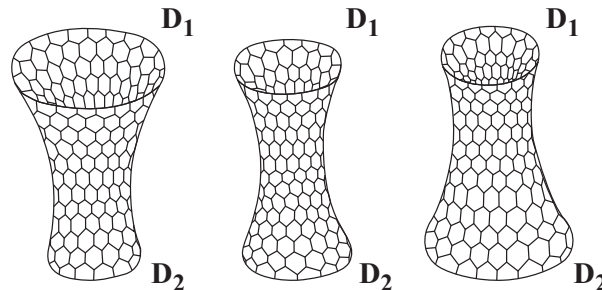


Figure 10. Change in shape of the hyperbolic shell under gravitation.

As (5) shows, the honeycomb shells could increase the curvature during the deployment of simply connected packages in Figure 2, much like a crayfish squeezing a victim with its claw within the volume V (Figure 11).

The simply connected honeycomb shell can occupy an extremely small volume. If $\psi_2 = 0$, then $A_2 = 0$, and the area of the shell is zero. This situation is possible in two cases: when $\Psi = 0$ or when $\Psi = 2\pi$. The first option corresponds to the initial position of the package in Figure 1, while the second option corresponds to a wrapped “crib sheet” (or “cheat sheet”). The process of the shell “collapsing” into a point is shown in Figure 12 for one strip. The picture would not change if one strip was replaced with the simply connected lattice shell.

The stated features can serve as the basis for an advanced transportation technology of lattice systems: the wrapped strips are packed into a small box with dimensions similar to $(a + b)$ and transported at a long distance; the strips can subsequently be connected according to Figure 1 and unwrapped into the designed position.

The model shown in Figures 13–15 demonstrates the abovementioned features.

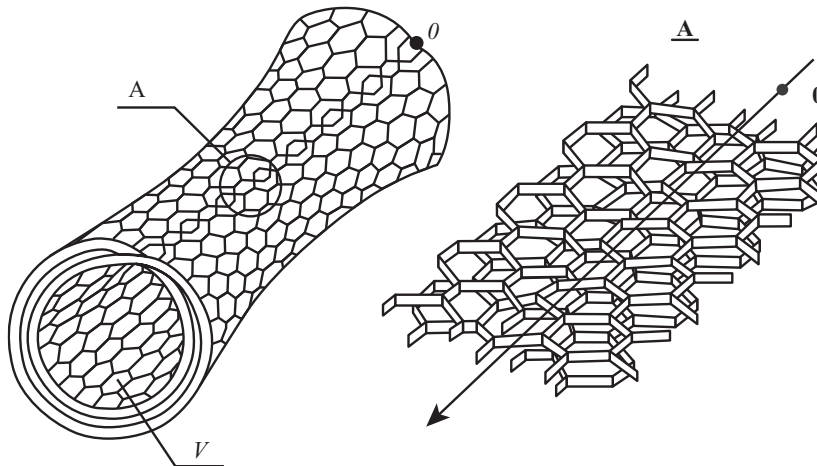


Figure 11. Reduction in internal volume when the shell is deployed. On the right, the arrow indicates the intersection line arising at deployment. The volume V within the surface reduces when the shell deploys.

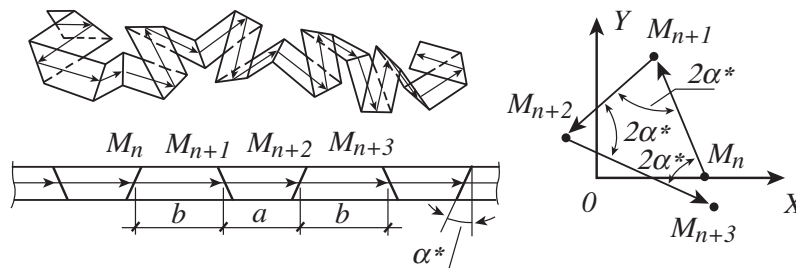


Figure 12. Strip packaged as a “crib sheet”.

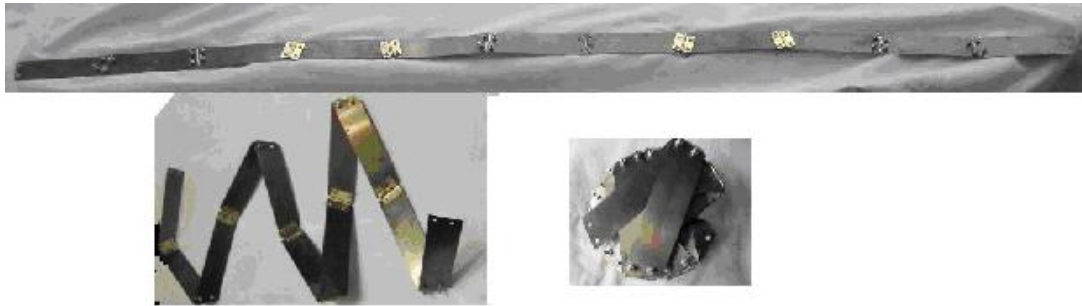


Figure 13. Strip in initial, intermediate, and packed states.



Figure 14. Cell at different Ψ angles.

Figures 13 and 14 show a strip and a cell at the stage of preliminary assembly. The strips are put together from 0.2 mm-thick plates (the trapezoid middle line is 115 mm long and 30 mm high, the sharp angle at the base is 75°) that are made of high-carbon steel with a yield strength of 1000 MPa. The hinged loops, which are 0.8 mm thick, are made of mild steel.

The loops and the plates are glued at 170°C with a special film adhesive after preliminary assembly in the casing ensuring 0.1 mm accuracy of linear dimensions.

Figure 13 shows the consistent process of packing the strip into a coil-globule that looks like a school crib.

Figure 14 demonstrates the deformation of the mirror-symmetric six-link loop when the dihedral angle Ψ is changed. When $\Psi = 2\pi$, the cell's area is maximal. Further increase in this angle results in collapse of the cell (and the entire shell) because the area of any simply connected section of the lattice surface becomes negligibly small.

Figure 15, left, shows a model of the lattice shell comprising twenty strips joined into a single system with diameter 3 mm nylon thermoplastic rivets. The contacting surfaces are put together with six rivets: by two via hinged loops and by two along the middle line. The boundary conditions on the contours of the rotational shells are met by rigid rings where the hinged loops are attached.

If there were quite a few strips, then the arbitrarily set boundary conditions (diameters of the top and bottom rings) could change over a wide range and the lattice shell could simulate the situation represented

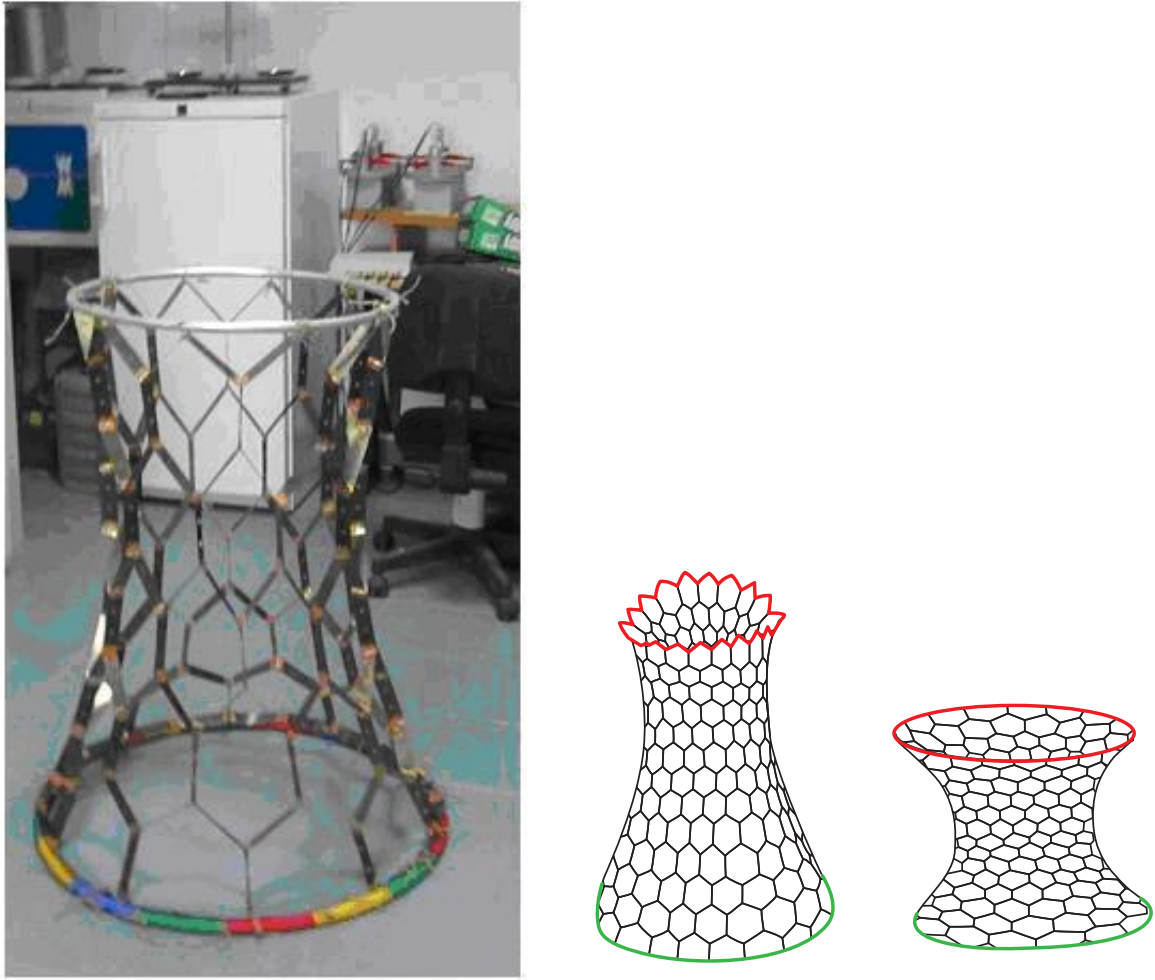


Figure 15. Left: model of the lattice shell. Right: Shell with a variable surface.

in Figure 10. If the cylinder was cut along the generating line, the crayfish behavior shown in Figure 11 would be reproduced.

If the rigid top ring was replaced with a flexible hose, as shown in red in Figure 15, right, then by injecting air inside this chamber, we would create a surface of variable area simulating a piston-free press or a pump. Obviously, such a surface can be used as a kagome structure upside down (a basketball hoop) with very few degrees of freedom. It would be much more difficult for players to shoot a ball through this basket than in a normal basketball game.

Figures 10–15 do not encompass all of the possible thin wall six-link loop structures [Hutchinson et al. 2003; Grachev and Neustadt 2008; 2009].

It should be emphasized once again that the deployable systems described above are not classic mechanisms with absolute rigid links. Their deployment is possible only if the plates are thin and durable, which explains why the proposed mechanisms based on the principles of mobility of the Bricard and

Schatz six-link loops [Bricard 1927; Schatz 1975; Phillips 1984] have not been widely applied. Materials developed in recent decades, including shape memory alloys, encourage the development of new mechanisms of deployable systems and new applications in such fields as traditional engineering, medicine, and biotechnology.

Acknowledgements

The authors express their cordial thanks to the staff members of Samara Aerospace University, V. A. Koshelev and V. D. Falkin, and representatives of the Laktest laboratory, G. I. Weingarten and G. A. Makarov, for their tremendous support in the manufacturing of the lattice shells.

References

- [Bricard 1927] R. Bricard, *Leçons de cinématique, 2: Cinématique appliquée*, Gauthier-Villars, Paris, 1927.
- [Cartan 1945] É. Cartan, *Les systèmes différentiels extérieurs et leurs applications géométriques*, Actualités Sci. Ind. **994**, Hermann, Paris, 1945.
- [Chen and You 2008a] Y. Chen and Z. You, “An extended Myard linkage and its derived 6R linkage”, *J. Mech. Des. (ASME)* **130**:5 (2008), Article ID #052301.
- [Chen and You 2008b] Y. Chen and Z. You, “On mobile assemblies of Bennett linkages”, *Proc. R. Soc. Lond. A* **464**:2093 (2008), 1275–1283.
- [Gan and Pellegrino 2006] W. Gan and S. Pellegrino, “Numerical approach to the kinematic analysis of deployable structures forming a closed loop”, *Proc. Inst. Mech. Eng. C, J. Mech. Eng. Sci.* **220**:7 (2006), 1045–1056.
- [Gantes 2001] C. J. Gantes, *Deployable structures: analysis and design*, WIT Press, Boston, 2001.
- [Grachev and Neustadt 1995] V. A. Grachev and Y. S. Neustadt, *Континуальные трансформирующиеся оболочки из прямолинейных полос (Continuum deployable shells made of rectilinear strips)*, Tertsia, St. Petersburg, 1995.
- [Grachev and Neustadt 1996] V. A. Grachev and Y. S. Neustadt, *Управляемые трансформирующиеся оболочки (Controlled deployable shells)*, St. Petersburg University Press, St. Petersburg, 1996.
- [Grachev and Neustadt 1999a] V. A. Grachev and Y. S. Neustadt, “Способ изготовления плоских и пространственных сотовых структур и конструкций на их основе (Manufacturing process for plain and spatial honeycomb structures and constructions based on them)”, 1999, <http://ru-patent.info/21/25-29/2126875.html>. Russian patent 2126875, filed 15 June 1992.
- [Grachev and Neustadt 1999b] V. A. Grachev and Y. S. Neustadt, *Трансформирующиеся среды из прямолинейных полос (Deployable media made of rectilinear strips)*, St. Petersburg University Press, St. Petersburg, 1999.
- [Grachev and Neustadt 2008] V. A. Grachev and Y. S. Neustadt, “Трансформирующиеся системы на основе правильных шестизвенников (*Deployable systems based on regular six link loops*)”, pp. 131–139 in *Математика, компьютер, образование, 2.5: Вычислительные методы и математическое моделирование (Mathematics, computer, education, 2.5: Calculation methods and mathematical modeling)* (Dubna, 2008), edited by G. Y. Riznichenko, Scientific Publishing Center “Regular and Chaotic Dynamics”, Izhevsk, 2008.
- [Hutchinson et al. 2003] R. G. Hutchinson, N. Wicks, A. G. Evans, N. A. Fleck, and J. W. Hutchinson, “Kagome plate structures for actuation”, *Int. J. Solids Struct.* **40**:25 (2003), 6969–6980.
- [Jensen and Pellegrino 2002] F. Jensen and S. Pellegrino, “Expandable structures formed by hinged plates”, pp. 263–272 in *Space structures 5* (Surrey, 2002), vol. 1, edited by G. A. R. Parke and P. Disney, Thomas Telford, London, 2002.
- [Leung and Guest 2007] A. C. H. Leung and S. D. Guest, “Single member actuation of kagome lattice structures”, *J. Mech. Mater. Struct.* **2**:2 (2007), 303–317.
- [Luchsinger et al. 2004] R. H. Luchsinger, M. Pedretti, and A. Reinhard, “Pressure induced stability: from pneumatic structures to Tensairity®”, *J. Bionic Eng.* **1**:3 (2004), 141–148.
- [Lurye 1961] A. I. Lurye, *Аналитическая механика (Analytical mechanics)*, GIFML, Moscow, 1961.

- [Novozhilov 1962] V. V. Novozhilov, Теория тонких оболочек (*The theory of thin shells*), Sudpromgiz, Leningrad, 1962. Reprinted by St. Petersburg University Press, St. Petersburg, 2010.
- [Otto and Rasch 1995] F. Otto and B. Rasch, *Finding form: towards an architecture of the minimal*, Axel Menges, Stuttgart, 1995.
- [Phillips 1984] J. Phillips, *Freedom in machinery, 2: Screw theory exemplified*, Cambridge University Press, Cambridge, 1984.
- [Schatz 1975] P. Schatz, *Rhythmusforschung und Technik*, Freiesleben, Stuttgart, 1975.
- [Sclater and Chironis 2011] N. Sclater and N. P. Chironis, *Mechanisms and mechanical devices sourcebook*, 5th ed., McGraw Hill, New York, 2011.
- [Swank 1991] M. W. Swank, "Non-planar expandable honeycomb structure", 1991, <http://www.google.com/patents/US4981744>. USA patent 4981744, filed 24 April 1990.
- [Vepa 2010] R. Vepa, *Dynamics of smart structures*, Wiley, Hoboken, NJ, 2010.

Received 4 Sep 2012. Revised 7 Nov 2012. Accepted 18 Nov 2012.

VLADIMIR A. GRACHEV: grach_va@rambler.ru

Samara State Architectural and Building University, 194 Molodogvardeyskaya Str., Samara, 443001, Russia

YURIY S. NEUSTADT: neustadt99@mail.ru

Samara State Architectural and Building University, 194 Molodogvardeyskaya Str., Samara, 443001, Russia

SELF-FOLDING OF A SLENDER MICROBEAM AND THIN FILM: AN ELASTICA MODEL

JIANLIN LIU AND JUNG HOON LEE

Thin wires or films can be spontaneously folded into different shapes, and such phenomena hold promising applications in engineering, especially at micro and nanoscales. Based upon the established potential energy functional, we derived the governing equation and adhesive boundary condition for a self-folding system. Considering the inextensible condition of the structure, a closed-form solution for the deflection of a racket-like structure was obtained in terms of elliptical integrals, which applies for both macro and nanodimensions. We then determined the critical adhesive length under specified geometric and energetic constraints. The results show that self-folding is energetically favorable and thermodynamically stable with the cohesive work being strong enough and the structure being sufficiently flexible. As soon as the self-folding configuration is formed, the slender structure must possess an initial adhesive length. These conclusions are beneficial for the design of nanostructures, and the enhancement of their mechanical, chemical, optical, and electronic properties.

1. Introduction

Self-folding phenomena of thin films and wires, spanning the micro, macro, and nanoscales, are widely observable in nature and daily life. For example, when a piece of paper is coiled up in a tube, it does not make complete contact near its ends but makes a certain angle with the inner tube wall [Romero et al. 2008]. In addition, a flexible thin sheet can be self-folded or wrapped by capillary forces; Py et al. [2007; 2009] and Pineirua et al. [2010] carried out a series of experimental studies on such processes. They found that the surface tension of a droplet or a liquid film can cause the thin sheet to fold, origami-like, into different geometric shapes. They also provided numerical solutions to calculate the adhered configuration, which are consistent with their experimental results.

Nature often miraculously creates similar phenomena at different length scales; likewise, self-folding exists widely in the nanoworld. On the one hand, the creation of self-folded structures is technologically important in such practical applications as the self-assembly of nanostructures. A typical example is that silicon–germanium nanotubes can be formed by the self-folding of a thin film through an inexpensive label method [Schmidt and Eberl 2001]. During this process, the freed thin film is rolled up, with one of the film edges being brought into contact with the film itself and finally stuck by van der Waals forces [Glassmaker and Hui 2004]. Moreover, folding a two-dimensional graphene will significantly alter its properties, because the deformed morphology modifies the electronic band structure of the graphene and creates localized electronic states in the folded regions [Kim et al. 2011]. Using the folding method, one can control the shape of a graphene sheet, and then tailor its mechanical, chemical, optical, and electronic properties. On the other hand, self-folding or cross-section collapse can induce undesirable

Keywords: self-folding, elastica, adhesive boundary condition, energetic constraint, deflection.

deformation or even failure of micro/nanosized devices and systems. For example, the circular cross section of a carbon nanotube (CNT) with a large diameter may collapse into a ribbon or dumbbell shape under van der Waals forces [Pantano et al. 2004]. Through molecular dynamic (MD) simulations, Gao et al. [1998] discovered that there are two possible configurations for a CNT in equilibrium state, one circular and one collapsed, corresponding to two determinate radius ranges, respectively. Recently, Tang et al. [2005] and Tang and Glassmaker [2010] studied the energetics of self-collapse of a single CNT by using the continuum mechanics method, and also calculated the critical radius for collapse.

The self-folding of thin films or microbeams may lead to different shapes, especially at micro and nanoscales [Cohen and Mahadevan 2003]. Like a microtubule inside a vesicle buckling into a racket-like shape [Fygenson et al. 1997], CNTs with a similar shape were also observed in a sample of high-pressure carbon monoxide single-walled nanotubes after 30 minutes of sonication in dichloroethane [Cohen and Mahadevan 2003]. The occurrence of self-folding in such small scaled materials as nanowires, microtubules, nanotubes, and thin films is mainly attributed to their high aspect ratios. More precisely, the maximal size (for example, the length of nanowire or the length/width of a thin film) is much larger than the persistence length [Zheng et al. 2004; Lee et al. 2007]. Due to carbon-carbon covalent bonding and seamless hexagonal network architecture, a CNT can be easily bent into an arc shape with significant curvature [Buehler et al. 2004]. This special racket-like configuration is actually an energetically favorable state, with the interplay of elastic deformation and van der Waals attraction between different parts of the CNTs.

Much effort has been directed toward understanding the physical mechanisms of self-folding processes. The first atomistic simulation of single-wall CNTs with very large aspect ratios subject to compressive loading was carried out in Buehler et al. [2004]. They investigated the shell-rod-wire transition of the mechanical behavior of CNTs with increasing aspect ratios. Following this work, Buehler et al. [2006] utilized atomistic simulation to study the deformation of a highly flexible nanotube forming a thermodynamically stable self-folded structure, and presented the critical length and critical temperature for folding or unfolding. Zhou et al. [2007] obtained the critical length for the self-folding of CNTs by MD simulations and infinitesimal deformation analysis. Mikata [2010] then derived an approximate solution for the self-folding of CNTs on the assumption that the curvature at the adhesion point is zero. Glassmaker and Hui [2004] modeled the CNT as an elastica, presented the close-formed differential equation set, and gave the numerical results. Similar to CNT folding, Cranford et al. [2009] studied the self-folding of mono and multilayer graphene sheets, utilizing a coarse-grained hierarchical multiscale model derived directly from atomistic simulation. Although the aforementioned studies have been devoted to self-folding problems, to date there is still a lack of systematic theoretical analysis on the underlying physical mechanisms, which involve very large deformation and strong geometric nonlinearity. In this paper, we present an elastica model to quantitatively study the mechanism of self-folding. Our motivation is to provide the explicit solution of the considered problem, then develop a new method to analyze the racket-like shape of self-folded structures via the classical elastica solution. This landmark theory, which can be traced back to the historic contribution of Euler [Love 1906], has been successfully used to solve some finite deformation problems of slender structures [Bisshopp and Drucker 1945; Liu and Feng 2007; Majidi 2007; Neukirch et al. 2012].

This article is organized as follows. In Section 2, we present a mechanics model to analyze the self-folding of structures in terms of energy, and derive the nonlinear governing equation and the adhesive

boundary condition. In Section 3, we discuss the critical adhesive length under specified geometric and energetic constraints. Finally, we present the explicit solution for the deflection of a flexible structure.

2. Elastica model

2.1. Model formulation. First, we analyze the physical mechanisms of self-folding of a flexible structure, such as a filament or a thin film, by means of scaling laws. If the typical length of a planar structure is denoted as L_c , then the interfacial or surface energy $U_S \propto L_c$, the elastic strain energy $U_E \propto L_c^2$, and the potential energy due to gravity $U_G \propto L_c^3$ [Roman and Bico 2010]. As the dimension of a macroscopic fiber or film shrinks to nanometers, the effect of surface energy becomes significant and should be taken into account. Therefore, it can naturally be assumed that the effect of gravity is negligible. Given a sufficiently large flexibility or aspect ratio, the structure can reach an energetically stable self-folding shape like a tennis racket. For instance, a CNT can experience a shell-rod-wire transition as its aspect ratio increases [Buehler et al. 2004]. If a straight and slender CNT is subject to two compressive loads with magnitude of P exerted at its two ends, it will buckle when the load is bigger than a critical value:

$$P_{\text{cr}} = \left(\frac{\pi}{L}\right)^2 EI, \quad (1)$$

where L is the total length of the CNT, EI the bending stiffness of the CNT, E the Young's modulus of the material, and I the moment of inertia of the cross section of the beam. After it buckles, the CNT may become a ring-shaped structure [Bigoni 2012, 52–69] with radius R , and it can continue to be self-folded if the van der Waals force q exceeds a critical value:

$$q_{\text{cr}} = \frac{3EI}{R^3}. \quad (2)$$

In this situation, the van der Waals force between the upper and lower portions of the CNT will attract each other, and the interfacial energy actually plays the role of a transmural pressure. In the present study, we only concentrate on the folded morphology of the glued CNT.

In what follows, we consider a slender filament or a sheet stuck by the adhesion force of the solid contact surface or a trapped liquid film, as shown in Figure 1a. Due to the symmetry and smoothness of this configuration, the upper half portion of the structure can be modeled as a beam with two clamped ends, as shown in Figure 1b. The total length of the rod is $L/2$, and the adhered segment is l . We introduce a Cartesian coordinate system ($o-xy$). Besides the Euler coordinates x and y , the arc length s , a Lagrange coordinate, is also employed as a variable in our analysis. The slope angle of the beam at an arbitrary point is ϕ , which continuously changes from 0° at its left end to -90° at its right end.

According to Figure 1, the fixed boundary conditions of the elastic system are prescribed as

$$\phi(l) = 0, \quad \phi\left(\frac{L}{2}\right) = -\frac{\pi}{2}, \quad \phi(L-l) = -\pi; \quad (3)$$

$$y(l) = 0, \quad y\left(\frac{L}{2}\right) = 0. \quad (4)$$

The geometric conditions of the elastica are

$$\dot{x} = \cos \phi, \quad \dot{y} = \sin \phi, \quad (5)$$

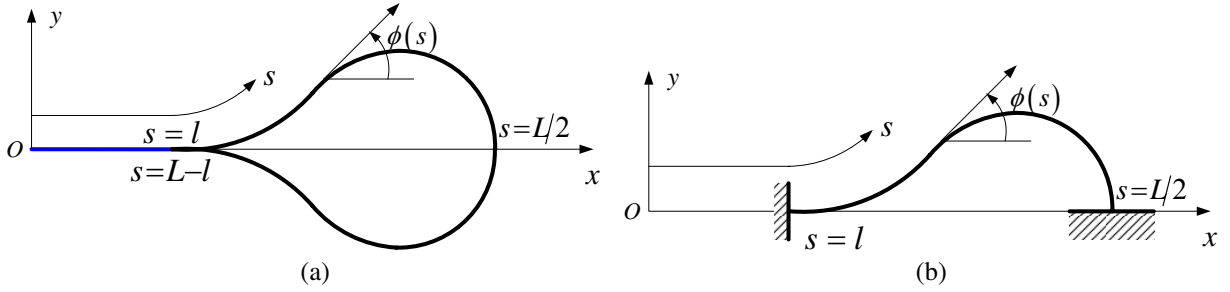


Figure 1. Schematic diagram of a slender structure self-folded into a racket-like shape. (a) The left segment is adhered by solid interface or liquid film. (b) The total length of the rod is L , the adhered segment l , and the slope angle at an arbitrary point ϕ .

where a dot above a character stands for the derivative of a variable with respect to the arc length s .

The total potential energy of the system consists of two parts, namely the elastic strain energy and surface energy. Considering the symmetry of this configuration, the energy functional of the system can be written as

$$\Pi = \int_l^{L/2} [EI\dot{\phi}^2 + \lambda_1(\dot{x} - \cos \phi) + \lambda_2(\dot{y} - \sin \phi)] ds - W_a l, \quad (6)$$

where λ_1 and λ_2 are two Lagrange multipliers, enforcing the additional geometrical relations of (5).

The second term of at the right end of (6) stands for the surface energy, and the symbol W_a is defined as the work of adhesion between two surfaces [Dupré 1969]. It is expressed as

$$W_a = (\gamma_1 + \gamma_2 - \gamma_{12})b, \quad (7)$$

where b is the contact width out of the plane, γ_1 and γ_2 are the surface energies of the two different phases, and γ_{12} the interfacial energy. In the conventional definition, the work of adhesion is actually the work per unit area necessary to create two new surfaces from a unit area of an adhered interface, which is a positive constant for any two homogeneous materials binding at an interface at a fixed temperature [Tang et al. 2005]. The cohesive work can be defined as the work of adhesion between two identical material interfaces, which reads

$$W_c = 2\gamma_1 b. \quad (8)$$

For a slender structure with the interface adhered by a liquid film, the cohesive work or the interfacial energy per unit length is

$$W_c = 2(\gamma_l + \gamma_{SV} - \gamma_{SL})b = 2\gamma_l(1 + \cos \theta_Y)b, \quad (9)$$

where γ_{SV} , γ_{SL} , and γ_l designate the interfacial tensions of the solid/vapor, solid/liquid, and liquid/vapor interfaces, respectively, and θ_Y is the Young's contact angle. At micro and nanoscales, the cohesive work is normally termed the binding energy E_B [Zhou et al. 2007].

Although the intrinsic boundary condition of the present problem is fixed, we can view it as movable, and then the new variation scheme can be introduced (see Appendix A). During the variation operation, we should stress that the variation of the total potential energy can be separated to two portions: the first part $\delta\Pi_1$ is the variation when the adhesive point $s = l$ is assumed to be fixed; the second $\delta\Pi_2$ is the

additional variation on the movable point at $s = l$. The additional term of the variation for the considered problem is because the adhesive length l is yet to be determined, which leads to the movable boundary condition. Therefore, according to the principle of least potential energy one has

$$\delta\Pi = \delta\Pi_1 + \delta\Pi_2 = 0. \quad (10)$$

A detailed derivation of (10) can be found in Appendix B, and we can clearly obtain the governing equation of the elastica

$$2EI\ddot{\phi} - \lambda_1 \sin\phi + \lambda_2 \cos\phi = 0 \quad (11)$$

and the adhesive boundary condition at the moving point

$$EI\dot{\phi}(l)^2 - W_c = 0. \quad (12)$$

The symbols λ_1 and λ_2 in (11) can be easily identified as the horizontal and vertical components of the internal forces in the beam. It can be seen that the governing equation in (11) was obtained from the perspective energy functional, which conforms to the result derived by Tang and Glassmaker [2010], who adopted the analysis method of force equilibrium.

The transversality boundary condition represents the balance of the strain energy and the cohesive work, which is called the adhesive boundary condition or transversality condition in mathematical terminology. It is worth mentioning that the adhesive boundary condition in (12) can also be deduced via the concept of the J -integral in fracture mechanics, as described by Glassmaker and Hui [2004] in their analysis of silicon–germanium nanotube formation. The stationary potential and material force balance methods have also been adopted to derive the adhesive boundary condition [Majidi 2007]. The discrepancy between (12) and the result of [Glassmaker and Hui 2004] is due to a difference in geometry; the current model is symmetric in the configuration, in comparison with the single-side adhesive interface in the reference. In addition, the framework of the energy functional variation in consideration of the adhesive boundary condition can also be extended to solve other problems, where the boundary conditions can also be regarded as movable. The proposed method proves efficient and essential for calculating the contact angle of a droplet, the morphology of a cell, and the peeling of a CNT from the substrate [Seifert and Lipowsky 1990; Oyharcalbal and Frisch 2005; Bormasshenko and Whyman 2008].

Multiplying both sides of (11) by $\dot{\phi}$ and integrating, one has

$$EI\dot{\phi}^2 = D - \lambda_1 \cos\phi - \lambda_2 \sin\phi, \quad (13)$$

where the parameter D is an integration constant. Making use of (3), one obtains

$$EI\dot{\phi}(l)^2 = D - \lambda_1, \quad (14)$$

$$EI\dot{\phi}(L-l)^2 = D + \lambda_1. \quad (15)$$

The symmetry of the configuration results in $\dot{\phi}(l)^2 = \dot{\phi}(L-l)^2$, and then the Lagrange multiplier $\lambda_1 = 0$.

Considering (12) and (14), one has

$$D = W_c. \quad (16)$$

We introduce the parameter $\alpha = \sqrt{\lambda_2/(2EI)}$, and replace $D/(2EI)$ with $\alpha^2 C$, where the symbol $C = W_c/\lambda_2$. Apparently, the physical meaning of α is the square ratio between the internal force and the bending stiffness. Thus the governing equation (13) and the adhesive boundary condition (12) are respectively transformed into

$$\frac{1}{2}\dot{\phi}^2 = \alpha^2(C - \sin\phi), \quad \frac{1}{2}\dot{\phi}(l)^2 = \alpha^2 C. \quad (17)$$

The combination of (14) and (17)₂ gives

$$2\alpha^2 L_{ec}^2 C = 1. \quad (18)$$

Here, we have defined a new characteristic length, that is, the elastocohesive length $L_{ec} = \sqrt{EI/W_c}$, which is different from the elastocapillary length L_{EC} used in [Roman and Bico 2010]. The elastocohesive length can be equivalently written in another format, as the parameter $1/\sqrt{Q}$ determined in [Glassmaker and Hui 2004]. For a slender structure adhered by a liquid film, the elastocohesive length $L_{ec} = (\sqrt{2}/2)L_{EC}$ when $\theta_Y = 0$. It can be seen that in this case, (14) and (18) are consistent with the result of [Py et al. 2007].

2.2. Displacement boundary condition. As ds is always positive and the increment of the slope angle is not monotonic, (17)₁ is simplified as

$$\alpha ds = \frac{|d\phi|}{\sqrt{2(C - \sin\phi)}}. \quad (19)$$

For convenient integration, the variable ϕ is replaced with θ . They are related by

$$(1 + C) \sin^2 \theta = 2k^2 \sin^2 \theta = 1 + \sin \phi \quad (0 \leq \theta \leq \pi, k > 0), \quad (20)$$

and

$$C = 2k^2 - 1, \quad \sqrt{2(C - \sin\phi)} = 2k|\cos\theta|, \quad |d\phi| = \frac{2k|\cos\theta|}{\sqrt{1 - k^2 \sin^2 \theta}} d\theta. \quad (21)$$

In these equations, we consider the uniqueness of the solution in light of the physical meaning of the problem.

Substituting (21)₂ and (21)₃ into the displacement boundary condition in (3) leads to

$$\alpha \left[y\left(\frac{L}{2}\right) - y(l) \right] = \int_0^{-\pi/2} \frac{\sin\phi |d\phi|}{\sqrt{2(C - \sin\phi)}} = F(k, \pi) - F(k, \theta_0) - 2[E(k, \pi) - E(k, \theta_0)] = 0, \quad (22)$$

where $\sin\theta_0 = 1/(\sqrt{2}k)$ and $F(k, \theta)$ and $E(k, \theta)$ are the elliptic integrals of the first and second kinds, which are respectively defined as

$$F(k, \theta) = \int_0^\theta \frac{1}{\sqrt{1 - k^2 \sin^2 \theta}} d\theta, \quad E(k, \theta) = \int_0^\theta \sqrt{1 - k^2 \sin^2 \theta} d\theta. \quad (23)$$

2.3. Inextensible condition. To close this mathematical problem, we complement the inextensible condition of the elastic rod [Liu and Feng 2007; Neukirch et al. 2012], which is written as

$$\alpha \left(\frac{L}{2} - l \right) = \int_0^{-\pi/2} \frac{|d\phi|}{\sqrt{2(C - \sin\phi)}} = F(k, \pi) - F(k, \theta_0). \quad (24)$$

3. Critical adhesion parameters

3.1. Geometric constraint. From (22), one can solve for the corresponding values of $k = 0.855092$ and $C = 0.462366$, both of which are independent of the material parameters of the beam. Furthermore, (18) gives the following relation between the nondimensional internal force αL and the normalized elastocohesive length:

$$\alpha L = \frac{1}{\sqrt{4k^2 - 2(L_{ec}/L)}}, \quad (25)$$

and the function curve is exhibited in Figure 2. It can be seen that the vertically internal force of the cross section on the beam will increase with the increase of the cohesive work. This means that the stronger interfacial adhesion ability will produce larger reaction force and internal force. The reduced vertical force αL can be solved from (25) provided that the elastocohesive length and the total length of the beam are given.

Substitution of (25) into (24) yields

$$\frac{l}{L} = \frac{1}{2} - \sqrt{4k^2 - 2} [F(k, \pi) - F(k, \theta_0)] \frac{L_{ec}}{L}. \quad (26)$$

The symbol l in (26) is the critical adhesive length, which is a linear function of the elastocohesive length. This relation agrees with the previous scaling analysis [Py et al. 2007] and infinitesimal deformation calculations [Buehler et al. 2006; Zhou et al. 2007; Mikata 2010]. However, the slope of the linear function in (26) is about -3.03 and differs from the experimental result of -4.9 [Py et al. 2007]. In comparison, the previous work [Py et al. 2007] deals with the function of the attached length ($L - 2l$) about the elastocapillary length, and the slope is approximately obtained by a linear regression method. The deviation between our theoretical result and their experiment may stem from their data processing method and the zero Young's contact angle assumption.

The linear relation in (26) also indicates that the adhesive length will be in the range of $0 < l/L < 0.5$, and the elastocohesive length meets the condition

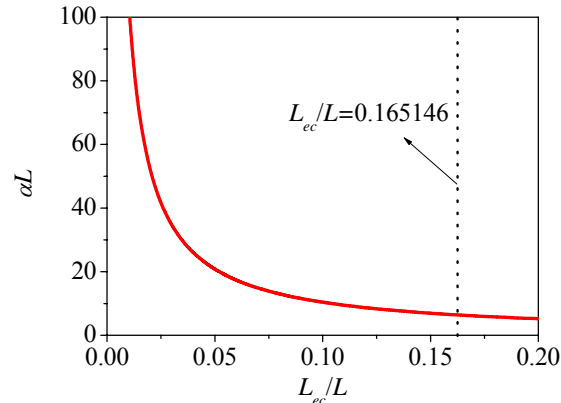


Figure 2. Variation of the nondimensional internal force with respect to the normalized elastocohesive length.

$$0 < \frac{L_{ec}}{L} < \frac{1}{2\sqrt{4k^2 - 2}[F(k, \pi) - F(k, \theta_0)]}. \quad (27)$$

Equation (27) is an intuitively geometric constraint for the nondimensional cohesive length to ensure the self-folding shape. It indicates that this dimensionless length has an upper limit (as schematized in the dotted line in Figure 2, where $L_{ec}/L = 0.165146$), that is, the cohesive work must be strong enough, and simultaneously the rod should be sufficiently slender.

3.2. Energy constraint. Besides the aforementioned geometric constraint condition for the adhesive length, another stronger constraint can be derived from the consideration of energy. Using (17)₁, (19), (21)₂, (21)₂, and (25), the analytical solution of the reduced potential energy on the system can be derived as

$$\frac{\Pi L}{EI} = L \int_l^{L/2} \dot{\phi}^2 ds - \frac{Ll}{L_{ec}^2} = \frac{2\sqrt{4k^2 - 2}[F(k, \pi) - F(k, \theta_0)]}{L_{ec}/L} - \frac{1}{2(L_{ec}/L)^2}. \quad (28)$$

The total potential energy is shown in Figure 3 as a function of the normalized elastocohesive length, which is not a monotonic function but has an extreme point. For a structure with extremely large elastocohesive length, its potential energy is higher than zero. In reality, the flexible structure takes a rectilinear shape for the ground state, whose total potential energy should be zero (there is no deformation). The thermodynamic law tells us that the self-folding is energetically favorable only if the current energy is smaller than that of the ground state. For a very short rod or a quite low cohesive work, the nondimensional elastocohesive length is very large, the total potential energy Π can be higher than zero (see Figure 3), and it is difficult for the driving force to change the configuration from the ground state to the self-folding state. Therefore, there must exist a critical adhesive length to ensure a stable configuration. On the basis of (28), the energy requirement $\Pi < 0$ leads to

$$\frac{L_{ec}}{L} < \frac{1}{4\sqrt{4k^2 - 2}[F(k, \pi) - F(k, \theta_0)]}. \quad (29)$$

This energetic constraint condition gives a more strict limitation for the normalized elastocohesive length, which can only make sense in a much narrower range than that of (27). Beyond this scope, the

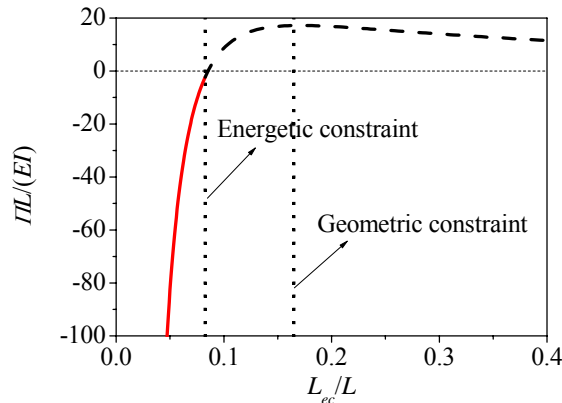


Figure 3. The dependence relationship between the nondimensional total potential energy of the system and the normalized elastocohesive length.

racket-like shape of the structure is in a metastable state, as the dashed line shown in Figure 3. In other words, the elastocohesive length must meet both the energy constraint in (29) (the first vertical line in Figure 3) and the geometric constraint in (27) (the second vertical line in Figure 3), and the final adhesive length satisfies $1/4 < l/L < 1/2$. This newly presented conclusion indicates that, as soon as the self-folding configuration is formed, the slender structure must possess an initial adhesive length larger than $L/4$. Otherwise, the racket-like morphology due to self-folding is not energetically favorable, and would seldom happen in reality. The corresponding critical total length to be self-folded is $L_{cr} = 12.11L_{ec}$ from (29), nearly equal to the calculated value $L_{cr} = 12.57L_{ec}$ in [Zhou et al. 2007].

3.3. Deflection. After the adhesive length has been determined, the deflection of the rod can be determined by

$$\alpha x = \alpha \int_0^s \cos \phi ds = \alpha l + \int_{\theta_0}^{\theta} 2k \sin \theta d\theta = \alpha l + \sqrt{4k^2 - 2} - 2k \cos \theta, \quad (30)$$

$$\alpha y = \alpha \int_0^s \sin \phi ds = F(k, \theta) - F(k, \theta_0) - 2[E(k, \theta) - E(k, \theta_0)]. \quad (31)$$

This is the analytical expression on the deflection of the elastica, which is different from the previous work, which was mostly conducted by numerical methods [Glassmaker and Hui 2004; Tang and Glassmaker 2010]. Equations (30) and (31) indicate that the nondimensional deflection of the rod is independent of the material parameters, showing the self-similarity of this racket configuration. The analytical solution of the displacement normalized by the total length of the beam reads

$$\begin{aligned} \frac{x}{L} &= \frac{1}{2} - \sqrt{4k^2 - 2} [F(k, \pi) - F(k, \theta_0)] \frac{L_{ec}}{L} + \frac{\sqrt{4k^2 - 2} L_{ec}}{L} (\sqrt{4k^2 - 2} - 2k \cos \theta), \\ \frac{y}{L} &= \sqrt{4k^2 - 2} \frac{L_{ec}}{L} \{F(k, \theta) - F(k, \theta_0) - 2[E(k, \theta) - E(k, \theta_0)]\}, \end{aligned} \quad (32)$$

and the width of the loop can also be deduced as

$$2y_{\max} = \sqrt{4k^2 - 2} \{F(k, \pi - \theta_0) - F(k, \theta_0) - 2[E(k, \pi - \theta_0) - E(k, \theta_0)]\} L_{ec}. \quad (33)$$

The loop of the racket has the value $2y_{\max} = 1.236L_{ec} = 0.874L_{EC}$, which is quite close to the numerical result of $0.89L_{EC}$ given in [Py et al. 2007].

Comparison with the experiments in [Py et al. 2007] shows that our exact solution successfully predicts the sheet wrapping behavior at the macro scale, and, in fact, it also applies to nanoscopic problems. For example, if the CNT is flexible and long enough, the gain in the potential energy due to van der Waals interaction (that is, the binding energy) is higher than the elastic strain energy necessary to bend the CNT. Under these circumferences, the tennis racket-like shaped CNTs can be formed. To simulate the morphology of self-folded CNTs, we select the following parameters [Mikata 2010]: Young's modulus $E = 1000$ GPa, moment of inertia $I = 5.2678 \times 10^{-38}$ m⁴, binding energy $E_B = 8.65 \times 10^{-11}$ J/m. Hence the elastocohesive length is $L_{ec} = 24.6778$ nm, and the corresponding critical length of the CNT is $L_{cr} = 298.861$ nm. We take the total length as $L = 400$ nm in computation. The deflection of the CNT self-folding is determined from (32) and plotted in Figure 4 under two representative values of the nondimensional elastocohesive length $L_{ec}/L = 0.0617$ (corresponding to $L_{ec} = 24.6778$ nm) and 0.05,

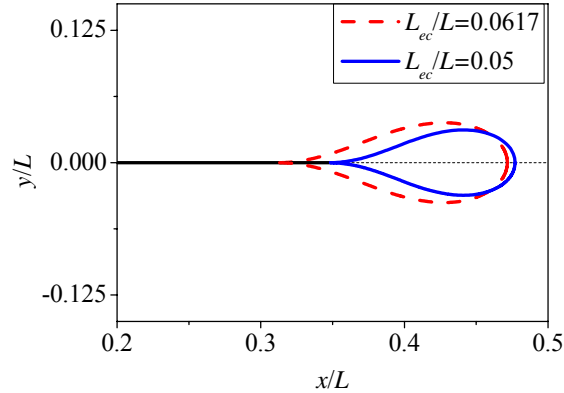


Figure 4. Normalized deflections of self-folding to a racket for a CNT, where $L_{ec}/L = 0.0617$ and $L_{ec}/L = 0.05$, respectively.

respectively. Clearly, the CNT will adhere more tightly with the increase of the cohesive work, and the width of the loop will shorten further.

4. Conclusions

We have presented an exact elastica model for analyzing the self-folding of slender structures. First, the potential energy functional of the system was constructed, which included the elastic strain energy and surface energy. We derived the governing equation and the adhesive boundary condition of the elastica, which stands for the balance of strain energy and surface energy at the movable boundary. Under the inextensible condition of the rod, we obtained the closed-form solution for the deflection of the beam in terms of elliptical integrals.

Furthermore, to ensure the self-folding of the slender structure into a tennis racket shape, the system must satisfy both the geometric and energetic constraints. The results show that self-folding is energetically favorable and thermodynamically stable with the cohesive work being strong enough and the structure being sufficiently flexible. The calculated result shows that, as soon as the self-folding configuration is formed, the structure must have an initial adhesive length after contact, of larger than $0.25L$. The corresponding critical total length to be self-folded agrees well with the previous result.

This model can be used to investigate both a macroscopic sheet wrapped by a liquid film, and a CNT self-folded by van der Waals forces. In this paper, our attention is only on planar problems, while an extension of the presented elastica model to three-dimensional spatial problems, for example, the coiling of DNA [Manohar et al. 2008; Huang 2011], would be of great interest.

Acknowledgements

This project was supported by the National Natural Science Foundation of China (11272357 and 11320003), the opening project of the State Key Laboratory of Explosion Science and Technology (Beijing Institute of Technology) (KFJJ12-11M), and the Pioneer R&D program for converging technology through the

Korea Science and Engineering Foundation funded by the Ministry of Education, Science and Technology (Grant M10711270001-08M1127-00110). We also thank Prof. Xi-Qiao Feng for modifying the manuscript.

Appendix A

The transversality condition dealing with movable boundaries was in [Courant and Hilbert 1953, pp. 211–214] and a more detailed deduction is presented here. A similar discussion can also be found in [Majidi et al. 2012].

Normally, the forced or fixed boundary conditions of an energy functional are prescribed as

$$y(0) = y_0, \quad y'(0) = y'_0; \quad y(a) = y_a, \quad y'(a) = y'_a. \quad (\text{A.1})$$

If the energy functional is expressed as

$$\Pi[y(s, a)] = \int_0^a F[s, y(s, a), y'(s, a), y''(s, a)] ds - \int_a^L W ds, \quad (\text{A.2})$$

then we consider the variation

$$y(s) = y_0(s) + \epsilon Y(s), \quad (\text{A.3})$$

where $y_0(s)$ denotes the extreme solution to be found, and $s = a$ is a moving point to be determined.

According to the prescribed boundary condition of (A.1), the extreme and varied solution must fulfill

$$y_0(a_0) = y_a, \quad y'_0(a_0) = y'_a; \quad y(a) = y_a, \quad y'(a) = y'_a; \quad Y(0) = Y'(0) = 0. \quad (\text{A.4})$$

The unknown a can be expanded as

$$a(\epsilon) = a_0 + \epsilon \left. \frac{da}{d\epsilon} \right|_{\epsilon=0} + O(\epsilon^2). \quad (\text{A.5})$$

The boundary value in (A.3) can also be expanded as

$$y(a) = y_0(a_0) + \epsilon y'(a_0) \left. \frac{da}{d\epsilon} \right|_{\epsilon=0} + \epsilon Y(a_0) + O(\epsilon^2), \quad (\text{A.6})$$

$$y'(a) = y'_0(a_0) + \epsilon y''(a_0) \left. \frac{da}{d\epsilon} \right|_{\epsilon=0} + \epsilon Y'(a_0) + O(\epsilon^2). \quad (\text{A.7})$$

Comparing (A.3), (A.6), and (A.7), one arrives at

$$Y(a_0) = -y'(a_0) \left. \frac{da}{d\epsilon} \right|_{\epsilon=0}, \quad Y'(a_0) = -y''(a_0) \left. \frac{da}{d\epsilon} \right|_{\epsilon=0}. \quad (\text{A.8})$$

Equations (A.8) give the variation of the “new” end point $a(\epsilon)$ as a function of the variation in y and the derivatives y' and y'' at the “old” end point a_0 .

Before proceeding, we recall the formula for the derivative for an integral including a parameter α . Let

$$\phi(\alpha) = \int_{a(\alpha)}^{b(\alpha)} F(x, \alpha) dx. \quad (\text{A.9})$$

Its derivative with respect to α is

$$\phi'(\alpha) = \int_{a(\alpha)}^{b(\alpha)} F_\alpha(x, \alpha) dx + F[b(\alpha), \alpha]b'(\alpha) - F[a(\alpha), \alpha]a'(\alpha). \quad (\text{A.10})$$

Now let us return to the variation of the energy functional in (A.2). Substituting (A.1), (A.3), (A.4) and (A.8) into (A.2), and using (A.9), one can obtain the derivative of the functional

$$\begin{aligned} \left. \frac{d\Pi}{d\epsilon} \right|_{\epsilon=0} &= [W + F]_{s=a_0} \left. \frac{da}{d\epsilon} \right|_{\epsilon=0} + \int_0^{a_0} [F_y Y + F_{y'} Y' + F_{y''} Y''] ds \\ &= [W + F]_{s=a_0} \left. \frac{da}{d\epsilon} \right|_{\epsilon=0} + [F_{y'} Y + F_{y''} Y']_0^{a_0} + \int_0^{a_0} \left[F_y Y - \frac{dF_{y'}}{ds} Y - \frac{dF_{y''}}{ds} Y' \right] ds \\ &= [W + F]_{s=a_0} \left. \frac{da}{d\epsilon} \right|_{\epsilon=0} + \left[F_{y'} Y + F_{y''} Y' - \frac{dF_{y''}}{ds} Y \right]_0^{a_0} + \int_0^{a_0} \left[F_y - \frac{dF_{y'}}{ds} + \frac{d^2 F_{y''}}{ds^2} \right] Y ds \\ &= \left[W + F - y' F_{y'} - y'' F_{y''} + y' \frac{dF_{y''}}{ds} \right]_{s=a_0} \left. \frac{da}{d\epsilon} \right|_{\epsilon=0} + \left[F_{y'} Y + F_{y''} Y' - \frac{dF_{y''}}{ds} Y \right]_0^{a_0} \\ &\quad + \int_0^{a_0} \left[F_y - \frac{dF_{y'}}{ds} + \frac{d^2 F_{y''}}{ds^2} \right] Y ds = 0. \quad (\text{A.11}) \end{aligned}$$

The fact that the above integral equals zero leads to the Euler–Poisson equation

$$F_y - \frac{dF_{y'}}{ds} + \frac{d^2 F_{y''}}{ds^2} = 0. \quad (\text{A.12})$$

The remainder of (A.11) comes to the following form

$$\left[W + F - y' F_{y'} - y'' F_{y''} + y' \frac{dF_{y''}}{ds} \right]_{s=a_0} \left. \frac{da}{d\epsilon} \right|_{\epsilon=0} = 0. \quad (\text{A.13})$$

This expression vanishes for arbitrary $da/d\epsilon|_{\epsilon=0}$, which corresponds to arbitrary $Y(a_0)$ if the bracket is zero. Then we can obtain the transversality condition for this variational problem:

$$W = \left[y' F_{y'} + y'' F_{y''} - y' \frac{dF_{y''}}{ds} - F \right]_{s=a_0}. \quad (\text{A.14})$$

Appendix B

The detailed variation process on the energy functional proceeds as follows. Taking the variation on the energy functional, the principle of least potential energy leads to

$$\delta\Pi = \delta\Pi_1 + \delta\Pi_2 = 0. \quad (\text{B.1})$$

The first part of the variation is under the assumption that the boundary condition is fixed, namely

$$\begin{aligned}\delta\Pi_1 &= \int_l^{L/2} [2EI\dot{\phi} \delta\dot{\phi} + \delta\lambda_1(\dot{x} - \cos\phi) + \delta\lambda_2(\dot{y} - \sin\phi) \\ &\quad + \lambda_1 \delta\dot{x} + \lambda_1 \sin\phi \delta\phi + \lambda_2 \delta\dot{y} - \lambda_2 \cos\phi \delta\phi] ds \\ &= \int_l^{L/2} [-2EI\ddot{\phi} \delta\phi + \delta\lambda_1(\dot{x} - \cos\phi) + \delta\lambda_2(\dot{y} - \sin\phi) \\ &\quad + \lambda_1 \sin\phi \delta\phi - \lambda_2 \cos\phi \delta\phi] ds + [2EI\dot{\phi} \delta\phi + \lambda_1 \delta x + \lambda_2 \delta y]_l^{L/2}. \quad (\text{B.2})\end{aligned}$$

In view of the fixed boundary conditions (3) and (4), (B.2) can be reduced to

$$\delta\Pi_1 = \int_l^{L/2} [\delta\lambda_1(\dot{x} - \cos\phi) + \delta\lambda_2(\dot{y} - \sin\phi) - (2EI\ddot{\phi} - \lambda_1 \sin\phi + \lambda_2 \cos\phi) \delta\phi] ds - \lambda_1 \delta l. \quad (\text{B.3})$$

Then we consider the corresponding variation on the movable boundary condition at the point $s = l$, which is written as

$$\begin{aligned}\delta\Pi_2 &= -[EI\dot{\phi}^2 + \lambda_1(\dot{x} - \cos\phi) + \lambda_2(\dot{y} - \sin\phi) - 2\dot{\phi}(EI\dot{\phi}) - \dot{x}\lambda_1 - \dot{y}\lambda_2]_{s=l} \delta l - W_c \delta l \\ &= [EI\dot{\phi}(l)^2 - W_c + \lambda_1] \delta l. \quad (\text{B.4})\end{aligned}$$

Considering the arbitrariness of the variation, one can obtain the following governing equation:

$$2EI\ddot{\phi} - \lambda_1 \sin\phi + \lambda_2 \cos\phi = 0, \quad (\text{B.5})$$

and the transversality boundary condition at the moving point:

$$EI\dot{\phi}(l)^2 - W_c = 0. \quad (\text{B.6})$$

References

- [Bigoni 2012] D. Bigoni, *Nonlinear solid mechanics: bifurcation theory and material instability*, Cambridge University Press, 2012.
- [Bisshopp and Drucker 1945] K. E. Bisshopp and D. C. Drucker, "Large deflection of cantilever beams", *Quart. Appl. Math.* **3** (1945), 272–275.
- [Bormasshenko and Whyman 2008] E. Bormasshenko and G. Whyman, "Variational approach to wetting problems: calculation of a shape of sessile liquid drop deposited on a solid substrate in external field", *Chem. Phys. Lett.* **463**:1–3 (2008), 103–105.
- [Buehler et al. 2004] M. J. Buehler, Y. Kong, and H. Gao, "Deformation mechanisms of very long single-wall carbon nanotubes subject to compressive loading", *J. Eng. Mater. Technol.* **126**:3 (2004), 245–249.
- [Buehler et al. 2006] M. J. Buehler, Y. Kong, H. Gao, and Y. Huang, "Self-folding and unfolding of carbon nanotubes", *J. Eng. Mater. Technol.* **128**:1 (2006), 3–10.
- [Cohen and Mahadevan 2003] A. E. Cohen and L. Mahadevan, "Kinks, rings, and rackets in filamentous structures", *Pro. Natl. Acad. Sci.* **100**:21 (2003), 12141–12146.
- [Courant and Hilbert 1953] R. Courant and D. Hilbert, *Methods of mathematical physics*, vol. 1, Interscience, New York, 1953.
- [Cranford et al. 2009] S. Cranford, D. Sen, and M. J. Buehler, "Meso-origami: folding multilayer graphene sheets", *Appl. Phys. Lett.* **95**:12 (2009), 123121.
- [Dupré 1969] A. Dupré, *Théorie mécanique de la chaleur*, Gauthier-Villars, Paris, France, 1969.
- [Fygenson et al. 1997] D. K. Fygenson, J. F. Marko, and A. Libchaber, "Mechanics of microtubule-based membrane extension", *Phys. Rev. Lett.* **79** (1997), 4497–4500.

- [Gao et al. 1998] G. Gao, T. Çağın, and W. A. Goddard, III, “Energetics, structure, mechanical and vibrational properties of single-walled carbon nanotubes”, *Nanotechnology* **9**:3 (1998), 184–191.
- [Glassmaker and Hui 2004] N. J. Glassmaker and C. Y. Hui, “Elastica solution for a nanotube formed by self-adhesion of a folded thin film”, *J. Appl. Phys.* **96**:6 (2004), 3429–3435.
- [Huang 2011] Z. Huang, “Modulating DNA configuration by interfacial traction: an elastic rod model to characterize DNA folding and unfolding”, *J. Biol. Phys.* **37**:1 (2011), 79–90.
- [Kim et al. 2011] K. Kim, Z. Lee, B. D. Malone, K. T. Chan, B. Alemán, W. Regan, W. Gannett, M. F. Crommie, M. L. Cohen, and A. Zettl, “Multiply folded graphene”, *Phys. Rev. B* **83**:24 (June 2011), 245433.
- [Lee et al. 2007] H. S. Lee, C. H. Yun, H. M. Kim, and C. J. Lee, “Persistence length of multiwalled carbon nanotubes with static bending”, *J. Phys. Chem. C* **111**:51 (2007), 18882–18887.
- [Liu and Feng 2007] J.-L. Liu and X.-Q. Feng, “Capillary adhesion of microbeams: finite deformation analyses”, *Chin. Phys. Lett.* **24**:8 (2007), 2349–2352.
- [Love 1906] A. E. H. Love, *A treatise on the mathematical theory of elasticity*, Second ed., Cambridge University Press, 1906.
- [Majidi 2007] C. Majidi, “Remarks on formulating an adhesion problem using Euler’s elastica (draft)”, *Mech. Res. Comm.* **34**:1 (2007), 85–90.
- [Majidi et al. 2012] C. Majidi, O. M. O’Reilly, and J. A. Williams, “On the stability of a rod adhering to a rigid surface: shear-induced stable adhesion and the instability of peeling”, *J. Mech. Phys. Solids* **60**:5 (2012), 827–843.
- [Manohar et al. 2008] S. Manohar, A. R. Mantz, K. E. Bancroft, C.-Y. Hui, A. Jagota, and D. V. Vezenov, “Peeling single-stranded DNA from graphite surface to determine oligonucleotide binding energy by force spectroscopy”, *Nano Lett.* **8**:12 (2008), 4365–4372.
- [Mikata 2010] Y. Mikata, “Approximate solutions for a self-folding problem of carbon nanotubes”, *J. Eng. Mater. Technol.* **132**:1 (2010), 011013.
- [Neukirch et al. 2012] S. Neukirch, J. Frelat, A. Goriely, and C. Maurini, “Vibrations of post-buckled rods: the singular inextensible limit”, *J. Sound Vibr.* **331** (2012), 704–720.
- [Oyharcabal and Frisch 2005] X. Oyharcabal and T. Frisch, “Peeling off an elastica from a smooth attractive substrate”, *Phys. Rev. E* **71** (2005), 036611.
- [Pantano et al. 2004] A. Pantano, D. M. Parks, M. C. Boyce, and M. Buongiorno Nardelli, “Mixed finite element-tight-binding electromechanical analysis of carbon nanotubes”, *J. Appl. Phys.* **96** (2004), 6756–6760.
- [Pineirua et al. 2010] M. Pineirua, J. Bico, and B. Roman, “Capillary origami controlled by an electric field”, *Soft Matter* **6**:18 (2010), 4491–4496.
- [Py et al. 2007] C. Py, P. Reverdy, L. Doppler, J. Bico, B. Roman, and C. N. Baroud, “Capillary origami: spontaneous wrapping of a droplet with an elastic sheet”, *Phys. Rev. Lett.* **98**:15 (Apr 2007), 156103.
- [Py et al. 2009] C. Py, P. Reverdy, L. Doppler, J. Bico, B. Roman, and C. N. Baroud, “Capillarity induced folding of elastic sheets”, *Eur. Phys. J. Special Topics* **166** (2009), 67–71.
- [Roman and Bico 2010] B. Roman and J. Bico, “Elasto-capillarity: deforming an elastic structure with a liquid droplet”, *J. Phys.: Condensed Matter* **22**:49 (2010), 493101.
- [Romero et al. 2008] V. Romero, T. A. Witten, and E. Cerda, “Multiple coiling of an elastic sheet in a tube”, *Proc. R. Soc. Lond. Ser. A Math. Phys. Eng. Sci.* **464**:2099 (2008), 2847–2866.
- [Schmidt and Eberl 2001] O. G. Schmidt and K. Eberl, “Thin solid films roll up into nanotubes”, *Nature* **410**:6825 (2001), 168.
- [Seifert and Lipowsky 1990] U. Seifert and R. Lipowsky, “Adhesion of vesicles”, *Phys. Rev. A* **42** (1990), 4768–4771.
- [Tang and Glassmaker 2010] T. Tang and N. J. Glassmaker, “On the inextensible elastica model for the collapse of nanotubes”, *Math. Mech. Solid.* **15**:5 (2010), 591–606.
- [Tang et al. 2005] T. Tang, A. Jagota, C.-Y. Hui, and N. J. Glassmaker, “Collapse of single-walled carbon nanotubes”, *J. Appl. Phys.* **97** (2005), 074310.
- [Zheng et al. 2004] L. X. Zheng, M. J. O’Connell, S. K. Doorn, X. Z. Liao, Y. H. Zhao, E. A. Akhadow, M. A. Hoffbauer, B. J. Roop, Q. X. Jia, R. C. Dye, D. E. Peterson, S. M. Huang, J. Liu, and Y. T. Zhu, “Ultralong single-wall carbon nanotubes”, *Nat. Mater.* **3** (2004), 673–676.

[Zhou et al. 2007] W. Zhou, Y. Huang, B. Liu, K. C. Hwang, J. M. Zuo, M. J. Buehler, and H. Gao, "Self-folding of single- and multiwall carbon nanotubes", *Appl. Phys. Lett.* **90**:7 (2007), 073107.

Received 25 Sep 2012. Revised 11 Dec 2012. Accepted 26 Jan 2013.

JIANLIN LIU: liujianlin@upc.edu.cn

Department of Engineering Mechanics, China University of Petroleum, Qingdao, 266580, China

<http://dem.upc.edu.cn/contents/38/96.html>

JUNG HOON LEE: jleenano@snu.ac.kr

School of Mechanical and Aerospace Engineering, Seoul National University, Seoul 151-744, South Korea

DISPERSION OF GUIDED WAVES IN INITIALLY STRESSED LAYERED PLATES

JIANGONG YU AND SHENLEI LI

Based on the theory of the mechanics of incremental deformations, guided wave propagation in multi-layered plates under initial stresses in the thickness and wave-propagation directions is investigated. The Legendre polynomial series method is used to solve the coupled wave equations and its convergence is discussed along with numerical examples. The effects of initial stresses on Lamb-like waves and SH waves are analyzed, and numerical results show that they are quite distinct. The frequency variation is not linear with the increase of the initial stresses in both directions. The effects of the initial stress in the thickness direction are very different from those in the longitudinal direction.

1. Introduction

Because of the limitations of manufacturing and assembling technology, initial stresses in structural elements, especially in layered structures, are inevitable. The working loads on structures can be taken as the initial stresses. Thus, the problem of initially stressed structures is very common and it is very important to study it in both the practical and the theoretical sense.

Wave propagation in structures with initial stresses has received considerable attention. Chen and Wright [1966] derived the frequency equations for wave propagation in an initially stressed circular cylinder. Murdoch [1977] considered the effect of interfacial stress on the propagation of Stoneley waves. Ogden and Sotiropoulos [1995] studied interfacial waves in prestressed layered incompressible elastic solids. Gei [2008] investigated small-amplitude interfacial waves along a thin film between two prestressed, incompressible elastic media. Rayleigh waves in a magnetoelastic initially stressed conducting medium with a gravity field were investigated in [El-Naggar et al. 1994]. Abd-Alla and Ahmed [1999] investigated Love wave propagation in a nonhomogeneous orthotropic elastic layer with initial stress overlying a semiinfinite medium. Abd-Alla [1999] presented the effect of initial stress on axisymmetric waves in an orthotropic hollow cylinder. Qian et al. [2004] studied the effect of initial stress on Love waves in an elastic substrate with a piezoelectric layer and a piezoelectric substrate with an elastic layer. Du et al. [2007] studied Love wave propagation in layered magnetoelastoelectric structures with initial stress. Garg [2007] considered the effect of initial stress on harmonic plane waves in viscoelastic anisotropic media. Gupta et al. [2012] investigated torsional surface waves in an initially stressed heterogeneous half-space covered by a homogeneous layer. Bigoni et al. [2008] studied the filtering and band gap characteristics of a prestressed, stiff layer on an elastic half-space.

The above investigations are all about surface waves, subsurface waves, and interfacial waves. Guided wave propagation in structures with initial stresses has also received attention. Akbarov and Guliev [2009] studied axisymmetric longitudinal waves in a prestrained compound circular cylinder. Akbarov et al. [2011b] studied the case of torsional waves. Akbarov and Guliev [2010] investigated axisymmetric

Keywords: multilayered plate, guided waves, initial stress, orthogonal polynomial, dispersion curves.

longitudinal waves in a prestrained circular cylinder embedded in a prestrained compressible infinite medium. These three papers are all about circular cylinders. As they are more common structures, initially stressed multilayered plates have received more attention. Kayestha et al. [2010] obtained dispersion curves for a perfectly bonded prestressed compressible elastic bilayered plate. Wijeyewickrema and Leungvichcharoen [2009] investigated the influence of imperfections in the contact conditions between the layers of a prestrained three-layered plate. These two investigations do not allow readers to draw any concrete conclusions about the influence of the initial strains on the wave propagation velocity or on wave dispersion in layered media. Akbarov et al. [2008; 2011a] and Zamanov and Agasiyev [2011] investigated these issues. Akbarov et al. [2008] and Zamanov and Agasiyev [2011] studied the influence of initial strains in the wave-propagation direction on the Lamb wave dispersion curves. Akbarov et al. [2011a] studied the influence of initial strains in the thickness direction on the Lamb wave dispersion curves. Furthermore, small-amplitude waves in prestressed [Rogerson and Sandiford 1996; Gei et al. 2004; Gei 2008] and large deformed [Shmuel et al. 2012] multilayered structures have been given attention.

This paper simultaneously investigates the influence of initial stresses in two directions, the thickness and wave-propagation directions. Their different effects are discussed. We also illustrate the case of SH waves. The influences on Lamb waves and on SH waves are very different.

2. Mathematics and formulation of the problem

Consider an orthotropic N -layered plate with initial stresses in two directions, $S_{xx} = -\sum_{n=1}^N P_n \pi_{h_{n-1}, h_n}(z)$ and $S_{zz} = -Q$, as shown in Figure 1. The rectangular window function is

$$\pi_{h_{n-1}, h_n}(z) = \begin{cases} 1, & h_{n-1} \leq z \leq h_n, \\ 0, & \text{elsewhere.} \end{cases}$$

The plate is infinite in the horizontal direction and has a total thickness h_N . We place the horizontal (x, y) -plane of a Cartesian coordinate system on the bottom surface and let the plate be in the positive z region, where the medium occupies the region $0 \leq z \leq h_N$.

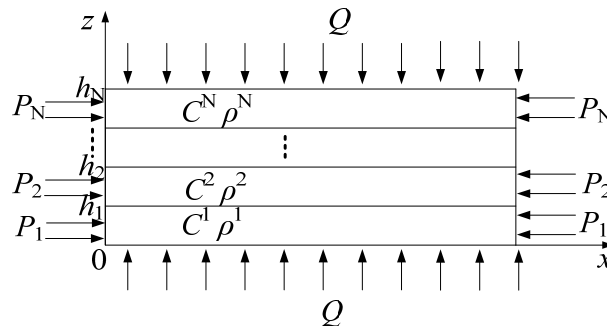


Figure 1. Schematic diagram of a layered plate under initial stresses.

According to [Biot 1965] (see also [Selim and Ahmed 2006]) the dynamic equations for the plate with initial stresses are governed by

$$\begin{aligned} \frac{\partial T_{xx}}{\partial x} + \frac{\partial T_{xy}}{\partial y} + \frac{\partial T_{xz}}{\partial z} - \frac{1}{2} \left(\frac{\partial u_x}{\partial z} + \frac{\partial u_z}{\partial x} \right) \frac{\partial S_{xx}}{\partial z} + S_{xx} \frac{\partial \omega_z}{\partial y} + (S_{zz} - S_{xx}) \frac{\partial \omega_y}{\partial z} &= \rho \frac{\partial^2 u_x}{\partial t^2}, \\ \frac{\partial T_{xy}}{\partial x} + \frac{\partial T_{yy}}{\partial y} + \frac{\partial T_{yz}}{\partial z} - S_{zz} \frac{\partial \omega_x}{\partial z} + S_{xx} \frac{\partial \omega_z}{\partial x} &= \rho \frac{\partial^2 u_y}{\partial t^2}, \\ \frac{\partial T_{xz}}{\partial x} + \frac{\partial T_{yz}}{\partial y} + \frac{\partial T_{zz}}{\partial z} + (S_{zz} - S_{xx}) \frac{\partial \omega_y}{\partial x} - S_{zz} \frac{\partial \omega_x}{\partial y} &= \rho \frac{\partial^2 u_z}{\partial t^2}, \end{aligned} \quad (1)$$

where

$$\omega_x = \frac{1}{2} \left(\frac{\partial u_z}{\partial y} - \frac{\partial u_y}{\partial z} \right), \quad \omega_y = \frac{1}{2} \left(\frac{\partial u_x}{\partial z} - \frac{\partial u_z}{\partial x} \right), \quad \omega_z = \frac{1}{2} \left(\frac{\partial u_y}{\partial x} - \frac{\partial u_x}{\partial y} \right). \quad (2)$$

The relationships between the strain and displacement components can be expressed as

$$\begin{aligned} \epsilon_{xx} &= \frac{\partial u_x}{\partial x}, & \epsilon_{yy} &= \frac{\partial u_y}{\partial y}, & \epsilon_{zz} &= \frac{\partial u_z}{\partial z}, \\ \epsilon_{yz} &= \frac{1}{2} \left(\frac{\partial u_y}{\partial z} + \frac{\partial u_z}{\partial y} \right), & \epsilon_{xz} &= \frac{1}{2} \left(\frac{\partial u_x}{\partial z} + \frac{\partial u_z}{\partial x} \right), & \epsilon_{xy} &= \frac{1}{2} \left(\frac{\partial u_x}{\partial y} + \frac{\partial u_y}{\partial x} \right). \end{aligned} \quad (3)$$

Here u_i , T_{ij} and ϵ_{ij} are the elastic displacements, stresses, and strains, respectively, while ρ is the density of the plate.

By introducing the rectangular window function $\pi_{0,h_N}(z)$, the stress-free boundary ($T_{zz} = T_{xz} = T_{yz} = 0$ at $z = 0$, $z = h_N$) is automatically incorporated in the constitutive relations of the plate [Datta and Hunsinger 1978]

$$\begin{aligned} T_{xx} &= C_{11}\epsilon_{xx} + C_{12}\epsilon_{yy} + C_{13}\epsilon_{zz}, & T_{yy} &= C_{12}\epsilon_{xx} + C_{22}\epsilon_{yy} + C_{23}\epsilon_{zz}, \\ T_{zz} &= (C_{13}\epsilon_{xx} + C_{23}\epsilon_{yy} + C_{33}\epsilon_{zz})\pi_{0,h_N}(z), & T_{yz} &= 2C_{44}\epsilon_{yz}\pi_{0,h_N}(z), \\ T_{xz} &= 2C_{55}\epsilon_{xz}\pi_{0,h_N}(z), & T_{xy} &= 2C_{66}\epsilon_{xy}, \end{aligned} \quad (4)$$

where C_{ij} are the elastic coefficients.

For the layered plate these coefficients are expressed as

$$C_{ij} = \sum_{n=1}^N C_{ij}^n \pi_{h_{n-1},h_n}(z), \quad (5a)$$

where N is the number of the layers and C_{ij}^n is the elastic constant of the N -th material. Similarly, the mass density can be expressed as

$$\rho = \sum_{n=1}^N \rho^n \pi_{h_{n-1},h_n}(z). \quad (5b)$$

For a free harmonic wave being propagated in the x direction in a plate, we assume the displacement components to be of the form

$$u_x(x, y, z, t) = \exp(ikx - i\omega t)U(z), \quad (6a)$$

$$u_y(x, y, z, t) = \exp(ikx - i\omega t)V(z), \quad (6b)$$

$$u_z(x, y, z, t) = \exp(ikx - i\omega t)W(z). \quad (6c)$$

$U(z)$, $V(z)$, and $W(z)$ represent the amplitude of vibration in the x , y , and z directions, respectively, while k is the magnitude of the wave vector in the propagation direction and ω is the angular frequency.

Substituting (3)–(6) into (1), the governing differential equations in terms of displacement components can be obtained:

$$\begin{aligned} U'' \sum_{n=1}^N (C_{55}^n + 0.5P_n - 0.5Q)\pi_{h_{n-1}, h_n}(z) + U' \left(\sum_{n=1}^N (C_{55}^n + 0.5P_n)\pi_{h_{n-1}, h_n}(z) \right)' \\ - k^2 U \sum_{n=1}^N (C_{11}^n + P_n)\pi_{h_{n-1}, h_n}(z) + ikW' \sum_{n=1}^N (C_{13}^n + C_{55}^n + 0.5P_n + 0.5Q)\pi_{h_{n-1}, h_n}(z) \\ + ikW \left(\sum_{n=1}^N (C_{55}^n + 0.5P_n)\pi_{h_{n-1}, h_n}(z) \right)' = -\omega^2 U \sum_{n=1}^N \rho^n \pi_{h_{n-1}, h_n}(z), \quad (7a) \end{aligned}$$

$$\begin{aligned} V'' \sum_{n=1}^N (C_{44}^n - 0.5Q)\pi_{h_{n-1}, h_n}(z) + V' \left(\sum_{n=1}^N C_{44}^n \pi_{h_{n-1}, h_n}(z) \right)' - k^2 V \sum_{n=1}^N (C_{66}^n - 0.5P_n)\pi_{h_{n-1}, h_n}(z) \\ = -\omega^2 V \sum_{n=1}^N \rho^n \pi_{h_{n-1}, h_n}(z), \quad (7b) \end{aligned}$$

$$\begin{aligned} W'' \sum_{n=1}^N (C_{33}^n + Q)\pi_{h_{n-1}, h_n}(z) + ikU' \sum_{n=1}^N (C_{13}^n + C_{55}^n + 0.5P_n + 0.5Q)\pi_{h_{n-1}, h_n}(z) \\ - k^2 W \sum_{n=1}^N (C_{55}^n - 0.5P_n + 0.5Q)\pi_{h_{n-1}, h_n}(z) + W' \left(\sum_{n=1}^N (C_{33}^n + Q)\pi_{h_{n-1}, h_n}(z) \right)' \\ + ikU \left(\sum_{n=1}^N (C_{13}^n + Q)\pi_{h_{n-1}, h_n}(z) \right)' = -\omega^2 W \sum_{n=1}^N \rho^n \pi_{h_{n-1}, h_n}(z) \quad (7c) \end{aligned}$$

where the superscript (\prime) is the partial derivative for z . Obviously, (7b) is independent of the other two equations. It represents the antiplane SH waves. The other two, (7a) and (7c), control the in-plane Lamb-like waves.

To solve the coupled wave (7), we expand the field quantities of each layer into one specific Legendre orthogonal polynomial series:

- In the first layer

$$u_a^1 = \sum_{m=0}^{\infty} p_{m,1}^a Q_m^1(z) \exp(ikx), \quad (8a)$$

with

$$Q_m^1(z) = \sqrt{\frac{2m+1}{h_1}} L_m\left(\frac{2}{h_1}z - 1\right)$$

and

$$u_a^1(z = h_1) = u_a^{1,h_1} = \sum_{m=0}^{\infty} p_{m,1}^a Q_m^1(z = h_1) \exp(ikx).$$

- In the second layer

$$u_a^2 = u_a^{1,h_1} + (z - h_1) \sum_{m=0}^{\infty} p_{m,2}^a Q_m^2(z) \exp(ikx), \quad (8b)$$

with

$$Q_m^2(z) = \sqrt{\frac{2m+1}{h_2-h_1}} L_m\left(\frac{2}{h_2-h_1}z - \frac{h_2+h_1}{h_2-h_1}\right)$$

and

$$u_a^2(z = h_2) = u_a^{2,h_2} = u_a^{1,h_1} + (h_2 - h_1) \sum_{m=0}^{\infty} p_{m,2}^a Q_m^2(z = h_2) \exp(ikx).$$

- The subsequent layers follow as such.
- In the last layer

$$u_a^N = u_a^{N-1,h_{N-1}} + (z - h_{N-1}) \sum_{m=0}^{\infty} p_{m,N}^a Q_m^N(z) \exp(ikx), \quad (8c)$$

with

$$Q_m^N(z) = \sqrt{\frac{2m+1}{h_N-h_{N-1}}} L_m\left(\frac{2}{h_N-h_{N-1}}z - \frac{h_N+h_{N-1}}{h_N-h_{N-1}}\right)$$

and

$$u_a^N(z = h_N) = u_a^{N,h_N} = u_a^{N-1,h_{N-1}} + (h_N - h_{N-1}) \sum_{m=0}^{\infty} p_{m,N}^a Q_m^N(z = h_N) \exp(ikx)$$

and so on.

Here, L_m is the m -th order Legendre polynomial. Theoretically, m runs from 0 to ∞ . In practice, the summation over the polynomials in (8) can be truncated at some finite value $m = M$, at which higher-order terms become negligible.

The forms of u_a ($a = 1, 2, 3$) and (u_x, u_y, u_z) are chosen in order to automatically incorporate in the calculation the continuity conditions at the interfaces relative to the components of the mechanical displacement.

Equation (7) is multiplied by $Q_j^{1*}(z), Q_j^{2*}(z), \dots, Q_j^{N*}(z)$, with j running from 0 to M , so that integration over z from 0 to h_N yields the following $3N(M+1)$ equations:

$${}^n A_{11}^{j,m} p_{m,n}^1 + {}^n A_{12}^{j,m} p_{m,n}^2 + {}^n A_{13}^{j,m} p_{m,n}^3 = -\omega^2 \cdot {}^n M_m^j p_{m,n}^1, \quad (9a)$$

$${}^n A_{21}^{j,m} p_{m,n}^1 + {}^n A_{22}^{j,m} p_{m,n}^2 + {}^n A_{23}^{j,m} p_{m,n}^3 = -\omega^2 \cdot {}^n M_m^j p_{m,n}^1, \quad (9b)$$

$${}^n A_{31}^{j,m} p_{m,n}^1 + {}^n A_{32}^{j,m} p_{m,n}^2 + {}^n A_{33}^{j,m} p_{m,n}^3 = -\omega^2 \cdot {}^n M_m^j p_{m,n}^1. \quad (9c)$$

where ${}^n A_{\alpha\beta}^{j,m}$ ($\alpha, \beta = 1, 2, 3$) and ${}^n M_m^j$ are the elements of a nonsymmetric matrix. They can be easily obtained according to (7).

Equation (9) can be written as

$$\begin{bmatrix} {}^n A_{11}^{j,m} & {}^n A_{12}^{j,m} & {}^n A_{13}^{j,m} \\ {}^n A_{21}^{j,m} & {}^n A_{22}^{j,m} & {}^n A_{23}^{j,m} \\ {}^n A_{31}^{j,m} & {}^n A_{32}^{j,m} & {}^n A_{33}^{j,m} \end{bmatrix} \begin{Bmatrix} p_{m,n}^1 \\ p_{m,n}^2 \\ p_{m,n}^3 \end{Bmatrix} = -\omega^2 \begin{bmatrix} {}^n M_m^j & 0 & 0 \\ 0 & {}^n M_m^j & 0 \\ 0 & 0 & {}^n M_m^j \end{bmatrix} \begin{Bmatrix} p_{m,n}^1 \\ p_{m,n}^2 \\ p_{m,n}^3 \end{Bmatrix}. \quad (10)$$

So, (10) yields a form of the eigenvalue problem. The eigenvalue ω^2 gives the angular frequency of the guided wave; eigenvectors $p_{m,n}^i$ ($i = 1, 2, 3$) allow the components of the particle displacement to be calculated. According to $V_{ph} = \omega/k$ and $V_g = d\omega/dk$, the phase velocity and group velocity can be obtained. Equation (10) can be solved numerically making use of standard computer programs for the diagonalization of nonsymmetric square matrices. $3N(M+1)$ eigenmodes are generated from the order- M expansion. Acceptable solutions are those eigenmodes for which convergence is obtained as M is increased. We determine that the eigenvalues obtained are converged when a further increase in the matrix dimension does not result in a significant change in the eigenvalue. We consider 0.5% as a significant change.

3. Numerical results

Based on the foregoing formulations, computer programs have been written using Mathematica to calculate the dispersion curves. We take common ceramic-metal (silicon nitride (N) and steel (S)) layered plates as examples. Their material properties are listed in Table 1. Because SH waves and Lamb-like waves are independent, we will discuss them respectively.

3.1. Convergence of the method. In order to verify the convergence of the method, the Lamb-like wave and SH wave dispersion curves for a three-layered plate under an uniform initial stress $Q = 20$ GPa are calculated for $M = 6, 7, 8$, and 9, as shown in Figure 2. The stacking sequence and thickness (m) of the plate are N/S/N-1/2/1.

Material	C_{11}	C_{13}	C_{33}	C_{44}	C_{55}	C_{66}	ρ
Steel	282	113	282	84	84	84	7.932
Silicon nitride	380	120	380	130	130	130	2.37

Table 1. The material properties of the layered plate. C_{ij} values are in units of 10^9 N/m², ρ values in 10^3 kg/m³.

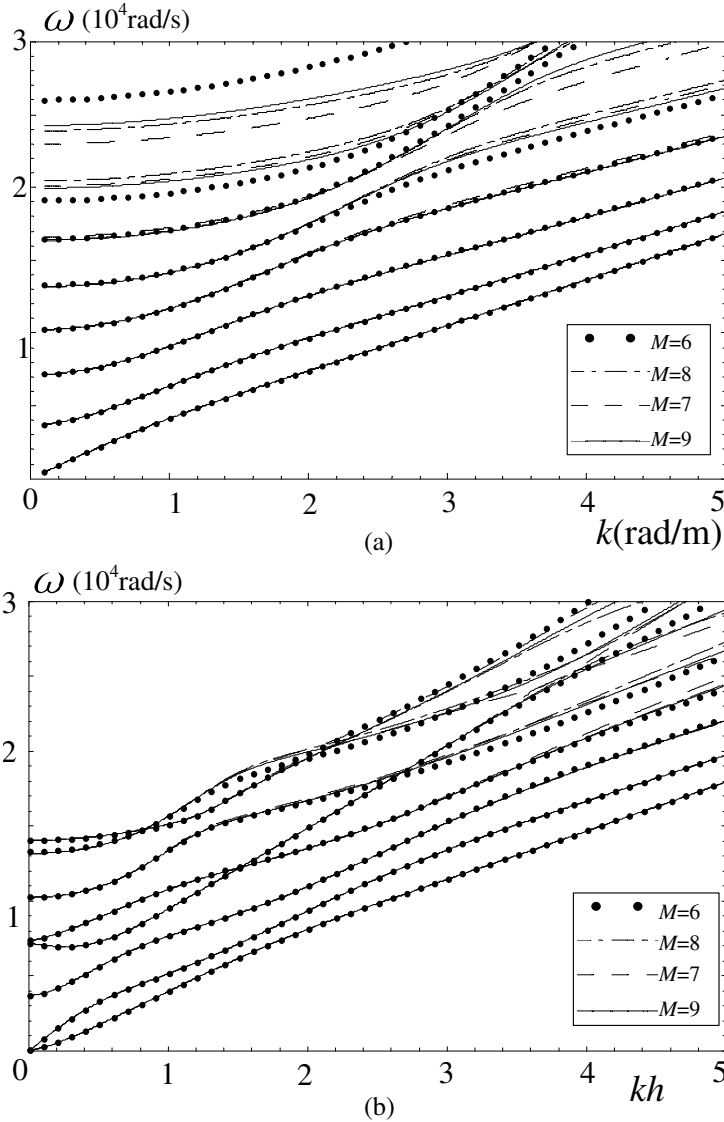


Figure 2. Dispersion curves for the N/S/N-1/2/1 plate under uniform initial stress $Q = 20$ GPa for various M values. (a) SH waves and (b) Lamb-like waves.

For SH waves, the first three modes are convergent when $M = 6$; the first four modes are convergent when $M = 7$ and 8. So, we think that at least the first $M/2$ SH modes are convergent. Similarly, for Lamb-like waves, the first three modes are convergent when $M = 6$; the first four modes are convergent when $M = 7$ and 8. So, we believe that at least the first $M/2$ Lamb-like wave modes are convergent.

For all the numerical calculations presented below, the series expansion is truncated at $M = 16$.

3.2. Effects of the initial stresses on Lamb-like waves. Figure 3 shows the phase velocity dispersion curves for the N/S/N-1/2/1 plate under different uniform initial stresses. Figure 3a is for the plate under initial stresses Q and Figure 3b is for the plate under uniform initial stresses P , that is, $P_1 = P_2 = P_3$.

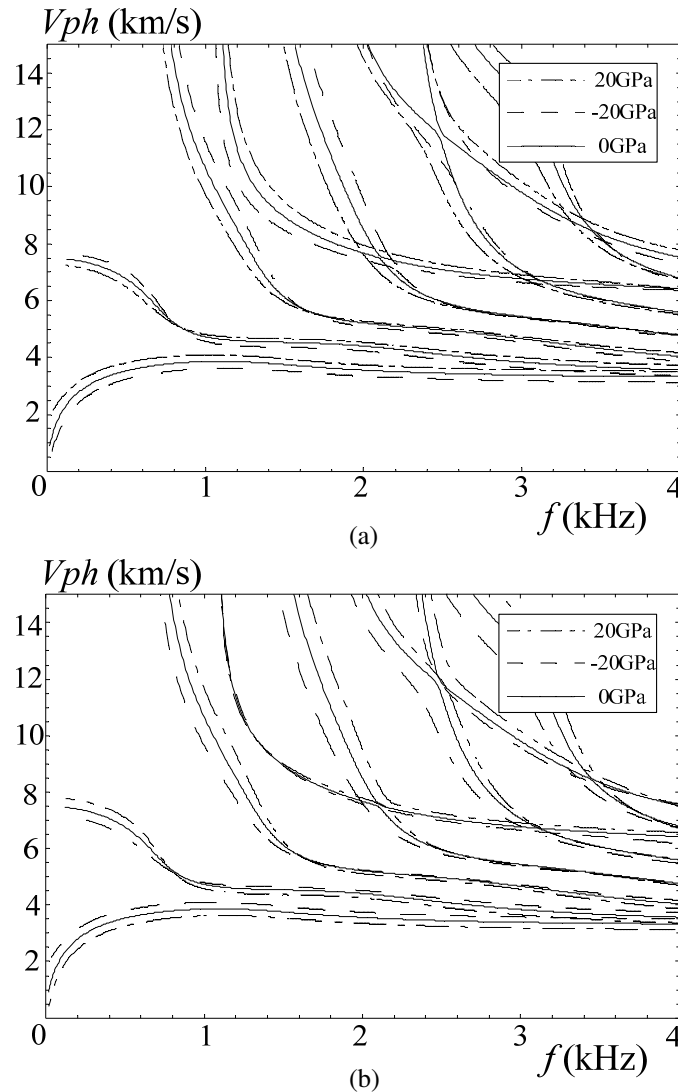


Figure 3. Lamb-like wave phase velocity spectra for the N/S/N-1/2/1 plate, (a) under initial stresses Q and (b) under uniform initial stresses P .

According to Figure 3a, a tensile stress in the thickness direction usually makes the wave speed lower at low frequencies (except for the first mode). As the frequency increases, a tensile stress makes the wave speed higher. In many cases, the effect of the tensile stress is contrary to that of the compressive stress. Comparing the two figures, we can see that the effect of the initial stress P is quite different from that of the initial stress Q . In many cases, the effect of the initial stress P is almost contrary to that of the initial stress Q .

Figure 3 reflects the relation between the effect of the initial stress and frequency. We observe the relation between the frequency (or wave speed) and the magnitudes of initial stress Q and P , as shown in Figures 4a and 4b, which show the frequency versus initial stress Q and P at $k = 1$ rad/m. In fact,

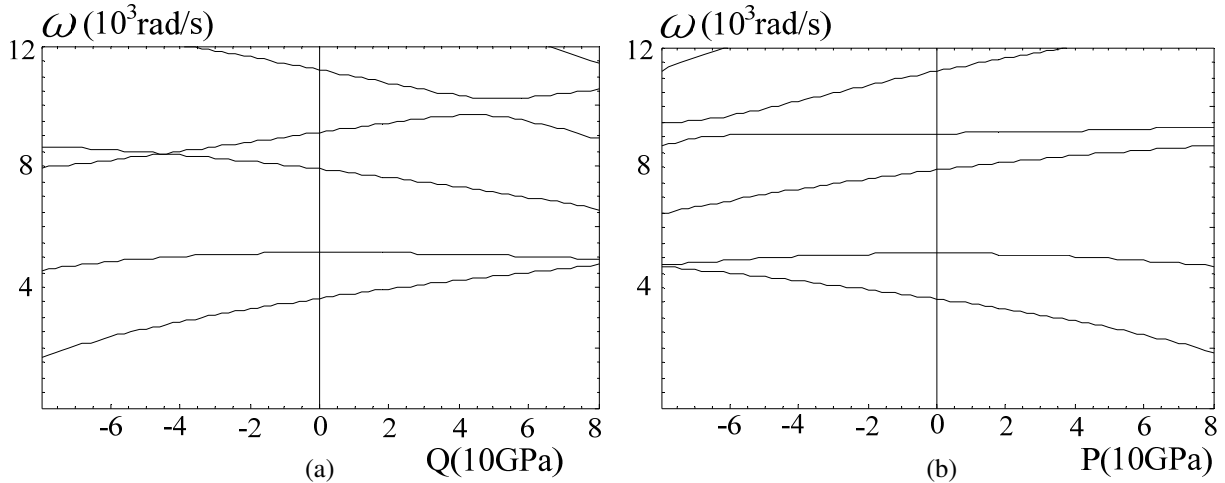


Figure 4. Lamb-like wave frequency curves versus initial stresses for the N/S/N-1/2/1 plate at $k = 1$ rad/m, with (a) uniform initial stresses Q and (b) uniform initial stresses P .

these two figures also reflect the relation between the wave speed and initial stress because of the fixed wave number. It can be seen that with the increase of the initial stresses in both directions, the frequency variation is not linear and the varying trends of each mode are different. The effects of the compressive stress and tensile stress do not always contrast. For instance, for mode 2, the highest frequency is at about the initial stress $Q = 0$ and $P = 0$; both compressive stress and tensile stress make the wave speed and frequency lower.

In the above examples, the initial stresses in the wave-propagation direction are uniform, that is, $P_1 = P_2 = P_3$. Now we illustrate the differences in the effects of P_1 and P_2 . In order to facilitate the comparison, we take an equal-thickness layered plate, N/N/N-1/1/1, as an example. We calculate three cases: $P_1 = P_2 = P_3 = 0$; $P_1 = -80$ GPa, $P_2 = P_3 = 0$; and $P_2 = -80$ GPa, $P_1 = P_3 = 0$. The obtained dispersion curves and the frequency-stress curves are shown in Figures 5 and 6. It can be seen that the effects of P_1 and P_2 are different. We cannot conclude that the effect of one is stronger than that of another one. For different modes, the extents of their influence are different, and vary as the frequency increases.

3.3. Effects of the initial stresses on SH waves. This section concerns the effects of the initial stresses on SH waves. Figures 7 and 8 show the dispersion curves for the N/S/N-1/2/1 plate under different uniform initial stresses P and Q . It can be seen that the effects of initial stresses are very regular. For the case of initial stress in the wave-propagation direction, compressive stress always makes the wave speed lower but tensile stress makes the wave speed higher. At small wavenumbers, the effect is weak. As the wavenumber increases, the effect becomes stronger. The effect of initial stresses Q is quite different from that of initial stresses P except that compressive stress still makes the wave speed lower. For a plate with the initial stress in the thickness direction, the effect of initial stresses does not change significantly as the wavenumber increases, but it becomes stronger as the mode order increases and it is very weak on the first mode.

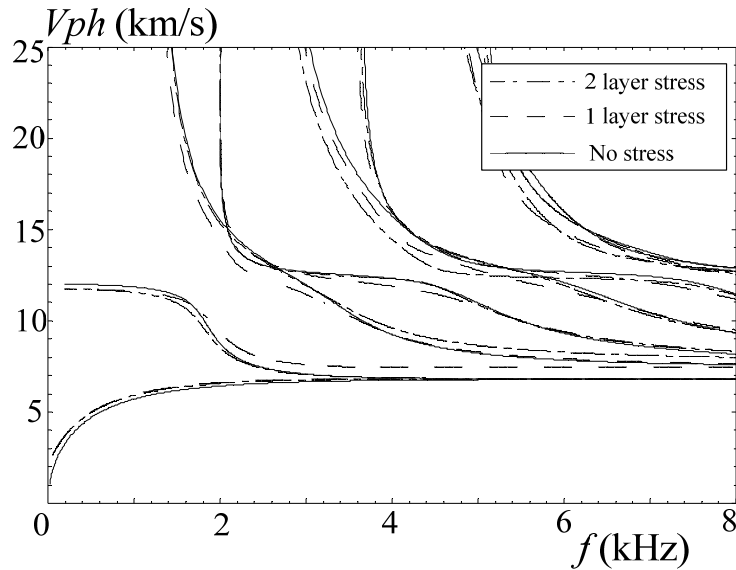


Figure 5. Lamb-like wave phase velocity spectra for the N/N/N-1/1/1 plate under initial stresses P ; 1 layer stress represents $P_1 = -80$ GPa, $P_2 = P_3 = 0$; and 2 layer stress represents $P_2 = -80$ GPa, $P_1 = P_3 = 0$.

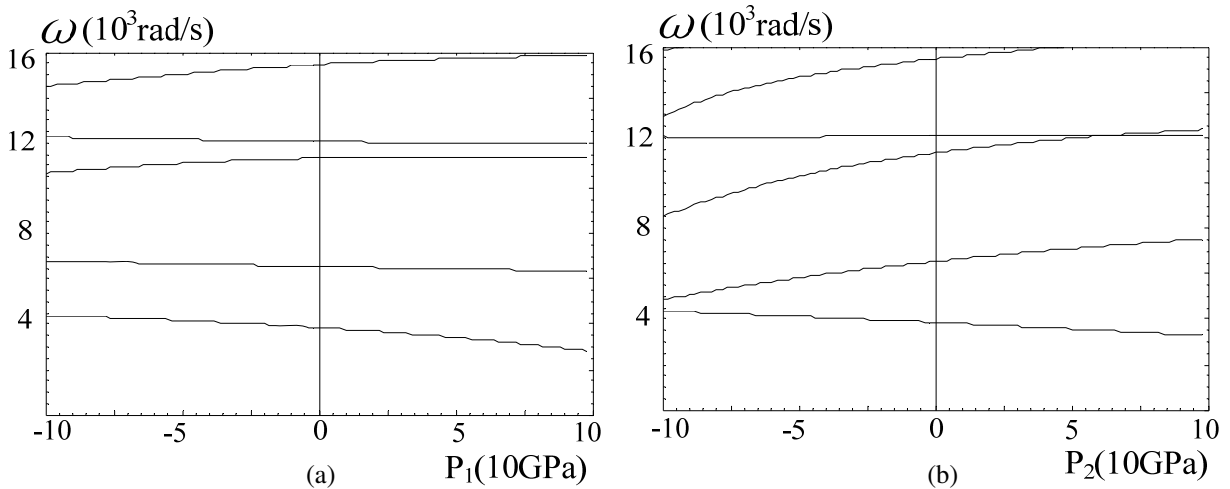


Figure 6. Lamb-like wave frequency curves versus initial stresses for the N/N/N-1/1/1 plate at $k = 1$ rad/m, with (a) initial stresses P_1 and (b) initial stresses P_2 .

Figure 9 illustrates the curves of frequency with initial stresses P and Q for the N/S/N-1/2/1 plate at $k = 1$ rad/m. It can be seen that with the increase of the initial stresses in both directions, the frequencies of all modes approximately linearly lower. The effect of compressive stress is entirely contrary to that of tensile stress. For the initial stresses in the wave-propagation direction, the slopes of the frequency curves

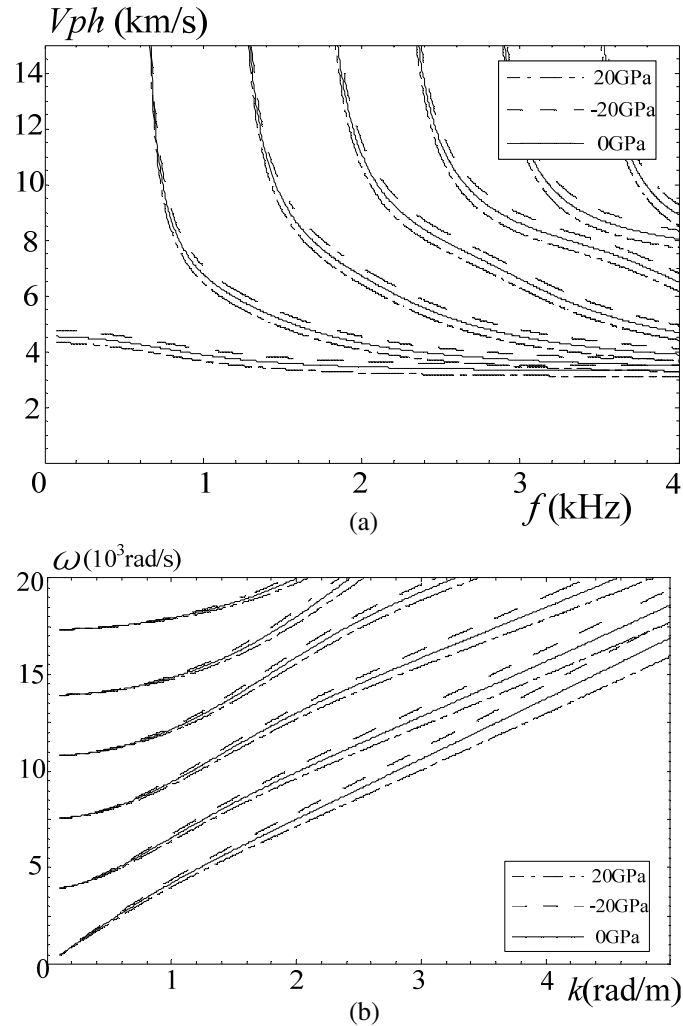


Figure 7. SH wave dispersion curves for the N/S/N-1/2/1 plate under uniform initial stresses P ; (a) phase velocity spectra and (b) frequency spectra.

for all modes are similar. For the initial stresses in the thickness direction, the slope of the frequency curve for the first mode is very small. As the mode order increases, the slope becomes larger.

4. Conclusions

Following [Biot 1965], guided wave propagation in layered plates under initial stresses in the thickness and wave-propagation directions are investigated. The Legendre polynomial series method is used to solve the coupled wave equations. The effects of the initial stresses on the dispersion curves are discussed. Based on the calculated results, the following conclusions can be drawn:

- (1) The effect of the initial stress on Lamb-like waves is quite different from that on the SH waves. The effect on SH waves is very regular.

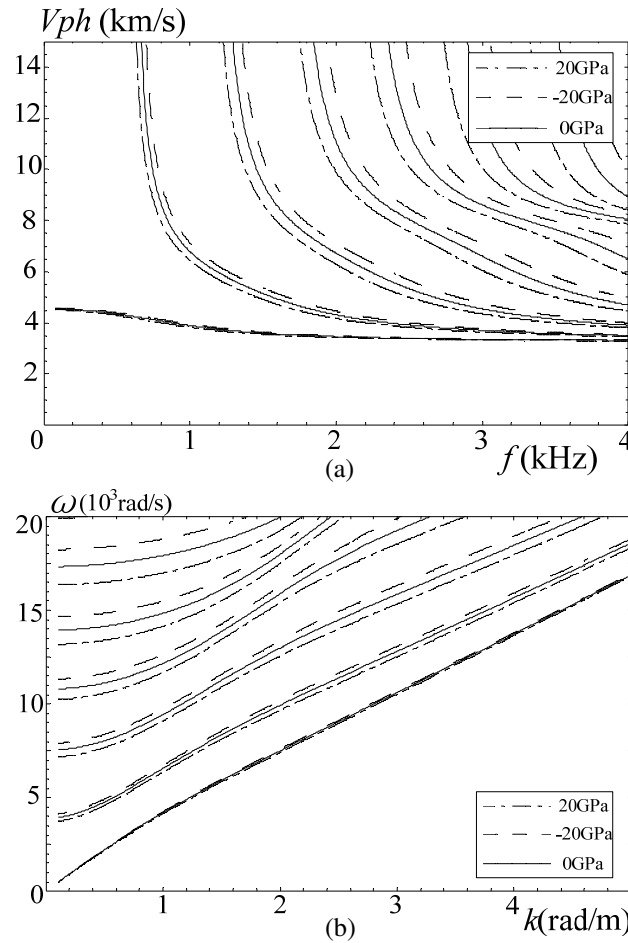


Figure 8. SH wave dispersion curves for the N/S/N-1/2/1 plate under initial stresses Q ; (a) phase velocity spectra and (b) frequency spectra.

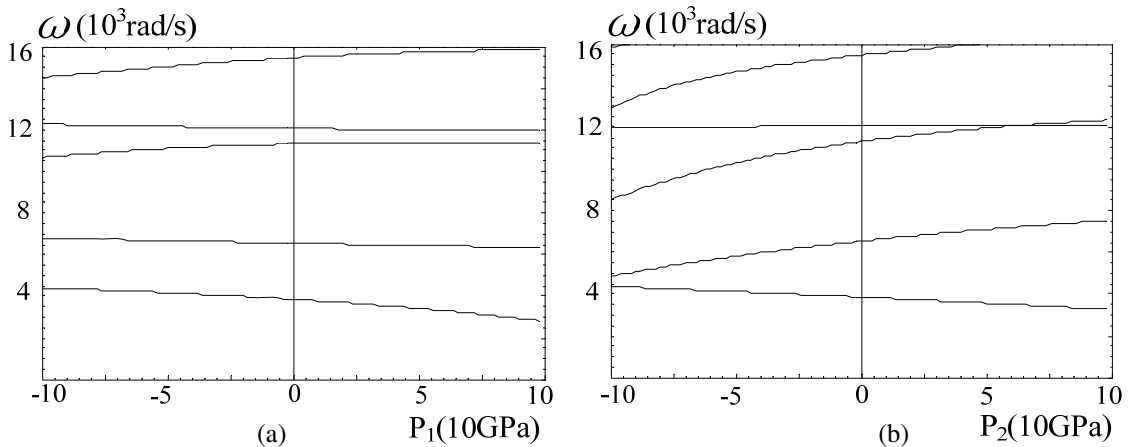


Figure 9. SH wave frequency curves versus initial stresses for the N/S/N-1/2/1 plate at $k = 1$ rad/m, with (a) uniform initial stresses Q and (b) uniform initial stresses P .

- (2) The effect of the compressive stress on Lamb-like waves is not always contrary to that of the tensile stress. But the effect of the compressive stress on SH waves is almost entirely contrary to that of the tensile stress.
- (3) For Lamb-like waves, the effect of the initial stress in the thickness direction usually is contrary to that of the initial stress in the wave-propagation direction. However, for SH waves, the effects of initial stresses in the two directions do not contrast, but their influential patterns are different.
- (4) For Lamb-like waves, with the increase of the initial stresses in both directions, the frequency variation is not linear and the varying trends of every mode are different. For SH waves, the curves of the frequency versus the stresses are approximately linear for all modes.

Acknowledgment

The work was supported by the National Natural Science Foundation of China (No. 11272115). Jiangong Yu gratefully acknowledges the support of the Alexander von Humboldt-Foundation for conducting research work at the university of Siegen, Germany.

References

- [Abd-Alla 1999] A. M. Abd-Alla, "The effect of initial stress and orthotropy on the propagation waves in a hollow cylinder", *Appl. Math. Comput.* **106**:2–3 (1999), 237–244.
- [Abd-Alla and Ahmed 1999] A. M. Abd-Alla and S. M. Ahmed, "Propagation of Love waves in a non-homogeneous orthotropic elastic layer under initial stress overlying semi-infinite medium", *Appl. Math. Comput.* **106**:2–3 (1999), 265–275.
- [Akbarov and Guliev 2009] S. D. Akbarov and M. S. Guliev, "Axisymmetric longitudinal wave propagation in a finite pre-strained compound circular cylinder made from compressible materials", *CMES Comput. Model. Eng. Sci.* **39**:2 (2009), 155–177.
- [Akbarov and Guliev 2010] S. D. Akbarov and M. S. Guliev, "The influence of the finite initial strains on the axisymmetric wave dispersion in a circular cylinder embedded in a compressible elastic medium", *International Journal of Mechanical Sciences* **52**:1 (2010), 89–95.
- [Akbarov et al. 2008] S. D. Akbarov, A. D. Zamanov, and E. R. Agasiyev, "On the propagation of Lamb waves in a sandwich plate made of compressible materials with finite initial strains", *Mechanics of Composite Materials* **44**:2 (2008), 155–164.
- [Akbarov et al. 2011a] S. D. Akbarov, E. R. Agasiyev, and A. D. Zamanov, "Wave propagation in a pre-strained compressible elastic sandwich plate", *European Journal of Mechanics A/Solids* **30**:3 (2011), 409–422.
- [Akbarov et al. 2011b] S. D. Akbarov, T. Kepceler, and M. M. Egilmez, "Torsional wave dispersion in a finitely pre-strained hollow sandwich circular cylinder", *Journal of Sound and Vibration* **330**:18–19 (2011), 4519–4537.
- [Bigoni et al. 2008] D. Bigoni, M. Gei, and A. B. Movchan, "Dynamics of a prestressed stiff layer on an elastic half space: filtering and band gap characteristics of periodic structural models derived from long-wave asymptotics", *J. Mech. Phys. Solids* **56**:7 (2008), 2494–2520.
- [Biot 1965] M. A. Biot, *Mechanics of incremental deformations: theory of elasticity and viscoelasticity of initially stressed solids and fluids, including thermodynamic foundations and applications to finite strain*, Wiley, New York, 1965.
- [Chen and Wright 1966] W. T. Chen and T. W. Wright, "Frequency equations for wave propagation in an initially stressed circular cylinder", *The Journal of the Acoustical Society of America* **39**:5A (1966), 847–848.
- [Datta and Hunsinger 1978] S. Datta and B. J. Hunsinger, "Analysis of surface waves using orthogonal functions", *Journal of Applied Physics* **49**:2 (1978), 475–479.
- [Du et al. 2007] J. Du, X. Jin, and J. Wang, "Love wave propagation in layered magneto-electro-elastic structures with initial stress", *Acta Mechanica* **192**:1–4 (2007), 169–189.

- [El-Naggar et al. 1994] A. M. El-Naggar, A. M. Abd-Alla, and S. M. Ahmed, “Rayleigh waves in a magnetoelastic initially stressed conducting medium with the gravity field”, *Bull. Calcutta Math. Soc.* **86**:3 (1994), 51–56.
- [Garg 2007] N. Garg, “Effect of initial stress on harmonic plane homogeneous waves in viscoelastic anisotropic media”, *J. Sound Vib.* **303**:3–5 (2007), 515–525.
- [Gei 2008] M. Gei, “Elastic waves guided by a material interface”, *Eur. J. Mech. A Solids* **27**:3 (2008), 328–345.
- [Gei et al. 2004] M. Gei, D. Bigoni, and G. Franceschini, “Thermoelastic small-amplitude wave propagation in nonlinear elastic multilayers”, *Mathematics and Mechanics of Solids* **9**:5 (2004), 555–568.
- [Gupta et al. 2012] S. Gupta, D. K. Majhi, S. Kundu, and S. K. Vishwakarma, “Propagation of torsional surface waves in a homogeneous layer of finite thickness over an initially stressed heterogeneous half-space”, *Appl. Math. Comput.* **218**:9 (2012), 5655–5664.
- [Kayestha et al. 2010] P. Kayestha, A. C. Wijeyewickrema, and K. Kishimoto, “Time-harmonic wave propagation in a pre-stressed compressible elastic bi-material laminate”, *Eur. J. Mech. A Solids* **29**:2 (2010), 143–151.
- [Murdoch 1977] A. I. Murdoch, “The effect of interfacial stress on the propagation of Stoneley waves”, *Journal of Sound and Vibration* **50**:1 (1977), 1–11.
- [Ogden and Sotiropoulos 1995] R. W. Ogden and D. A. Sotiropoulos, “On interfacial waves in pre-stressed layered incompressible elastic solids”, *Proc. Roy. Soc. London Ser. A* **450**:1939 (1995), 319–341.
- [Qian et al. 2004] Z. Qian, F. Jin, Z. Wang, and K. Kishimoto, “Love waves propagation in a piezoelectric layered structure with initial stresses”, *Acta Mech.* **171**:1–2 (2004), 41–57.
- [Rogerson and Sandiford 1996] G. A. Rogerson and K. J. Sandiford, “On small amplitude vibrations of pre-stressed laminates”, *International Journal of Engineering Science* **34**:8 (1996), 853–872.
- [Selim and Ahmed 2006] M. M. Selim and M. K. Ahmed, “Plane strain deformation of an initially stressed orthotropic elastic medium”, *Appl. Math. Comput.* **175**:1 (2006), 221–237.
- [Shmuel et al. 2012] G. Shmuel, M. Gei, and G. deBotton, “The Rayleigh–Lamb wave propagation in dielectric elastomer layers subjected to large deformations”, *International Journal of Non-linear Mechanics* **47**:2 (2012), 307–316.
- [Wijeyewickrema and Leungvichcharoen 2009] A. C. Wijeyewickrema and S. Leungvichcharoen, “Wave propagation in pre-stressed imperfectly bonded compressible elastic layered composites”, *Mechanics of Materials* **41**:10 (2009), 1192–1203.
- [Zamanov and Agasiyev 2011] A. D. Zamanov and E. R. Agasiyev, “Dispersion of lamb waves in a three-layer plate made from compressible materials with finite initial deformations”, *Mechanics of Composite Materials* **46**:6 (2011), 583–592.

Received 26 Oct 2012. Revised 31 Jan 2013. Accepted 31 Jan 2013.

JIANGONG YU: yu@emails.bjut.edu.cn

School of Mechanical and Power Engineering, Henan Polytechnic University, Jiaozuo, 454003 Henan, China

SHENLEI LI: 982368392@qq.com

School of Mechanical and Power Engineering, Henan Polytechnic University, Jiaozuo, 454003 Henan, China

EMPIRICAL MODELS FOR PREDICTING PROTECTIVE PROPERTIES OF CONCRETE SHIELDS AGAINST HIGH-SPEED IMPACT

GABI BEN-DOR, ANATOLY DUBINSKY AND TOV ELPERIN

We have accumulated practically all the information available in the literature regarding empirical models used for describing high-speed normal penetration of rigid strikers into concrete shields, including recently posed models. The description of the models is unified; this includes recommendations on the range of applicability of the models and additional restrictions implied by the used mathematical formulations. The description of the models is quite comprehensive, and allows their direct application. All the relevant formulas are presented in SI units. In addition to this extensive survey we include the results of original comparative investigations on the performance of various models for describing penetration into semiinfinite and finite-thickness shields.

Nomenclature

b	Thickness of the shield
b_{perf}	Perforation thickness
b_{scab}	Scabbing thickness
BLV	Ballistic limit velocity
c	Maximum aggregate size of concrete
c_{\times}	Half-size of the concrete aggregate
CRH	Caliber radius head of a ogive-nosed projectile
d	Maximum diameter of impactor, reference size
DOP	Depth of penetration
\bar{e}	Parameter, (24)
E	Young's modulus of material of projectile
E_{steel}	Young's modulus of steel
f'_c	Unconfined compressive strength (Pa)
H	Depth of penetration
$\bar{H}_{\text{min}}^{(i)}, \bar{H}_{\text{max}}^{(i)}$	Parameters in functions $\Psi_{\text{perf}}(\bar{H})$ and $\Psi_{\text{scab}}(\bar{H})$, (A.1)
$\bar{H}_*^{(i)}$	Parameter, (A.4)
H_{exp}	DOP obtained in experiment

Keywords: protection, concrete, shield, penetration, impact, scabbing, perforation, ballistic limit.

I	Parameter, (36)
I_*	Parameter, (45)
$I_{\min}^{(i)}, I_{\max}^{(i)}$	Parameters of penetration model, (35)
J	Parameter defined in (39)
K_{CRH}	$= \rho_{\text{og}}/(2R)$, CRH of the ogive-nosed projectile
K_{shape}	Nose shape coefficient of impactor in Young's model
$K_{\text{shape}}^{(1)}$	Nose shape coefficient of impactor, (18)
$K_{\text{shape}}^{(2)}$	Nose shape coefficient of impactor, (25)
$K_{\text{shape}}^{(3)}$	Nose shape coefficient of impactor, (54)
$K_{\text{shape}}^{(4)}$	Nose shape coefficient of impactor, (39)
m	Mass of impactor
v_{imp}	Impact velocity
v_{res}	Residual velocity
v_0	Reference velocity, 1000 m/s
v_{sl}	Scabbing limit velocity
v_{bl}	Ballistic limit velocity
$\alpha_{\text{pen}}, \beta_{\text{pen}}, \gamma_{\text{pen}}$	Parameters of penetration model, (41)
$\alpha_{\text{perf}}, \beta_{\text{perf}}, \gamma_{\text{perf}}$	Parameters of perforation model, (42)
$\alpha_{\text{scab}}, \beta_{\text{scab}}, \gamma_{\text{scab}}$	Parameters of scabbing model, (43)
$\alpha^{(i)}, \beta^{(i)}, \gamma^{(i)}$	Parameters in functions $\Psi_{\text{perf}}(\bar{H})$ and $\Psi_{\text{scab}}(\bar{H})$, (A.1)
$\tilde{\alpha}_{\text{pen}}^{(i)}, \tilde{\beta}_{\text{pen}}^{(i)}$	Parameters of penetration model, (35)
μ	Parameter of model (can be different for different models)
$\tilde{\mu}$	Parameter, (36)
$\bar{\mathcal{E}}_{\text{perf}}$	Function determining dependence on \bar{b}_{perf} versus \bar{v}_{imp}
$\bar{\mathcal{E}}_{\text{scab}}$	Function determining dependence on \bar{b}_{scab} versus \bar{v}_{imp}
ρ_{sh}	Density of concrete
ρ_{og}	Radius of the arc of the ogive
ϕ	Function determining dependence on \bar{H} versus \bar{v}_{imp}
Ψ_{perf}	Function determining dependence on \bar{b}_{perf} versus \bar{H}
Ψ_{scab}	Function determining dependence on \bar{b}_{scab} versus \bar{H}

A bar over a parameter indicates a dimensionless parameter. Parameters having dimensions of length are normalized by the diameter of impactor d while parameters having dimensions of velocity are normalized by the characteristic velocity $v_0 = 1000$ m/s.

1. Introduction

Hereafter we use the term “empirical model” for formulas describing penetration which have been obtained by statistical analysis of experimental results and are not based on physical laws. Relations between “integral characteristics” of penetration, namely, the impact velocity and the depth of penetration (DOP) for a semiinfinite shield and the ballistic limit velocity (BLV) and the thickness of the plate for a shield having a finite thickness, are examples of these empirical models.

Engineering models of penetration into concrete shields, including empirical models, can be found in the dedicated surveys [Kennedy 1976; Adeli and Amin 1985; Williams 1994; Teland 1998; Li et al. 2005]. Reviews and research papers [Walter and Wolde-Tinsae 1984; Brown 1986; Corbett et al. 1996; Dancygier and Yankelevsky 1996; Yankelevsky 1997; Dancygier 2000; Linderman et al. 1974; Ben-Dor et al. 2005; Vossoughi et al. 2007; Guirgis and Guirguis 2009; Daudeville and Malécot 2011], monographs [Bulson 1997; Bangash and Bangash 2006; Ben-Dor et al. 2006; Carlucci and Jacobson 2007; Bangash 2009; Szuladziński 2009], and a publication of the Department of Energy [2006] also include information on this topic. Few of the studies compare predictions of models with experimental results.

In this study we have accumulated practically all the available information in the literature regarding empirical models which are used for describing high-speed normal penetration of rigid strikers into concrete shields, including models formulated in recent years. This comprehensive survey also has the following characteristics: the description of the models is unified; it includes recommendations on the range of applicability of the models and additional restrictions implied by the used mathematical formulations; the descriptions of the models are quite comprehensive, allowing for their direct application; and all the relevant formulas are presented in SI units.

In addition to this extensive survey we include the results of original comparative investigations on the performance of various models for describing penetration into semiinfinite and finite-thickness shields.

2. Basic definitions

The local response of a shield is initiated with spalling (Figure 1a) and subsequently can result in penetration, scabbing of the shield material from the back face of the shield (Figure 1b), and eventual perforation of the shield (Figure 1c), transporting the projectile through the shield [DOE 2006].

We consider normal penetration (with zero angle of attack) of rigid (nondeformable) projectiles into a shield. If otherwise not indicated, we consider lightly reinforced concrete shields and flat-nosed projectiles. Formulas given for projectiles with a circular cross-section may be applied for projectiles having more complicated shapes by replacing the diameter by the equivalent diameter, based on the perimeter [Walter and Wolde-Tinsae 1984; Barr 1990].

Hereafter the following definitions are used [Kennedy 1976; DOE 2006].

The *depth of penetration (DOP)*, H , is defined as the depth to which a projectile penetrates into a massive (semiinfinite) concrete shield, for a given impact velocity.

The *scabbing thickness*, b_{scab} , for a given impact velocity, is defined as the shield thickness that is just large enough to prevent the peeling off of the back face of the panel opposite the face of impact. In other words, scabbing thickness is the minimum thickness of the shield required to prevent scabbing.

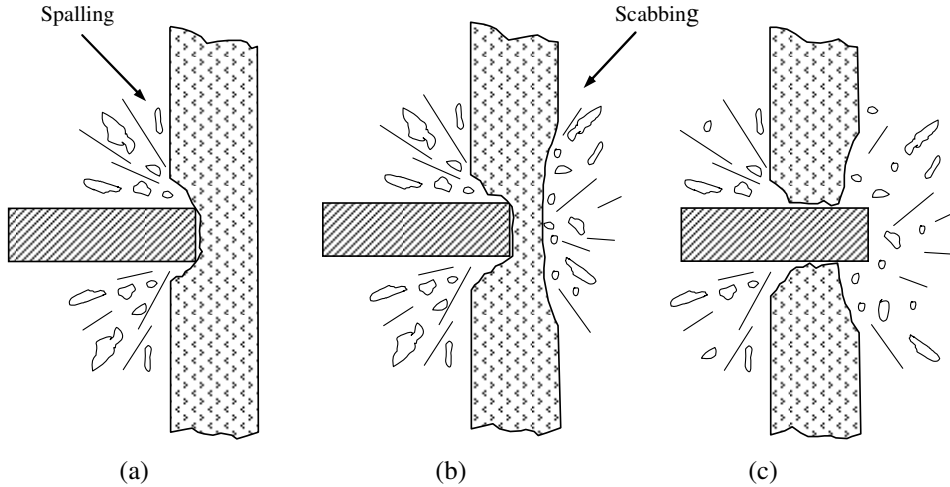


Figure 1. Local response of a shield: (a) penetration and spalling, (b) scabbing, and (c) perforation.

The *perforation thickness*, b_{perf} , for a given impact velocity, is defined as the shield thickness that is just large enough to allow a missile to emerge from the back face of the shield with zero exit velocity. In other words, the perforation thickness is the minimum thickness of the shield required to prevent perforation.

The *ballistic limit velocity (BLV)*, v_{bl} , is defined as the minimum impact (initial) velocity required to perforate a shield with a given thickness.

Similarly to the BLV, we introduce the *scabbing limit velocity*, v_{sl} , as the minimum impact (initial) velocity required for scabbing a shield with a given thickness.

Note that [DOE 2006] recommends, for practical calculations of the shield thicknesses that prevent scabbing and perforation, using values of b_{scab} and b_{perf} obtained from empirical formulas and increased by 10% and 20%, respectively.

We assume that $b_{\text{scab}} < b_{\text{perf}}$ in the range of validity of the models.

3. Unified approach

An empirical model is determined by a triad of equations having the form

$$\bar{H} = \phi(\bar{v}_{\text{imp}}), \quad \bar{b}_{\text{perf}} = \Psi_{\text{perf}}(\bar{H}), \quad \bar{b}_{\text{scab}} = \Psi_{\text{scab}}(\bar{H}), \quad (1)$$

where ϕ , Ψ_{perf} , and Ψ_{scab} are known functions. Analysis of penetration into a finite-thickness shield involves the DOP into a semiinfinite shield, which is not directly related with the problem. Therefore, it is convenient to present the model for a finite-thickness shield by a pair of equations that are obtained after eliminating \bar{H} from (1):

$$\bar{b}_{\text{perf}} = \Xi_{\text{perf}}(\bar{v}_{\text{imp}}), \quad \bar{b}_{\text{scab}} = \Xi_{\text{scab}}(\bar{v}_{\text{imp}}), \quad (2)$$

where

$$\Xi_{\text{perf}}(z) = \Psi_{\text{perf}}(\phi(z)), \quad \Xi_{\text{scab}}(z) = \Psi_{\text{scab}}(\phi(z)). \quad (3)$$

Taking into account that Ξ_{perf} and Ξ_{scab} are increasing functions, (2) and (3) yield the formulas for \bar{v}_{bl} and \bar{v}_{sl} :

$$\bar{v}_{\text{bl}} = \Xi_{\text{perf}}^{-1}(\bar{b}), \quad \bar{v}_{\text{sl}} = \Xi_{\text{scab}}^{-1}(\bar{b}). \tag{4}$$

Figure 2 illustrates the derivation of the first relationship in (4). The curve described by the equation $\bar{b} = \Xi_{\text{perf}}(\bar{v}_{\text{imp}})$ separates the domain of parameters \bar{v}_{imp} and \bar{b} into two subdomains. The subdomain under the curve corresponds to perforation of the shield while the subdomain above the curve corresponds to nonperforation. Let \bar{b}_0 be an arbitrary thickness of the shield. Inspection of Figure 2 shows that the minimum value of \bar{v}_{imp} for which perforation occurs (by definition this value equals the BLV) is $\Xi_{\text{perf}}^{-1}(\bar{b}_0)$, and, consequently, the first relationship in (4) is valid. The validity of the second relationship in (4) can be proved similarly.

Therefore a model for a plate having a finite thickness is determined by a pair of relationships given by (2) or (4). Hereafter we use this fact for shortening descriptions of models.

Some typical classes of penetration models are considered in the Appendix. This will allow us in describing particular models to present only the values of the coefficients and avoid rewriting bulky formulas.

4. Modified Pétry formulas

The Pétry formula [Pétry 1910] has a modified version [Kennedy 1976] which can be written similarly to [Li et al. 2005]:

$$\bar{H} = \phi(\bar{v}_{\text{imp}}) = \frac{0.0795K_p m}{d^3} \log_{10}(1 + 50\bar{v}_{\text{imp}}^2), \tag{5}$$

where K_p is a coefficient depending on the type of the concrete. The coefficients in (5) are selected so that the dimensional parameters m and d are measured in SI units while British units (ft³/lb) are retained for K_p in order to use generally adopted values of this parameter.

Amirikian [1950], with reference to [Samuely and Hamann 1939], prescribed the following values of the parameter K_p for different types of concrete: 0.00799 for massive concrete, 0.00426 for normal reinforced concrete, and 0.00284 for specially reinforced concrete. This version of the model is called the

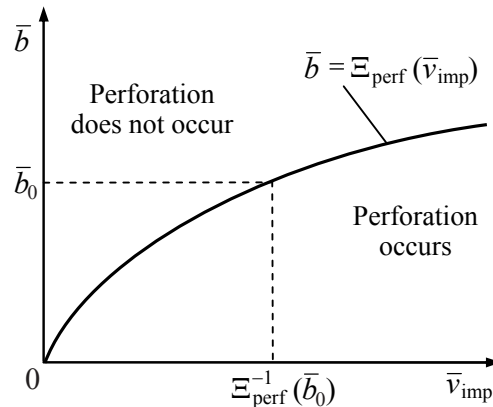


Figure 2. BLV and perforation thickness.

modified Pétry I model by Kennedy [1976], who recommended using an additional dependence between K_p and f'_c . For reinforced concrete this dependence has been presented in a graphical form in [Kennedy 1976], in what is called a modified Pétry II model. A convenient analytical form of this dependence was suggested in [Walter and Wolde-Tinsae 1984]:

$$K_p = 6.34 \cdot 10^{-3} \exp(-0.2937 \cdot 10^{-7} f'_c). \quad (6)$$

Amirikian [1950] suggested taking into account the thickness of the shield when the DOP is calculated. He recommended using (5) if $\bar{b} \geq 3\bar{H}$, assumed that perforation begins when $\bar{b} = 2\bar{H}$, that is,

$$\bar{b}_{\text{perf}} = \Psi_{\text{perf}}(\bar{H}) = 2\bar{H}, \quad (7)$$

and proposed, instead of (5), the following expression for the DOP, \bar{H}_\times , in the intermediate domain, $2\bar{H} \leq \bar{b} \leq 3\bar{H}$:

$$\bar{H}_\times = \Lambda(\bar{H}) = [1 + \exp(4(\bar{b}/\bar{H} - 2))]\bar{H}. \quad (8)$$

Kennedy [1976] proposed using the modified Pétry formulas for the scabbing thickness:

$$\bar{b}_{\text{scab}} = \Psi_{\text{scab}}(\bar{H}) = 2.2\bar{H}. \quad (9)$$

Equations (7) and (9) can be written in the form given by (A.5) with the following coefficients: $\alpha_{\text{perf}}^{(1)} = \alpha_{\text{scab}}^{(1)} = \gamma_{\text{perf}}^{(1)} = \gamma_{\text{scab}}^{(1)} = 0$, $\beta_{\text{perf}}^{(1)} = 2.0$, $\beta_{\text{scab}}^{(1)} = 2.2$, and $n = 1$.

Taking into account the modifications proposed by Amirikian [1950] the expression for the DOP for a shield with thickness \bar{b} can be written as

$$\bar{H}_\times = \begin{cases} \phi(\bar{v}_{\text{imp}}) & \text{if } \bar{v}_{\text{imp}} \leq \phi^{-1}(\bar{b}/3), \\ \Lambda(\phi(\bar{v}_{\text{imp}})) & \text{if } \phi^{-1}(\bar{b}/3) < \bar{v}_{\text{imp}} < \phi^{-1}(\bar{b}/2), \\ \text{perforation} & \text{if } \bar{v}_{\text{imp}} \geq \phi^{-1}(\bar{b}/2). \end{cases} \quad (10)$$

Other basic ballistic characteristics are determined by (A.5), (A.6), and (A.9). Amde et al. [1997] presented the following the Pétry formula for the residual velocity referring to Gilbert Associates:

$$v_{\text{res}} = v_{\text{imp}} \sqrt{1 - (0.5b/H)}. \quad (11)$$

It should be noted that classifying the Pétry formulas, (5), as empirical models is done here partly in order to follow tradition. Indeed, their form implies that these formulas were derived by integrating the equation of motion of the penetrator under the assumption of two-term quadratic dependence (without the linear term) of drag force on velocity.

5. Ballistic research laboratory (BRL) formulas

The BRL formula does not take into account the influence of the unconfined compressive strength on the protective properties of a shield, and the value $f'_c = 20.7$ MPa was assumed [Kennedy 1976]. In order to remedy this shortcoming the modified BRL formula was suggested. Kennedy [1976] emphasized that this modified formula, in contrast to the common approach, directly predicts the perforation thickness:

$$\bar{b}_{\text{perf}} = \Xi_{\text{perf}}(\bar{v}_{\text{imp}}) = \frac{13m}{d^{2.8} \sqrt{f'_c}} \bar{v}_{\text{imp}}^{1.33}, \quad (12)$$

while the scabbing thickness can be estimated as

$$\bar{b}_{\text{scab}} = 2\bar{b}_{\text{perf}}. \tag{13}$$

The BLV and scrubbing limit velocity can be calculated using the formulas

$$\bar{v}_{\text{bl}} = \Xi_{\text{perf}}^{-1}(\bar{b}), \quad \bar{v}_{\text{sl}} = \Xi_{\text{perf}}^{-1}(\bar{b}/2). \tag{14}$$

Chelapati et al. [1972] obtained a similar result starting from the expression for the DOP. Their formula for the DOP, \bar{H} , coincides with the right-hand side of (12) divided by 1.3, which yields $\bar{b}_{\text{perf}} = 1.3\bar{H}$.

6. Whiffen formula

Bulson [1997], with reference to [Whiffen 1943], suggested the model

$$\bar{H} = \phi(\bar{v}_{\text{imp}}) = \frac{2.6m}{d^3 \bar{c}^{0.1} \sqrt{f'_c}} (1.87\bar{v}_{\text{imp}})^{\bar{n}}, \quad \bar{n} = \frac{97.5}{\sqrt[4]{f'_c}}, \quad \bar{c} = \frac{c}{d}, \tag{15}$$

where c is the maximum aggregate size of concrete.

The latter equation is based on experiments with ogival-nosed projectiles conducted for the following ranges of parameters: $0.8 \leq K_{\text{CRH}} \leq 3.5$, $5 \text{ MPa} < f'_c < 70 \text{ MPa}$, $12 \text{ mm} < d < 965 \text{ mm}$, $0.02 < \bar{c} < 2$, $v_{\text{imp}} < 1130 \text{ m/s}$, $136 \text{ g} < m < 10,000 \text{ kg}$. This formula fits the experimental data within a scatter band of the order of $\pm 15\%$.

Note that Teland [1998] referred to this model as the ‘‘TBAA formula’’.

7. Army corporations of engineers (ACE) formula

The ACE formula [ACE 1946; Gwaltney 1968], written using variables \bar{H} and \bar{v}_{imp} and SI units, reads

$$\bar{H} = \phi(\bar{v}_{\text{imp}}) = \frac{11.1m}{d^{2.785} \sqrt{f'_c}} \bar{v}_{\text{imp}}^{1.5} + 0.5. \tag{16}$$

There are two versions of the dependencies between the perforation/scabbing thickness and the DOP which differ only slightly [Gwaltney 1968; Chelapati et al. 1972; Li et al. 2005]. Following [Kennedy 1976] we have selected the version of this formula with the coefficients shown in Table 1, which is associated with the model given by (A.1).

Formulas for the other basic ballistic characteristics are given by (A.5), (A.6), and (A.9).

	$\alpha^{(1)}$	$\beta^{(1)}$	$\gamma^{(1)}$	$\bar{H}_{\text{min}}^{(1)}$	$\bar{H}_{\text{max}}^{(1)}$
Perforation	1.24	1.32	0	1.35	13.5
Scabbing	1.36	2.12	0	0.65	11.75

Table 1. ACE model for perforation and scabbing. Coefficients in (A.1), $n = 1$.

8. Ammann and Whitney formula

The Ammann and Whitney formula was suggested for predicting perforation by small explosively generated fragments having impact velocity larger than 300 m/s [Kennedy 1976]:

$$\bar{H} = \phi(\bar{v}_{\text{imp}}) = \frac{15K_{\text{shape}}^{(1)}m}{d^{2.8}\sqrt{f_c}}\bar{v}_{\text{imp}}^{1.8}, \quad (17)$$

where

$$K_{\text{shape}}^{(1)} = \begin{cases} 0.72 & \text{for a flat nose,} \\ 0.84 & \text{for a blunt nose,} \\ 1.00 & \text{for an average nose (spherical end),} \\ 1.14 & \text{for a very sharp nose.} \end{cases} \quad (18)$$

9. Modified national defense research committee (NDRC) formula

The modified NDRC formula can be written in a commonly accepted form as an implicit function with respect to the DOP [NDRC 1946; Kennedy 1976]. Using the dimensionless variables \bar{H} and \bar{v}_{imp} and SI units for the dimensional parameters this formula reads

$$G(\bar{H}) = \mu\bar{v}_{\text{imp}}^{1.8}, \quad (19)$$

where

$$\mu = 9.55 \frac{K_{\text{shape}}^{(1)}m}{d^{2.8}\sqrt{f_c}}, \quad (20)$$

$$G(\bar{H}) = \begin{cases} 0.25\bar{H}^2 & \text{if } \bar{H} \leq 2, \\ \bar{H} - 1 & \text{if } \bar{H} > 2, \end{cases} \quad (21)$$

and the effect of the unconfined compressive strength is included in the model following the suggestion of Kennedy [1976].

In the universal form given by (1), this model can be rewritten as

$$\bar{H} = \phi(\bar{v}_{\text{imp}}) = \begin{cases} 2\sqrt{\mu}\bar{v}_{\text{imp}}^{0.9} & \text{if } \bar{v}_{\text{imp}} \leq 1/\mu^{5/9}, \\ \mu\bar{v}_{\text{imp}}^{1.8} + 1 & \text{if } \bar{v}_{\text{imp}} > 1/\mu^{5/9}. \end{cases} \quad (22)$$

The modified NDRC model for perforation and scabbing [Kennedy 1976] can be written in the form of (A.1) with coefficients from Table 2. The dependencies \bar{b}_{perf} and \bar{b}_{scab} versus \bar{v}_{imp} as well as \bar{v}_{bl} and \bar{v}_{sl} versus \bar{b} are given by (A.5)–(A.9), where

$$\phi^{-1}(z) = \begin{cases} (0.5z/\sqrt{\mu})^{10/9} & \text{if } z \leq 2, \\ [(z-1)/\mu]^{5/9} & \text{if } z \geq 2. \end{cases} \quad (23)$$

Inspection of Table 2 shows that the inequalities given by (A.4) are satisfied.

	i	$\beta^{(i)}$	$\alpha^{(i)}$	$\gamma^{(i)}$	$\bar{H}_{\min}^{(i)}$	$\bar{H}_{\max}^{(i)}$	$\bar{H}_*^{(i)}$
Perforation	1	0	3.19	0.718	–	1.35	2.22
	2	1.32	1.24	0	1.35	13.5	–
Scabbing	1	0	7.91	5.06	–	0.65	0.78
	2	2.12	1.36	0	0.65	11.75	–

Table 2. Modified NDRC model for perforation and scabbing. Coefficients in (A.1), $n = 2$.

According to [DOE 2006], the NDRC formula was derived for the following ranges of impact parameters: $v_{\text{imp}} > 152$ m/s, 2.54 cm $< b < 40.6$ cm and $b/d \geq 3$. However, as suggested by Kennedy [1976], this formula can be extrapolated beyond these ranges.

10. Kar's formula

Kar's formula [Kar 1978; Bangash and Bangash 2006] is an improved modified NDRC formula that takes into account the size of the aggregates of concrete and the type of the projectile material.

In the universal form given by (1), Kar's formula is given by (22) where

$$\mu = 9.55 \frac{K_{\text{shape}}^{(2)} m \bar{e}^{6.25}}{d^{2.8} \sqrt{f_c^i}}, \quad \bar{e} = \left(\frac{E}{E_{\text{steel}}} \right)^{0.2}, \quad (24)$$

and E and E_{steel} are the Young's moduli of the material of the projectile and steel. The nose shape parameter, $K_{\text{shape}}^{(2)}$, is calculated as

$$K_{\text{shape}}^{(2)} = \begin{cases} 0.72 & \text{for a flat-nosed projectile,} \\ \min(\hat{K}_{\text{nose}}, 1.17) & \text{for an ogive-nosed projectile,} \end{cases} \quad (25)$$

where

$$\hat{K}_{\text{nose}} = 0.72 + 0.25 \sqrt{K_{\text{CRH}} - 0.25}. \quad (26)$$

Kar's model for perforation and scabbing can be written in the form of (A.1) where the coefficients are presented in Table 3 and \bar{c}_x is the half-size of the concrete aggregate.

The dependence of \bar{b}_{perf} and \bar{b}_{scab} on \bar{v}_{imp} , and of \bar{v}_{bl} and \bar{v}_{sl} on \bar{b} , is given by (A.5)–(A.9) with $\phi^{-1}(z)$ calculated from (23).

	i	$\beta^{(i)}$	$\alpha^{(i)}$	$\gamma^{(i)}$	$\bar{H}_{\min}^{(i)}$	$\bar{H}_{\max}^{(i)}$	$\bar{H}_*^{(i)}$
Perforation	1	\bar{c}_x	3.19	0.718	–	1.35	2.22
	2	$\bar{c}_x + 1.32$	1.24	0	1.35	13.5	–
Scabbing	1	\bar{c}_x	$7.91\bar{e}$	$5.06\bar{e}$	–	0.65	0.71
	2	$\bar{c}_x + 2.12\bar{e}$	$1.36\bar{e}$	0	0.65	11.75	–

Table 3. Kar's model for perforation and scabbing. Coefficients in (A.1), $n = 2$.

11. Healey–Weissman formula

The Healey–Weissman penetration formula [Healey and Weissman 1974; Li et al. 2005] can be considered as a version of Kar’s formula where the expression for μ given by (24) is replaced by

$$\mu = 10.95 \left(\frac{E}{E_{\text{steel}}} \right) \frac{K_{\text{shape}}^{(2)} m}{d^{2.8} \sqrt{f'_c}}. \quad (27)$$

The formula for the residual velocity reads [Healey et al. 1975; Kar 1979]:

$$\frac{v_{\text{res}}}{v_{\text{imp}}} = \begin{cases} [1 - (b/b_{\text{perf}})^2]^{0.555} & \text{if } b \leq 2d, \\ [1 - (b/b_{\text{perf}})]^{0.555} & \text{if } b > 2d. \end{cases} \quad (28)$$

12. Bechtel formula

The Bechtel Corporation proposed the following formula for scabbing thickness that is valid for a hard cylindrical projectile [Rotz 1975; 1977; Bangash and Bangash 2006]:

$$\bar{b}_{\text{scab}} = \Xi_{\text{scab}}(\bar{v}_{\text{imp}}) = \frac{1.23 \cdot 10^3 m^{0.4}}{d^{1.2} \sqrt{f'_c}} \bar{v}_{\text{imp}}^{0.5}. \quad (29)$$

This equation is based on twelve tests with solid missiles and nine tests with half-pipe missiles. The tests were conducted for the following ranges of parameters: [Teland 1998]: $37 \text{ m/s} < v_{\text{imp}} < 144 \text{ m/s}$, $20.3 \text{ cm} < d < 21.8 \text{ cm}$, and $30.5 \text{ cm} < b < 61 \text{ cm}$; and $7.6 \text{ cm} < b < 22.9 \text{ cm}$, $30 \text{ MPa} < f'_c < 40 \text{ MPa}$, and $3.6 \text{ kg} < m < 97.1 \text{ kg}$.

13. Stone and Webster formula

The following formula was proposed for calculating the scabbing thickness [Jankov et al. 1977; Li et al. 2005; Bangash and Bangash 2006]:

$$\bar{b}_{\text{scab}} = \Xi_{\text{scab}}(\bar{v}_{\text{imp}}) = \frac{100}{d} \left(\frac{m}{K_{\bar{b}}} \right)^{1/3} \bar{v}_{\text{imp}}^{2/3}, \quad (30)$$

where $K_{\bar{b}}$ is the dimensionless coefficient which can be approximated by the formula [Li et al. 2005]

$$K_{\bar{b}} = 0.013\bar{b} + 0.33, \quad 1.5 \leq \bar{b} \leq 3. \quad (31)$$

The equation is based on seven tests with solid missiles and 21 tests with half-pipe missiles. The tests were conducted for the following ranges of parameters [Teland 1998]: $27 \text{ m/s} < v_{\text{imp}} < 157 \text{ m/s}$, $4.1 \text{ cm} < d < 8.9 \text{ cm}$, $11.4 \text{ cm} < b < 15.2 \text{ cm}$, $22 \text{ MPa} < f'_c < 30 \text{ MPa}$, and $1.9 \text{ kg} < m < 12.8 \text{ kg}$.

14. CEA-EDF formula

The CEA-EDF (Commissariat à l’énergie atomique et Électricité de France) formula [Berriaud et al. 1978] reads:

$$\bar{b}_{\text{perf}} = \Xi_{\text{perf}}(\bar{v}_{\text{imp}}) = \frac{146m^{0.5}}{d^{1.5} (f'_c)^{0.375} \rho_c^{0.125}} \bar{v}_{\text{imp}}^{0.75}, \quad (32)$$

where ρ_{sh} is the density of concrete.

This model is valid in the following ranges of parameters: $v_{\text{imp}} < 200$ m/s, $150 \text{ kg/m}^3 < \rho_{\text{sh}} < 300 \text{ kg/m}^3$, $20 \text{ kg} < m < 300 \text{ kg}$, $0.35 < b/d < 4.17$, and $23 \text{ MPa} < f'_c < 46 \text{ MPa}$.

15. Degen's formula

Based on the available experimental data, Degen [1980] suggested a formula for the perforation thickness that can be written in the form given by (A.1) with the coefficients shown in Table 4, where \bar{H} is determined from the modified NDRC model, (22). The dependence \bar{v}_{sl} versus \bar{b} is given by (A.6) where $\phi^{-1}(z)$ is determined by (23).

The tests were conducted in the following ranges of parameters: $25 \text{ m/s} < v_{\text{imp}} < 310 \text{ m/s}$, $15 \text{ kg} < m < 134 \text{ kg}$, $28 \text{ MPa} < f'_c < 43 \text{ MPa}$, $10 \text{ cm} < d < 31 \text{ cm}$, and $15 \text{ cm} < b < 60 \text{ cm}$. The concrete reinforcement varied in the range between 160 kg/m^3 and 350 kg/m^3 , and penetrators having flat, conical, and hemispherical nose shapes were used.

16. Chang's formula

Chang's formulas [Chang 1981] for flat-nosed projectiles penetrating into a reinforced concrete shield read:

$$\bar{b}_{\text{perf}} = \Xi_{\text{perf}}(\bar{v}_{\text{imp}}) = \frac{497}{d^{1.5}} \sqrt{\frac{m}{f'_c}} \bar{v}_{\text{imp}}^{0.75}, \quad (33)$$

$$\bar{b}_{\text{scab}} = \Xi_{\text{scab}}(\bar{v}_{\text{imp}}) = \frac{321}{d^{1.2}} \left(\frac{m}{f'_c}\right)^{0.4} \bar{v}_{\text{imp}}^{2/3}. \quad (34)$$

These formulas are based on experiments conducted in the following ranges of parameters: $17 \text{ m/s} < v_{\text{imp}} < 312 \text{ m/s}$, $110 \text{ g} < m < 344 \text{ kg}$, $23 \text{ MPa} < f'_c < 46 \text{ MPa}$, $5.1 \text{ cm} < b < 61 \text{ cm}$, and $2 \text{ cm} < d < 30.5 \text{ cm}$.

17. Haldar–Miller formula

The Haldar–Miller model for penetration [Haldar and Miller 1982] can be described as

$$\bar{H} = \phi(\bar{v}_{\text{imp}}) = \begin{cases} \tilde{\alpha}_{\text{pen}}^{(1)} I + \tilde{\beta}_{\text{pen}}^{(1)} & \text{if } \sqrt{I_{\text{min}}^{(1)}/\tilde{\mu}} \leq \bar{v}_{\text{imp}} \leq \sqrt{I_{\text{max}}^{(1)}/\tilde{\mu}}, \\ \tilde{\alpha}_{\text{pen}}^{(2)} I + \tilde{\beta}_{\text{pen}}^{(2)} & \text{if } \sqrt{I_{\text{min}}^{(2)}/\tilde{\mu}} \leq \bar{v}_{\text{imp}} \leq \sqrt{I_{\text{max}}^{(2)}/\tilde{\mu}}, \\ \tilde{\alpha}_{\text{pen}}^{(3)} I + \tilde{\beta}_{\text{pen}}^{(3)} & \text{if } \sqrt{I_{\text{min}}^{(3)}/\tilde{\mu}} \leq \bar{v}_{\text{imp}} \leq \sqrt{I_{\text{max}}^{(3)}/\tilde{\mu}}, \end{cases} \quad (35)$$

	i	$\beta^{(i)}$	$\alpha^{(i)}$	$\gamma^{(i)}$	$\bar{H}_{\text{min}}^{(i)}$	$\bar{H}_{\text{max}}^{(i)}$	$\bar{H}_*^{(i)}$
Perforation	1	0	2.2	0.3	–	1.52	3.67
	2	0.69	1.29	0	1.52	13.42	–

Table 4. Degen's model for perforation. Coefficients in (A.1), $n = 2$.

where

$$I = \tilde{\mu} \bar{v}_{\text{imp}}^2, \quad \tilde{\mu} = 10^6 \frac{K_{\text{shape}}^{(1)} m}{d^3 f'_c}, \quad (36)$$

with the coefficients presented in Table 5.

Haldar and Miller considered their model an improved modified NDRC model.

18. Haldar–Hamieh–Miller formula

This penetration model [Haldar et al. 1984; Haldar and Hamieh 1984] is described by (35) with the coefficients shown in Table 6.

The Haldar–Hamieh–Miller formula yields the following expression for the scabbing thickness:

$$\bar{b}_{\text{scab}} = 0.0342 \tilde{\mu} \bar{v}_{\text{imp}}^2 + 3.3437, \quad 4.58/\sqrt{\tilde{\mu}} \leq \bar{v}_{\text{imp}} \leq 19.6/\sqrt{\tilde{\mu}}. \quad (37)$$

19. Hughes' formula

Hughes' formula for penetration [Hughes 1984] reads:

$$\bar{H} = 0.19 K_{\text{shape}}^{(4)} \frac{J}{1 + 12.3 \ln(1 + 0.03J)}, \quad (38)$$

where

$$J = 10^6 \frac{m \bar{v}_{\text{imp}}^2}{d^3 f_t}, \quad K_{\text{shape}}^{(4)} = \begin{cases} 1.00 & \text{for a flat nose,} \\ 1.12 & \text{for a blunt nose,} \\ 1.26 & \text{for a spherical nose,} \\ 1.39 & \text{for a very sharp nose,} \end{cases} \quad (39)$$

and f_t is the tensile strength of concrete. With reference to [ACI 1978], Hughes [1984] recommended using the relationship between f_t and f'_c :

$$f_t = 630 \sqrt{f'_c}. \quad (40)$$

i	$\tilde{\alpha}_{\text{pen}}^{(i)}$	$\tilde{\beta}_{\text{pen}}^{(i)}$	$I_{\text{min}}^{(i)}$	$I_{\text{max}}^{(i)}$
1	0.22024	-0.02725	0.3	2.5
2	0.446	-0.592	2.5	3.0
3	0.06892	0.53886	3.0	21.0

Table 5. Haldar–Miller model for penetration. Coefficients in (35).

i	$\tilde{\alpha}_{\text{pen}}^{(i)}$	$\tilde{\beta}_{\text{pen}}^{(i)}$	$I_{\text{min}}^{(i)}$	$I_{\text{max}}^{(i)}$
1	0.2251	-0.0308	0.3	4.0
2	0.0567	0.6740	4.0	21.0
3	0.0299	1.1875	21.0	455

Table 6. Haldar–Hamieh–Miller model for penetration. Coefficients in (35).

The dependencies \bar{b}_{perf} versus \bar{H} and \bar{b}_{scab} versus \bar{H} are the same as given by (A.1) ($n = 2$) with the coefficients shown in Table 7.

Hughes [1984] noted that his formulas are valid in the range $J < 3500$ but they will be conservative for $J < 40$ and $\bar{b} < 3.5$.

20. Adeli–Amin formula

Using a large set of experimental data from [Sliter 1980], Adeli and Amin [1985] proposed a model that, similarly to the Haldar–Miller and Haldar–Hamieh–Miller models, is based on the factor I given by (36). This model can be written as

$$\bar{H} = \psi(\alpha_{\text{pen}}, \beta_{\text{pen}}, \gamma_{\text{pen}}; I), \tag{41}$$

$$\bar{b}_{\text{perf}} = \psi(\alpha_{\text{perf}}, \beta_{\text{perf}}, \gamma_{\text{perf}}; I), \tag{42}$$

$$\bar{b}_{\text{scab}} = \psi(\alpha_{\text{scab}}, \beta_{\text{scab}}, \gamma_{\text{scab}}; I), \tag{43}$$

where

$$\psi(\alpha, \beta, \gamma; I) = \beta + \alpha I - \gamma I^2 \tag{44}$$

and parameters α , β , and γ for penetration, perforation, and scabbing are given in Table 8. The parameter

$$I_* = 0.5\alpha/\gamma \tag{45}$$

is shown in the last column of Table 8. This parameter is the upper limit of the increasing function ψ versus I . The requirement similar to the inequality in (A.4) reads:

$$I < I_*. \tag{46}$$

Instead of (41), Adeli and Amin suggested using

$$\bar{H} = 0.0123 + 0.196I - 0.008I^2 + 0.0001I^3, \tag{47}$$

	i	$\beta^{(i)}$	$\alpha^{(i)}$	$\gamma^{(i)}$	$\bar{H}_{\min}^{(i)}$	$\bar{H}_{\max}^{(i)}$
Perforation	1	0	3.6	0	–	0.7
	2	1.4	1.58	0	0.7	–
Scabbing	1	0	5.0	0	–	0.7
	2	2.3	1.74	0	0.7	–

Table 7. Hughes’ model for perforation and scabbing. Coefficients in (A.1), $n = 2$.

	β	α	γ	I_*
Penetration	0.0416	0.1698	0.0045	18.8
Perforation	0.906	0.3214	0.0106	15.1
Scabbing	1.8685	0.4035	0.0114	17.7

Table 8. Adeli–Amin model. Coefficients in (41)–(43).

where the function $\bar{H}(I)$ increases when $I < I_* = 19.1$.

The Adeli–Amin formulas are valid in the following ranges of parameters [Adeli and Amin 1985]: $27 \text{ m/s} < v_{\text{imp}} < 312 \text{ m/s}$, $110 \text{ g} < m < 344 \text{ kg}$, $0.7 < b/d < 18$, $d < 30 \text{ cm}$, $\bar{H} < 2.0$, and $0.3 < I < 21$. The range for the parameter I should be decreased taking into account (46) and values of I_* in Table 8.

21. CRIEPI formula

The model of the Central Research Institute of the Electric Power Industry (CRIEPI) of Japan gives the following relationship for the DOP [Ohnuma et al. 1985; Li et al. 2005]:

$$\bar{H} = \phi(\bar{v}_{\text{imp}}) = \frac{26.1m}{d^{1.8}} \left(\frac{16.7 \cdot 10^4}{(f'_c)^{2/3}} - 1 \right) \left[\frac{d + 0.25}{(1.25\bar{b} + 1)\bar{b}} \right] \bar{v}_{\text{imp}}^2. \quad (48)$$

Ohnuma et al. [1985] recommended using (48) for $v_{\text{imp}} \leq 50 \text{ m/s}$. Clearly, the constraints $f'_c < 68.2$ and $\bar{H} \leq \bar{b}$ must be satisfied.

They also proposed the following formulas for calculating perforation and scabbing thicknesses:

$$\bar{b}_{\text{perf}} = \Xi_{\text{perf}}(\bar{v}_{\text{imp}}) = \frac{447}{d^{1.5}} \sqrt{\frac{m}{f'_c}} \bar{v}_{\text{imp}}^{0.75}, \quad (49)$$

$$\bar{b}_{\text{scab}} = \Xi_{\text{scab}}(\bar{v}_{\text{imp}}) = \frac{306}{d^{1.2}} \left(\frac{m}{f'_c} \right)^{0.4} \bar{v}_{\text{imp}}^{2/3}. \quad (50)$$

These formulas differ from (33) and (34) (Chang's model) by the values of the coefficients.

22. Vretblad (British) formula

Teland [1998], with reference to [Vretblad 1988], presented the following penetration model, also known as the ‘‘British formula’’:

$$\bar{H} = \phi(\bar{v}_{\text{imp}}) = \frac{0.76 \cdot 10^{-3} (1 - 0.6 \cdot 10^{-8} f'_c) m}{d^3 \bar{c}_x} \bar{v}_{\text{imp}}^{1.5}. \quad (51)$$

23. UKAEA-CEBG-NNC formulas

This section is mainly based on the guidelines given in [Barr 1990]. Some additional information on this subject can be also found in [Fullard and Barr 1989; Fullard et al. 1991]. According to [Barr 1990], major contributions to this model were made by the UK Atomic Energy Authority (UKAEA), the Central Electricity Generating Board (CEGB), and the National Nuclear Corporation (NNC), so we refer to this model by the names of these organizations.

For calculation of the DOP of a solid missile penetrating into a reinforced concrete barrier with sufficient thickness so as to suffer no scabbing, the following model is recommended:

$$g(\bar{H}) = \mu \bar{v}_{\text{imp}}^{1.8}, \quad (52)$$

where

$$\mu = 9.55 \frac{K_{\text{shape}}^{(3)} m}{d^{2.8} \sqrt{f'_c}}, \quad (53)$$

$$K_{\text{shape}}^{(3)} = \begin{cases} 0.72 & \text{for a flat nose,} \\ 0.84 & \text{for a spherical nose,} \\ 1.00 & \text{for a blunt (conic frustum or ogive) nose,} \\ 1.14 & \text{for a sharp (conical) nose,} \end{cases} \quad (54)$$

$$g(\bar{H}) = \begin{cases} 0.55\bar{H} - \bar{H}^2 & \text{if } \bar{H} < 0.22, \\ 0.25\bar{H}^2 + 0.0605 & \text{if } 0.22 \leq \bar{H} \leq 2, \\ \bar{H} - 0.9395 & \text{if } \bar{H} > 2. \end{cases} \quad (55)$$

In the unified form given by (1), the UKAEA-CEBG-NNC model can be rewritten as

$$\bar{H} = \phi(\bar{v}_{\text{imp}}) = \begin{cases} 0.275 - \sqrt{0.0756 - \mu \bar{v}_{\text{imp}}^{1.8}} & \text{if } \bar{v}_{\text{imp}} < 0.233/\mu^{5/9}, \\ 2\sqrt{\mu \bar{v}_{\text{imp}}^{1.8} - 0.0605} & \text{if } 0.233/\mu^{5/9} \leq \bar{v}_{\text{imp}} \leq 1.033/\mu^{5/9}, \\ \mu \bar{v}_{\text{imp}}^{1.8} + 0.9395 & \text{if } \bar{v}_{\text{imp}} > 1.033/\mu^{5/9}. \end{cases} \quad (56)$$

The ranges of parameters in this formula are as follows: +20% to -20% for $\bar{H} > 0.75$ and +100% to -50% for $\bar{H} < 0.75$, $25 \text{ m/s} < v_{\text{imp}} < 300 \text{ m/s}$, $5 \cdot 10^3 \text{ kg/m}^3 < m/d^3 < 2 \cdot 10^5 \text{ kg/m}^3$, and $22 \text{ MPa} < f'_c < 44 \text{ MPa}$.

For predicting the scabbing thickness the following formula was suggested:

$$\bar{b}_{\text{scab}} = \Xi_{\text{scab}}(\bar{v}_{\text{imp}}) = 5.3\mu^{1/3}\bar{v}_{\text{imp}}^{0.6}. \quad (57)$$

The accuracy of this formula is $\pm 40\%$ for $2 < \bar{b}_{\text{scab}} < 5.6$ within the following ranges of parameters: $29 \text{ m/s} < v_{\text{imp}} < 238 \text{ m/s}$, $26 \text{ MPa} < f'_c < 44 \text{ MPa}$, and $1.5 \cdot 10^3 \text{ kg/m}^3 < m/(d^2 b_{\text{scab}}) < 4 \cdot 10^4 \text{ kg/m}^3$.

The formula for the BLV of a flat-nosed missile with a circular or noncircular cross-section against a reinforced concrete shield reads:

$$\bar{v}_{\text{bl}} = \begin{cases} \bar{v}_{\text{bl}}^* & \text{if } \bar{v}_{\text{bl}}^* \leq 0.07, \\ \bar{v}_{\text{bl}}^* (4 \cdot \bar{v}_{\text{bl}}^{*2} + 1) & \text{if } \bar{v}_{\text{bl}}^* > 0.07, \end{cases} \quad (58)$$

where

$$\bar{v}_{\text{bl}}^* = \frac{1.3 \cdot 10^{-3} k_R k_p^{2/3} \rho_{\text{sh}}^{1/6} d^2 \sqrt{f'^*}}{m^{2/3}} \sqrt{r + 0.3\bar{b}^{4/3}}, \quad (59)$$

$$f'_c = \begin{cases} f'_c & \text{if } f'_c \leq 37 \text{ MPa,} \\ 37 \text{ MPa} & \text{if } f'_c > 37 \text{ MPa,} \end{cases} \quad (60)$$

$$k_R = \begin{cases} 1.2 - 0.6c_R/b & \text{if } 0.12 \leq c_R/b \leq 0.49, \\ 1 & \text{if } c_R/b < 0.12 \text{ or } c_R/b > 0.49, \end{cases} \quad (61)$$

$$r = \frac{100}{b} \left(\frac{a_F}{3c_F} + \frac{2a_R}{3c_R} \right), \quad k_p = p/(\pi d). \quad (62)$$

Here a_F (a_R) is the cross-sectional area of a single front (rear) rebar; c_F (c_R) is a front (rear) rebar spacing (see Figure 3; a steel plate at the distal face of the shield is lacking in the considered model); p is the perimeter of the impactor; f'_c is the characteristic compressive strength of concrete measured for 150 mm diameter, 300 mm long cylinders; and $k_p = 1$ for a missile with a circular cross-section.

This model is valid in the following ranges of parameters: $11 \text{ m/s} < v_{bl} < 300 \text{ m/s}$, $0 < r < 0.75$, $0.2 < p/(\pi b) < 3$, $150 \text{ kg/m}^3 < m/(p^2 b) < 10^4 \text{ kg/m}^3$, and $f'_c > 15 \text{ MPa}$.

In the case in which a steel plate is installed at the distal face of the shield (Figure 3) to improve its protective effectiveness, the following formula is recommended instead of (88):

$$v_{bl}^* = \frac{1.3\rho_{sh}^{1/6} \sqrt{f'_c}}{m^{2/3}} \left(\frac{p}{\pi} \right)^{2/3} \sqrt{B + 0.3b^{4/3}}, \quad (63)$$

where

$$B = r + 100b_{steel}/b \quad (64)$$

and b_{steel} is the steel plate thickness.

This formula is valid in the following ranges of parameters: $45 \text{ m/s} < v_{bl} < 300 \text{ m/s}$, $0 < r < 0.75$, $150 \text{ kg/m}^3 < m/(p^2 b) < 10^4 \text{ kg/m}^3$, $1.2 < B < 4.3$, $0.2 < p/(\pi b) < 3$, and $f'_c > 15 \text{ MPa}$.

24. Young's formula

24.1. Original model. After some algebra, Young's equation [Young 1997] can be written as

$$\bar{H} = \phi(\bar{v}_{imp}) = \frac{K_S K_{shape} K_m}{d^{2.4}} P(\bar{v}_{imp}), \quad (65)$$

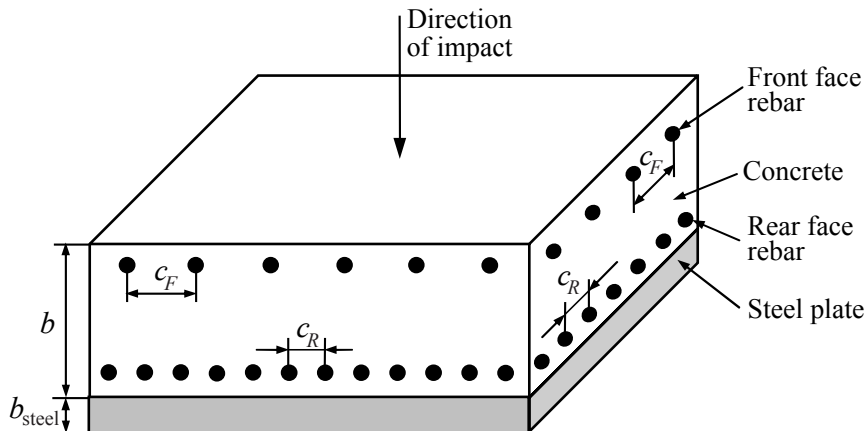


Figure 3. Reinforced concrete barrier, with notation.

where the coefficients K_S and K_{shape} will be defined subsequently, and

$$P(\bar{v}_{\text{imp}}) = \begin{cases} P_a(\bar{v}_{\text{imp}}) & \text{if } \bar{v}_{\text{imp}} < \bar{v}_*, \\ P_b(\bar{v}_{\text{imp}}) & \text{if } \bar{v}_{\text{imp}} \geq \bar{v}_*, \end{cases} \quad (66)$$

$$P_a(\bar{v}_{\text{imp}}) = \alpha_1 \ln(1 + \alpha_2 \bar{v}_{\text{imp}}^2), \quad \alpha_1 = 9.48 \cdot 10^{-4}, \quad \alpha_2 = 215, \quad (67)$$

$$P_b(\bar{v}_{\text{imp}}) = k(\bar{v}_{\text{imp}} - \bar{v}_0), \quad k = 0.0213, \quad \bar{v}_0 = 0.0305, \quad (68)$$

$$\bar{v}_* = 0.061, \quad (69)$$

$$K_m = \begin{cases} 0.46m^{0.85} & \text{if } m < 182, \\ m^{0.7} & \text{if } m \geq 182. \end{cases} \quad (70)$$

Coefficient K_{shape} depends on the shape of the impactor and is determined as

$$K_{\text{shape}} = \begin{cases} 0.18\bar{L}_{\text{nose}} - 0.09\Delta\bar{L}_{\text{nose}} + 0.56 & \text{for an ogive nose,} \\ 0.25\bar{L}_{\text{nose}} - 0.125\Delta\bar{L}_{\text{nose}} + 0.56 & \text{for a conic nose,} \end{cases} \quad (71)$$

where \bar{L}_{nose} and $\Delta\bar{L}_{\text{nose}}$ are the dimensionless (measured in impactor's diameter units) length of the nose and reduction of this length because of the bluntness (if any), respectively.

For sharp ogive-nosed shapes, the following equation can also be used:

$$K_{\text{shape}} = 0.56 + 0.18\sqrt{K_{\text{CRH}} - 0.25}. \quad (72)$$

If the nose of the impactor is neither ogive nor cone, Young [1997] recommended approximating the actual nose shape with ogive or conic shapes. If the bluntness is less than 10% of the penetrator diameter, it can be ignored.

Coefficient K_S depends on the properties of the concrete and is determined as

$$K_S = \frac{0.247K_e(11 - K_D)}{(t'_c \bar{b}')^{0.06} (f'_c)^{0.3}}, \quad (73)$$

where

$$t'_c = \min(t_c, 1), \quad \bar{b}' = \min(\bar{b}, 6), \quad K_e = \max\left[\left(\frac{K_F F}{\bar{W}}\right)^{0.3}, 1\right], \quad (74)$$

$$K_F = \begin{cases} 0.5 & \text{if } \bar{b} \leq 2, \\ 1 & \text{if } \bar{b} > 2, \end{cases} \quad F = \begin{cases} 20 & \text{for reinforced concrete,} \\ 30 & \text{for nonreinforced concrete.} \end{cases} \quad (75)$$

K_D is the volumetric rebar content, t_c is the cure time in days, and \bar{W} is the shield thickness. Bars over variables denote dimensionless parameters which are normalized as indicated in the beginning of this section.

If there is no available data for calculating the coefficient K_S , the default value, $K_S = 0.9$, can be used.

This model is recommended for $7 \text{ MPa} < f'_c < 124 \text{ MPa}$, $m > 5 \text{ kg}$, $\bar{H} \geq 3$, and $v_{\text{imp}} < 1220 \text{ m/s}$.

24.2. Modifications of the models. Function $P(\bar{v}_{\text{imp}})$ is discontinuous at the point $\bar{v}_{\text{imp}} = \bar{v}_*$, which has no physical meaning and can cause problems when applying these relations. Ben-Dor et al. [2008a; 2008b] proposed two modifications of the model that improve the smoothness of $P(\bar{v}_{\text{imp}})$.

The first modification [Ben-Dor et al. 2008a] is based on the correction of the parameters α_1 , α_2 , and \bar{v}_* in (67)–(69). In order to satisfy the requirements that $P_a(\bar{v}_*) = P_b(\bar{v}_*)$ and $P'_a(\bar{v}_*) = P'_b(\bar{v}_*)$, their new values of these parameters are selected as

$$\bar{v}_* = 0.065, \quad \alpha_1 = 6.092 \cdot 10^{-3}, \quad \alpha_2 = 30.34. \quad (76)$$

In the second modification [Ben-Dor et al. 2008b], a more smooth approximation of the function $P(\bar{v}_{\text{imp}})$ is proposed. This approximation is continuous and has continuous first and second derivatives for $\bar{v} = \bar{v}_*$ (and, consequently, for all $\bar{v}_{\text{imp}} > 0$). Toward this end, Ben-Dor et al. [2008b] modified the model for relatively small \bar{v}_{imp} while keeping the Young's approximation for large \bar{v}_{imp} . Specifically, the function $P_b(\bar{v}_{\text{imp}})$ is given by (68) while the following approximation of $P_a(\bar{v}_{\text{imp}})$ for small values of \bar{v}_{imp} is used:

$$P_a(\bar{v}_{\text{imp}}) = (-4.95\bar{v}_{\text{imp}}^2 + 0.196)\bar{v}_{\text{imp}}^2, \quad \bar{v}_{\text{imp}} \leq \bar{v}_*, \quad \bar{v}_* = 0.0813. \quad (77)$$

25. UMIST formulas

This section is based on [Li et al. 2005; 2006], which refer to the approach suggested in the studies conducted at the University of Manchester Institute of Science and Technology (UMIST) [Reid and Wen 2001; BNFL 2003].

25.1. Penetration model. The formula for the DOP reads [Li et al. 2005]:

$$\bar{H} = \phi(\bar{v}_{\text{imp}}) = \frac{0.88 \cdot 10^6 K_{\text{shape}}^{(3)} m}{\sigma_t(\bar{v}_{\text{imp}}) d^3} \bar{v}_{\text{imp}}^2, \quad (78)$$

where σ_t is the rate-dependent characteristic strength of concrete,

$$\sigma_t(\bar{v}) = \zeta_0(f'_c) + \zeta_1(f'_c)\bar{v}, \quad (79)$$

$$\zeta_0(f'_c) = 4.2f'_c + 1.35 \cdot 10^8, \quad \zeta_1(f'_c) = 14f'_c + 0.45 \cdot 10^8. \quad (80)$$

Equation (78) has been validated in the following ranges of parameters: $\bar{H} < 2.5$, $3 \text{ m/s} < v_{\text{imp}} < 66 \text{ m/s}$, $35 \text{ kg} < m < 2500 \text{ kg}$, and $5 \text{ cm} < d < 60 \text{ cm}$.

25.2. Perforation and scabbing model and its analysis. On the basis of formulas presented in [Li et al. 2005] (in [Li et al. 2006] a similar model is described for flat-nosed projectiles when the concrete reinforcement is ignored), the relations for the BLV and the scabbing limit velocity can be written as

$$\frac{\bar{v}_{\text{bl}}^2}{\kappa \sigma_t(\bar{v}_{\text{bl}})} = \begin{cases} \chi_{\text{perf}}^{(1)}(\bar{b}) & \text{if } 0.5 < \bar{b} \leq 1, \\ \chi_{\text{perf}}^{(2)}(\bar{b}) & \text{if } 1 \leq \bar{b} < 5, \\ \chi_{\text{perf}}^{(3)}(\bar{b}) & \text{if } \bar{b} \geq 5, \end{cases} \quad (81)$$

$$\frac{\bar{v}_{\text{sl}}^2}{\kappa \sigma_t(\bar{v}_{\text{sl}})} = \begin{cases} \chi_{\text{scab}}^{(1)}(\bar{b}) & \text{if } 0.5 < \bar{b} < 5, \\ \chi_{\text{scab}}^{(2)}(\bar{b}) & \text{if } \bar{b} \geq 5, \end{cases} \quad (82)$$

where

$$\begin{aligned}
 \chi_{\text{perf}}^{(1)}(\bar{b}) &= \eta(1.506\bar{b}^2 - 0.506\bar{b}), & \chi_{\text{perf}}^{(2)}(\bar{b}) &= \eta(2\bar{b}^3 - \bar{b}), \\
 \chi_{\text{perf}}^{(3)}(\bar{b}) &= 78.5\bar{b} - 235.5, & \chi_{\text{scab}}^{(2)}(\bar{b}) &= (56.52\bar{b} - 24.3)K_{\text{shape}}^{(3)}, \\
 \chi_{\text{scab}}^{(1)}(\bar{b}) &= \eta(1.386\bar{b}^2 - 0.5441\bar{b})/K_{\text{shape}}^{(3)}, & \kappa &= 2 \cdot 10^{-8}d^3/m.
 \end{aligned} \tag{83}$$

Parameter η is associated with the reinforcement of the shield and is given by

$$\eta = \begin{cases} 1.5r(d/c_{FR}) + 0.5 & \text{if } d/c_{FR} < \sqrt{d/d_{FR}}, \\ 1.5r(d/d_{FR}) + 0.5 & \text{if } d/c_{FR} \geq \sqrt{d/d_{FR}}, \end{cases} \tag{84}$$

where $r = 100a_{FR}/(c_{FR}b)$ is determined by (62) with $a_F = a_R = a_{FR} = \pi d_{FR}^2/4$ and $c_F = c_R = c_{FR}$; a_{FR} and d_{FR} are the cross-sectional area and the diameter of the rebar, respectively; and c_{FR} is the rebar spacing (see Figure 3).

These scabbing and perforation models are valid for $2.2 \text{ cm} < d < 60 \text{ cm}$, $1 \text{ kg} < m < 2622 \text{ kg}$, $20 \text{ MPa} < f'_c < 79 \text{ MPa}$, $0 < r < 4$, $5.1 \text{ cm} < b < 64 \text{ cm}$, and $0 < v_{\text{imp}} < 427 \text{ m/s}$ [Li et al. 2005].

Since σ_t is a linear function of \bar{v} , determining $\bar{v} = \bar{v}_{\text{bl}}$ or $\bar{v} = \bar{v}_{\text{sl}}$ in terms of \bar{b} requires solving the quadratic equation $f(\bar{v}) = 0$, where

$$f(\bar{v}) = \bar{v}^2 - (\kappa\zeta_1\Theta)\bar{v} - \kappa\zeta_0\Theta, \tag{85}$$

and Θ is the right-hand side of (81) or (82). It can be easily shown that the equation $f(\bar{v}) = 0$ has a single positive root:

$$\bar{v} = \omega(\Theta), \quad \omega(\Theta) = 0.5\kappa\zeta_1\Theta + \sqrt{\kappa\Theta(0.25\kappa\zeta_1\Theta + \zeta_0)}. \tag{86}$$

Taking into account (86), \bar{v}_{bl} and \bar{v}_{sl} , which are determined by (81) and (82), can be expressed as increasing functions of \bar{b} . Consequently, the suggested model adequately describes the physics of penetration, and the single-valued inverse functions $\bar{b}_{\text{perf}}(\bar{v}_{\text{imp}})$ and $\bar{b}_{\text{scab}}(\bar{v}_{\text{imp}})$ exist. Since the functions determined by (81) and (82) are discontinuous at the point $\bar{b} = 5$, the function $\bar{v}_{\text{bl}} = \bar{v}_{\text{bl}}(\bar{b})$ assumes different values, \bar{v}'_{bl} and \bar{v}''_{bl} , to the left and to the right of this point. Therefore the inverse function, $\bar{b}_{\text{perf}} = \Xi_{\text{perf}}(\bar{v}_{\text{imp}})$, cannot be defined in the interval $\bar{v}'_{\text{bl}} < \bar{v}_{\text{imp}} < \bar{v}''_{\text{bl}}$. The discontinuity of the function $\bar{v}_{\text{sl}} = \bar{v}_{\text{sl}}(\bar{b})$ causes similar problems.

26. Malaysia models

Zaidi et al. [2010], of the Universiti Tun Hussein Onn Malaysia (UTHM), proposed a linear model (hereafter, UTHM model) describing the dependence between the DOP, \bar{H} , and the parameter $mv_{\text{imp}}^2/(f'_c d^3)$ which is valid for ogive-nosed impactors:

$$\bar{H} = \frac{0.5 \cdot 10^6 m \bar{v}_{\text{imp}}^2}{f'_c d^3} q_1 + q_0, \tag{87}$$

where the coefficients depend on the CRH of the impactor, K_{CRH} :

$$\begin{aligned} q_0 &= -0.6256K_{\text{CRH}}^3 + 7.9656K_{\text{CRH}}^2 - 32.892K_{\text{CRH}} + 48.008, \\ q_1 &= 0.014K_{\text{CRH}}^3 - 0.1585K_{\text{CRH}}^2 + 0.5606K_{\text{CRH}} - 0.5405. \end{aligned} \quad (88)$$

This formula can be applied in the following ranges of parameters: $139 \text{ m/s} < v_{\text{imp}} < 1225 \text{ m/s}$, $13.5 \text{ MPa} \leq f'_c \leq 108 \text{ MPa}$, $64 \text{ g} < m < 13.2 \text{ kg}$, $2 \leq K_{\text{CRH}} \leq 6$, and $13 \text{ mm} < d < 76.2 \text{ mm}$.

Both Rahman et al. [2010] and Latif et al. [2011] considered perforation by flat-nosed (cylindrical) impactors. Rahman et al. proposed the scabbing limit velocity

$$\bar{v}_{\text{sl}} = 10^{-3} d \sqrt{\frac{2f'_c d}{m} \psi_1(\bar{b})}, \quad (89)$$

where

$$\psi_1(\bar{b}) = \begin{cases} 0.87\bar{b} - 0.29 & \text{if } 0.69 \leq \bar{b} \leq 3.0, \\ 3.31\bar{b} - 7.58 & \text{if } 3.0 < \bar{b} \leq 6.0, \\ 4279.181\bar{b} - 25662.82 & \text{if } 6.0 < \bar{b} \leq 14.86. \end{cases} \quad (90)$$

The latter formula is valid in the following ranges of parameters: $0.69 < b/d < 14.86$, $24.15 \text{ MPa} \leq f'_c \leq 50.2 \text{ MPa}$, $17.5 \text{ mm} < d < 305.0 \text{ mm}$, $0.92 \text{ kg} < m < 309 \text{ kg}$, $29 \text{ m/s} < v_{\text{sl}} < 427 \text{ m/s}$, and $50.8 \text{ mm} < b < 609.6 \text{ mm}$.

Latif et al. [2011] suggested a formula for the BLV that can be written as

$$\bar{v}_{\text{bl}} = 10^{-3} d \sqrt{\frac{2f'_c d}{m} \psi_2(\bar{b})}, \quad (91)$$

where

$$\psi_2(\bar{b}) = 0.174\bar{b}^3 + 0.169\bar{b}^2 + 0.0577\bar{b} + 0.2969. \quad (92)$$

This formula is valid in the following ranges of parameters: $0.92 \text{ kg} < m < 309 \text{ kg}$, $29 \text{ m/s} < v_{\text{bl}} < 427 \text{ m/s}$, $0.69 < b/d < 14.86$, $24.15 \text{ MPa} \leq f'_c \leq 50.2 \text{ MPa}$, and $17.5 \text{ mm} < d < 305.0 \text{ mm}$.

27. TM 5-855-1 formulas

The formulas of [TM 5-855-1 1986] are proposed for describing penetration by a standard fragment in the shape of a cylinder of diameter d and length $0.5d$ with a hemispherical nose. The mass of the fragment that is used in the formulas is calculated as

$$m = (5\pi/24)\rho_{\text{imp}}d^3 = 0.654\rho_{\text{imp}}d^3. \quad (93)$$

The model of [TM 5-1300 1990] employs the following formula for the fragment mass (after conversion to SI units): $m = 5.149 \cdot 10^3 d^3$, that is, the density is assumed to be $\rho_{\text{imp}} = 7873 \text{ kg/m}^3$.

After some transformations the formulas of [TM 5-855-1 1986] can be written in the form

$$H = \begin{cases} \frac{13.46m^{0.37}\bar{v}_{\text{imp}}^{0.9}}{(f'_c)^{0.25}} & \text{if } \bar{v}_{\text{imp}} \leq \bar{v}_{\text{imp}}^*, \\ \frac{1.09 \cdot 10^3 m^{0.4} \bar{v}_{\text{imp}}^{1.8}}{(f'_c)^{0.5}} + 0.395m^{0.33} & \text{if } \bar{v}_{\text{imp}} > \bar{v}_{\text{imp}}^*, \end{cases} \quad (94)$$

$$b_{\text{perf}} = 0.0311Hm^{0.033} + 2.95m^{0.33}, \quad (95)$$

$$b_{\text{scab}} = 0.0334Hm^{0.033} + 4.465m^{0.33}, \quad (96)$$

$$\bar{v}_{\text{res}} = \begin{cases} \bar{v}_{\text{imp}}[1 - (b/b_{\text{perf}})^2]^{0.555} & \text{if } \bar{v}_{\text{imp}} \leq \bar{v}_{\text{imp}}^*, \\ \bar{v}_{\text{imp}}[1 - (b/b_{\text{perf}})]^{0.555} & \text{if } \bar{v}_{\text{imp}} > \bar{v}_{\text{imp}}^*, \end{cases} \quad (97)$$

where

$$\bar{v}_{\text{imp}}^* = 5.13 \cdot 10^{-3} (f'_c)^{0.278} / m^{0.044}. \quad (98)$$

28. Folsom's model for penetration into a shield with a predrilled hole

Folsom [1987] proposed a formula for the DOP of ogive-nosed projectile into a predrilled shield that can be written, in the interpretation of [Teland 2001], in the form

$$\bar{H} = \frac{17.3m\bar{v}_{\text{imp}}^{1.5}}{f'_c d^{2.785}} \cdot \frac{1 - 038\eta^2}{1 - \eta^2} - \frac{4\Omega(K_{\text{CRH}}, \eta)}{1 - \eta^2} + \sqrt{K_{\text{CRH}} - 0.25}, \quad (99)$$

where d_0 is diameter of the hole and

$$\Omega(z, \eta) = \left(\frac{1 - \eta^2}{4} - z + 2z^2 \right) g + \frac{1 - 2z}{2} [g\sqrt{z^2 - g^2} + z^2 \sin^{-1}(g/z)] - \frac{g^3}{3}, \quad (100)$$

$$g(z, \eta) = \sqrt{(1 - \eta)[z - 0.25(1 - \eta)]}, \quad \eta = d_0/d.$$

29. Some other models and related problems

Walter and Wolde-Tinsae [1984] proposed a modified version of several empirical formulas that account for the presence of a steel plate at the distal face of a shield by introducing an artificial thickness of the shield. Riera [1989] presented the relationship between H and v_{imp} as an implicit function and suggested and discussed equations for determining v_{bl} and v_{sl} . Al-Hachamee and Azeez [2010] proposed formulas for H , b_{perf} , and b_{scab} on the basis of the results of 20 experiments from the literature. Dancygier [1997] proposed a method that allowed for including the reinforcement ratio as a parameter in the existing semiempirical perforation formulas.

Me-Bar [1997] proposed a method for scaling ballistic penetration into concrete shields using energy balance whereby the energy absorbed by a shield during penetration was expressed as a sum of the energy expended for surface effects and the energy expended for volume effects. Dancygier [2000] investigated the effects of impact by similarly (though not necessarily geometrically similar) shaped impactors on the reinforced concrete barriers. Based on the widely known empirical formulae he derived expressions

for the velocity ratios between the simulator (reference impactor) and the simulated impactors that are required in order to yield the same DOP and the same perforation limit thickness.

30. Comparison between models and their experimental validations

30.1. Brief review. Plots which allow comparing the dependencies obtained using various phenomenological models can be found in [Kennedy 1976; Yankelevsky 1997; Teland 1999; Li and Tong 2003] as well as other studies.

Analysis of the models based on comparison of their predictions with experimental results is complicated for the following reasons: the small number of performed experiments, the narrow range of parameters within which the experiments are usually conducted, and the lack of information concerning the properties of the concrete in the shield (reinforcement, aggregate size, etc.). Also, in some cases the accuracy of the model is evaluated using the same experimental data as used in the derivation of the model.

Kennedy [1976] examined the ACE, NDRC, BBL, Ammann–Whitney and Pétry models using experimental data and recommended the modified NDRC formula for calculating b_{scab} and b_{perf} in the following ranges of the parameters: $d < 41$ cm, $0.02 \text{ kg/m}^3 < m/d^3 < 0.54 \text{ kg/m}^3$, and $30 \text{ m/s} < v_{\text{imp}} < 900 \text{ m/s}$. He concluded that this formula generally agrees with the test results within an accuracy of $\pm 20\%$ in these ranges of the parameters.

Sliter [1980] collected experimental data on the penetration of cylindrical projectiles into finite-thickness shields and calculated the DOP using the NDRC model, the scabbing thickness using the NDRC, Bechtel, and Stone–Webster models, and the perforation thickness using the NDRC and CEA-EDF models. He found that the values of the DOP predicted by the NDRC formula are within an experimental scatter of $\pm 25\%$ for $v_{\text{imp}} > 152 \text{ m/s}$ while the agreement between the predicted and the observed values of the DOP is unsatisfactory for relatively low impact velocities. As far as scabbing thickness prediction concerns, Sliter [1980] noted that the NDRC, Bechtel, and Stone–Webster models may all be used equally well for missiles having relatively small diameters. Regarding perforation, he indicated that damage is predicted better by the CEA-EDF formula than by the NDRC model.

On the basis of experimental data collected by Sliter [1980], Adeli and Amin [1985] examined the modified NDRC, Haldar–Miller, Hughes, and Adeli–Amin models for penetration, the Pétry I, Pétry II, ACE, modified NDRC, BRL, Bechtel, Chang, Hughes, and Adeli–Amin models for scabbing, and the Pétry I, Pétry II, ACE, modified NDRC, BRL, CEA-EDF, Degen, Chang, Hughes, and Adeli–Amin models for perforation. Their conclusions are as follow.

Penetration modeling. For $\bar{H}_{\text{exp}} \geq 0.6$, where $\bar{H}_{\text{exp}} = H_{\text{exp}}/d$ and H_{exp} is the experimentally observed DOP, the modified NDRC, Haldar–Miller, Hughes, and Adeli–Amin models “tend to agree with the experimental results within $\pm 25\%$ ”. For $\bar{H}_{\text{exp}} < 0.6$, the Pétry II, Haldar–Miller, and cubic Adeli–Amin models perform better than the other models. The ACE and Pétry I models considerably overestimate the DOP. Consequently, for estimating the DOP Adeli and Amin [1985] recommended applying the quadratic Adeli–Amin formula for $v_{\text{imp}} < 145 \text{ m/s}$ and the quadratic Adeli–Amin model or modified NDRC formula for $145 \text{ m/s} \leq v_{\text{imp}} < 305 \text{ m/s}$.

Scabbing modeling. The Adeli–Amin, Bechtel, and Chang models perform better and, generally, are the least conservative among all the models. The Hughes model is the most conservative while the

Pétry I, Pétry II, and BRL equations performance is the poorest in predicting the scabbing thickness. Consequently, for scabbing modeling quadratic the Adeli–Amin, Bechtel, or Chang’s formulas for $v_{\text{imp}} < 310 \text{ m/s}$ are recommended.

Perforation modeling. The CEA-EDF, Degen, Chang, and Adeli–Amin models perform better than the other models although the predictions of the modified NDRC and Pétry I formulas also agree with the experimental data. The predictions of the Pétry II, BRL, and ACE formulas do not exhibit good agreement with the results of experiments. Consequently, the CEA-EDF, Degen, Chang, and Adeli–Amin models for $v_{\text{imp}} < 310 \text{ m/s}$ are recommended for perforation modeling.

Walter and Wolde-Tinsae [1984] used the results of 45 experiments for comparing the performance of the basic empirical models. They concluded that among nine empirical models the best predictions of perforation/nonperforation events are provided by the Pétry I, Pétry II, Degen, BRL, and CEA-EDF formulas whereby the percentage of the correct prediction varies in the range 71–75% while the percentage of the correct prediction is small for the NDRC and Kar’s formulas (53%).

In [DOE 2006] Chang’s formula is recommended for calculating b_{scab} and b_{perf} .

30.2. Evaluation of performance of different models: Finite-thickness shields. The evaluation of the performance of different empirical models in this section is based on the results of experiments collected in [Sliter 1980]. The input data for the evaluated models are also adopted from [ibid.], and only those experiments that satisfy the conditions for the validity of the model are used for evaluating each of the models. The UMIST model is not included in the list of analyzed models because most of the experiments from [ibid.] fall outside the range of validity of this model. Comparison of the UMIST model and the NDRC model with other sets of experimental data can be found in [Li et al. 2006].

General results on the performance of the various models are summarized in Table 9. The denominator in the fraction in the penetration (scabbing, perforation) column denotes the number of experiments in which penetration (scabbing, perforation) was observed, while the numerator is the number of calculations which predicted the corresponding phenomenon. The last column contains similar characteristics for all types of damage (penetration, scabbing, and perforation) so that the numerator of the fraction equals the sum of the numerators of the fractions in the preceding columns and the denominator is the sum of the denominators of the fractions in the preceding columns. Clearly, only the experiments that were calculated using the empirical models are taken into account. Parameters b_{perf} and b_{scab} in the average model are determined as arithmetic means of the values of the corresponding parameters in the models which predicted these parameters. It is assumed that penetration, scabbing, or perforation occurs if $b < b_{\text{scab}}$, $b_{\text{scab}} \leq b < b_{\text{perf}}$, or $b \geq b_{\text{perf}}$, respectively.

Analysis of the data presented in Table 9, conducted taking into account the number of the experiments included in the evaluation of each model, reveals the advantages of Chang’s model and the CRIEPI model over the other models.

30.3. Evaluation of performance of different models: Semiinfinite shields. Evaluation of the performance of different models for semiinfinite shields is based on the experimental data on ogive-nosed impactors collected in [Hansson 2003]. These experiments were conducted in the following ranges of parameters: $13 \text{ mm} \leq d \leq 365 \text{ mm}$, $132 \text{ m/s} \leq v_{\text{imp}} \leq 1050 \text{ m/s}$, $64 \text{ g} \leq m \leq 485 \text{ kg}$, $21.6 \text{ MPa} \leq f'_c \leq 140 \text{ MPa}$, $55 \text{ mm} \leq H_{\text{exp}} \leq 1.96 \text{ m}$, and $1.5 \leq K_{\text{CRH}} \leq 6$.

Model	Penetration	Scabbing	Perforation	Penetration, scabbing, perforation
Pétry II	$\frac{31}{35} = 89\%$	$\frac{3}{51} = 6\%$	$\frac{2}{16} = 13\%$	$\frac{36}{102} = 35\%$
BRL	$\frac{29}{35} = 83\%$	$\frac{9}{51} = 18\%$	$\frac{4}{16} = 25\%$	$\frac{42}{102} = 41\%$
ACE	$\frac{17}{19} = 89\%$	$\frac{4}{6} = 67\%$	$\frac{5}{5} = 100\%$	$\frac{26}{30} = 87\%$
NDRC	$\frac{28}{35} = 80\%$	$\frac{11}{51} = 22\%$	$\frac{12}{16} = 75\%$	$\frac{51}{102} = 50\%$
Chang	$\frac{30}{35} = 86\%$	$\frac{41}{51} = 80\%$	$\frac{8}{16} = 50\%$	$\frac{79}{102} = 77\%$
Adeli–Amin	$\frac{20}{22} = 91\%$	$\frac{9}{18} = 50\%$	$\frac{4}{5} = 80\%$	$\frac{33}{45} = 73\%$
CRIEPI	$\frac{31}{35} = 89\%$	$\frac{48}{51} = 94\%$	$\frac{4}{16} = 25\%$	$\frac{83}{102} = 81\%$
Average	$\frac{34}{35} = 97\%$	$\frac{32}{51} = 63\%$	$\frac{6}{16} = 31\%$	$\frac{71}{102} = 70\%$

Table 9. Comparison of empirical models based on type of shield damage with experimental data from [Sliter 1980].

In the calculations for evaluating the performances of different empirical models, we included only those models which are applicable for ogive-shaped impactors: the Ammann–Whitney model, the modified NDRC model, Degen’s model, Kar’s model, the Healey–Weissman model, the Haldar–Hamieh–Miller model, Hughes’ model, the UKAEA-CEBG-NNC model, Young’s model, the Whiffen formula, and the UTHM formula. The UMIST, Haldar–Miller, and Adeli–Amin formulas are not included because most or all the experiments fall outside the range of validity of these models. A value of $\bar{c} = 1$ is used in Whiffen’s model.

Detailed results of the calculations are shown in Figure 4, where circles indicate experiments for which the constraints for applicability of the model (if any) are satisfied while triangles denote experiments that fall outside the range of validity of the particular model. The average model is constructed using values of the DOP equal to the arithmetic mean of the values of the DOPs for all models where the model’s constraints are satisfied. The error, $\tilde{\epsilon}$, is calculated for each experiment as

$$\tilde{\epsilon} = \frac{H - H_{\text{exp}}}{H_{\text{exp}}} 100\%, \quad (101)$$

where H_{exp} is the DOP observed in the experiment. Horizontal lines denote the values of $\tilde{\epsilon}$ which are considered the minimum $\tilde{\epsilon}_{\text{min}}$ and maximum $\tilde{\epsilon}_{\text{max}}$ values of $\tilde{\epsilon}$; in some cases we excluded outliers with anomalously high deviations from the mean. Hereafter in calculating $\tilde{\epsilon}_{\text{min}}$ and $\tilde{\epsilon}_{\text{max}}$ (and in other calculations) for each model, we take into account only those experiments that correspond to the range of the validity of the model (denoted by the circles in Figure 4).

The results of calculations are summarized in Table 10, where the name of the model is indicated in the first column. In some cases the whole range of variation of \bar{H}_{exp} is divided into two subranges. The number of experiments in each subrange or the whole range, where the value of the parameter $\tilde{\epsilon}$ falls in the interval between $\tilde{\epsilon}_{\text{min}}$ and $\tilde{\epsilon}_{\text{max}}$, is indicated in column 2 (index N); the end-points of the range (or

subrange) are presented in column 3; $\tilde{\epsilon}_{\min}$ and $\tilde{\epsilon}_{\max}$ in columns 4 and 5, respectively. The indexes in the rest of the columns are described below.

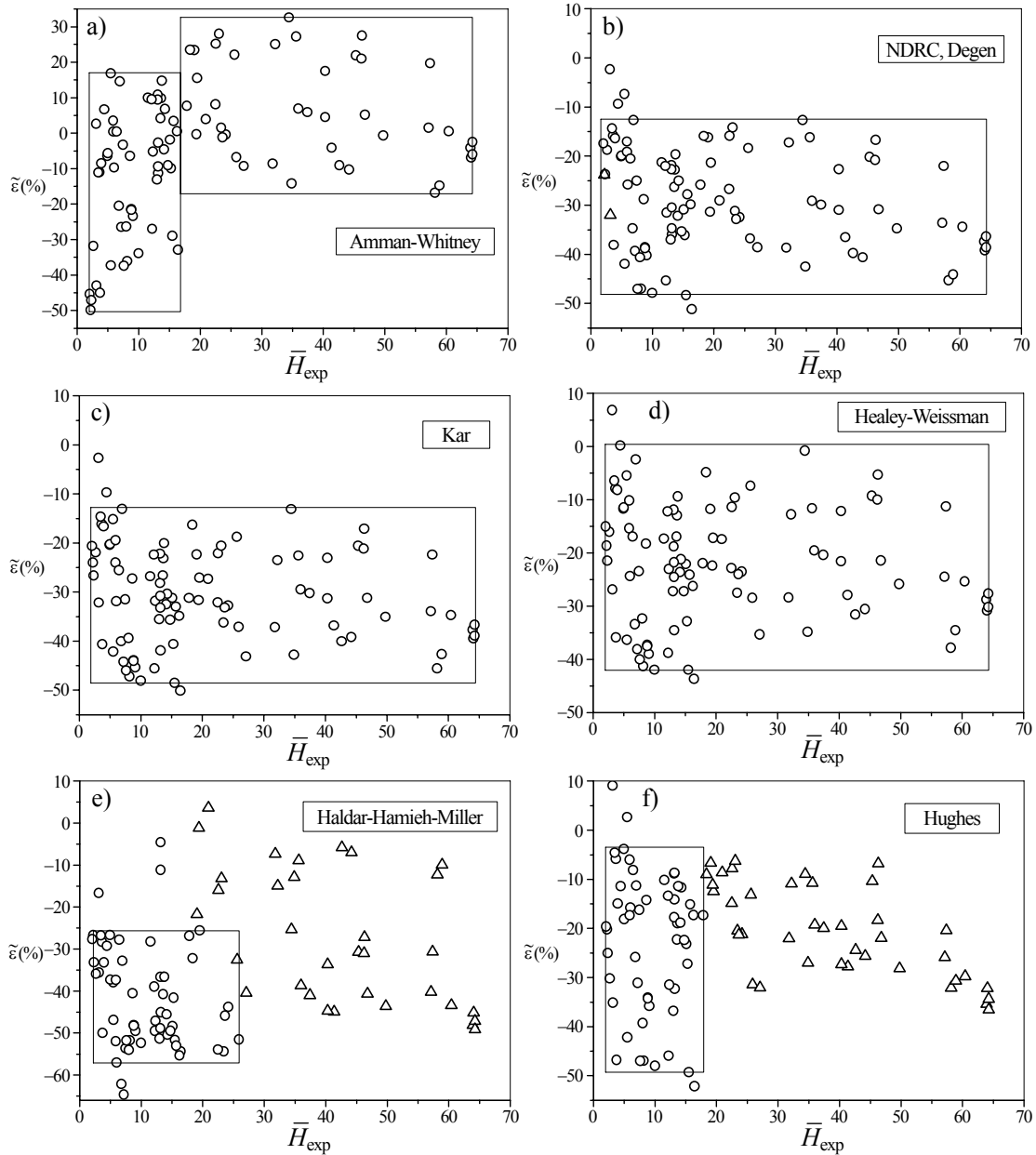


Figure 4. Comparison of DOPs predicted using empirical model with results of experiments, taking (circles) and not taking (triangles) into account model constraints (continued on next page).

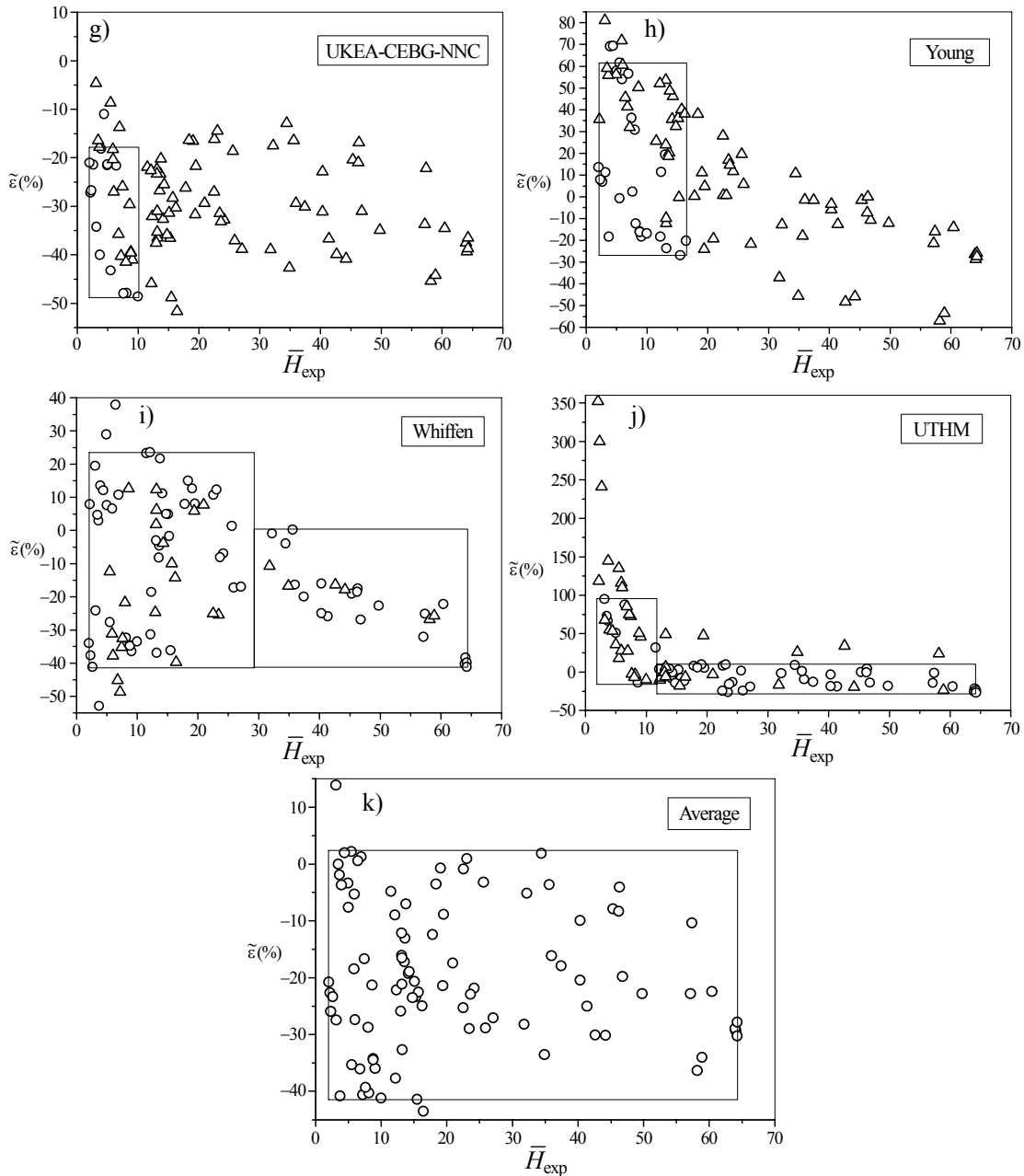


Figure 4 (cont.)

Inspection of Table 10 and Figure 4 shows that for the modified NDRC, Degen, Kar, Haldar–Hamieh–Miller, UKAEA-CEBG-NNC, Hughes, and average models, $\tilde{\epsilon}_{\text{max}} < 0$ or slightly larger than 0. Consequently, practically all predicted values of the DOP are smaller than the experimental values, and the predictions of the models are expected to be biased towards smaller magnitudes of the DOP. Since for the other models as well the interval of variation of $\tilde{\epsilon}$ is strongly asymmetrical with respect to $\tilde{\epsilon} = 0$

Model	N	\bar{H}_{exp}	$\tilde{\epsilon}_{\text{min}}$	$\tilde{\epsilon}_{\text{max}}$	\hat{k}	$\hat{\epsilon}_*$
Ammann–Whitney	53	2 ÷ 18	−50%	+17%	1.20	40%
	41	18 ÷ 65	−17%	+33%	0.93	23%
NDRC, Degen	88	2 ÷ 65	−49%	−12%	1.44	26%
Kar	91	2 ÷ 65	−49%	−13%	1.44	26%
Healey–Weissman	92	2 ÷ 65	−42%	0%	1.26	27%
Haldar–Hamieh–Miller	56	2 ÷ 26	−57%	−25%	1.70	27%
Hughes	51	2 ÷ 18	−50%	−3%	1.36	31%
UKEA-CEBG-NNC	14	2 ÷ 10	−50%	−18%	1.50	23%
Young’s	24	2 ÷ 17	−30%	+62%	0.85	38%
Whiffen	44	2 ÷ 28	−41%	+24%	1.10	35%
	20	28 ÷ 65	−41%	0%	1.26	26%
UTHM	8	2 ÷ 12	−14%	+95%	0.71	39%
	43	12 ÷ 65	−27%	+9%	1.10	20%
Average	92	2 ÷ 65	−42%	+2%	1.25	27%

Table 10. Summary of data for evaluating performance of penetration models on the basis of the indexes \hat{k} and $\hat{\epsilon}_*$.

($\tilde{\epsilon}_{\text{max}}$ strongly deviates from $-\tilde{\epsilon}_{\text{min}}$), predictions of the models are also biased in these cases. Therefore in practice it is not recommended to directly use the predictions of any one of these models for the indicated range of penetration conditions.

Let us introduce for each model the correction factor, $\hat{k} > 0$, which allows us to reduce or increase the predicted value of the DOP, that is, replace the calculated values, H , by $\hat{k}H$. Then, taking into account (101), the *new* errors of the model’s predictions, $\hat{\epsilon}$, can be expressed through the *old*, $\tilde{\epsilon}$, as

$$\hat{\epsilon} = \frac{\hat{k}H - H_{\text{exp}}}{H_{\text{exp}}} \cdot 100\% = \left[\hat{k} \left(\frac{H}{H_{\text{exp}}} \right) - 1 \right] \cdot 100\% = [\hat{k}(0.01\tilde{\epsilon} + 1) - 1] \cdot 100\%. \quad (102)$$

The value of \hat{k} is selected by applying the following criterion: all values of $\hat{\epsilon}$ must fall in the interval between the minimum, $-\hat{\epsilon}_*$, and the maximum, $+\hat{\epsilon}_*$, values of the errors of the corrected model. Equation (102) implies that $\hat{\epsilon}$ increases when $\tilde{\epsilon}$ is increased. Therefore, the above requirement yields the following system of equations:

$$\hat{k}(0.01\tilde{\epsilon}_{\text{min}} + 1) - 1 = -0.01\hat{\epsilon}_*, \quad \hat{k}(0.01\tilde{\epsilon}_{\text{max}} + 1) - 1 = 0.01\hat{\epsilon}_*, \quad (103)$$

which has the solution

$$\hat{k} = \frac{2}{2 + 0.01(\tilde{\epsilon}_{\text{min}} + \tilde{\epsilon}_{\text{max}})}, \quad \hat{\epsilon}_* = \frac{\tilde{\epsilon}_{\text{max}} - \tilde{\epsilon}_{\text{min}}}{2 + 0.01(\tilde{\epsilon}_{\text{min}} + \tilde{\epsilon}_{\text{max}})}. \quad (104)$$

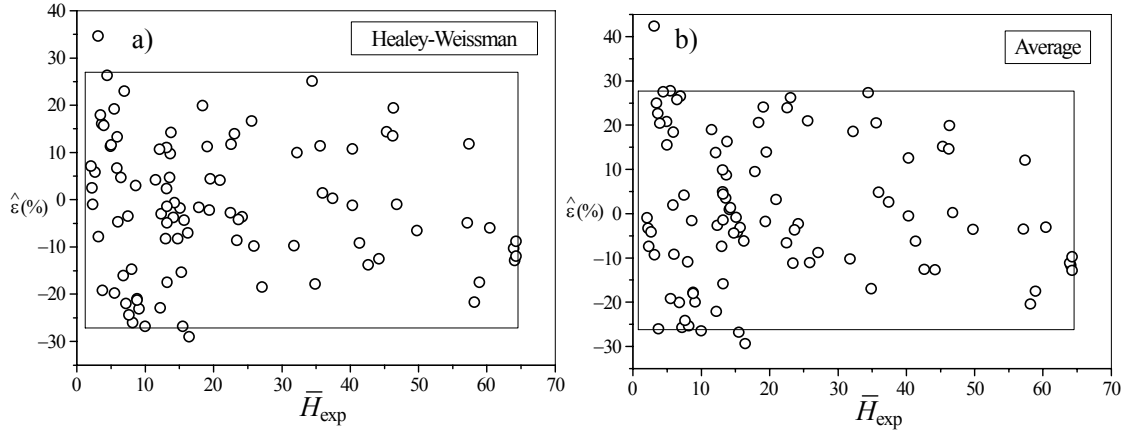


Figure 5. Comparison of the DOPs predicted using the recommended corrected empirical model with the results of experiments.

The values of parameters \hat{k} and $\hat{\epsilon}_*$ for all models are presented in Table 10. Now the performances of the corrected models can be evaluated by using only one fundamental parameter, $\tilde{\epsilon}$, which is related with their errors. In the study of the performance of a certain empirical model which is based on the same experimental data, Hansson [2003] also suggested introducing a correction factor, although he did not devise an unambiguous procedure for determining the correction coefficient.

In selecting the best model, we take into account the following considerations: the number of sub-ranges; the error interval of the corrected model, $2\hat{\epsilon}_*$; the proximity of the absolute value of the coefficient \hat{k} to 1; and the number of points, N . Inspection of Table 10 shows that at the first stage it is appropriate to select for further consideration those models which span the whole range $2 \leq \bar{H}_{\text{exp}} \leq 65$ without dividing it into subranges and having a parameter $\hat{\epsilon}_*$ that only slightly differs from the minimal (among all models) value. These models include the modified NDRC, Degen, Kar, Healey–Weissman, and average models, for which $26\% \leq \hat{\epsilon}_* \leq 27\%$. Among the remaining five models the performance of the modified NDRC, Degen, and Kar models is inferior to the rest as they are characterized by comparatively large values of \hat{k} .

Therefore, the most appropriate models are the Healey–Weissman and average models, which are corrected using the correction factors 1.26 and 1.25, respectively, and which are expected to have error $\pm 27\%$. Figure 5 illustrates the distribution of errors for these corrected models.

We used a comparatively simple approach for the comparison and evaluation of the performance of different penetration models. It is feasible to employ other approaches that are more heavily based on the methods of mathematical statistics. In particular, different models can be interpreted as regression equations, and the correction factor for each model can be interpreted as a regression coefficient. Clearly, models with several regression coefficients can be also considered. However, in this case as well, unambiguous procedures for solving the problem cannot be devised [Draper and Smith 1998].

31. Concluding remarks

We would like to draw attention to some peculiarities of the procedures for evaluating the performance and accuracy of empirical penetration models.

Firstly, analysis of the accuracy of a model which employs the same data used for the model derivation is questionable. Secondly, while a model with multiple parameters, based on a few experimental points, can be quite accurate at these points, good predictive properties of the model cannot be guaranteed. In the limiting case, one can suggest a model where the number of parameters is equal to the number of the experimental points. The errors of the approximation at these experimental points vanish while the accuracy of the model at other points can be inadequate. Thirdly, it is not worthwhile to overvalue statistical estimates of the reliability of a model since many of these estimates are based on a number of questionable assumptions.

Appendix

Most of the types of dependencies between \bar{b}_{perf} and \bar{H} and between \bar{b}_{scab} and \bar{H} can be described as

$$\bar{b}_{p/s} = \Psi_{p/s}(\bar{H}) = \begin{cases} \beta^{(1)} + \alpha^{(1)}\bar{H} - \gamma^{(1)}\bar{H}^2 & \text{if } \bar{H}_{\min}^{(1)} \leq \bar{H} \leq \bar{H}_{\max}^{(1)}, \\ \vdots & \vdots \\ \beta^{(i)} + \alpha^{(i)}\bar{H} - \gamma^{(i)}\bar{H}^2 & \text{if } \bar{H}_{\min}^{(i)} \leq \bar{H} \leq \bar{H}_{\max}^{(i)}, \\ \vdots & \vdots \\ \beta^{(n)} + \alpha^{(n)}\bar{H} - \gamma^{(n)}\bar{H}^2 & \text{if } \bar{H}_{\min}^{(n)} \leq \bar{H} \leq \bar{H}_{\max}^{(n)}, \end{cases} \quad (\text{A.1})$$

where it is assumed that all parameters $\alpha^{(i)}$, $\beta^{(i)}$, and $\gamma^{(i)}$ are nonnegative and functions $\Psi_{p/s}$ are continuous at the joint points of the adjacent segments:

$$\bar{H}_{\max}^{(i)} = \bar{H}_{\min}^{(i+1)}, \quad i = 1, 2, \dots, n-1, \quad (\text{A.2})$$

$$\beta^{(i)} + \alpha^{(i)}\bar{H}_{\max}^{(i)} - \gamma^{(i)}[\bar{H}_{\max}^{(i)}]^2 = \beta^{(i)} + \alpha^{(i)}\bar{H}_{\min}^{(i+1)} - \gamma^{(i)}[\bar{H}_{\min}^{(i+1)}]^2, \quad i = 1, 2, \dots, n-1. \quad (\text{A.3})$$

The subscript p/s denotes ‘‘perforation’’ or ‘‘scabbing’’. Clearly, the parameters $\alpha^{(i)}$, $\beta^{(i)}$, $\gamma^{(i)}$, $\bar{H}_{\min}^{(i)}$, and $\bar{H}_{\max}^{(i)}$ should have the same additional subscripts, p or s , which are omitted for simplicity.

If $\gamma^{(i)} = 0$, then $\Psi_{p/s}(\bar{H})$ is an increasing function on the i -th interval ($i = 1, 2, \dots, n$). If $\gamma^{(i)} > 0$, then $\Psi_{p/s}(\bar{H})$ is an increasing function when

$$\bar{H}_{\max}^{(i)} < \bar{H}_*^{(i)}, \quad \bar{H}_*^{(i)} = 0.5\alpha^{(i)}/\gamma^{(i)}, \quad i = 1, 2, \dots, n \quad (\text{A.4})$$

The constraints given by (A.4) must be taken into account when the admissible ranges of the parameters are indicated.

Taking into account (A.1), (2) and (4) can be rewritten as

$$\bar{b}_{p/s} = \Xi_{p/s}(\bar{v}_{\text{imp}}) = \begin{cases} \beta^{(1)} + \alpha^{(1)}\phi(\bar{v}_{\text{imp}}) - \gamma^{(1)}[\phi(\bar{v}_{\text{imp}})]^2 & \text{if } \phi^{-1}(\bar{H}_{\min}^{(1)}) \leq \bar{v}_{\text{imp}} \leq \phi^{-1}(\bar{H}_{\max}^{(1)}), \\ \vdots & \vdots \\ \beta^{(i)} + \alpha^{(i)}\phi(\bar{v}_{\text{imp}}) - \gamma^{(i)}[\phi(\bar{v}_{\text{imp}})]^2 & \text{if } \phi^{-1}(\bar{H}_{\min}^{(i)}) \leq \bar{v}_{\text{imp}} \leq \phi^{-1}(\bar{H}_{\max}^{(i)}), \\ \vdots & \vdots \\ \beta^{(n)} + \alpha^{(n)}\phi(\bar{v}_{\text{imp}}) - \gamma^{(n)}[\phi(\bar{v}_{\text{imp}})]^2 & \text{if } \phi^{-1}(\bar{H}_{\min}^{(n)}) \leq \bar{v}_{\text{imp}} \leq \phi^{-1}(\bar{H}_{\max}^{(n)}), \end{cases} \quad (\text{A.5})$$

$$\bar{v}_{bl/sl} = \Xi_{\text{perf}}^{-1}(\bar{b}) = \begin{cases} \phi^{-1}(\bar{H}^{(1)}) & \text{if } \beta^{(1)} + \alpha^{(1)}\bar{H}_{\min}^{(1)} - \gamma^{(1)}[\bar{H}_{\min}^{(1)}]^2 \leq \bar{b} \leq \beta^{(1)} + \alpha^{(1)}\bar{H}_{\max}^{(1)} - \gamma^{(1)}[\bar{H}_{\max}^{(1)}]^2, \\ \vdots & \vdots \\ \phi^{-1}(\bar{H}^{(i)}) & \text{if } \beta^{(i)} + \alpha^{(i)}\bar{H}_{\min}^{(i)} - \gamma^{(i)}[\bar{H}_{\min}^{(i)}]^2 \leq \bar{b} \leq \beta^{(i)} + \alpha^{(i)}\bar{H}_{\max}^{(i)} - \gamma^{(i)}[\bar{H}_{\max}^{(i)}]^2, \\ \vdots & \vdots \\ \phi^{-1}(\bar{H}^{(n)}) & \text{if } \beta^{(n)} + \alpha^{(n)}\bar{H}_{\min}^{(n)} - \gamma^{(n)}[\bar{H}_{\min}^{(n)}]^2 \leq \bar{b} \leq \beta^{(n)} + \alpha^{(n)}\bar{H}_{\max}^{(n)} - \gamma^{(n)}[\bar{H}_{\max}^{(n)}]^2, \end{cases} \quad (\text{A.6})$$

where the subscript *bl/sl* denotes the BLV and scabbing limit velocity, and $\bar{H}^{(i)}$ is a root of the equation

$$\beta^{(i)} + \alpha^{(i)}\bar{H}^{(i)} - \gamma^{(i)}[\bar{H}^{(i)}]^2 = \bar{b}, \quad (\text{A.7})$$

which is given by

$$\bar{H}^{(i)} = \sqrt{\left[\frac{\alpha^{(i)}}{2\gamma^{(i)}}\right]^2 + \frac{\bar{b} - \beta^{(i)}}{\gamma^{(i)}}} - \frac{\alpha^{(i)}}{2\gamma^{(i)}} \quad \text{if } \gamma^{(i)} > 0, \quad (\text{A.8})$$

$$\bar{H}^{(i)} = \frac{\bar{b} - \beta^{(i)}}{\alpha^{(i)}} \quad \text{if } \gamma^{(i)} = 0. \quad (\text{A.9})$$

References

- [ACE 1946] “Fundamentals of protective structures”, Report AT120 AT1207821, Army Corps of Engineers, Office of the Chief of Engineers, 1946.
- [ACI 1978] “Building code requirements for reinforced concrete”, ACI Standard 318-77, American Concrete Institute, Detroit, MI, 1978.
- [Adeli and Amin 1985] H. Adeli and A. M. Amin, “Local effects of impactors on concrete structures”, *Nucl. Eng. Des.* **88**:3 (1985), 301–317.
- [Al-Hachamee and Azeez 2010] E. K. S. Al-Hachamee and H. A. Azeez, “Scabbing and perforation local effect of impactors on concrete structures”, *Eng. Tech. J.* **28**:9 (2010), 1757–1770.
- [Amde et al. 1997] A. M. Amde, A. Mirmiran, and T. A. Walter, “Local damage assessment of turbine missile impact on composite and multiple barriers”, *Nucl. Eng. Des.* **178**:1,2 (1997), 145–156.
- [Amirikian 1950] A. Amirikian, “Design of protective structures: a new concept of structural behavior”, Report NT-3726, Bureau of Yards and Docks, Department of the Navy, Washington, DC, 1950.
- [Bangash 2009] M. Y. H. Bangash, *Shock, impact and explosion: structural analysis and design*, Springer, Berlin, 2009.
- [Bangash and Bangash 2006] M. Y. H. Bangash and T. Bangash, *Explosion-resistant buildings: design, analysis, and case studies*, Springer, Berlin, 2006.

- [Barr 1990] P. Barr (editor), *Guidelines for the design and assessment of concrete structures subjected to impact*, United Kingdom Atomic Energy Authority, Safety and Reliability Directorate, 1990.
- [Ben-Dor et al. 2005] G. Ben-Dor, A. Dubinsky, and T. Elperin, “Ballistic impact: recent advances in analytical modeling of plate penetration dynamics — a review”, *Appl. Mech. Rev. (ASME)* **58**:6 (2005), 355–371.
- [Ben-Dor et al. 2006] G. Ben-Dor, A. Dubinsky, and T. Elperin, *Applied high-speed plate penetration dynamics*, Solid mechanics and its applications **132**, Springer, Dordrecht, 2006.
- [Ben-Dor et al. 2008a] G. Ben-Dor, A. Dubinsky, and T. Elperin, “Engineering approach to penetration modeling”, *Eng. Fract. Mech.* **75**:14 (2008), 4279–4282.
- [Ben-Dor et al. 2008b] G. Ben-Dor, A. Dubinsky, and T. Elperin, “Optimization of penetration into geological and concrete shields by impactor with jet thruster”, *J. Mech. Mater. Struct.* **3**:4 (2008), 707–727.
- [Berriaud et al. 1978] C. Berriaud, A. Sokolovsky, R. Gueraud, J. Dulac, and R. Labrot, “Local behaviour of reinforced concrete walls under missile impact”, *Nucl. Eng. Des.* **45**:2 (1978), 457–469.
- [BNFL 2003] “Reinforced concrete slab local damage assessment, R3 impact assessment procedure”, Magnox Electric plc and Nuclear Electric Limited, 2003. Appendix H.
- [Brown 1986] S. J. Brown, “Energy release protection for pressurized systems, II: Review of studies into impact/terminal ballistics”, *Appl. Mech. Rev. (ASME)* **39**:2 (1986), 177–201.
- [Bulson 1997] P. S. Bulson, *Explosive loading of engineering structures: A history of research and a review of recent developments*, E. & F. N. Spon, London, 1997.
- [Carlucci and Jacobson 2007] D. E. Carlucci and S. S. Jacobson, *Ballistics: theory and design of guns and ammunition*, CRC Press, 2007.
- [Chang 1981] W. S. Chang, “Impact of solid missiles on concrete barriers”, *J. Struct. Div. (ASCE)* **107**:2 (1981), 257–271.
- [Chelapati et al. 1972] C. V. Chelapati, R. P. Kennedy, and I. B. Wall, “Probabilistic assessment of aircraft hazard for nuclear power plants”, *Nucl. Eng. Des.* **19**:2 (1972), 333–364.
- [Corbett et al. 1996] G. G. Corbett, S. R. Reid, and W. Johnson, “Impact loading of plates and shells by free-flying projectiles: a review”, *Int. J. Impact Eng.* **18**:2 (1996), 141–230.
- [Dancygier 1997] A. N. Dancygier, “Effect of reinforcement ratio on the resistance of reinforced concrete to hard projectile impact”, *Nucl. Eng. Des.* **172**:1–2 (1997), 233–245.
- [Dancygier 2000] A. N. Dancygier, “Scaling of non-proportional non-deforming projectiles impacting reinforced concrete barriers”, *Int. J. Impact Eng.* **24**:1 (2000), 33–55.
- [Dancygier and Yankelevsky 1996] A. N. Dancygier and D. Z. Yankelevsky, “High strength concrete response to hard projectile impact”, *Int. J. Impact Eng.* **18**:6 (1996), 583–599.
- [Daudeville and Malécot 2011] L. Daudeville and Y. Malécot, “Concrete structures under impact”, *Eur. J. Environ. Civ. Eng.* **15**:(SI) (2011), 101–140.
- [Degen 1980] P. P. Degen, “Perforation of reinforced concrete slabs by rigid missiles”, *J. Struct. Div. (ASCE)* **106**:7 (1980), 1623–1642.
- [DOE 2006] “Accident analysis for aircraft crash into hazardous facilities”, DOE-STD-3014-2006, U. S. Department of Energy, Washington, DC, 2006.
- [Draper and Smith 1998] N. R. Draper and H. Smith, *Applied regression analysis*, 3rd ed., Wiley, New York, 1998.
- [Folsom 1987] E. N. Folsom, Jr., “Projectile penetration into concrete with an inline hole”, Report UCRL-53786, Lawrence Livermore National Laboratory, Livermore, CA, 1987.
- [Fullard and Barr 1989] K. Fullard and P. Barr, “Development of design guidance for low velocity impacts on concrete floors”, *Nucl. Eng. Des.* **115**:1 (1989), 113–120.
- [Fullard et al. 1991] K. Fullard, M. R. Baum, and P. Barr, “The assessment of impact on nuclear power plant structures in the United Kingdom”, *Nucl. Eng. Des.* **130**:2 (1991), 113–120.
- [Guirgis and Guirguis 2009] S. Guirgis and E. Guirguis, “An energy approach study of the penetration of concrete by rigid missiles”, *Nucl. Eng. Des.* **239**:4 (2009), 819–829.

- [Gwaltney 1968] R. C. Gwaltney, "Missile generation and protection in light-water-cooled power reactor plants", Report ORNL-NSIC-22, Oak Ridge National Laboratory, Oak Ridge, TN, 1968, Available at <http://www.ornl.gov/info/reports/1968/3445605812920.pdf>.
- [Haldar and Hamieh 1984] A. Haldar and H. Hamieh, "Local effect of solid missiles on concrete structures", *J. Struct. Eng. (ASCE)* **110**:5 (1984), 948–960.
- [Haldar and Miller 1982] A. Haldar and F. J. Miller, "Penetration depth in concrete for nondeformable missiles", *Nucl. Eng. Des.* **71**:1 (1982), 79–88.
- [Haldar et al. 1984] A. Haldar, H. A. Hamieh, and F. J. Miller, "Penetration and spallation depth estimation for concrete structures", in *7th International Conference on Structural Mechanics in Reactor Technology* (Chicago, 1983), 1984. Paper J7/2.
- [Hansson 2003] H. Hansson, "A note on empirical formulas for the prediction of concrete penetration", Report FOI-R-0968-SE, Swedish Defence Research Agency (FOI), Tumba, Sweden, 2003, Available at <http://nisee.berkeley.edu/elibrary/Text/201202295>.
- [Healey and Weissman 1974] J. J. Healey and S. Weissman, "Primary fragment characteristics and impact effects in protective design", pp. 1107–1141 in *Minutes of the 16th Explosives Safety Seminar* (Hollywood, FL, 1974), Department of Defense Explosives Safety Board, Washington, DC, 1974.
- [Healey et al. 1975] J. Healey, S. Weissman, H. Werner, N. Dobbs, and P. Price, "Primary fragment characteristics and impact effects on protective barriers", Report 4903, Picatinny Arsenal, Dover, NJ, 1975.
- [Hughes 1984] G. Hughes, "Hard missile impact on reinforced concrete", *Nucl. Eng. Des.* **77**:1 (1984), 23–35.
- [Jankov et al. 1977] Z. D. Jankov, J. A. Shanahan, and M. P. White, "Missile tests of quarter-scale reinforced concrete barriers", in *Proceedings of the Symposium on Tornadoes, Assessment of Knowledge and Implications for Man* (Lubbock, TX, 1976), Institute for Disaster Research, Texas Tech University, Lubbock, TX, 1977.
- [Kar 1978] A. K. Kar, "Local effects of tornado-generated missiles", *J. Struct. Div. (ASCE)* **104**:5 (1978), 809–816.
- [Kar 1979] A. K. Kar, "Residual velocity for projectiles", *Nucl. Eng. Des.* **53**:1 (1979), 87–95.
- [Kennedy 1976] R. P. Kennedy, "A review of procedures for the analysis and design of concrete structures to resist missile impact effects", *Nucl. Eng. Des.* **37**:2 (1976), 183–203.
- [Latif et al. 2011] Q. B. I. Latif, I. A. Rahman, and A. M. A. Zaidi, "Development of empirical formula prediction on critical impact energy for perforation phenomena on concrete structures", *J. Math. Res.* **3**:1 (2011), 83–87.
- [Li and Tong 2003] Q. M. Li and D. J. Tong, "Perforation thickness and ballistic limit of concrete target subjected to rigid projectile impact", *J. Eng. Mech. (ASCE)* **129**:9 (2003), 1083–1091.
- [Li et al. 2005] Q. M. Li, S. R. Reid, H. M. Wen, and A. R. Telford, "Local impact effects of hard missiles on concrete targets", *Int. J. Impact Eng.* **32**:1–4 (2005), 224–284.
- [Li et al. 2006] Q. M. Li, S. R. Reid, and A. M. Ahmad-Zaidi, "Critical impact energies for scabbing and perforation of concrete target", *Nucl. Eng. Des.* **236**:11 (2006), 1140–1148.
- [Linderman et al. 1974] R. B. Linderman, J. V. Rotz, and G. C. K. Yeh, "Design of structures for missile impact", Topical report BC-TOP-9, Bechtel Power Corporation, San Francisco, CA, 1974. Revision 2.
- [Me-Bar 1997] Y. Me-Bar, "A method for scaling ballistic penetration phenomena", *Int. J. Impact Eng.* **19**:9–10 (1997), 821–829.
- [NDRC 1946] "Effects of impact and explosion", National Defence Research Committee, Washington, DC, 1946, Available at <http://www.dtic.mil/docs/citations/AD0221586>. Summary technical report of division 2.
- [Ohnuma et al. 1985] H. Ohnuma, C. Ito, and S. G. Nomachi, "Dynamic response and local rupture of reinforced concrete beam and slab under impact loading", pp. 179–184 in *8th International Conference on Structural Mechanics in Reactor Technology* (Brussels, Belgium, 1985), 1985. Paper J5/3.
- [Pétry 1910] L. Pétry, *Monographies de systèmes d'artillerie*, Brussels, 1910.
- [Rahman et al. 2010] I. A. Rahman, A. M. A. Zaidi, Q. B. I. Latif, and M. Y. Ismail, "Empirical formula prediction on critical impact energy for scabbing phenomena on concrete structures", *Appl. Phys. Res.* **2**:2 (2010), 192–197.

- [Reid and Wen 2001] S. R. Reid and H. Wen, “Predicting penetration, cone cracking, scabbing and perforation of reinforced concrete targets struck by flat-faced projectiles”, Report ME/AM/02.01/TE/G/018507/Z, University of Manchester Institute of Science and Technology, Manchester, United Kingdom, 2001.
- [Riera 1989] J. D. Riera, “Penetration, scabbing and perforation of concrete structures hit by solid missiles”, *Nucl. Eng. Des.* **115**:1 (1989), 121–131.
- [Rotz 1975] J. V. Rotz, “Results of missile impact tests on reinforced concrete panels”, pp. 720–738 in *2nd ASCE Specialty Conference on Structural Design of Nuclear Plant Facilities* (New Orleans, LA, 1975), vol. 1-A, American Society of Civil Engineers, 1975.
- [Rotz 1977] J. V. Rotz, “Evaluation of tornado missile impact effects on structures”, in *Proceedings of the Symposium on Tornadoes, Assessment of Knowledge and Implications for Man* (Lubbock, TX, 1976), Institute for Disaster Research, Texas Tech University, Lubbock, TX, 1977.
- [Samuely and Hamann 1939] F. J. Samuely and C. W. Hamann, *Civil protection: the application of the civil defence act and other government requirements for air raid shelters etc.*, Architectural Press, London, 1939.
- [Sliter 1980] G. E. Sliter, “Assessment of empirical concrete impact formulas”, *J. Struct. Div. (ASCE)* **106**:5 (1980), 1023–1045.
- [Szuladziński 2009] G. Szuladziński, *Formulas for mechanical and structural shock and impact*, CRC Press, Boca Raton, FL, 2009.
- [Teland 1998] J. A. Teland, “A review of empirical equations for missile impact effects on concrete”, Report FFI/RAPPORT-97/05856, Norwegian Defence Research Establishment (FFI), Kjeller, Norway, 1998, Available at <http://rapporter.ffi.no/rapporter/97/05856.pdf>.
- [Teland 1999] J. A. Teland, “A review of analytical penetration mechanics”, Report FFI/RAPPORT-99/01264, Norwegian Defence Research Establishment (FFI), Kjeller, Norway, 1999.
- [Teland 2001] J. A. Teland, “Cavity expansion theory applied to penetration of targets with pre-drilled cavities”, pp. 1329–1335 in *Proceedings of the 19th International Symposium on Ballistics* (Interlaken, Switzerland, 2001), vol. 3, edited by I. R. Crewther, 2001.
- [TM 5-1300 1990] “Structures to resist the effect of accidental explosions”, Army TM 5-1300, Navy NAVFAC P-397, Air Force AFR 88-22, U.S. Departments of the Army, the Navy, and the Air Force, 1990.
- [TM 5-855-1 1986] “Fundamentals of protective design for conventional weapons”, TM 5-855-1, U.S. Department of the Army, Washington, DC, 1986, Available at <http://pbadupws.nrc.gov/docs/ML1019/ML101970069.pdf>.
- [Vossoughi et al. 2007] F. Vossoughi, C. P. Ostertag, P. J. M. Monteiro, and G. C. Johnson, “Resistance of concrete protected by fabric to projectile impact”, *Cement Concrete Res.* **37**:1 (2007), 96–106.
- [Vretblad 1988] B. Vretblad, “Penetration of projectiles in concrete according to Forth 1”, in *Proceedings from the Workshop on Weapon Penetration into Hard Targets* (Kjeller, Norway, 1988), Norwegian Defence Research Establishment (FFI), 1988.
- [Walter and Wolde-Tinsae 1984] T. A. Walter and A. M. Wolde-Tinsae, “Turbine missile perforation of reinforced concrete”, *J. Struct. Eng. (ASCE)* **110**:10 (1984), 2439–2455.
- [Whiffen 1943] P. Whiffen, Note no. MOS/311, UK Road Research Laboratory, 1943.
- [Williams 1994] M. S. Williams, “Modeling of local impact effects on plain and reinforced concrete”, *ACI Struct. J.* **91**:2 (1994), 178–187.
- [Yankelevsky 1997] D. Z. Yankelevsky, “Local response of concrete slabs to low velocity missile impact”, *Int. J. Impact Eng.* **19**:4 (1997), 331–343.
- [Young 1997] C. W. Young, “Penetration equations”, Report SAND97-2426, Sandia National Laboratories, Albuquerque, NM, 1997.
- [Zaidi et al. 2010] A. M. A. Zaidi, Q. B. A. I. Latif, I. A. Rahman, and M. Y. Ismail, “Development of empirical prediction formula for penetration of ogive nose hard missile into concrete targets”, *Amer. J. Appl. Sci.* **7**:5 (2010), 711–716.

Received 22 Dec 2012. Revised 21 Mar 2013. Accepted 3 Jun 2013.

GABI BEN-DOR: bendorg@bgu.ac.il

*Pearlstone Center for Aeronautical Engineering, Department of Mechanical Engineering, Ben-Gurion University of the Negev,
P.O. Box 653, 84105 Beer-Sheva, Israel*

ANATOLY DUBINSKY: dubin@bgu.ac.il

*Pearlstone Center for Aeronautical Engineering, Department of Mechanical Engineering, Ben-Gurion University of the Negev,
P.O. Box 653, 84105 Beer-Sheva, Israel*

TOV ELPERIN: elperin@bgu.ac.il

*Pearlstone Center for Aeronautical Engineering, Department of Mechanical Engineering, Ben-Gurion University of the Negev,
P.O. Box 653, 84105 Beer-Sheva, Israel*

TRANSIENT RESPONSE OF A GENERAL ANISOTROPIC SOLID TO DISLOCATION GROWTH: ALTERNATIVE FORMULATION

LOUIS MILTON BROCK

The response of an unbounded homogeneous general anisotropic solid to dislocation growth can be obtained from a convolution of the body force equivalent of the dislocation with the Green's function. This work considers the transient case of a surface of discontinuity in displacement that expands with time from a point source. The expansion rate is subsonic, but largely arbitrary otherwise. The surface need not be planar, and if so, need not lie in a principal material plane. Some differences in procedure from related studies are noted. The solution expressions use a dislocation description in terms of surface geometry, and have a hybrid but somewhat more explicit form.

1. Introduction

The radiation field from a spreading dislocation is known [Nabarro 1951; Knopoff and Gilbert 1960] to be obtainable in terms of solutions to the fundamental problems of point forces and couples and their line load counterparts. Such loads can be generalized as the transient body-force equivalent for a dislocation distribution on an internal surface [Burrige and Knopoff 1964]. The equivalent is valid for the inhomogeneous, anisotropic solid, and surface and distribution are (largely) arbitrary.

This article gives an exact transient solution for the growth of a dislocation distribution in a homogeneous, general anisotropic and unbounded solid in terms of the Burrige–Knopoff equivalent. The dislocation spreads at a subsonic (possibly nonuniform) rate from a point source. The dislocation distribution is single valued and remains finite for finite time after its appearance. This problem is not new, but the present study includes some alternative features.

In [Burrige and Knopoff 1964] the dislocation field is defined in terms of the components of a prescribed displacement discontinuity in the principal material basis. For insight into the roles of climb and glide mechanisms, two descriptions of the displacement discontinuity vector are treated here. The first resolves the prescribed displacement discontinuity vector into components normal to, and in the plane of, the surface. Coefficient arrays (d_{ik}^{NS} , d_{ik}^{NN}) arise, and a third, d_{ik}^{SS} , can be defined. Subscripts (i , k) refer to Cartesian coordinates (x_1 , x_2 , x_3) in the principal material basis, and (N , S) refer to coordinates normal to and in the plane of the discontinuity surface. The arrays are symmetric in (N , S), and the six elements of each array are symmetric in (i , k). The form of d_{ik}^{NS} resembles the constitutive equation for the general anisotropic solid.

The second description treated is local, that is, it is the components of the displacement discontinuity vector with respect to surface geometry that are prescribed. Three coefficient arrays (d_{ik}^{NT} , d_{ik}^{NS} , d_{ik}^{NN}) arise, and arrays (d_{ik}^{TT} , d_{ik}^{SS} , d_{ik}^{TS}) are also defined. Here N refers to the surface normal and (T , S) are

Keywords: transient 3D, dislocation, exact solution, general anisotropy, wave speeds.

two perpendicular directions in the surface plane. Use of this description in the transient solutions is demonstrated for a planar discontinuity surface, for which coefficient arrays are constant.

The analysis is similar to that for the anisotropic Green's function. That problem is also not new, nor is the use of integral transforms [Willis 1980; Payton 1983; Wang and Achenbach 1994; 1995; Ting and Lee 1997]. Here unilateral temporal and bilateral spatial Laplace transforms [van der Pol and Bremmer 1950; Sneddon 1972] are employed. The spatial transforms are with respect to the Cartesian principal basis, but quasispherical coordinates are introduced in the inversion process. This facilitates the residue calculation process common in anisotropic Green's function study in, for example, [Payton 1983; Wang and Achenbach 1994; 1995; Ting and Lee 1997]. Moreover, the displacements take a hybrid form: their components and coordinates are Cartesian, but the expressions are integrals of real-valued functions in a unit quarter-sphere. Although lacking the simplicity of integration based on the hypercircle or unit sphere [Synge 1957; Wang and Achenbach 1995], the integration is explicitly in terms of polar and azimuthal angles defined in the fixed principal basis. For the uniform dislocation distribution, in fact, integration can be transformed to the contour of the dislocation surface; see [Brock 1986]. Analytical expressions for the poles in the residue calculation — and therefore the three anisotropic wave speeds — are also presented; see [Wang and Achenbach 1995].

Finally, it is noted that some well-known formalisms for anisotropy, for example, [Stroh 1958; 1962; Barnett and Lothe 1973; Ting 1996; Ting and Lee 1997], are not invoked here. However, analogous formulas arise in the course of analysis. Solution expression development is the focus here but, for illustration, sample wave speed calculations are given for a transversely isotropic graphite-epoxy solid.

2. Governing equations

A Cartesian basis $\mathbf{x}(x_1, x_2, x_3)$ defines the principal material axes for an unbounded, homogeneous linear anisotropic solid. In contracted notation, the stress and strain measures (σ_k, ϵ_k) for the solid are related by

$$\sigma_k = C_{kl}\epsilon_l, \quad C_{kl} = C_{lk}. \quad (1)$$

Here (k, l) take on values $(1, 2, 3, 4, 5, 6)$ and the 21 elasticity parameters C_{kl} are constants. These measures correspond to those in the Cartesian basis as follows: For $k = (1, 2, 3)$

$$\sigma_k = \sigma_{kk}, \quad \epsilon_k = \partial_k u_k. \quad (2)$$

The range $k = (4, 5, 6)$ corresponds to Cartesian shear stresses and strains:

$$\sigma_4 = \sigma_{23} = \sigma_{32}, \quad \epsilon_4 = \partial_2 u_3 + \partial_3 u_2, \quad (3a)$$

$$\sigma_5 = \sigma_{31} = \sigma_{13}, \quad \epsilon_5 = \partial_3 u_1 + \partial_1 u_3, \quad (3b)$$

$$\sigma_6 = \sigma_{12} = \sigma_{21}, \quad \epsilon_6 = \partial_1 u_2 + \partial_2 u_1. \quad (3c)$$

Equation (1) is associated with positive strain energy density when $\epsilon_k^T C_{kl} \epsilon_l > 0$. Because C_{kl} constitutes a symmetric 6×6 matrix with real elements, it can be shown [Hohn 1964; Ting 1996] that the inequality is satisfied when the leading principal minors of C_{kl} are positive, that is,

$$\begin{vmatrix} C_{11} & C_{12} & \cdots & C_{1n} \\ C_{12} & C_{22} & \cdots & C_{2n} \\ \vdots & \vdots & \ddots & \vdots \\ C_{1n} & C_{2n} & \cdots & C_{nn} \end{vmatrix} > 0 \quad (n \leq 6). \tag{4}$$

In (1)–(3) u_k are the components of \mathbf{u} in the x_k -direction, and ∂_k signifies differentiation with respect to x_k . It is convenient to introduce reference shear modulus and rotational wave speed (μ, v_S) , where

$$\mu = \max(C_{44}, C_{55}, C_{66}), \quad v_S = \sqrt{\frac{\mu}{\rho}}. \tag{5}$$

Here ρ is the mass density, and use of (5) gives the time-dependent length measure $\tau = v_S \times (\text{time})$. Therefore $u_k = u_k(\mathbf{x}, \tau)$ and $\sigma_{kl} = \sigma_{kl}(\mathbf{x}, \tau)$ in (2) and (3), and for $\tau < 0$ the unbounded solid is at rest. For $\tau > 0$, however, a surface \mathfrak{R} expands from point $\mathbf{x} = 0$ at a subsonic rate, that is, for a given $\tau > 0$ all parts of its boundary contour C lie within the volumes defined by the fronts of body waves radiating from source point $\mathbf{x} = 0$. Unit vector $\mathbf{n}(\mathbf{x})$ defines the normal to \mathfrak{R} and is a continuous function of $\mathbf{x} \in \mathfrak{R}$. Surface \mathfrak{R} remains simply connected, and contour C is continuous and piecewise smooth. The surface exhibits a dislocation distribution described by a jump in displacement $[\mathbf{u}(\mathbf{x}, \tau)]$ as \mathfrak{R} is crossed in the direction of \mathbf{n} . Discontinuity $[\mathbf{u}]$ is finite and continuous in (\mathbf{x}, τ) for $\mathbf{x} \in \mathfrak{R}$ and finite $\tau > 0$. Thus, for $\tau < 0$ initial conditions are $(\mathbf{u}, \nabla \mathbf{u}) \equiv 0$, and for $\tau > 0$ the linear momentum balance can, in view of (1), be written as

$$\nabla_{kl} \epsilon_l = \mu \partial^2 u_k + Q_k(\mathbf{x}, \tau). \tag{6}$$

Here $k = (1, 2, 3)$, $l = (1, 2, 3, 4, 5, 6)$, and the summation condition applies. Operator ∂ signifies differentiation with respect to τ , and ∇_{kl} are spatial derivative operators:

$$\begin{bmatrix} \nabla_{1l} \\ \nabla_{2l} \\ \nabla_{3l} \end{bmatrix} = \begin{bmatrix} C_{1l} & C_{l6} & C_{l5} \\ C_{l6} & C_{l2} & C_{l4} \\ C_{l5} & C_{l4} & C_{l3} \end{bmatrix} \begin{bmatrix} \partial_1 \\ \partial_2 \\ \partial_3 \end{bmatrix}, \quad C_{kl} = C_{lk}. \tag{7}$$

Function Q_k is the dislocation body-force equivalent of [Burridge and Knopoff 1964] for the homogeneous case. Discontinuity $[\mathbf{u}]$ is prescribed, but vector decomposition gives

$$[\mathbf{u}] = [u_N] \mathbf{n} + [u_S] \mathbf{s}, \tag{8a}$$

$$[u_N] = [\mathbf{u}] \cdot \mathbf{n}, \quad [u_S] = |[\mathbf{u}] - ([\mathbf{u}] \cdot \mathbf{n}) \mathbf{n}|, \tag{8b}$$

$$\mathbf{s} = \frac{[\mathbf{u}] - ([\mathbf{u}] \cdot \mathbf{n}) \mathbf{n}}{|[\mathbf{u}] - ([\mathbf{u}] \cdot \mathbf{n}) \mathbf{n}|}, \quad \mathbf{n} \cdot \mathbf{s} = 0. \tag{8c}$$

Here $\mathbf{s}(\mathbf{x}, \tau)$ is a unit vector in the plane of \mathfrak{R} . Thus,

$$\frac{1}{\mu} Q_i(\mathbf{x}, \tau) = \iint_{\mathfrak{R}} dA G_{ik}(\mathbf{x}', \tau) \delta_k(\mathbf{x}; \mathbf{x}'), \tag{9a}$$

$$G_{ik}(\mathbf{x}', \tau) = d_{ik}^{NS}(\mathbf{x}', \tau) [u_S(\mathbf{x}', \tau)] + d_{ik}^{NN}(\mathbf{x}', \tau) [u_N(\mathbf{x}', \tau)], \tag{9b}$$

$$\delta_k(\mathbf{x}; \mathbf{x}') = \partial_k \delta(x_1 - x'_1) \delta(x_2 - x'_2) \delta(x_3 - x'_3). \tag{9c}$$

Area integration is over surface \mathfrak{R} with respect to the Cartesian variable \mathbf{x}' , and the δ symbol in (9c) is the Dirac function. Expressions for dimensionless coefficient arrays $(d_{ik}^{NS}, d_{ik}^{NN})$ are given in terms of

(8) in Appendix A. Combining (1)–(3) and (5)–(9) gives the uncoupled equations for u_j :

$$Du_j = D_{jk} Q_k(\mathbf{x}, \tau). \quad (10)$$

In (9) $(j, k) = (1, 2, 3)$, the summation convention applies, and

$$D = (P_{11} - \partial^2)(P_{22} - \partial^2)(P_{33} - \partial^2) + 2P_{12}P_{23}P_{31} - P_{23}^2(P_{11} - \partial^2) - P_{31}^2(P_{22} - \partial^2) - P_{12}^2(P_{33} - \partial^2), \quad (11a)$$

$$D_{ii} = (P_{jj} - \partial^2)(P_{kk} - \partial^2) - P_{jk}^2, \quad (11b)$$

$$D_{ij} = D_{ji} = P_{ik}P_{jk} - P_{ij}(P_{kk} - \partial^2). \quad (11c)$$

In (11) the subscripts (i, j, k) are not equal and take on values $(1, 2, 3)$, and the P terms are operators, where $P_{kl} = P_{lk}$ and

$$\begin{bmatrix} P_{11} \\ P_{22} \\ P_{33} \end{bmatrix} = \mathbf{K} \begin{bmatrix} \partial_1^2 \\ \partial_2^2 \\ \partial_3^2 \end{bmatrix} + 2\mathbf{L}^T \begin{bmatrix} \partial_1 \partial_2 \\ \partial_2 \partial_3 \\ \partial_3 \partial_1 \end{bmatrix}, \quad (12a)$$

$$\begin{bmatrix} P_{12} \\ P_{23} \\ P_{31} \end{bmatrix} = \mathbf{L} \begin{bmatrix} \partial_1^2 \\ \partial_2^2 \\ \partial_3^2 \end{bmatrix} + \mathbf{M} \begin{bmatrix} \partial_1 \partial_2 \\ \partial_2 \partial_3 \\ \partial_3 \partial_1 \end{bmatrix}. \quad (12b)$$

In (12) the matrices $(\mathbf{K}, \mathbf{L}, \mathbf{M})$ are given — see [Ting 1996] — by

$$\mathbf{K} = \begin{bmatrix} d_{11} & d_{66} & d_{55} \\ d_{66} & d_{22} & d_{44} \\ d_{55} & d_{44} & d_{33} \end{bmatrix}, \quad \mathbf{L} = \begin{bmatrix} d_{16} & d_{26} & d_{45} \\ d_{56} & d_{24} & d_{34} \\ d_{15} & d_{46} & d_{35} \end{bmatrix}, \quad (13a)$$

$$\mathbf{M} = \begin{bmatrix} d_{12} + d_{66} & d_{46} + d_{25} & d_{14} + d_{56} \\ d_{46} + d_{25} & d_{23} + d_{44} & d_{45} + d_{36} \\ d_{14} + d_{56} & d_{45} + d_{36} & d_{13} + d_{55} \end{bmatrix}, \quad (13b)$$

$$d_{ik} = \frac{C_{ik}}{\mu} = \frac{C_{ki}}{\mu}. \quad (13c)$$

It is noted that \mathbf{L} is asymmetric. In addition \mathbf{u} is finite as $|\mathbf{x}| \rightarrow \infty$ for finite $\tau > 0$.

3. Transform solution

To determine $\mathbf{u}(\mathbf{x}, \tau)$ the unilateral Laplace transform and multiple bilateral transform are employed [van der Pol and Bremmer 1950; Sneddon 1972]:

$$\hat{f}(p) = \int f(\tau) \exp(-p\tau) d\tau, \quad (14a)$$

$$f^*(p, q_1, q_2, q_3) = \iiint \hat{f}(p, \mathbf{x}) \exp[-p(q_1x_1 + q_2x_2 + q_3x_3)] dx_1 dx_2 dx_3. \quad (14b)$$

Here $\text{Re}(p) > 0$, the integration in (14a) is over positive τ , and the integration in (14b) is over the entire $\text{Re}(x_k)$ -axis. Application of (14) to (6) and (9) and imposing conditions for $\tau < 0$ and $|\mathbf{x}| \rightarrow \infty$ gives

the formal transform solution

$$u_j^* = \frac{q_l}{p} \int_0^\infty d\tau' \iint_{\Re} dA \frac{D_{jk}}{D} G_{kl}(x', \tau') \exp(-p)(q_1 x'_1 + q_2 x'_2 + q_3 x'_3 + \tau'). \quad (15)$$

In (15) $(j, k, l) = (1, 2, 3)$, the summation convention applies, and, from (11):

$$D = (P_{11} - 1)(P_{22} - 1)(P_{33} - 1) + 2P_{12}P_{23}P_{31} - P_{23}^2(P_{11} - 1) - P_{31}^2(P_{22} - 1) - P_{12}^2(P_{33} - 1), \quad (16a)$$

$$D_{ii} = (P_{jj} - 1)(P_{kk} - 1) - P_{jk}^2, \quad (16b)$$

$$D_{ij} = D_{ji} = P_{ik}P_{jk} - P_{ij}(P_{kk} - 1). \quad (16c)$$

In (16) the P terms follow from (12) as functions of q_k , where $P_{kl} = P_{lk}$:

$$\begin{bmatrix} P_{11} \\ P_{22} \\ P_{33} \end{bmatrix} = \mathbf{K} \begin{bmatrix} q_1^2 \\ q_2^2 \\ q_3^2 \end{bmatrix} + 2\mathbf{L}^T \begin{bmatrix} q_1 q_2 \\ q_2 q_3 \\ q_3 q_1 \end{bmatrix}, \quad (17a)$$

$$\begin{bmatrix} P_{12} \\ P_{23} \\ P_{31} \end{bmatrix} = \mathbf{L} \begin{bmatrix} q_1^2 \\ q_2^2 \\ q_3^2 \end{bmatrix} + \mathbf{M} \begin{bmatrix} q_1 q_2 \\ q_2 q_3 \\ q_3 q_1 \end{bmatrix}. \quad (17b)$$

4. Transform inversion

The formal inversion of (14b) is [van der Pol and Bremmer 1950; Sneddon 1972]

$$\hat{f}(p, x) = \left(\frac{p}{2i\pi}\right)^3 \iiint f^*(p, q_1, q_2, q_3) \exp p(x_1 q_1 + x_2 q_2 + x_3 q_3) dq_1 dq_2 dq_3. \quad (18)$$

Barring the existence of poles or branch points in f^* there, integration with respect to q_k can be taken over the entire $\text{Im}(q_k)$ -axis. Consistent with an operation commonly used in equilibrium analysis, for example, in [Ting 1996], it is convenient to introduce an orthogonal transformation

$$\begin{bmatrix} x_1 \\ x_2 \\ x_3 \end{bmatrix} = \begin{bmatrix} \cos \psi' \sin \phi' & \cos \psi' \cos \phi' & -\sin \psi' \\ \sin \psi' \sin \phi' & \sin \psi' \cos \phi' & \cos \psi' \\ \cos \phi' & -\sin \phi' & 0 \end{bmatrix} \begin{bmatrix} x \\ y \\ z \end{bmatrix}. \quad (19)$$

Here $|x, y, z| < \infty$, $|\psi'| \leq \pi/2$, and $0 \leq \phi' \leq \pi/2$ so that (x, ψ', ϕ') represents a quasispherical coordinate system, where ψ' and ϕ' correspond to the polar and azimuthal angles. Equation (19) suggests in turn the transformation

$$q_1 = q \cos \psi' \sin \phi', \quad q_2 = q \sin \psi' \sin \phi', \quad q_3 = q \cos \phi'. \quad (20)$$

Here $|\text{Im}(q)| < \infty$, $|\psi'| \leq \pi/2$, and $0 \leq \phi' \leq \pi/2$. Use of (15), (19), and (20) in (18) gives

$$\hat{u}_j = -\frac{2p\partial_l}{\pi^2} \int_0^\infty d\tau' \int_{\Phi} \sin \phi' d\phi' \int_{\Psi} d\psi' \iint_{\Re} G_{kl} \frac{dA}{2i\pi} \int |q|^2 dq \frac{\Delta_{jk}}{\Delta} \exp p[q(x - x') - \tau']. \quad (21)$$

In (21), $G_{kl} = G_{kl}(x', y', z', \psi, \phi, \tau')$, $(j, k, l) = (1, 2, 3)$, and the summation convention applies. Symbols (Φ, Ψ) signify integration over, respectively, ranges $|\psi'| \leq \pi/2$ and $0 \leq \phi' \leq \pi/2$, and q -integration

is over the entire $\text{Im}(q)$ -axis. Terms (Δ, Δ_{jk}) are

$$\Delta = III q^6 - II q^4 + I q^2 - 1, \quad (22a)$$

$$\Delta_{ii} = (q^2 B_{jj} - 1)(q^2 B_{kk} - 1) - q^4 B_{jk}^2, \quad (22b)$$

$$\Delta_{ij} = \Delta_{ji} = q^4 B_{ik} B_{jk} - q^2 B_{ij} (q^2 B_{kk} - 1). \quad (22c)$$

In (22) we have from (17)

$$\begin{bmatrix} B_{11} \\ B_{22} \\ B_{33} \end{bmatrix} = \mathbf{K} \begin{bmatrix} \cos^2 \psi' \sin^2 \phi' \\ \sin^2 \psi' \sin^2 \phi' \\ \cos^2 \phi' \end{bmatrix} + 2\mathbf{L}^T \begin{bmatrix} \cos \psi' \sin \psi' \sin^2 \phi' \\ \sin \psi' \sin \phi' \cos \phi' \\ \cos \psi' \sin \phi' \cos \phi' \end{bmatrix}, \quad (23a)$$

$$\begin{bmatrix} B_{12} \\ B_{23} \\ B_{31} \end{bmatrix} = \mathbf{L} \begin{bmatrix} \cos^2 \psi' \sin^2 \phi' \\ \sin^2 \psi' \sin^2 \phi' \\ \cos^2 \phi' \end{bmatrix} + \mathbf{M} \begin{bmatrix} \cos \psi' \sin \psi' \sin^2 \phi' \\ \sin \psi' \sin \phi' \cos \phi' \\ \cos \psi' \sin \phi' \cos \phi' \end{bmatrix}. \quad (23b)$$

These elements constitute a symmetric matrix

$$\mathbf{B} = \begin{bmatrix} B_{11} & B_{12} & B_{31} \\ B_{12} & B_{22} & B_{23} \\ B_{31} & B_{23} & B_{33} \end{bmatrix}. \quad (24)$$

Terms (I, II, III) in (22a) are the first, second, and third invariants of \mathbf{B} . In view of (20) B_{kl} are generated by a rotation in terms of (ψ', ϕ') involving array d_{kl} . Condition (4) is equivalent to the requirement that the principal minors of C_{kl} , and therefore d_{kl} , are positive definite (see also [Hohn 1964; Ting 1996]). This, in turn, guarantees that the principal minors of array (24) are positive definite and (22a) has three positive real roots. Because Δ is a cubic polynomial in q^2 , this is equivalent to the condition $\alpha^3 - \beta^2 > 0$, and so the three positive real roots are given by [Abramowitz and Stegun 1972]:

$$q_A^2 = \frac{1}{c_A^2}, \quad q_B^2 = \frac{1}{c_B^2}, \quad q_C^2 = \frac{1}{c_C^2}, \quad (25a)$$

$$c_A^2 = \frac{I}{3} + 2\sqrt{\alpha} \cos \frac{\Omega}{3}, \quad (c_B^2, c_C^2) = \frac{I}{3} - 2\sqrt{\alpha} \cos \frac{1}{3}(\Omega \pm \pi), \quad (25b)$$

$$\Omega = \tan^{-1} \frac{1}{\beta} \sqrt{\alpha^3 - \beta^2}, \quad \alpha = \left(\frac{I}{3}\right)^2 - \frac{II}{3}, \quad \beta = \frac{III}{3} + \frac{I}{3} \left[\left(\frac{I}{3}\right)^2 - \frac{II}{2}\right]. \quad (25c)$$

When $\alpha^3 - \beta^2 = 0$, two of the results in (25b) are identical. In view of (25a), (22a) can then be written as

$$\Delta = III (q^2 - q_A^2)(q^2 - q_B^2)(q^2 - q_C^2). \quad (26)$$

Residue theory is now used for q -integration in (21), where it is noted that nonanalytic function $|q|$ is defined on the $\text{Im}(q)$ -axis. The Δ_{11} term, for example, gives

$$\begin{aligned} & \frac{q_A \Delta_{11}(q_A)}{2III (q_A^2 - q_B^2)(q_A^2 - q_C^2)} \exp(-p)(q_A |x - x'| + \tau') + \frac{q_B \Delta_{11}(q_B)}{2III (q_B^2 - q_C^2)(q_B^2 - q_A^2)} \exp(-p)(q_B |x - x'| + \tau') \\ & + \frac{q_C \Delta_{11}(q_C)}{2III (q_C^2 - q_A^2)(q_C^2 - q_B^2)} \exp(-p)(q_C |x - x'| + \tau'). \quad (27) \end{aligned}$$

The exponential argument in (27) implies the existence of three wave speeds

$$v_A = c_A(\psi', \phi')v_S, \quad v_B = c_B(\psi', \phi')v_S, \quad v_C = c_C(\psi', \phi')v_S. \quad (28)$$

Each exponential in (27) is the unilateral transform (14a) of the Dirac function [Sneddon 1972], and analogous results hold for the other Δ terms defined by (22b) and (22c). Thus the inverse of (21) is obtained by inspection:

$$u_j = -\frac{1}{\pi^2} \int_{\Phi} \sin \phi' d\phi' \int_{\Psi} d\psi' \frac{\partial_t \partial}{III} \int_0^{\tau} d\tau' \iiint_{\mathfrak{R}} dA \Delta'_{jk} G_{kl} (T_A + T_B + T_C), \quad (29a)$$

$$T_L = \frac{\tau - \tau'}{|x - x'|M_L} \left(\tau - \tau' > \frac{|x - x'|}{c_L} \right). \quad (29b)$$

In (29b) subscript L represents A , B , or C , and

$$M_A = \left[(\tau - \tau')^2 - \left(\frac{x - x'}{c_B} \right)^2 \right] \left[(\tau - \tau')^2 - \left(\frac{x - x'}{c_C} \right)^2 \right], \quad (30a)$$

$$M_B = \left[(\tau - \tau')^2 - \left(\frac{x - x'}{c_C} \right)^2 \right] \left[(\tau - \tau')^2 - \left(\frac{x - x'}{c_A} \right)^2 \right], \quad (30b)$$

$$M_C = \left[(\tau - \tau')^2 - \left(\frac{x - x'}{c_A} \right)^2 \right] \left[(\tau - \tau')^2 - \left(\frac{x - x'}{c_B} \right)^2 \right]. \quad (30c)$$

Function Δ'_{jk} follows from (22b) and (22c) as

$$\Delta'_{ii} = [B_{jj}(\tau - \tau')^2 - (x - x')^2][B_{kk}(\tau - \tau')^2 - (x - x')^2] - B_{jk}^2(\tau - \tau')^4, \quad (31a)$$

$$\Delta'_{ij} = \Delta'_{ji} = (\tau - \tau')^2 (B_{ik}B_{jk}(\tau - \tau')^2 - B_{ij}[B_{kk}(\tau - \tau')^2 - (x - x')^2]). \quad (31b)$$

In view of (19)

$$x - x' = (x_1 - x'_1) \cos \psi' \sin \phi' + (x_2 - x'_2) \sin \psi' \sin \phi' + (x_3 - x'_3) \cos \phi'. \quad (32)$$

The subsonic restriction on the expansion of \mathfrak{R} guarantees that no part of its boundary C at a given $0 < \tau' < \tau$ violates the inequality in (29b).

5. Planar \mathfrak{R} : Adoption of local description

While the decomposition (8a) and (9b) allows identification of climb and glide, development of (29a) depends on function $[u(\mathbf{x}, \tau)]$, and use of (9b) involves time-dependent unit vector \mathbf{s} . If a local description of displacement discontinuity, that is, in terms of the geometry of \mathfrak{R} , is available, then a more explicit result is possible — especially in the case of planar \mathfrak{R} . Then (8a) and (9b) are replaced by

$$[\mathbf{u}] = [u_T]\mathbf{t} + [u_S]\mathbf{s} + [u_N]\mathbf{n}, \quad (33a)$$

$$G_{ik} = G_{ik}(t, s, \tau) = d_{ik}^{NT}[u_T] + d_{ik}^{NS}[u_S] + d_{ik}^{NN}[u_N]. \quad (33b)$$

Unit vectors $(\mathbf{t}, \mathbf{s}, \mathbf{n})$ form a fixed right-handed set ($\mathbf{t} \times \mathbf{s} = \mathbf{n}$, $\mathbf{s} \times \mathbf{n} = \mathbf{t}$, $\mathbf{n} \times \mathbf{t} = \mathbf{s}$). They are invariant in \mathfrak{R} , but the (T, S, N) components of \mathbf{u} are functions of (t, s, τ) , where (t, s) correspond to (\mathbf{t}, \mathbf{s}) and

$$\begin{bmatrix} \mathbf{n} \\ \mathbf{t} \\ \mathbf{s} \end{bmatrix} = \begin{bmatrix} n_1 & n_2 & n_3 \\ t_1 & t_2 & t_3 \\ s_1 & s_2 & s_3 \end{bmatrix} \begin{bmatrix} \mathbf{e}_1 \\ \mathbf{e}_2 \\ \mathbf{e}_3 \end{bmatrix}. \quad (34)$$

Terms (n_k, t_k, s_k) are (constant) direction cosines, \mathbf{e}_k are Cartesian basis vectors, and dimensionless coefficient arrays $(d_{ik}^{NT}, d_{ik}^{NS}, d_{ik}^{NN})$ are given in Appendix B. Normal \mathbf{n} is known, but vectors (\mathbf{t}, \mathbf{s}) in the plane of \mathfrak{R} are somewhat arbitrary. In light of (19), a convenient choice is to define \mathbf{n} in terms of polar and azimuthal angles (ψ, ϕ) , where $|\psi| < \pi/2$ and $0 < \phi < \pi/2$, and introduce for integration over \mathfrak{R} the transformation and corresponding direction cosines:

$$\begin{bmatrix} x'_1 \\ x'_2 \\ x'_3 \end{bmatrix} = \begin{bmatrix} \cos \psi \sin \phi & \cos \psi \cos \phi & -\sin \psi \\ \sin \psi \sin \phi & \sin \psi \cos \phi & \cos \psi \\ \cos \phi & -\sin \phi & 0 \end{bmatrix} \begin{bmatrix} 0 \\ t \\ s \end{bmatrix}, \quad (35a)$$

$$n_1 = \cos \psi \sin \phi, \quad n_2 = \sin \psi \sin \phi, \quad n_3 = \cos \phi, \quad (35b)$$

$$t_1 = \cos \psi \cos \phi, \quad t_2 = -\sin \psi \cos \phi, \quad t_3 = -\sin \phi, \quad (35c)$$

$$s_1 = -\sin \psi, \quad s_2 = \cos \psi, \quad s_3 = 0. \quad (35d)$$

In view of (33)–(35) the integrand of the $\psi' \phi'$ -integration in (29a) can be written as

$$\begin{aligned} d_{kl}^{NT} \partial \int_0^\tau d\tau' \iint_{\mathfrak{R}} dA [P_{jk} \partial'_l [u_T] - \partial'_l (P_{jk} [u_T])] + d_{kl}^{NS} \partial \int_0^\tau d\tau' \iint_{\mathfrak{R}} dA [P_{jk} \partial'_l [u_S] - \partial'_l (P_{jk} [u_S])] \\ + d_{kl}^{NN} \partial \int_0^\tau d\tau' \iint_{\mathfrak{R}} dA [P_{jk} \partial'_l [u_N] - \partial'_l (P_{jk} [u_N])], \end{aligned} \quad (36a)$$

where

$$P_{jk} = \Delta'_{jk} (T_A + T_B + T_C). \quad (36b)$$

Here ∂'_l represents differentiation with respect to x'_l in (32), and $(d_{kl}^{NT}, d_{kl}^{NS}, d_{kl}^{NN})$ are independent of (t, s, τ') . From (35a), P_{jk} and $([u_T], [u_S], [u_N])$ depend on (t, s, τ') and

$$\partial'_1 \rightarrow \cos \psi \sin \phi \frac{\partial}{\partial t} - \sin \psi \frac{\partial}{\partial s}, \quad \partial'_2 \rightarrow \sin \psi \cos \phi \frac{\partial}{\partial t} + \cos \psi \frac{\partial}{\partial s}, \quad \partial'_3 \rightarrow \sin \phi \frac{\partial}{\partial t}. \quad (37)$$

Use of (37) in (36) and application of Stokes's theorem [Hay 1953] allows the second terms in (36) to be replaced by line integrals around contour C . For example, the first integral over \mathfrak{R} in (36) gives for $l = (1, 2, 3)$, respectively,

$$\iint_{\mathfrak{R}} dA P_{jk} \left(\cos \psi \sin \phi \frac{\partial}{\partial t} - \sin \psi \frac{\partial}{\partial s} \right) [u_T] + \oint_C dc P_{jk} [u_T] (\sin \psi \mathbf{t} + \cos \psi \sin \phi \mathbf{s}) \cdot \mathbf{t}_C, \quad (38a)$$

$$\iint_{\mathfrak{R}} dA P_{jk} \left(\sin \psi \cos \phi \frac{\partial}{\partial t} + \cos \psi \frac{\partial}{\partial s} \right) [u_T] - \oint_C dc P_{jk} [u_T] (\cos \psi \mathbf{t} - \sin \psi \cos \phi \mathbf{s}) \cdot \mathbf{t}_C, \quad (38b)$$

$$\sin \phi \iint_{\mathfrak{R}} dA P_{jk} \frac{\partial}{\partial t} [u_T] + \sin \phi \oint_C dc P_{jk} [u_T] \mathbf{s} \cdot \mathbf{t}_C. \quad (38c)$$

Integration is counterclockwise around C in the ts -plane, \mathbf{t}_C is the unit vector tangent to C and in the direction of integration, and (32) takes the form

$$x - x' = (x_1 \cos \psi' + x_2 \sin \psi') \sin \phi' + x_3 \cos \phi' \\ - [\sin \phi' \cos \phi \cos(\psi' - \psi) - \cos \phi' \sin \phi]t + \sin \phi' \sin(\psi' - \psi)s. \quad (39)$$

The subsonic restriction on the growth of \mathfrak{R} guarantees that the wave front history defined in (29b) does not affect the limits of integration over (\mathfrak{R}, C) .

6. Planar \mathfrak{R} : Traction field

A local description does not imply knowledge of the traction field $(\sigma_{NS}, \sigma_{NT}, \sigma_{NN})$ on \mathfrak{R} . However, with (29) and (36)–(39) in hand, this field can be obtained by evaluation of the following expressions for $\mathbf{x} \in \mathfrak{R}$:

$$\begin{bmatrix} \sigma_{NN} \\ \sigma_{TT} \\ \sigma_{SS} \\ \sigma_{SN} \\ \sigma_{NT} \\ \sigma_{TS} \end{bmatrix} = \mu \begin{bmatrix} d_{11}^{NN} & d_{22}^{NN} & d_{33}^{NN} & d_{23}^{NN} & d_{31}^{NN} & d_{12}^{NN} \\ d_{11}^{TT} & d_{22}^{TT} & d_{33}^{TT} & d_{23}^{TT} & d_{31}^{TT} & d_{12}^{TT} \\ d_{11}^{SS} & d_{22}^{SS} & d_{33}^{SS} & d_{23}^{SS} & d_{31}^{SS} & d_{12}^{SS} \\ d_{11}^{SN} & d_{22}^{SN} & d_{33}^{SN} & d_{23}^{SN} & d_{31}^{SN} & d_{12}^{SN} \\ d_{11}^{NT} & d_{22}^{NT} & d_{33}^{NT} & d_{23}^{NT} & d_{31}^{NT} & d_{12}^{NT} \\ d_{11}^{TS} & d_{22}^{TS} & d_{33}^{TS} & d_{23}^{TS} & d_{31}^{TS} & d_{12}^{TS} \end{bmatrix} \begin{bmatrix} \partial_1 u_1 \\ \partial_2 u_2 \\ \partial_3 u_3 \\ \partial_2 u_3 + \partial_3 u_2 \\ \partial_3 u_1 + \partial_1 u_3 \\ \partial_1 u_2 + \partial_2 u_1 \end{bmatrix}, \quad (40a)$$

$$d_{ik}^{SN} = d_{ik}^{NS}, \quad d_{ik}^{NT} = d_{ik}^{TN}, \quad d_{ik}^{TS} = d_{ik}^{ST}. \quad (40b)$$

Dimensionless coefficient arrays $(d_{ik}^{NS}, d_{ik}^{NT}, d_{ik}^{NN})$ appear in (33), and are defined in Appendix B. Definitions of coefficient arrays $(d_{ik}^{TT}, d_{ik}^{SS}, d_{ik}^{TS})$ are also found there.

7. Planar \mathfrak{R} : Two special cases with application

Dip-slip and strike-slip faulting in seismology [Canitez and Toksoz 1972] and slip mechanisms in a crystal lattice [Read 1953] can be modeled as a spatially invariant dislocation distribution on an expanding surface. For such a distribution on \mathfrak{R} , the terms in (38) reduce to

$$[u_T] \oint_C dc P_{jk}(\sin \psi t + \cos \psi \sin \phi s) \cdot \mathbf{t}_C, \quad (41a)$$

$$-[u_T] \oint_C dc P_{jk}(\cos \psi t - \sin \psi \cos \phi s) \cdot \mathbf{t}_C, \quad (41b)$$

$$[u_T] \sin \phi \oint_C dc P_{jks} \cdot \mathbf{t}_C. \quad (41c)$$

The use of dislocation distributions that exhibit spatial variation to model internal cracks is well established [Bilby and Eshelby 1968; Barber 1992]. If \mathfrak{R} represents a crack plane, then $[\mathbf{u}] = 0$ ($\mathbf{x} \in C$) and only the integration over \mathfrak{R} in (38) remains. Results analogous to (41) exist, for example, [Brock 1986], for a nonplanar surface in an isotropic solid.

If the additional condition is imposed that a radial line from $\mathbf{x} = 0$ to any point on C lies within \mathfrak{R} , it is convenient to define (\mathfrak{R}, C) in terms of polar coordinates:

$$\mathfrak{R} : r < r_C(\theta', \tau), \quad C : r = r_C(\theta', \tau), \quad (42a)$$

$$t = r \cos \theta', \quad s = r \sin \theta' \quad (0 \leq \theta' \leq 2\pi). \quad (42b)$$

Here $(r_C, \partial r_C / \partial \theta')$ are single-valued and continuous in θ' . Quantities $(\partial r_C / \partial \theta', \partial r_C)$ are finite and, in particular, $\partial r_C < \min[c_A(\psi, \phi), c_B(\psi, \phi), c_C(\psi, \phi)]$. Use of (42) in (41c), for example, gives

$$[u_T] \sin \phi \int_0^{2\pi} P_{jk} \frac{\partial}{\partial \theta'} (r_C \sin \theta') d\theta'. \quad (43)$$

For the crack plane case, the corresponding result is

$$\sin \phi \int_0^{2\pi} P_{jk} d\theta' \int_0^{r_C} dr \left(r \frac{\partial}{\partial r} \sin \theta' + \cos \theta' \frac{\partial}{\partial \theta'} \right) [u_T]. \quad (44)$$

In the case of (44),

$$x - x' = (x_1 \cos \psi' + x_2 \sin \psi') \sin \phi' + x_3 \cos \phi' - r F(\phi, \phi', \psi' - \psi, \theta'), \quad (45a)$$

$$F = [\cos \theta' \sin(\psi' - \psi) + \cos \phi \sin \theta' \cos(\psi' - \psi)] \sin \phi' - \sin \theta' \sin \phi \cos \phi'. \quad (45b)$$

For (43), the symbol r in (45a) is replaced with $r_C(\theta', \tau')$.

8. Limit results

For an orthotropic solid [Ting 1996; Jones 1999] matrix \mathbf{K} is again defined by (13a), but $\mathbf{L} = 0$ and

$$\mathbf{M} = \begin{bmatrix} d_{12} + d_{66} & 0 & 0 \\ 0 & d_{23} + d_{44} & 0 \\ 0 & 0 & d_{13} + d_{55} \end{bmatrix}. \quad (46)$$

For transverse isotropy with respect to the $x_1 x_2$ -plane [Ting 1996; Jones 1999] $\mathbf{L} = 0$ and

$$\mathbf{K} = \begin{bmatrix} d_{11} & d_{66} & d_{55} \\ d_{66} & d_{11} & d_{55} \\ d_{55} & d_{55} & d_{33} \end{bmatrix}, \quad (47a)$$

$$\mathbf{M} = \begin{bmatrix} d_{11} - d_{66} & 0 & 0 \\ 0 & d_{13} + d_{55} & 0 \\ 0 & 0 & d_{13} + d_{55} \end{bmatrix}. \quad (47b)$$

For a cubic solid [Crandall and Dahl 1959] $\mathbf{L} = 0$ and

$$\mathbf{K} = \begin{bmatrix} d_{11} & 1 & 1 \\ 1 & d_{11} & 1 \\ 1 & 1 & d_{11} \end{bmatrix}, \quad \mathbf{M} = (d_{12} + 1)\mathbf{1}. \quad (48)$$

Here $\mathbf{1}$ is the identity tensor. For isotropy [Ting 1996; Jones 1999] $\mathbf{L} = 0$, \mathbf{K} is defined by (48), and

$$\mathbf{M} = (d_{11} - 1)\mathbf{1}. \quad (49)$$

Equations (25), (29), and (30) still hold for the orthotropic solid. Transverse isotropy (47) yields the more explicit results

$$c_A = \sqrt{d_{44} \cos^2 \phi' + d_{66} \sin^2 \phi'}, \quad (50a)$$

$$(c_A^2, c_C^2) = \frac{1}{2} (d_{44} + d_{11} \sin^2 \phi' + d_{33} \cos^2 \phi') \pm \frac{1}{2} \sqrt{(d_{33} \cos^2 \phi' - d_{11} \sin^2 \phi' - d_4 \cos 2\phi')^2 + (d_{44} + d_{13})^2 \sin^2 2\phi'}. \quad (50b)$$

Moreover, $T_B + T_C$ replaces $T_A + T_B + T_C$ in terms that involve $(d_{31}^{NT}, d_{31}^{NS}, d_{31}^{NN})$ and $(d_{23}^{NT}, d_{23}^{NS}, d_{23}^{NN})$ in (37), where

$$T_L = \frac{\tau - \tau'}{M_L |x - x'|} \left(\tau - \tau' > \frac{|x - x'|}{c_L} \right), \quad (51a)$$

$$M_B = (\tau - \tau')^2 - \left(\frac{x - x'}{c_C} \right)^2, \quad M_C = (\tau - \tau')^2 - \left(\frac{x - x'}{c_B} \right)^2. \quad (51b)$$

It should be noted that conditions specific to transversely isotropic solids that guarantee that $\alpha^3 - \beta^2 > 0$ are given in detail in [Payton 1983]. For the cubic solid

$$c_A = 1, \quad (52a)$$

$$(c_B^2, c_C^2) = \frac{1}{2} (d_{11} + 1) \pm \frac{1}{2} \sin \phi' \sqrt{(d_{11} - 1)^2 \sin^2 \phi' + (d_{12} + 1)^2 \cos^2 \phi'}. \quad (52b)$$

The results associated with (51) still hold. For the isotropic solid $c_A = c_C$, so only two speeds $(v_B, v_C) = (c_B, c_C)v_S$ exist, where

$$c_B = \sqrt{d_{11}}, \quad c_C = 1. \quad (53)$$

Thus, isotropy corresponds to the case $\alpha^3 - \beta^2 = 0$ noted above, and (36) involves only terms of the type (51).

As an illustration of wave speed variation with propagation direction, a transversely isotropic graphite-epoxy [Jones 1999] is considered with

$$\mu = C_{44} = 7.07 \text{ GPa}, \quad v_S = 2546 \text{ m/s}, \quad d_{44} = 1.0, \quad d_{66} = 0.4951,$$

$$\begin{bmatrix} d_{11} & d_{12} & d_{31} \\ d_{12} & d_{11} & d_{31} \\ d_{31} & d_{31} & d_{33} \end{bmatrix} = \begin{bmatrix} 1.9689 & 0.9788 & 0.9109 \\ 0.9788 & 1.9689 & 0.9109 \\ 0.9109 & 0.9109 & 22.73 \end{bmatrix}.$$

Use of these properties in (50) gives the values of dimensionless speeds (c_A, c_B, c_C) shown in Table 1 for $0 \leq \phi' \leq 90^\circ$. It is seen that the values are quite sensitive to ϕ' ; compare [Wang and Achenbach 1994].

9. Concluding remarks

The present formulation leads to transient expressions that are multiple integrals in a unit spherical quadrant in terms of polar and azimuthal angles, that is, $(|\psi'| < \pi/2, 0 \leq \phi' \leq \pi/2)$, but are explicit functions of Cartesian principal material coordinates. Approaches used to produce the anisotropic Green's function, for example, [Wang and Achenbach 1995; Ting 1996], are similar but feature integration over the surface

	c_A	c_B	c_C
$\phi' = 0^\circ$	1.0	4.8197	0.7071
15°	0.9829	4.6650	0.7595
30°	0.9348	4.2094	0.9057
45°	0.8646	3.4926	1.0730
60°	0.7882	2.5908	1.2029
75°	0.7272	1.7096	1.1986
90°	0.7036	1.4042	1.0

Table 1. Graphite-epoxy: dimensionless speeds ($v_S = 2546$ m/s).

of a unit sphere or around a unit circle [Synge 1957]. Nevertheless, for a planar dislocation surface, the present integration process can in fact be carried out in terms of a polar coordinate system (r, θ') in the plane. Moreover, Stokes's theorem [Hay 1953] can be invoked to replace portions of the area integration with integration around the area contour. The description of the dislocation distribution in terms of surface geometry does produce lengthier solution expressions. However, climb and glide mechanisms can be identified explicitly in terms of matrix/tensor arrays that are similar to those defined in analyses of general anisotropy; see [Ting 1996], for example. Related arrays that characterize the orientation of the dislocation surface and its climb and glide components with respect to the principal material axes arise, and resemble in form the constitutive relation for the solid itself. In summary, the disadvantages of the length and complexity of these solutions, and their combination of standard coordinate systems, may be compensated for by a more explicit nature. This nature may be of advantage in cases where solution response to particular dislocation features is of interest.

Appendix A

The dimensionless coefficient array $d_{ik}^{NS}(\mathbf{x}', \tau)$ is defined by

$$\begin{bmatrix} d_{11}^{NS} \\ d_{22}^{NS} \\ d_{33}^{NS} \\ d_{23}^{NS} \\ d_{31}^{NS} \\ d_{12}^{NS} \end{bmatrix} = \begin{bmatrix} d_1 & d_{12} & d_{13} & d_{14} & d_{15} & d_{16} \\ d_{12} & d_{22} & d_{23} & d_{24} & d_{25} & d_{26} \\ d_{13} & d_{23} & d_{33} & d_{34} & d_{35} & d_{36} \\ d_{14} & d_{24} & d_{34} & d_{44} & d_{45} & d_{46} \\ d_{15} & d_{25} & d_{35} & d_{45} & d_{55} & d_{56} \\ d_{16} & d_{26} & d_{36} & d_{46} & d_{56} & d_{66} \end{bmatrix} \begin{bmatrix} s_1 n_1 \\ s_2 n_2 \\ s_3 n_3 \\ s_2 n_3 + s_3 n_2 \\ s_3 n_1 + s_1 n_3 \\ s_1 n_2 + s_2 n_1 \end{bmatrix}, \quad (\text{A.1a})$$

$$d_{ik}^{NS} = d_{ki}^{NS}. \quad (\text{A.1b})$$

Here $s_l(\mathbf{x}', \tau)$ and $n_l(\mathbf{x}')$ are the direction cosines of (\mathbf{s}, \mathbf{n}) in the principal material basis. It is noted that (A.1) resembles constitutive equations (1)–(3), with d_{ik}^{NS} playing the role of (dimensionless) stresses, and $(s_i n_i, s_i n_k + s_k n_i)$ acting as strains $(\partial_i u_i, \partial_i u_k + \partial_k u_i)$. Coefficients d_{ik}^{NS} follow by replacing s_l with n_l .

Appendix B

Dimensionless coefficient array d_{ik}^{NT} is defined by

$$\begin{bmatrix} d_{11}^{NT} \\ d_{22}^{NT} \\ d_{33}^{NT} \\ d_{23}^{NT} \\ d_{31}^{NT} \\ d_{12}^{NT} \end{bmatrix} = \begin{bmatrix} d_{11} & d_{12} & d_{13} & d_{14} & d_{15} & d_{16} \\ d_{12} & d_{22} & d_{23} & d_{24} & d_{25} & d_{26} \\ d_{13} & d_{23} & d_{33} & d_{34} & d_{35} & d_{36} \\ d_{14} & d_{24} & d_{34} & d_{44} & d_{45} & d_{46} \\ d_{15} & d_{25} & d_{35} & d_{45} & d_{55} & d_{56} \\ d_{16} & d_{26} & d_{36} & d_{46} & d_{56} & d_{66} \end{bmatrix} \begin{bmatrix} t_1 n_1 \\ t_2 n_2 \\ t_3 n_3 \\ t_2 n_3 + t_3 n_2 \\ t_3 n_1 + t_1 n_3 \\ t_1 n_2 + t_2 n_1 \end{bmatrix}, \quad (\text{B.1a})$$

$$d_{ik}^{NT} = d_{ki}^{NT}. \quad (\text{B.1b})$$

Terms (t_l, n_l) are direction cosines of (\mathbf{t}, \mathbf{n}) in the principal material basis. For planar \mathfrak{R} , of course, direction cosines are constant. Results for $(d_{ik}^{NS}, d_{ik}^{NN})$ follow from (B.1) by replacing direction cosine t_l with, respectively, direction cosine (s_l, n_l) .

Another set of dimensionless coefficients $(d_{ik}^{TS}, d_{ik}^{TT}, d_{ik}^{SS})$ can also be defined, where

$$\begin{bmatrix} d_{11}^{TS} \\ d_{22}^{TS} \\ d_{33}^{TS} \\ d_{23}^{TS} \\ d_{31}^{TS} \\ d_{12}^{TS} \end{bmatrix} = \begin{bmatrix} d_{11} & d_{12} & d_{13} & d_{14} & d_{15} & d_{16} \\ d_{12} & d_{22} & d_{23} & d_{24} & d_{25} & d_{26} \\ d_{13} & d_{23} & d_{33} & d_{34} & d_{35} & d_{36} \\ d_{14} & d_{24} & d_{34} & d_{44} & d_{45} & d_{46} \\ d_{15} & d_{25} & d_{35} & d_{45} & d_{55} & d_{56} \\ d_{16} & d_{26} & d_{36} & d_{46} & d_{56} & d_{66} \end{bmatrix} \begin{bmatrix} t_1 s_1 \\ t_2 s_2 \\ t_3 s_3 \\ t_2 s_3 + t_3 s_2 \\ t_3 s_1 + t_1 s_3 \\ t_1 s_2 + t_2 s_1 \end{bmatrix}, \quad (\text{B.2a})$$

$$d_{ik}^{TS} = d_{ki}^{TS}. \quad (\text{B.2b})$$

Terms $(d_{ik}^{TT}, d_{ik}^{SS})$ follow from (B.2) by, respectively, replacing s_l with t_l and t_l with s_l .

Equations (B.1) and (B.2) also show that

$$d_{ik}^{TN} = d_{ki}^{NT}, \quad d_{ik}^{SN} = d_{ik}^{NS}, \quad d_{ik}^{TS} = d_{ik}^{ST}. \quad (\text{B.3})$$

Equations (B.1) and (B.2) resemble (A.1), so that the forms of $(d_{ik}^{NT}, d_{ik}^{NS}, d_{ik}^{TS})$ also resemble constitutive equations (1)–(3).

References

- [Abramowitz and Stegun 1972] M. Abramowitz and I. A. Stegun, *Handbook of mathematical functions: With formulas, graphs, and mathematical tables*, Dover, New York, 1972.
- [Barber 1992] J. R. Barber, *Elasticity, Solid Mechanics and its Applications* **12**, Kluwer, Dordrecht, 1992.
- [Barnett and Lothe 1973] D. M. Barnett and J. Lothe, "Synthesis of the sextic and the integral formalism for dislocations, Green's function and surface waves in anisotropic elastic solids", *Physica Norvegica* **7** (1973), 13–19.
- [Bilby and Eshelby 1968] B. A. Bilby and J. D. Eshelby, "Dislocations and the theory of fracture", pp. 99–182 in *Fracture*, vol. 1, edited by H. Liebowitz, Academic Press, New York, 1968.
- [Brock 1986] L. M. Brock, "A transient three dimensional analysis of non-uniform dislocation distribution growth by climb and glide over non-planar surfaces", *Proceedings of the Royal Society of London, A* **407** (1986), 299–311.

- [Burridge and Knopoff 1964] R. Burridge and L. Knopoff, “Body force equivalents for seismic dislocations”, *Bulletin of the Seismological Society of America* **54** (1964), 1875–1888.
- [Canitez and Toksoz 1972] N. Canitez and M. N. Toksoz, “Static and dynamic study of earthquake source mechanisms: San Fernando earthquake”, *Journal of Geophysical Research* **77** (1972), 2583–2594.
- [Crandall and Dahl 1959] S. H. Crandall and N. C. Dahl, *An introduction to the mechanics of solids*, McGraw-Hill, New York, 1959.
- [Hay 1953] G. E. Hay, *Vector and tensor analysis*, Dover, New York, 1953.
- [Hohn 1964] F. E. Hohn, *Elementary matrix algebra*, 2nd ed., Macmillan, New York, 1964.
- [Jones 1999] R. M. Jones, *Mechanics of composite materials*, 2nd ed., Brunner-Routledge, New York, 1999.
- [Knopoff and Gilbert 1960] L. Knopoff and F. Gilbert, “First motions from seismic sources”, *Bulletin of the Seismological Society of America* **134** (1960), 117–134.
- [Nabarro 1951] F. R. N. Nabarro, “The synthesis of elastic dislocation fields”, *Philos. Mag.* (7) **42** (1951), 1224–1231.
- [Payton 1983] R. G. Payton, *Elastic wave propagation in transversely isotropic media*, Martinus Nijhoff, The Hague, 1983.
- [van der Pol and Bremmer 1950] B. van der Pol and H. Bremmer, *Operational calculus, based on the two-sided Laplace integral*, Cambridge University Press, 1950.
- [Read 1953] W. T. Read, *Dislocations in crystals*, McGraw-Hill, New York, 1953.
- [Sneddon 1972] I. N. Sneddon, *The use of integral transforms*, McGraw-Hill, New York, 1972.
- [Stroh 1958] A. N. Stroh, “Dislocations and cracks in anisotropic elasticity”, *Phil. Mag.* (8) **3** (1958), 625–646.
- [Stroh 1962] A. N. Stroh, “Steady state problems in anisotropic elasticity”, *J. Math. and Phys.* **41** (1962), 77–103.
- [Synge 1957] J. L. Synge, *The hypercircle in mathematical physics: a method for the approximate solution of boundary value problems*, Cambridge University Press, 1957.
- [Ting 1996] T. C. T. Ting, *Anisotropic elasticity: Theory and applications*, Oxford Engineering Science Series **45**, Oxford University Press, New York, 1996.
- [Ting and Lee 1997] T. C. T. Ting and V.-G. Lee, “The three-dimensional elastostatic Green’s function for general anisotropic linear elastic solids”, *Quart. J. Mech. Appl. Math.* **50**:3 (1997), 407–426.
- [Wang and Achenbach 1994] C.-Y. Wang and J. D. Achenbach, “Elastodynamic fundamental solutions for anisotropic solids”, *Geophysics Journal International* **118** (1994), 384–392.
- [Wang and Achenbach 1995] C.-Y. Wang and J. D. Achenbach, “Three-dimensional time-harmonic elastodynamic Green’s functions for anisotropic solids”, *Proc. Roy. Soc. London Ser. A* **449**:1937 (1995), 441–458.
- [Willis 1980] J. R. Willis, “A polarization approach to the scattering of elastic waves, I: Scattering by a single inclusion”, *J. Mech. Phys. Solids* **28**:5-6 (1980), 287–305.

Received 7 Jan 2013. Revised 5 Mar 2013. Accepted 5 Mar 2013.

LOUIS MILTON BROCK: brock@engr.uky.edu

Department of Mechanical Engineering, University of Kentucky, 265 Ralph G. Anderson Building, Lexington, KY 40506-0503, United States

SUBMISSION GUIDELINES

ORIGINALITY

Authors may submit manuscripts in PDF format online at the Submissions page. Submission of a manuscript acknowledges that the manuscript is original and has neither previously, nor simultaneously, in whole or in part, been submitted elsewhere. Information regarding the preparation of manuscripts is provided below. Correspondence by email is requested for convenience and speed. For further information, write to contact@msp.org.

LANGUAGE

Manuscripts must be in English. A brief abstract of about 150 words or less must be included. The abstract should be self-contained and not make any reference to the bibliography. Also required are keywords and subject classification for the article, and, for each author, postal address, affiliation (if appropriate), and email address if available. A home-page URL is optional.

FORMAT

Authors can use their preferred manuscript-preparation software, including for example Microsoft Word or any variant of $\text{T}_{\text{E}}\text{X}$. The journal itself is produced in $\text{L}^{\text{A}}\text{T}_{\text{E}}\text{X}$, so accepted articles prepared using other software will be converted to $\text{L}^{\text{A}}\text{T}_{\text{E}}\text{X}$ at production time. Authors wishing to prepare their document in $\text{L}^{\text{A}}\text{T}_{\text{E}}\text{X}$ can follow the example file at www.jomms.net (but the use of other class files is acceptable). At submission time only a PDF file is required. After acceptance, authors must submit all source material (see especially Figures below).

REFERENCES

Bibliographical references should be complete, including article titles and page ranges. All references in the bibliography should be cited in the text. The use of $\text{BibT}_{\text{E}}\text{X}$ is preferred but not required. Tags will be converted to the house format (see a current issue for examples); however, for submission you may use the format of your choice. Links will be provided to all literature with known web locations; authors can supply their own links in addition to those provided by the editorial process.

FIGURES

Figures must be of publication quality. After acceptance, you will need to submit the original source files in vector format for all diagrams and graphs in your manuscript: vector EPS or vector PDF files are the most useful. (EPS stands for Encapsulated PostScript.)

Most drawing and graphing packages—Mathematica, Adobe Illustrator, Corel Draw, MATLAB, etc.—allow the user to save files in one of these formats. Make sure that what you're saving is vector graphics and not a bitmap. If you need help, please write to graphics@msp.org with as many details as you can about how your graphics were generated.

Please also include the original data for any plots. This is particularly important if you are unable to save Excel-generated plots in vector format. Saving them as bitmaps is not useful; please send the Excel (.xls) spreadsheets instead. Bundle your figure files into a single archive (using zip, tar, rar or other format of your choice) and upload on the link you been given at acceptance time.

Each figure should be captioned and numbered so that it can float. Small figures occupying no more than three lines of vertical space can be kept in the text (“the curve looks like this:”). It is acceptable to submit a manuscript with all figures at the end, if their placement is specified in the text by means of comments such as “Place Figure 1 here”. The same considerations apply to tables.

WHITE SPACE

Forced line breaks or page breaks should not be inserted in the document. There is no point in your trying to optimize line and page breaks in the original manuscript. The manuscript will be reformatted to use the journal's preferred fonts and layout.

PROOFS

Page proofs will be made available to authors (or to the designated corresponding author) at a Web site in PDF format. Failure to acknowledge the receipt of proofs or to return corrections within the requested deadline may cause publication to be postponed.

Journal of Mechanics of Materials and Structures

Volume 8, No. 2-4

April–June 2013

- A diffuse cohesive energy approach to fracture and plasticity: the one-dimensional case**
GIANPIETRO DEL PIERO, GIOVANNI LANCIONI and RICCARDO MARCH 109
- Continuum deployable shells made of thin plates**
VLADIMIR A. GRACHEV and YURIY S. NEUSTADT 153
- Self-folding of a slender microbeam and thin film: an elastica model**
JIANLIN LIU and JUNG HOON LEE 169
- Dispersion of guided waves in initially stressed layered plates**
JIANGONG YU and SHENLEI LI 185
- Empirical models for predicting protective properties of concrete shields against high-speed impact**
GABI BEN-DOR, ANATOLY DUBINSKY and TOV ELPERIN 199
- Transient response of a general anisotropic solid to dislocation growth: alternative formulation**
LOUIS MILTON BROCK 233



1559-3959(2013)8:2;1-A